Optical Microwave Signal Generation for Data Transmission in Optical Networks

Christian Daniel Muñoz Arcos

Optical Microwave Signal Generation for Data Transmission in Optical Networks

Christian Daniel Muñoz Arcos

A dissertation submitted in partial satisfaction of the requirements for the degree of:
Doctor in Engineering − Electrical Engineering

International joint thesis supervision with the:
Institut Supérieur de l'Aéronautique et de l'Espace ISAE-SUPAERO

Directed by
Ph.D. Gloria Margarita Varón Durán
Departamento de Ingeniería Eléctrica y Electrónica. Universidad Nacional de Colombia.
Bogotá, Colombia

Ph.D. Angélique Rissons
Département Électronique, Optonique et Signal. Institut Supérieur de l'Aéronautique et de l'Espace ISAE-SUPAERO. Toulouse, France

Co-Directed by
Ph.D. Fabien Destic
Département Électronique, Optonique et Signal. Institut Supérieur de l'Aéronautique et de l'Espace ISAE-SUPAERO. Toulouse, France

Universidad Nacional de Colombia
Facultad de Ingeniería, Departamento de Ingeniería Eléctrica y Electrónica
Bogotá, Colombia
2020

A Lucía
y
Carlos Alberto

Acknowledgements

Abstract

The massive growth of telecommunication services and the increasing global data traffic boost the development, implementation, and integration of different networks for data transmission. An example of this development is the optical fiber networks, responsible today for the inter-continental connection through long-distance links and high transfer rates. The optical networks, as well as the networks supported by other transmission media, use electrical signals at specific frequencies for the synchronization of the network elements. The quality of these signals is usually determined in terms of phase noise. Due to the major impact of the phase noise over the system performance, its value should be minimized.

The research work presented in this document describes the design and implementation of an optoelectronic system for the microwave signal generation using a vertical-cavity surface-emitting laser (VCSEL) and its integration into an optical data transmission system. Considering that the proposed system incorporates a directly modulated VCSEL, a theoretical and experimental characterization was developed based on the laser rate equations, dynamic and static measurements, and an equivalent electrical model of the active region. This procedure made possible the extraction of some VCSEL intrinsic parameters, as well as the validation and simulation of the VCSEL performance under specific modulation conditions. The VCSEL emits in C-band, this wavelength was selected because it is used in long-haul links.

The proposed system is a self-initiated oscillation system caused by internal noise sources, which includes a VCSEL modulated in large signal to generate optical pulses (gain switching). The optical pulses, and the optical frequency comb associated, generate in electrical domain simultaneously a fundamental frequency (determined by a band-pass filter) and several harmonics. The phase noise measured at 10 kHz from the carrier at 1.25 GHz was -127.8 dBc/Hz, and it is the lowest value reported in the literature for this frequency and architecture. Both the jitter and optical pulse width were determined when different resonant cavities and polarization currents were employed. The lowest pulse duration was 85 ps and was achieved when the fundamental frequency was 2.5 GHz. As for the optical frequency comb, it was demonstrated that its flatness depends on the electrical modulation conditions. The flattest profiles are obtained when the fundamental frequency is higher than the VCSEL relaxation frequency.

Both the electrical and the optical output of the system were integrated into an optical transmitter. The electrical signal provides the synchronization of the data generating equipment, whereas the optical pulses are employed as an optical carrier. Data transmissions at 155.52 Mb/s, 622.08 Mb/s and 1.25 Gb/s were experimentally validated. It was demonstrated that the fundamental frequency and harmonics could be extracted from the optical data signal transmitted by a band-pass filter. It was also experimentally proved that the pulsed return-to-zero (RZ) transmitter at 1.25 Gb/s, achieves bit error rates (BER) lower than 10^{-9} when the optical power at the receiver is higher than -33 dBm.

Resumen

La masificación de los servicios de telecomunicaciones y el creciente tráfico global de datos han impulsado el desarrollo, despliegue e integración de diferentes redes para la transmisión de datos. Un ejemplo de este despliegue son las redes de fibra óptica, responsables en la actualidad de la interconexión de los continentes a través de enlaces de grandes longitudes y altas tasas de transferencia. Las redes ópticas, al igual que las redes soportadas por otros medios de transmisión, utilizan señales eléctricas a frecuencias específicas para la sincronización de los elementos de red. La calidad de estas señales es determinante en el desempeño general del sistema, razón por la que su ruido de fase debe ser lo más pequeño posible.

El trabajo de investigación presentado en este documento describe el diseño e implementación de un sistema optoelectrónico para la generación de señales microondas utilizando diodos láser de cavidad vertical (VCSEL) y su integración en un sistema de transmisión de datos óptico. Teniendo en cuenta que el sistema propuesto incorpora un láser VCSEL modulado directamente, se desarrolló una caracterización teórico-experimental basada en las ecuaciones de evolución del láser, mediciones dinámicas y estáticas, y un modelo eléctrico equivalente de la región activa. Este procedimiento posibilitó la extracción de algunos parámetros intrínsecos del VCSEL, al igual que la validación y simulación de su desempeño bajo diferentes condiciones de modulación. El VCSEL emite en banda C y fue seleccionado considerando que esta banda es comúnmente utilizada en enlaces de largo alcance.

El sistema propuesto consiste en un lazo cerrado que inicia la oscilación gracias a las fuentes de ruido de los componentes y modula el VCSEL en gran señal para generar pulsos ópticos (conmutación de ganancia). Estos pulsos ópticos, que en el dominio de la frecuencia corresponden a un peine de frecuencia óptico, son detectados para generar simultáneamente una frecuencia fundamental (determinada por un filtro pasa banda) y varios armónicos. El ruido de fase medido a 10 kHz de la portadora a 1.25 GHz fue -127.8 dBc/Hz, y es el valor más bajo reportado en la literatura para esta frecuencia y arquitectura. Tanto la fluctuación de fase (jitter) y el ancho de los pulsos ópticos fueron determinados cuando diferentes cavidades resonantes y corrientes de polarización fueron empleadas. La duración de pulso más baja fue 85 ps y se obtuvo cuando la frecuencia fundamental del sistema era 2.5 GHz. En cuanto al peine de frecuencia óptico, se demostró que su planitud (flatness) depende de las condiciones eléctricas de modulación y que los perfiles más planos se obtienen cuando la frecuencia fundamental es superior a la frecuencia de relajación del VCSEL.

Tanto la salida eléctrica como la salida óptica del sistema fueron integradas en un transmisor óptico. La señal eléctrica permite la sincronización de los equipos encargados de generar los datos, mientras que los pulsos ópticos son utilizados como portadora óptica. La transmi-

sión de datos a 155.52 Mb/s, 622.08 Mb/s y 1.25 Gb/s fue validada experimentalmente. Se demostró que la frecuencia fundamental y los armónicos pueden ser extraídos de la señal óptica de datos transmitida mediante un filtro pasa banda. También se comprobó experimentalmente que el transmisor de datos pulsados con retorno a cero (RZ) a 1.25 Gb/s, logra tasas de error de bit (BER) menores a 10^{-9} cuando la potencia óptica en el receptor es mayor a -33 dBm.

Palabras clave: armónico, conmutación de ganancia, microondas, oscilador optoelectrónico, peine de frecuencia, ruido de fase, VCSEL.

Résumé

La croissance des services de télécommunications et l'augmentation du trafic de données à l'échelle mondiale favorise le développement et l'intégration de différents réseaux de transmission de données. Un exemple de ce développement est constitué par les réseaux de fibres optiques, qui sont actuellement chargés d'interconnecter les continents par des liaisons longues avec des taux de transfert importants. Les réseaux optiques, ainsi que les réseaux supportés par d'autres moyens de transmission, utilisent des signaux électriques à certaines fréquences pour la synchronisation des éléments du réseau. La qualité de ces signaux est un facteur décisif dans la performance globale du système, c'est pourquoi leur bruit de phase doit être aussi faible que possible.

Ce document décrit la conception et la mise en œuvre d'un système optoélectronique pour la génération de signaux micro-ondes à l'aide de diodes laser à cavité verticale (VCSEL) et son intégration dans un système de transmission optique de données. Compte tenu du fait que le système proposé intègre un laser VCSEL directement modulé, une caractérisation théorique et expérimentale a été élaborée sur la base des équations d'évolution du laser, de mesures dynamiques et statiques, et d'un modèle électrique équivalent de la région active. Cette methode a permis l'extraction de certains paramètres intrinsèques du VCSEL, ainsi que la validation et la simulation de ses performances dans différentes conditions de modulation. Le VCSEL utilisé émet en bande C et a été sélectionné en considérant que cette bande est couramment utilisée dans les liaisons à longue distance.

Le système proposé est constitué d'une boucle fermée qui déclenche l'oscillation grâce aux sources de bruit des composants et module le VCSEL en fort signal pour générer des impulsions optiques (gain switching). Ces impulsions optiques, qui dans le domaine des fréquences correspondent à un peigne de fréquences optiques, sont détectées pour générer simultanément une fréquence fondamentale (déterminée par un filtre passe-bande) et plusieurs harmoniques. Le bruit de phase mesuré à 10 kHz de la porteuse à 1,25 GHz est de -127,8 dBc/Hz, et constitue la valeur la plus faible signalée dans la littérature pour cette fréquence et cette architecture. La gigue et la largeur d'impulsion optique ont été déterminées lorsque différentes cavités résonantes et différents courants de polarisation étaient utilisés. La durée d'impulsion

la plus faible, 85 ps, a été obtenue lorsque la fréquence fondamentale du système était de 2,5 GHz. En ce qui concerne le peigne de fréquences optiques, il a été démontré que la forme du peigne dépend des conditions de modulation électrique et que les profils les plus plats sont obtenus lorsque la fréquence fondamentale est supérieure à la fréquence de relaxation du VCSEL.

Les sorties électrique et optique du système ont été intégrées dans un émetteur optique. Le signal électrique permet la synchronisation de l'équipement responsable de la génération des données, tandis que les impulsions optiques sont utilisées comme porteuse optique. La transmission de données à 155,52 Mb/s, 622,08 Mb/s et 1,25 Gb/s a été validée expérimentalement. Il a été démontré que la fréquence fondamentale et les harmoniques peuvent être extraits du signal de données optique transmis. Il a également été prouvé expérimentalement que l'émetteur de données pulsées à retour-à-zéro (RZ) à 1,25 Gb/s, permet d'obtenir des taux d'erreur binaire (BER) inférieurs à 10-9 lorsque la puissance optique reçue est supérieure à -33 dBm.

Mots-clés: bruit de phase, commutation de gain, harmonique, micro-ondes, oscillateur optoelectronique, peigne de frequénces, VCSEL.

Contents

List of Figures

List of Tables

Acronyms and Symbols

Acronyms

Acronym	Explanation
$ADEV$	Allan deviation
ADS	Advanced Design System
ASE	Amplified Spontaneous Emission
$AVAR$	Allan variance
BER	Bit error rate
BPF	Band-pass filter
$BPSK$	Binary phase-shift keying
BW	Bandwidth
CAD	Computer-aided design
CNR	Carrier-to-noise ratio
CW	Continuous-wave
DBR	Distributed Bragg reflectors
DFB	Distribute-feedback laser
DFB	Distribute-feedback
DJ	Deterministic jitter
$DRBS$	Double Rayleigh backscattering
EAM	Electro-absorption modulator
EC	Electrical coupler
$EDFA$	Erbium-doped fiber amplifier
ESA	Electrical spectrum analyzer
FBG	Fiber Bragg grating
FM	Frequency modulation
FSO	Free-space optical communications
FSR	Free spectral range
$FWHM$	Full-width at half-maximum
GS	Gain switching

HFG	Harmonic frequency generator
LW	Long-wavelength
$MATP$	Maximum transmission point
$MITP$	Minimum transmission point
MM	Multi-mode
$MOCVD$	Metalorganic chemical vapor deposition
MWP	Microwave photonics
MZM	Mach-Zehnder modulator
NRZ	Non-return-to-zero
OEO	Optoelectronic oscillator
OFC	Optical frequency comb
OIL	Optical injection locking
OOK	On-off keying
$OPLL$	Optical phase lock loop
OWC	Optical wireless communications
PAM	Pulse-amplitude modulation
PC	Polarization controller
PD	Photodetector
PJ	Periodic jitter
$PRBS$	Pseudorandom binary sequence
$PRBS$	Pseudorandom binary sequence
$QPSK$	Quadrature phase-shift keying
QW	Quantum well
RF	Radio frequency
RIN	Relative intensity noise
RJ	Random jitter
RZ	Return-to-zero
SBS	Stimulated Brillouin scattering
SM	Single-mode
$SMSR$	Side mode suppression ratio
$SRBS-SR$	Single Rayleigh backscattering - single reflection
SRS	Stimulated Raman scattering
SSB	Single sideband
$SVHFG$	Self-started VCSEL-based harmonic frequency generator
$SVOFC$	Self-started VCSEL-based optical frequency comb generator
SW	Short-wavelength
TIE	Time interval error
TJ	Tunnel junction
TO	Transistor outline package
TOD	Turn-on delay
VBO	VCSEL-base optoelectronic oscillator
$VCSEL$	Vertical-cavity surface-emitting laser
VNA	Vector network analyzer
VOA	Variable optical attenuator

VPI	VPIphotonics Design Suit™
WDM	Wavelength-division multiplexing
WPE	Wall-plug efficiency

Symbols

Symbol	Explanation
α_H	Henry Factor
β	Spontaneous emission coefficient
$\Delta\nu(t)$	Frequency chirp
ϵ	Gain compression factor
η_d	Differential quantum efficiency
η_i	Internal quantum efficiency
Γ	Longitudinal confinement factor
γ	Damping factor
λ_0	Zero dispersion wavelength
$\mathscr{L}(f)$	Single sideband phase noise
ν_0	Nominal oscillation frequency
ω_R	Relaxation resonance pulsation
$\phi(t)$	Optical phase
$\psi(s)$	Noise sources
$\Re$	Photodetector responsivity
σ_{RMS}	RMS phase-jitter
$\sigma_y^2(\tau)$	Allan variance or two-sample variance
τ_d	Optical fiber time delay
τ_N	Carrier lifetime
τ_P	Photon lifetime
υ_g	Group velocity
$\varepsilon(t)$	Amplitude variations
$\bar{y}_k$	Time average of fractional-frequency
$\varphi(t)$	Phase fluctuations
A	Shockly-Read-Hall non-radiative recombination coefficient
a_0	Differential gain coefficient
B	radiative recombination coefficient
B_d	Transfer function of the delay line
B_f	Transfer function of the band-pass filter
b_n	Noise level coefficients of power-law model
C	Auger non-radiative recombination coefficient
c	Speed of light
f	Fourier frequency
F	Noise figure
f_R	Relaxation resonance frequency

f_0	Oscillating or fundamental frequency
f_c	Corner frequency
f_L	Leeson frequency
$F_N(t)$	Langevin white-noise sources for carrier densities variations
$F_S(t)$	Langevin white-noise sources for photon densities variations
G	Optical gain
I	Injected current
I_{bias}	Bias current
I_{th}	Threshold current
L	Optical fiber length
m	Modulation index
$Mod\ \sigma_y^2(\tau)$	Modified Allan variance
n_F	Effective refractive index
$N(t)$	Carrier density
N_{tr}	Transparency carrier density
$P(t)$	Photon density
P_0	Electrical power at the amplifier input
Q	Resonator quality factor
Q_f	Filter quality factor
R_{ph}	Load photodetector resistance
S_ψ	Power spectral density of noise sources
$S_{\Delta\nu}(f)$	Power spectral density of frequency fluctuations
$S_\varphi(f)$	Power spectral density of phase fluctuations
$S_x(f)$	Power spectral density of phase-time fluctuations
$S_y(f)$	Power spectral density of fractional frequency fluctuations
S_0	Zero dispersion slope
t_D	Turn-on delay
V_{act}	Active region volume
V_{cav}	Cavity volume
$x(t)$	Phase-time fluctuation
$y(t)$	Fractional-frequency fluctuation
Z_{ph}	Impedance load of the photodetector
Z_A	Input impedance of the microwave amplifier

Introduction

The development of telecommunication systems over the last decades has been driven by the high demand for services generated by the growing user requirements. This process has included the improvement of old systems that are still operational today but has also implied the creation of new systems supported by different data transmission technologies to provide different qualities of service. One effect of this evolution on wireless technologies has been the exploration and use of new frequency bands. A clear example of this phenomenon is the latest generation of cellular data networks 5G, based on the Internet Protocol IP, with a network architecture that includes different technologies and radio frequencies above 50 GHz [11]. Along the same lines, wireless local area networks and, more precisely, Wireless Fidelity Wi-Fi networks, today include standards for data transmission using unlicensed millimeter waves at 60 GHz (standard referred to as WiGig [12]). Similarly, fiber-based telecommunications networks have become an essential element due to the high transfer rates achieved using low attenuation optical fibers and effective multiplexing techniques. The increasing use of fiber optic networks at different wavelengths has contributed to the development of semiconductor lasers with considerable bandwidths and fast detectors that are now also used in optical wireless communications.

At the beginning of the 90s and supported by the increasing bandwidth of optoelectronic components, the term microwave photonics (MWP) emerged [13], covering the generation and transport of microwave signals. However, since the '80s, different techniques of microwave signal generation based on optoelectronic components have been developed. MWP generation systems are highly applied in telecommunications systems (they require a clock or carrier signal) thanks to the high spectral purity, and the high frequencies achieved. One of the most used and sophisticated architectures is the Optoelectronic Oscillator (OEO) [14] due to its high configuration flexibility and outstanding performance (low phase noise). A remarkable advantage of the OEO is the possibility of extracting the microwave signal in the electrical and optical domains. In this way, the optical signal can be transported directly through an optical fiber link or employed for data generation and pulse shaping processes.

Laser sources, indispensable for MWP generation systems, have been developed in parallel thanks to improved manufacturing techniques and the incorporation of multiple quantum

wells in the active region. The use of these lasers depends on the emission characteristics (e.g., single-mode lasers) and technical requirements, such as the optical power and bandwidth for long haul optical links. The vertical-cavity surface-emitting lasers (VCSEL) emerged as a low optical power laser source used exclusively in short distance applications at short wavelengths. Although its low emission power limits its applicability, the reduced size and optical cavity structure generate a single-mode response, in addition to reducing the threshold current, power consumption, and manufacturing and wafer-level testability costs. These advantages, transferred to the VCSELs at long wavelengths (mainly covering O-band and C-band), have made possible the use of VCSELs in optical communications, sensing applications, and microwave signal generation.

The VCSEL-based optoelectronic oscillator (VBO), proposed in 2007 [15,16], is a closed-loop system where a VCSEL is modulated directly by the generated microwave signal. Although its simple architecture, low power consumption, and excellent performance (in terms of phase noise) are some of its major features, the oscillation frequencies are limited by the VCSEL bandwidth. At present, there is no scientific evidence that demonstrates the applicability of the VBO in telecommunications systems, either in the electrical or optical domain. Similar to other OEOs, the optical output of the VBO can be transported and recovered by a detector at a remote site, but it can also be used as an optical carrier for intensity-modulated data. Therefore, a remarkable alternative to the VBO is the simultaneous generation of microwave signals and optical pulses to be used for the transmission of pulsed optical data with reduced duty cycles.

Considering the broad spectrum of applications where optical pulses are applied, the generation of ultrashort pulses has been extensively researched by different authors during the last two decades. Three techniques are available for the optical pulses generation using laser diodes. The gain switching (GS) technique [17] is the simplest because the laser source is directly modulated with an electrical signal that defines the frequency of repetition and physical characteristics of the pulses such as the amplitude, timing jitter, and pulse width. Another advantage of the GS technique is the generation of optical frequency combs obtained under specific modulation conditions. This technique has also been applied to short and long-wavelength VCSELs for the generation of wide frequency combs thanks to their orthogonal polarization mode emission.

The general objective of this work is the design and implementation of an optoelectronic system for microwave signal generation integrating VCSEL technology and the concept of optoelectronic oscillators. To accomplish this objective, the process was divided into four specific objectives. Firstly, the study and evaluation of different architectures for the microwave signal generation in terms of phase noise. According to the results, the second objective is the design of an optoelectronic system capable of generating a microwave signal at a frequency established by the needs identified during the first objective. In the third objective, the proposed system is evaluated through experimental implementation and simulation. Finally, the system is integrated into an optical data transmission system to validate its applicability.

The results of this research are presented as follows:

- Chapter 1 presents some optical techniques for the generation and some applications of microwave signals. In the second section, the most commonly used parameters in the scientific and engineering fields to determine the performance of a microwave signal in the frequency and time domain are detailed. A complete state of the art of the optoelectronic oscillators, included in the third section, allows identifying the evolution and the most recent advances of their architectures. Considering the bandwidth of long-wavelength VCSELs, in the fourth section, some frequency multiplication mechanisms that can be implemented to increase the frequency of the microwave signal generated from a VCSEL-based system are discussed. The performance of some OEOs is summarized in a comparative table in the fifth section of the chapter.

- Chapter 2 describes the structure and manufacture of VCSELs, with particular emphasis on those emitting at long wavelengths used in this work. Considering that the VCSEL will be modulated directly in the proposed system, the third section of this chapter details the static and dynamic properties, including large signal modulation and gain switching technique. To extract some intrinsic parameters, the equivalent model of the active region is developed in the fourth section, including the mathematical expressions which relate the circuit elements to the VCSEL parameters. In the end, the main noise characteristics of the VCSELs and the Langevin approach applied to include the noise in the equivalent circuit model are presented.

- Chapter 3 is dedicated to the extraction of intrinsic parameters from a C-band VCSEL. The characterization includes a set of measurements to determine the static and dynamic characteristics of the laser. These characteristics, jointly with the electrical model, the linewidth enhancement factor measurement, and the relative intensity noise, are presented in the first four sections. The parameters extracted, summarized in the fifth section, are used to simulate the VCSEL in three software tools to validate the extraction process.

- Chapter 4 describes two systems for generating microwave signals. The first section focuses on the VBO from a theoretical perspective and includes the results of the experimental characterization when several elements of the VBO architecture are modified. The second section details the architecture and operating principle of the gain switching based harmonic generation system called self-started VCSEL-based harmonic frequency generator (SVHFG). It also describes a predictive model of SVHFG phase noise, considering the different additive and multiplicative noise sources coming from the different components. Finally, the experimental validation of the system is presented, and the results are compared with the proposed noise model.

- In Chapter 5, the self-started VCSEL-based optical frequency comb generator (SVOFC) is reported. First, the architecture and system operation are described; then, the simulation results and the experimental characterization of the optical pulses and optical frequency combs generated at different frequencies are presented. The optical pulses and frequency combs are used as optical carriers for the transmission of data modulated

through an intensity modulator. These results are presented in the second section of this chapter.

- Finally, the general conclusions of this work and some future works based on the results obtained and the experience acquired during the development of this thesis are presented.

Chapter 1

Microwave signal generation

At present, microwave signals are a crucial element for the operation of a wide variety of systems such as telecommunications, astronomy, and medicine. After the invention of radio transmission, the main systems used to generate these signals were vacuum tube oscillators, replaced few years later by electronic oscillators due to their smaller size and cost. Later, thanks to the integration of circuits (size and energy consumption reduction) and the popularity of radio communications, semiconductor oscillators became increasingly widespread and accurate.

The optoelectronic systems for the microwave generation, also referred as microwave photonics, appeared in the early 90s and promised signals of several gigahertz with high spectral purity. The evolution of these systems during the last three decades is marked by their high design freedom that allows the modification of optical or electronic segments in order to improve the overall system performance.

This chapter includes a description of the systems for microwave signal generation using optoelectronics, the mechanisms and measures to determine the purity of the signals generated, and a review of the state of the art of optoelectronic oscillators and frequency multipliers using the phase noise as a comparison parameter.

1.1. Microwave photonics: generation and applications of microwave signals

Microwave photonics (MWP) is a term used for the first time in 1991 [13] and can be defined as the study and use of optoelectronic components for the transport, generation, and processing of microwave signals [18, 19]. Its success is mostly due to the low optical losses and the evolution of the bandwidth of optoelectronic components, covering not only frequencies in the microwave range but also millimeter waves (mm-waves) and THz frequencies [20].

Besides the reduced attenuation in the mm-wave and microwave spectrum, the optical fiber has several advantages over electrical transmission systems such as electromagnetic immunity, high physical flexibility, low cost and weight, low cross-sectional area, and low dispersion [21]. Simultaneously, the development of low relative intensity noise (RIN) and high bandwidth lasers, external modulators with lower V_π voltage, and fast photodetectors with high responsivity and bandwidth, boosted the MWP improvement [22]. Thus, MWP was positioned as an attractive solution for analog microwave transmission to remote systems, for example, the radio astronomy Atacama Large Millimetre/Submillimeter Array (ALMA) [23] and the Square Kilometre Array (SKA) [24]. Optical single-mode (SM) fiber also provides a time-bandwidth product higher than 10^5 indispensable for processing of broadband signals and applications such as optical delay-line filters (also called microwave photonic filter) [25].

1.1.1. Microwave signal generation by optical techniques

As well as the transport and processing, the microwave photonic signal generation has been widely accepted as a result of the high spectral purity, increasing frequencies, and direct transmission by optical fiber of the signal generated. At present, there are several mechanisms for the generation of microwave signals. Some of them employ simple optical heterodyning, and some others have more complex and bulky architectures. The applicability of these systems includes the measurement of physical variables [26] and modern instrumentation [20].

The following section describes some of the most relevant techniques for microwave signal generation, whereas the optoelectronic oscillators (OEO) will be addressed in more detail in section 1.3.

1.1.1.1. Optical heterodyning

The optical heterodyning is the simplest technique for microwave signal generation and consists of beating two optical waves with different wavelengths (λ_1 and λ_2) at a photodetector. The wavelength difference corresponds to the microwave frequency [27]. The two optical waves can be expressed as:

$$E_1(t) = E_{01} \cos(\omega_1 t + \phi_1) \quad \text{and} \quad E_2(t) = E_{02} \cos(\omega_2 t + \phi_2) \tag{1-1}$$

where E_{01} and E_{02} are the amplitudes, ω_1 and ω_2 are the angular frequencies, and ϕ_1 and ϕ_2 are the phases. In a square-law detector, the photodetected current I_{PD} corresponds to $I_{PD}(t) = \Re|E_1(t) + E_2(t)|^2$, where $\Re$ is the photodetector responsivity. Due to the limited bandwidth, the solution can be written as:

$$I_{PD}(t) = A \cos\left[(\omega_1 - \omega_2)\,t + (\phi_1 - \phi_2)\right] \tag{1-2}$$

The constant A is determined by the responsivity as $A = 2\Re(P_1 P_2)^{1/2}$ with $P_1 = E_{01}^2/2$ and $P_2 = E_{02}^2/2$. Even though with this technique the frequency adjustment of the microwave signal is simple, the phase noise performance is limited. For low phase noise signals, the phase terms should be correlated with techniques such as optical phase lock loop (OPLL) [27].

1.1.1.2. Generation based on external modulation

This mechanism is based on the heterodyning of phase-correlated sidebands produced by external modulation. A Mach-Zehnder intensity modulator (MZM) is generally used instead of phase [28] and polarization modulators [29] owing to its non-linear transfer function. For sideband generation, the modulator must operate in the non-linear zone, i.e., the bias voltage should be set at the minimum transmission point (MITP) or the maximum transmission point (MATP) [30].
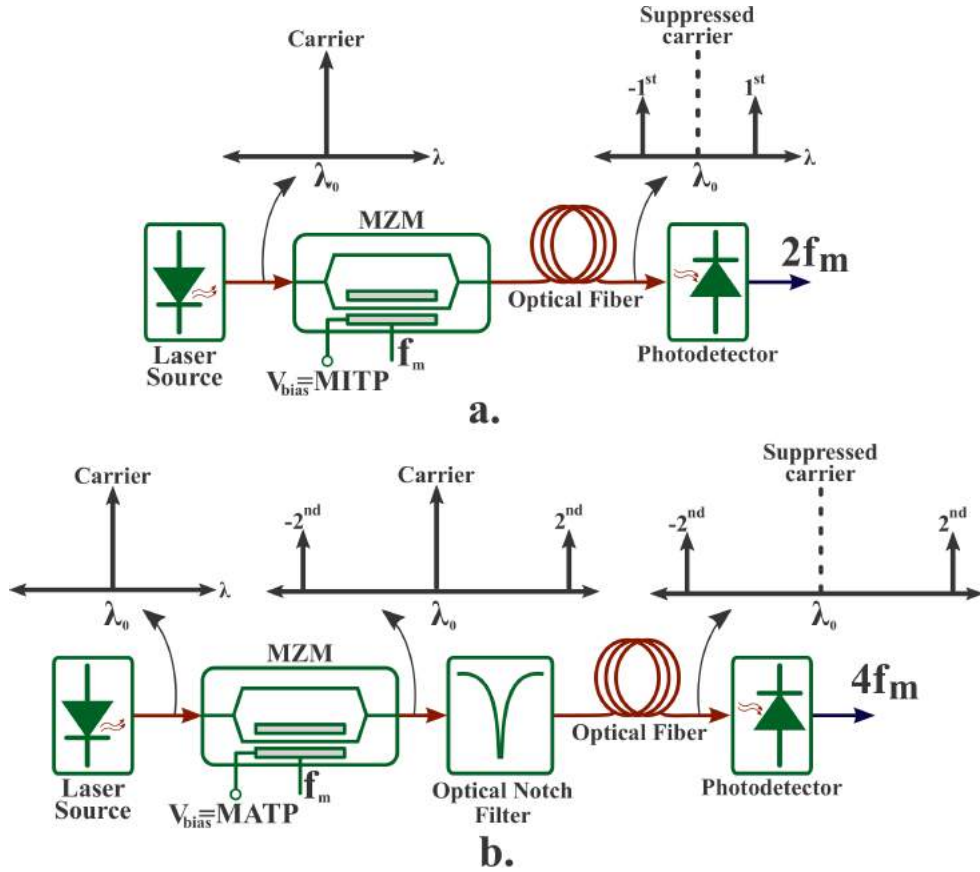
Figure 1-1.: Microwave generation using **a.** Null-bias mode **b.** Full-bias mode.

The null-bias point operation mode (Figure **1-1 a.**) occurs when the MZM modulator is biased at a minimum transmission point. In this operation mode, the optical carrier and the even-order optical sidebands are eliminated, whereas the odd-orders remain in the spectrum.

The frequency difference between two successive components is equal to twice the microwave drive signal.

In the other case, called full-bias point operation mode (Figure **1-1 b.**), the odd-order sideband components are suppressed by biasing the modulator at the maximum transmission point, and the even-order (zero and second-order) components remained. If the zero-order component is removed through an optical fixed notch filter, it is possible to generate a microwave signal whose frequency is four times the microwave drive signal.

Even though the system is highly tunable (by only adjusting the frequency of the microwave signal applied to the modulator) and simple to implement, the bias-drift caused by temperature changes is the most significant constraint affecting the overall system performance. Currently, several applications employ different methods to reduce the effect of bias-drift [31,32].

1.1.1.3. Optical phase lock loop (OPLL)

The optical phase lock loop architecture shown in Figure **1-2**, includes a phase detector, two lasers (master and slave), a photodetector, and a signal generator.
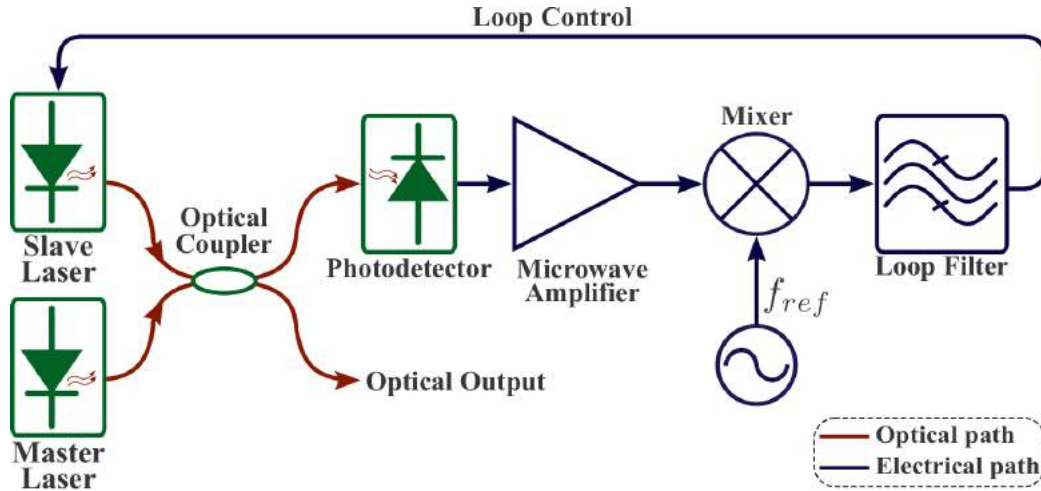
Figure 1-2.: OPLL architecture [1].

The system starts with the heterodyne signal generated from the beating of the master and slave lasers in the fast photodetector. This beat signal goes to a phase detector consisting of a mixer and a low-pass filter. The output signal is a phase error signal which is proportional to the phase difference between the generated microwave signal and the reference signal. Finally, the voltage error signal controls the slave laser by changing its injection current and locking its phase. The locking range is determined by the laser linewidth and the loop length. To achieve effective phase locking, narrow linewidth lasers and shorter loop length are necessary [20]. Some authors have achieved signals with linewidth in the range of tens of Hz and frequency generation up to 1.8 THz [33].

1.1.1.4. Optical injection locking (OIL)

Within optical communications systems, direct laser modulation is an attractive alternative for data transmission at reduced costs and size. However, the nonlinearities and noise impact the system performance and reduce its applicability. In this sense, optical injection locking reduces the RIN, suppresses the non-linear distortion, and increases the gain of an optical link [18].

Under this principle, a master laser is directly modulated by an electrical signal of frequency f_m to generate an optical carrier with a set of sidebands equally spaced at a distance equivalent to the modulating frequency. Then, the output signal is injected into two slave lasers with different wavelengths (λ_1 and λ_2). To achieve optical injection locking, these wavelengths have to be close to the two selected sidebands. Phase and frequency locking are produced when the slave wavelength is pulled towards the master wavelength. At a photodetector, the two signals are beating to generate a microwave signal with a frequency equal to the difference between the selected sidebands. For example, if the free-running wavelengths are close to the $+2^{nd}$ and -2nd order sidebands (see Figure **1-3**), the resulting signal after the photodetector is four times the reference frequency. The resulting phase noise is low (unlike heterodyning) because of the two injected lasers are phase-correlated [34].
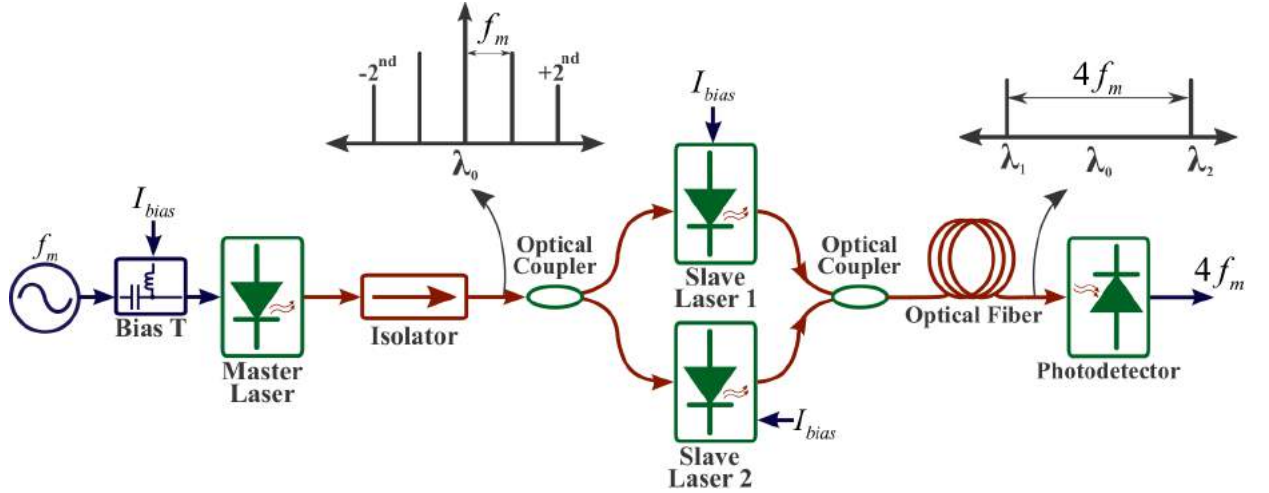
Figure 1-3.: OIL of two lasers for microwave generation.

In [35], the authors integrate the concept of OIL and OPLL in the same system called optical injection phase-lock loop (OIPLL) to generate low noise signals in a wide frequency tuning range (4 - 60 GHz). Meanwhile in [36], a vertical-cavity surface-emitting laser (VCSEL) injects a Fabry-Perot laser to produce 4.9 and 6 GHz signals. The system stability can be improved through temperature control to avoid wavelength drifting.

Additionally, the OIL characteristics have been used for optical transmission systems. For example, in [37], a four-port de-multiplexer is demonstrated experimentally using OIL. The system is validated in a 100-km Nyquist ultra-dense wavelength division multiplexed net-

work when the inputs are comb tones differently encoded. Finally, in [38], a directly-encoded multi-color laser is injected by a dual-color source produced by external modulation at 5G frequencies. The optical data is transmitted by optical fiber, converted to the electric domain, and re-transmitted using an antenna. In this way, the authors demonstrate the OIL applicability in wired and wireless millimeter-wave over fiber (MMWoF) links.

1.1.2. Microwave signals applications

Even if microwave signals are traditionally associated with communications, today they have a wide range of applications mainly due to their physical characteristics (such as propagation and their frequencies that cover an extensive range of the electromagnetic spectrum) and its interaction with different environments. For example, the microwave signals are employed in healthcare [39, 40] and remote sensing [41, 42]. Some applications in telecommunications are briefly presented below.

1.1.2.1. Wireless communications

Undoubtedly, wireless communications are an study area and dynamic market thanks to their importance for providing a wide variety of telecommunications services. This fact has boosted the use of frequency bands not assigned to services. For example, frequencies above 275 GHz can be employed with a considerable bandwidth of 50 GHz [43]. In this sense, microwave photonics provides solutions applicable in segments such as the generation of high-frequency carriers, carrier modulation at significant bit rates, and transport of signals to remote antennas over optical fiber.

The development and application of coherent detection in networks such as the next-generation cellular network 5G require the implementation of systems capable of detecting the amplitude and optical phase variations. Therefore, 5G can be enhanced through the application of signal processing functions for correcting the phase deviations produced by the transmitter and the local laser source. At the same time, a programmable silicon-based on-chip photonic signal processor can be used for true-time delay beamforming [44].

The simultaneous transmission over optical fiber of radio frequency (RF) carriers, information, and beamforming signals, was the main characteristic for the development of optically fed and controlled phased-array antenna (PAA). Besides, the use of photonic microwave true-time delay lines (TTDL) makes possible size and cost reduction [45]. The characteristics and the schemes to realize optical time delay lines determine the performance of PAA systems. For example, in [46], the authors use an integrated optical frequency comb source (generated with a micro-ring resonator (MRR)) with 81 channels and a time delay step of 14.8 ps, meanwhile in [47], eight thermo-optical switches and seven waveguide delay lines with different lengths produce a time delay step of 1.52 ps. In both cases, the time delay step impacts the angular resolution and the beam-steering range.

As mentioned earlier, there are free frequency bands in almost all regions of the world that can be used for wireless transmissions. The 60 GHz band is an unlicensed band with an available bandwidth of around 7 GHz. However, these high-frequency transmissions suffer from atmospheric losses, which limit their coverage to a few tens of meters. A simple and low-cost solution is the centralization of the transmission equipment in a central office and the installation of more remote antenna units (RAU) through optical links. One drawback is the dispersive effect of the fiber at high frequencies. Multiple authors propose different mechanisms to eliminate or reduce this effect [48], whereas others validate the use of advanced modulation schemes [49], coherent detection [50] or integrated optics [51].

1.1.2.2. Data processing

The microwave and mm-wave signals generated by processes with optical devices, as stated before, have advantageous characteristics in terms of high spectral purity and low phase noise. Therefore, some of them are used for pulse shaping and clock recovery [52], conversion of non-return-to-zero (NRZ) to return-to-zero (RZ) data signals, up-conversion of analog and digital baseband signals to a higher frequency carrier, and serial to parallel conversion of optical time-domain multiplexed (OTDM-RZ) data signals [53].

Digital communication systems include clock recovery within the receiver structure. This segment provides information about the sampling time used by the circuit decision to recover data. Some solutions for optical clock recovery include phase-locked loops, self-pulsating lasers, filtering methods, and multi-wavelength all-optical clock recovery [54]. Optoelectronic oscillators have also been used for clock recovery. In [55] and [56], the authors propose an OEO based on a polarization modulator which acts as an optoelectronic mixer for simultaneous data and clock recovery. In both cases, the loop incorporates an electric bandpass filter with a center frequency equal to half input signal frequency. A similar architecture is used in [57] with two polarization controllers to perform variations in the produced signal polarization and to obtain a pre-scaled clock of 10 GHz and a line-rate clock of 20 GHz when the bit rate is 20 Gbps. Other architectures use OEO based on MZM modulators in conjunction with polarization modulators [58, 59] and others use electro-absorption modulators (EAM) [60, 61]. In any case, the goal is to obtain a clock signal with an ultra-low jitter that guarantees an acceptable bit error rate at high bit rates.

A common factor between the methods developed for optical vector signal generation is the use of external modulation (intensity or phase) in order to transmit the signal in higher frequency bands. In [62], the authors used a phase modulator and a wavelength selective switch (WSS) to generate an optical binary phase-shift keying (BPSK) signal with a sextupled frequency. In this case, the phase modulator is driven by a 10 GHz signal and a BPSK electrical signal. The results showed the effect of modulation index change on the bit error rate (BER).

OTDM systems use high-frequency signals to change the encoding format (from NRZ to RZ), to recover the clock, and to upgrade the data rate. Through a conventional OEO and a pulse

carver modulator, an optical data stream at 40 Gbps was demonstrated in [63]. For this, the electrical signal is the clock signal to generate an electrical NRZ data stream through a pseudorandom binary sequence (PRBS), while the optical output at 40 GHz is the light source for the second modulator.

1.2. Performance parameters of microwave signals

From a broader perspective, a periodic signal that varies over time can be characterized in terms of its amplitude, frequency, and phase. In the case of an ideal microwave signal source, the three characteristics remain constant over time, whereas in real microwave signal sources, including high stability sources, some variations are produced due to noise instabilities. Figure **1-4** represents two signals generated by an ideal and a real source in time and frequency domain. The amplitude variations $\varepsilon(t)$ are represented by output power drifts, while the phase variations $\varphi(t)$ correspond to the fluctuations in the zero-crossing position, which generates a period change also resulting in frequency drifts.
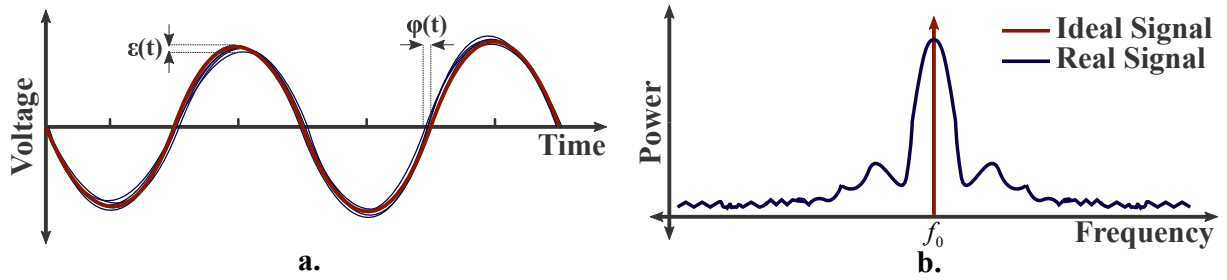
Figure 1-4.: Representation of signal instabilities in: **a.** Time domain **b.** Frequency domain.

Traditionally, the mechanism to differentiate and determine the performance of the sources is the frequency stability. This stability refers to the source ability to maintain its nominal frequency for a given period, and in many cases, determines the application in which it can be used. Depending on the observation time, the frequency stability can be divided into long and short term frequency stability.

Long-term frequency stability, also known as trends or frequency drift, refers to the slow deviations in periods equivalent to hours, days, months, and even years. These variations are mainly due to the aging of the components and source materials, and variations in temperature, humidity, and pressure.

On the other hand, short-term frequency stability is related to deterministic and random variations of the frequency source around the nominal frequency f_0 that occur in reduced periods (few seconds or less). This stability is commonly known as spectral purity or phase noise and will be addressed in the next section.

1.2.1. Phase noise

Phase noise is the preponderant metric for expressing frequency stability. The deterministic variations (also discrete, systematic, or periodic) are discrete spurious signals at different offset frequencies from the fundamental frequency produced by known phenomena such as mechanical vibrations. In contrast, random frequency variations are generated by different noise sources of electronic components such as thermal, flicker, and shot noise.

Phase fluctuations can be described through a simple model of time-dependent functions or by statistical tools more appropriate to their random nature. For this purpose, some definitions presented in [64] and [2] are developed below.

1.2.1.1. Time-dependent functions

The instantaneous output voltage of an ideal microwave signal source (for example an oscillator) can be expressed as:

$$V(t) = V_0 \cos(2\pi f_0 t) \tag{1-3}$$

where V_0 and f_0 are the nominal peak amplitude and frequency respectively. As shown in Figure **1-4**, a real oscillator signal fluctuates in amplitude and phase. Considering these variations, Equation 1-3 can be written as:

$$V(t) = [V_0 + \varepsilon(t)] \cos[2\pi f_0 t + \varphi(t)] \tag{1-4}$$

Here we include two random processes: $\varepsilon(t)$ represents the amplitude fluctuations (or random fractional amplitude) and $\varphi(t)$ the phase fluctuations linked to the frequency variations (phase noise). In current oscillators, the amplitude fluctuations are small ($|\varepsilon(t)| \ll 1$) and they will be neglected under the assumption that they do not affect frequency stability. For short-term measurements, it is assumed that the oscillator stability is less than a half-cycle of the carrier frequency ($-\pi < \varphi(t) > \pi$) and the instantaneous output voltage is reduced to:

$$V(t) = [V_0] \cos[2\pi f_0 t + \varphi(t)] \tag{1-5}$$

The instantaneous frequency is defined as:

$$f(t) = \frac{1}{2\pi} \frac{d}{dt}(2\pi f_0 t + \varphi(t)) = f_0 + \frac{1}{2\pi} \frac{d\varphi(t)}{dt} = f_0 + \frac{1}{2\pi} \dot{\varphi}(t) \tag{1-6}$$

From Equation 1-6, the frequency noise can be modeled by the random process $\Delta f(t)$ defined as:

$$\Delta f(t) = \frac{1}{2\pi} \dot{\varphi}(t) \tag{1-7}$$

Additionally, the random phase fluctuation can be converted into time (measured in seconds) through the phase-time fluctuation $x(t)$. This metric, given in Equation 1-8, allows the

accumulation of phase cycles.

$$x\left(t\right) = \frac{\varphi(t)}{2\pi f_0} \tag{1-8}$$

Also, the fractional-frequency fluctuation $y(t)$ can be obtained by the instantaneous frequency fluctuation normalized to the carrier frequency as follow:

$$y(t) = \dot{x}(t) = \frac{1}{2\pi f_0}\dot{\varphi}(t) \tag{1-9}$$

1.2.1.2. Power spectral density distributions

Due to its random nature, phase and frequency noise are described in terms of spectral density distributions, leading to an identification of the energy distribution for a given bandwidth. In the case of phase noise, the noise processes are located in a narrow band around the nominal frequency. The best-known density distributions are:

- **Power spectral density of phase fluctuations** $S_\varphi(f)$.

- **Single-sideband SSB phase noise** $\mathscr{L}(f)$.

- **Power spectral density of frequency fluctuations** $S_{\Delta\nu}(f)$.

- **Power spectral density of phase-time fluctuations** $S_x(f)$.

- **Power spectral density of fractional frequency fluctuations** $S_y(f)$.

The one-sided spectral density of phase fluctuations $S_\varphi(f)$ is the most used tool for characterizing the phase noise. It is formally defined as the Fourier transform of its autocorrelation function expressed as:

$$S_\varphi(f) = 2\int_0^\infty R_\varphi(\tau)e^{-j2\pi f\tau}d\tau \tag{1-10}$$

Its physical dimension is rad^2/Hz and f is the Fourier frequency used for the spectral analysis. The autocorrelation function $R_\varphi(\tau)$ corresponds to:

$$R_\varphi(\tau) = \mathbb{E}\left\{\varphi(t)\varphi(t-\tau)\right\} \tag{1-11}$$

where the $\mathbb{E}$ operator represents the statistical expectation (extension of the average to stochastic processes).

From Equations 1-7, 1-8, and 1-9, it is possible to determine the power spectral densities of the frequency and phase-time noise processes in terms of $S_\varphi(f)$ as follows:

$$S_x(f) = \frac{1}{(2\pi f_0)^2}S_\varphi(f) \tag{1-12}$$

$$S_y(f) = \frac{f^2}{f_0{}^2} S_\varphi(f) \tag{1-13}$$

$$S_{\Delta\nu}(f) = f^2 S_\varphi(f) \tag{1-14}$$

The complexity of some measurements has determined the employability of the previous definitions. For example, S_y is preferably used in radio frequency metrology, whereas $S_{\Delta\nu}$ in laser contexts.

Manufacturers, engineers, and general users prefer the single-sideband SSB $\mathscr{L}(f)$ to $S_{\Delta\nu}$ for quantifying phase noise. The IEEE standard 1139 [65] define this measurement as one half of the one-sided spectral density of phase fluctuations; this is:

$$\mathscr{L}(f) = \frac{1}{2} S_\varphi(f) \tag{1-15}$$

$\mathscr{L}(f)$ is usually plotted on a log-log scale and its units are dBc/Hz,

$$\mathscr{L}(f) \left[\frac{dBc}{Hz}\right] = 10\log_{10}\left[\frac{1}{2} S_\varphi(f)\right] = 10\log_{10}\left[S_\varphi(f)\right] - 3 \tag{1-16}$$

representing the dB below the carrier in a 1-Hz bandwidth. When the direct measurement method is employed (through an electric spectrum analyzer), the phase noise is determined by the ratio of one-sideband noise power in 1-Hz bandwidth P_{ssb} to the total carrier power P_t. This definition is represented in Figure **1-5** and described in Equation 1-17 where P_c is the carrier signal power.
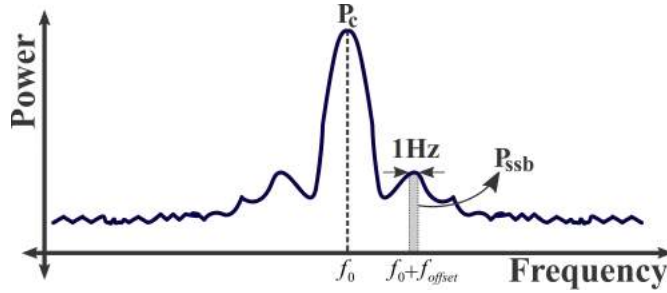
Figure 1-5.: Representation of single-sideband phase noise definition.

$$\mathscr{L}(f) \left[\frac{dBc}{Hz}\right] = \frac{P_{ssb}(f_0 + f_{offset})}{P_t} \approx \frac{P_{ssb}(f_0 + f_{offset})}{P_c} \tag{1-17}$$

Although this is the simplest and easiest method to measure the phase noise, it has several limitations, such as the lack of discrimination between amplitude-modulated AM noise and phase-modulated PM noise. Additionally, the measurement accuracy is restricted by the phase noise of the local oscillator employed to perform the measurement.

1.2.1.3. Power-law spectral density model

The power-law model [66] describes phase noise as the sum of main noise processes according to:

$$S_\varphi(f) = \sum_{n=-4}^{0} b_n f^n \tag{1-18}$$

where n denotes each noise process, the coefficients b_n are a measure of the noise level, and f^n is a straight line of slope $n * 10 \ dB/decade$ in a log-log scale representation. Sometimes noise processes appear below $n < -4$ at very low frequencies that can be neglected. The power-law also applies to the fractional frequency fluctuations $S_y(f)$ as follows:

$$S_y(f) = \sum_{n=-2}^{2} h_n f^n \tag{1-19}$$

given the following equivalence:

$$h_n = \frac{1}{f_0^2} b_{n-2} \tag{1-20}$$

The main noise processes described by the law-power are listed in the Table **1-1**.

Table 1-1.: Most important phase noise processes

Noise type	$S_\varphi(f)$		$S_y(f)$	
	Coefficient	Slope	Coefficient	Slope
Random walk frequency noise	b_{-4}	-4	h_{-2}	-2
Flicker frequency noise	b_{-3}	-3	h_{-1}	-1
White frequency noise	b_{-2}	-2	h_0	0
Flicker phase noise	b_{-1}	-1	h_1	1
White phase noise	b_0	0	h_2	2

1.2.1.4. Leeson model

The phase noise behavior can also be described by the model proposed by D.B. Leeson [67]. In this model, the oscillator is a time-invariant linear system composed by an ideal resonator of quality factor Q and half-bandwidth $B = \omega_0/2Q$, and an amplifier to compensate the loop losses. For physical oscillators, some corrections must be made to include non-linearities.

The model suggests a direct relationship between the spectral density of the phase fluctuations at the input $S_{\Delta\theta}$ and the spectral density of the phase fluctuations at the oscillator output S_φ. The swiftness of phase fluctuations over time governs this relationship. In the first case, when phase fluctuations $\varphi(t)$ are slower than the inverse of the resonator relaxation

time ($\tau_r = 2Q/\omega_0$), the spectrum of slow phase fluctuations is given by:

$$S_\varphi(f) = \frac{1}{f^2}\left(\frac{f_0}{2Q}\right)^2 S_{\Delta\theta}(f) \tag{1-21}$$

In the second case, for phase variations higher than τ_r, the spectrum of the phase fluctuations at the output is equal to the input spectrum $S_\varphi(f) = S_{\Delta\theta(f)}$. Thus, the Lesson formula relates only the effect of slow and fast fluctuations to the amplifier phase noise as follows:

$$S_\varphi(f) = \left[1 + \frac{1}{f^2}\left(\frac{f_0}{2Q}\right)^2\right] S_{\Delta\theta}(f) \tag{1-22}$$

Equation 1-22 reflects the up-conversion process of phase noise into the loop known as Lesson effect. With an ideal resonator, the loop phase noise is mainly due to the amplifier phase noise, as shown in Figure **1-6**. The amplifier phase noise exhibits two processes [68]: the white phase noise at higher frequencies and 0 dB/dec slope ($S_\varphi(f) = b_0 f^0$ *constant*), and close to the carrier, the flicker phase noise with a -10 dB/dec slope ($S_\varphi(f) = b_{-1}f^{-1}$ where $b_{-1} \approx constant$).
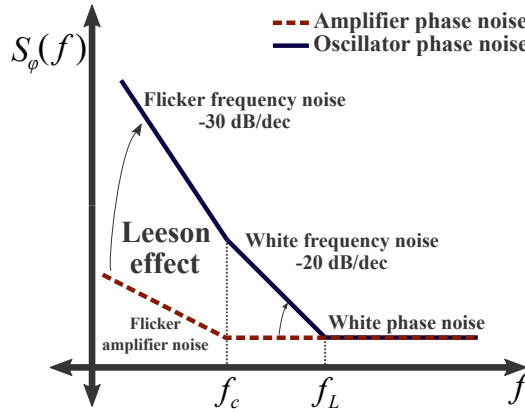
Figure 1-6.: Oscillator phase noise according to the Leeson model [2].

Inside the loop, the flicker phase noise of the amplifier is up-converted to a -30 dB/dec slope at frequencies below the corner frequency f_c (frequency at which the two amplifier noise processes are equals, this is $b_{-1}f^{-1} = b_0$). In contrast, the white noise approaches the carrier until it reaches the Leeson frequency f_L defined as:

$$f_L = \frac{f_0}{2Q} = \frac{1}{2\pi\tau_r} \tag{1-23}$$

According to this model, the close-to-the-carrier phase noise can be reduced by decreasing the Leeson frequency f_L, and this means an increase in the resonator quality factor Q. In the opposite direction, if the nominal or oscillation frequency f_0 increases, f_L increases, and the phase noise is deteriorated.

1.2.2. Time-domain characterization

Today, applications such as global positioning system (GPS) and digital communications networks need stable and accurate timing sources in order to avoid data errors. A source is stable when the frequency does not change too much in time and is accurate when the average frequency is equal to the nominal frequency [3]. The stability verification process in the time-domain, also called long-term stability, consists in measuring the source frequency variations in a specific time interval and processing these values through statistical tools (due to their random nature).

According to [64], the time average value of the instantaneous frequency $f(t)$ can be estimated through measurements taken in a time interval from t_k and $t_k + \tau$, and is given by:

$$\bar{f}_{t_k,\tau}(t) = f_0 + \frac{1}{\tau} \int\limits_{t_k}^{t_k+\tau} \Delta f(t) dt \tag{1-24}$$

Usign the normalization $\bar{y}_k = \left(\bar{f}_{t_k,\tau} - f_0 \right) / f_0$, the time average of fractional-frequency is expressed as:

$$\bar{y}_k = \frac{1}{\tau} \int\limits_{t_k}^{t_k+\tau} y(t) dt \tag{1-25}$$

From Equation 1-9, the averaged of fractional-frequency $\bar{y}_k$ is also expressed in terms of phase data as:

$$\bar{y}_k = \frac{\varphi\left(t_k + \tau\right) - \varphi\left(t_k\right)}{2\pi f_0 \tau} = \frac{x\left(t_k + \tau\right) - x\left(t_k\right)}{\tau} \tag{1-26}$$

The source stability can be characterized by determining the standard variance for N samples $\bar{y}_k$ of τ duration taken at a repetition interval T (Figure **1-7 a.**):

$$\sigma_y^2\left(N, T, \tau\right) = \frac{1}{N-1} \sum_{k=1}^{N} \left[\bar{y}_k - \langle \bar{y} \rangle_N\right]^2 \tag{1-27}$$

The standard variance estimator diverges when the number of samples and the values of τ increase due to the noise processes present in real oscillators. Some alternative definitions have been developed to achieve a less biased estimator [66] [69]. Among them, Allan variance is the most well-known and frequently used tool for time-domain characterization.

1.2.2.1. Allan variance (non-overlapping)

The Allan variance [70] is a convergent measurement of fractional-frequency fluctuations of timing sources with multiple noise processes. There are several versions for the Allan variance, which allow identifying some non-visible noise processes when the standard Allan variance is applied.
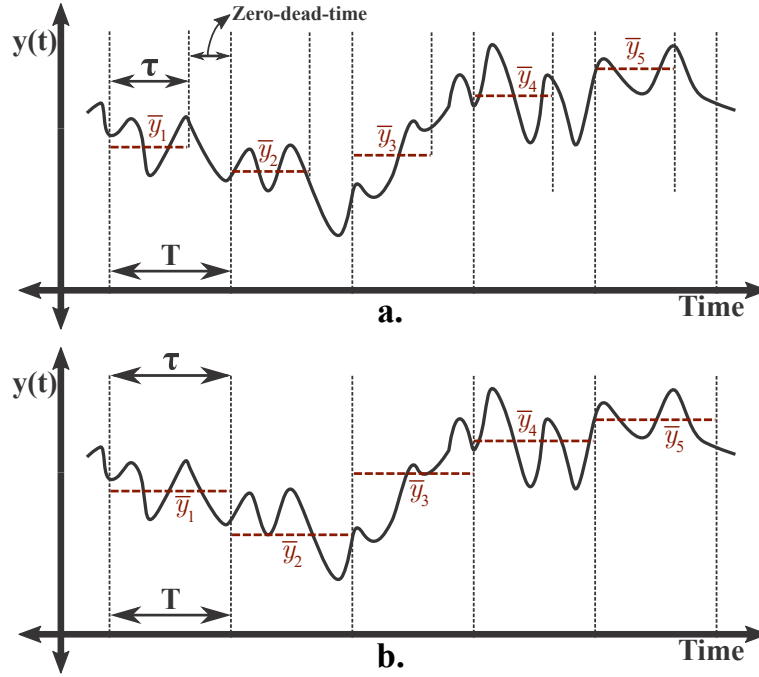
Figure 1-7.: Representation of fractional-frequency average. **a.** Simple variance **b.** Non-overlapping Allan variance. Adapted from [3]

The non-overlapping Allan variance (AVAR), known as two-sample variance and denoted as $\sigma_y^2(\tau)$, is defined as the expected value of the variance evaluated for two adjacent samples, i.e., $N = 2$ and $T = \tau$ (zero-dead-time). The Allan variance is represented in Figure **1-7 b.** and is expressed as:

$$\sigma_y^2(2, \tau, \tau) = \mathbb{E}\left\{\frac{1}{2}[\bar{y}_{k+1} - \bar{y}_k]^2\right\} = \sigma_y^2(\tau) \tag{1-28}$$

In a real scenario, the statistical expectation is calculated by the mean of a finite number of M samples. The $M - 1$ differences $(\bar{y}_{k+1} - \bar{y}_k)$ guarantee the convergence for several kind of oscillator noises. Thus, the statistical estimator (recommended by the IEEE [65]) is:

$$\sigma_y^2(\tau) = \frac{1}{2(M-1)} \sum_{k=1}^{M-1} (\bar{y}_{k+1} - \bar{y}_k)^2 \tag{1-29}$$

The square root $\sigma_y(\tau)$ is called Allan deviation (ADEV) and is usually used to express measurements in the time domain. Generally, the confidence interval of Allan estimator is evaluated using a χ^2 distribution, where the effective degrees of freedom depend on the noise type.

From Equation 1-26 it is possible to determine $N = M + 1$ phase values, and in this way, the AVAR estimator becomes:

$$\sigma_y^2(\tau) = \frac{1}{2(N-2)\tau^2} \sum_{k=1}^{N-2} (x_{k+2} - 2x_{k+1} + x_k)^2 \tag{1-30}$$

1.2.2.2. Overlapping Allan variance

Overlapping sampling is used to decrease variability and improve the statistical confidence of statistical estimators. The overlapping Allan variance applies the same concept of the non-overlapping Allan variance to different data groups formed from all possible combinations of overlapping samples in an average time τ. The drawback of this variance is the increase in computational time [71]. The overlapping Allan variance is estimated as:

$$\sigma_y^2\left(\tau\right) = \frac{1}{2m^2\left(M - 2m + 1\right)} \sum_{j=1}^{M-2m+1} \left\{ \sum_{k=j}^{j+m-1} \left(\bar{y}_{k+m} - \bar{y}_k\right) \right\}^2 \tag{1-31}$$

where the observation interval time is $\tau = m\tau_0$, m is the averaging factor and τ_0 is the sampling period. Using N phase values, $\sigma_y^2\left(\tau\right)$ corresponds to:

$$\sigma_y^2\left(\tau\right) = \frac{1}{2\left(N - 2m\right)\tau^2} \sum_{k=1}^{N-2m} \left(x_{k+2m} - 2x_{k+m} + x_k\right)^2 \tag{1-32}$$

Figure **1-8** shows the overlapping Allan variance for $m = 3$. The confidence interval of an overlapping Allan deviation estimate is better than other estimations because the additional overlapping differences increase the number of degrees of freedom and thus improve the confidence in the estimation.
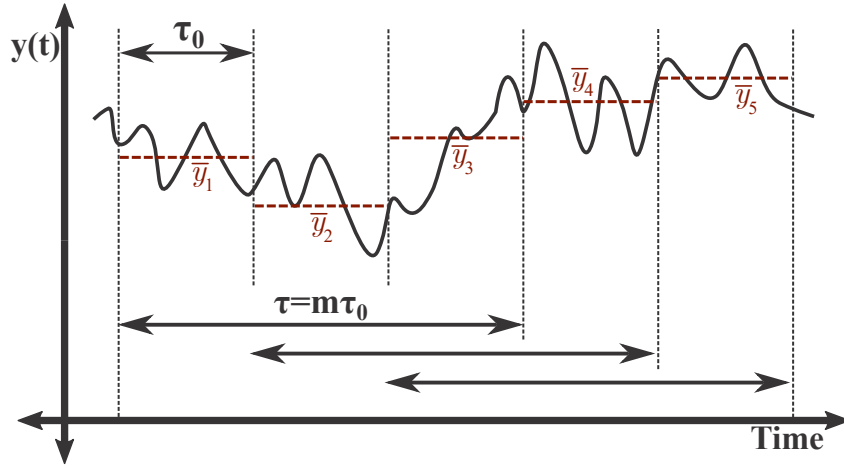
Figure 1-8.: Representation of overlapping Allan variance for $m = 3$

1.2.2.3. Modified Allan variance

The modified Allan variance (MAVAR) represented as $Mod\ \sigma_y^2\left(\tau\right)$, was introduced in 1981 [72] to distinguish between white and flicker PM noise. This variance includes an additional

average over m adjacent measurements [73] and is estimated as follow:

$$Mod\ \sigma_y^2\left(\tau\right) = \frac{1}{2m^4\left(M-3m+2\right)} \sum_{j=1}^{M-3m+2} \left\{ \sum_{k=j}^{j+m-1} \left(\sum_{i=k}^{k+m-1} \left[\left(\bar{y}_{k+m}-\bar{y}_k\right)\right] \right) \right\}^2 \tag{1-33}$$

where M is the number of fractional-frequency measurements, τ is the observation interval time defined as $\tau = m\tau_0$, m is the averaging factor, and τ_0 is the sampling period. For $m = 1$, $\tau = \tau_0$ and the modified Allan variance is the same as the non-overlapping Allan variance.

1.2.3. Timing jitter

Similarly to the phase noise, the timing jitter is used for quantifying the source phase variations and determining the source quality in the time domain. The timing jitter definition depends on the application, e.g., in the performance verification of digital data transmission, clock signals, and data recovery applications. Due to the lack of uniformity by defining jitter, the subcommittee on jitter measurement (ScoJM) from the IEEE Standards Association is focusing upon in the new standard P2414 to proportionate one unambiguous definition and methods for its measurement [74].

According to the recommendation ITU-T G.810 [75], the jitter is "*the short-term variations of the significant instants of a timing signal from their ideal positions in time*". In other words, the jitter is the time deviation of some events (usually the rise or fall edge in digital systems and clocks) from an ideal reference time frame or sampling point. These time increments are specified in time units (generally picoseconds and femtoseconds), and a larger number indicates poor timing performance. Many of the jitter measurements can be performed in data applications and clocks. Some of the most common jitter requirements are specified in period jitter, cycle-to-cycle jitter, phase-jitter, and time interval error.

In general, jitter measurements are taken using real-time oscilloscopes configured with an optimal bandwidth and vertical scale for minimizing noise and errors. During the thesis development, we used a real-time oscilloscope for measuring the **time interval error - TIE** of 10.000 edges generated by the proposed microwave signal generator. For jitter decomposition, the oscilloscope uses by default the spectrum analysis approach. The main measurements of jitter are briefly discussed below. From now on, the term source and clock will be used indifferently.

1.2.3.1. Types of jitter measurements

Below we present briefly some definitions of jitter measurements used to characterize sources of clock signals [3] [76].

1. **Period jitter**

   It is the most straightforward measurement process because it merely measures the period of a random number of cycles. Assuming that the period jitter is a discrete-time random process, the time variations are determined by comparing the measured periods to the nominal period. Technically speaking, the measurements are taken with an oscilloscope triggered with the first clock edge and looking at the variations of the next edges around its average position (instead of the ideal period). The period measurements PJ for four signal periods are depicted in Figure **1-9**.

2. **Cycle-to-cycle jitter**

   The standard JESD65B [77] defines the cycle-to-cycle jitter as the "*variation in cycle time of a signal between adjacent cycles, over a random sample of adjacent cycle pair*". It can be estimated from a sample size greater or equal to 1.000 by applying the first-order difference operation to two adjacent period jitter represented as CJ in Figure **1-9**. In the same way as the jitter period, cycle-to-cycle jitter measurement is based on comparing one event of the same clock at different times.

3. **Time interval error**

   The time error (TE) is defined in the recommendation ITU-T G.810 as the time difference between the observed clock and a reference clock. It is expressed through the time error function $x(t)$ as:

   $$x\left(t\right) := TE\left(t\right) := T\left(t\right) - T_{ref}\left(t\right) \tag{1-34}$$

   where $T(t)$ and $T_{ref}(t)$ are the time functions of the observed and reference clock described respectively as:

   $$T\left(t\right) = {\phi\left(t\right)}/{2\pi f_0} \quad \text{and} \quad T_{ref}\left(t\right) = {\phi_{ref}\left(t\right)}/{2\pi f_0} \tag{1-35}$$

   From Equation 1-5, the total phase of the observed clock signal is $\phi\left(t\right) = 2\pi f_0 t + \varphi\left(t\right)$ and $\phi_{ref}\left(t\right) = 2\pi f_0 t$ for an ideal clock reference with no excess phase.

   With the previous definitions, the time interval error (TIE) is the time difference of a time interval (called observation interval) generated by the observed clock and the same time interval from a reference clock. This definition is formulated in the Equation 1-36 and represented in the Figure **1-9** as TIE.

   $$TIE\left(t,\tau\right) := \left[T\left(t+\tau\right) - T\left(t\right)\right] - \left[T_{ref}\left(t+\tau\right) - T_{ref}\left(t\right)\right] := x\left(t+\tau\right) - x\left(t\right) \tag{1-36}$$

   In simple terms, the TIE is a discrete time-domain representation of the phase noise due to it represents the deviation of the observed clock edge from its ideal position measured from a reference point (accumulated error).

4. **Phase-jitter**

   Also known as integrated or cumulative jitter, it is determined by integrating the phase noise over a specified offset frequency range. This measurement represents the edge
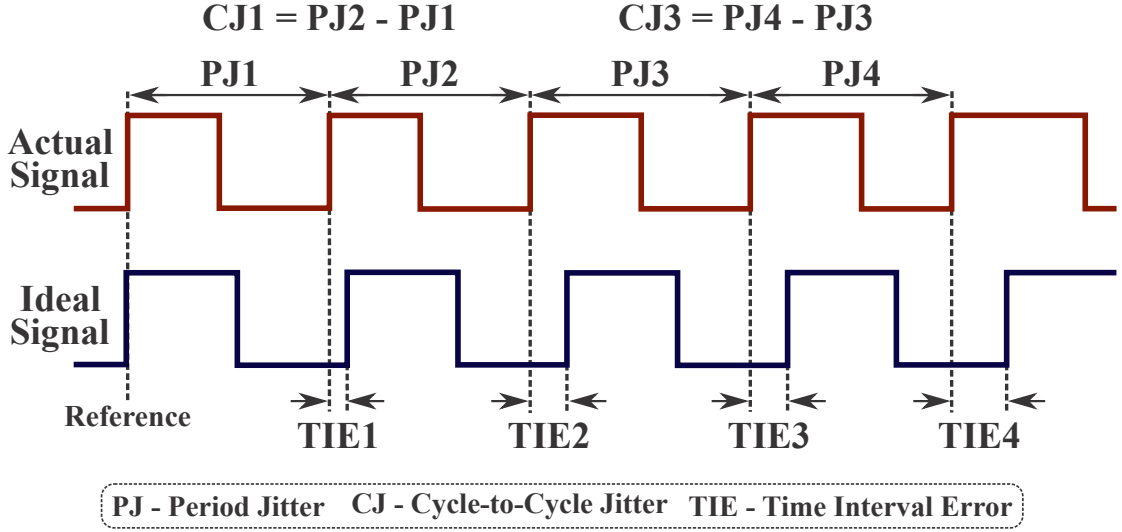
Figure 1-9.: Representation of different jitter measurements.

clock variations relative to an ideal clock, i.e., it also corresponds to the root mean square (RMS) of the absolute jitter for frequency components of the power spectral density in a given frequency interval. The RMS phase-jitter is related to the phase noise as:

$$\sigma_{RMS} = \frac{1}{2\pi f_0} \sqrt{2 \int_{f_1}^{f_2} 10^{\mathscr{L}(f)/10} df} \qquad (1\text{-}37)$$

where $10^{\mathscr{L}(f)/10}$ is the linear single-sideband phase noise, f_1 and f_2 are the lower and upper frequency limit of frequency interval respectively, and $2\pi f_0$ is the scale factor at the oscillation frequency f_0. The phase-jitter value can be compared with the RMS TIE; however, the TIE value is higher due to the aliasing and the noise floor of the oscilloscope used for its measurement.

1.2.3.2. Random and deterministic jitter

The types of measurements listed above and other more available in the literature can be decomposed and categorized into two categories: random and deterministic jitter.

1. **Random jitter [3] [76]**
   The random jitter (RJ) is produced by a non-predictable noise process inside the systems such as thermal, shot, and flicker noise. Owing to its random nature, its probability density function (PDF) consists of an unbounded Gaussian (normal) distribution, i.e., its range grows indefinitely when more jitter samples are analyzed and its peak-to-peak value is not well defined. For this, the RMS RJ value for clock analysis is frequently specified using the standard deviation of the distribution for a fixed jitter samples. A histogram is a tool for RJ determination by a plot of jitter values mea-

sured against its frequency of occurrence. Figure **1-10 a.** shows a typical histogram of random jitter measurements.
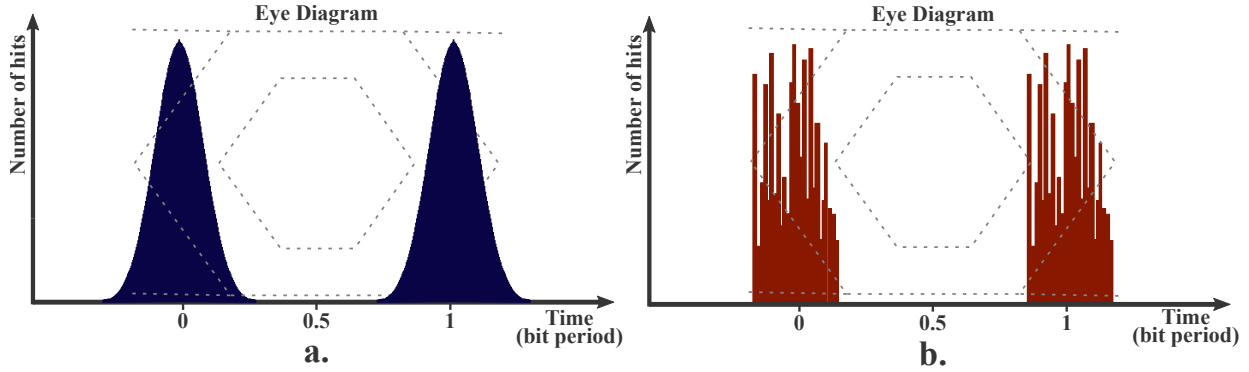
Figure 1-10.: a. Random jitter histogram **b.** Deterministic jitter histogram.

2. **Deterministic jitter [3] [76]**
   Unlike the random jitter, the probability density function of the deterministic jitter (DJ) is bounded. Therefore, the peak-to-peak value is well defined and predictable (Figure **1-10 b.**). The causes of DJ, e.g., channel bandwidth limitation, cross-talk, and the power supply noise are typically identifiable and, in this way, the DJ can be removed. Although there is no uniformity in the literature, the DJ is classified into several subcategories according to the originating mechanism. Usually, in clock jitter analysis, the only deterministic jitter process observed is the periodic jitter (PJ) (also called sinusoidal jitter SJ), identifiable through spurs in the SSB phase noise plot.

1.3. Optoelectronic oscillators - OEO

As we mentioned in section 1.1.1, there are several mechanisms for microwave signal generation by optical techniques. Today, one of the most sophisticated mechanism is the optoelectronic oscillator OEO, capable of generating spectrally pure microwave signals (low phase noise). The first OEO architecture was reported by Neyer and Voges in 1981 [14, 78] and was widely diffused in the 90s with the results of Yao and Maleki [79–81]. One of the main advantages of OEO architecture is the high configuration flexibility because it can be implemented in a wide variety of versions with different optical and electrical components to optimize its performance. For example, the amplifier and the filter can be implemented in either of the two segments (optical or electrical) [82], and the light laser can be modulated directly [83] or through an intensity modulator, phase modulator [84–86] or polarization modulator [57, 87–89].

The quality factor Q of the OEO resonant cavity, as in other oscillators, impacts the noise level of the overall system directly. Consequently, several authors have proposed different OEO implementations, among the most popular are the delay-line based OEO and optical

resonator based OEO. Some of the best known optoelectronic oscillators and their performance are presented below.

1.3.1. Optical delay-line based OEO

The first optical delay-line based OEO was presented by Yao and Maleki in 1994 [79]. This oscillator, illustrated in Figure **1-11 a.**, is a self-seeding ring oscillator composed of a laser source modulated by an intensity modulator and passed through a low-loss glass fiber that acts as an optical delay-line. Owing to the lower attenuation, long cavity length and high-quality factor Q are possible, allowing low phase noise. Then, the optical signal is converted to the electrical domain by a photodetector. The electrical signal is amplified by a microwave amplifier to compensate the loop losses, filtered by a band-pass filter to select the oscillation frequency and remove the spur modes (center frequency f_0 and quality factor Q_f) and finally, fed back to the electrical input port of the modulator.
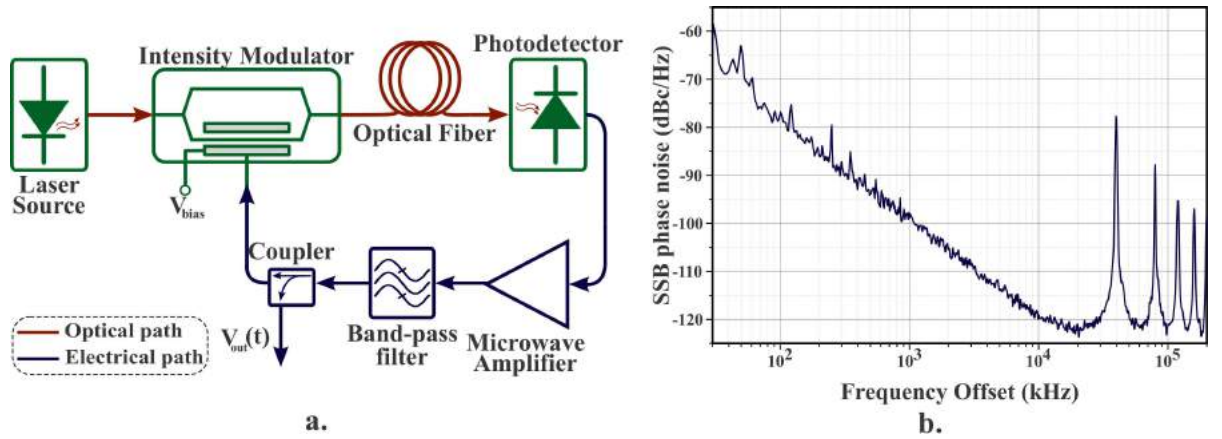
Figure 1-11.: a. Architecture of the delay-line based OEO **b.** Typical phase noise curve

The oscillation is achieved when phase and gain conditions are reached inside the loop, conditions known as Barkhausen conditions. Once there is oscillation, both the optical and electrical output signals can be analyzed in terms of stability. Figure **1-11 b.** shows a typical SSB phase noise spectrum of an electrical signal when the cavity length is around 5 km. The phase noise level and the selectivity of the oscillation mode depend on the Q factor, which is directly proportional to the optical fiber length, expressed as:

$$Q = \pi f_0 \tau_d \tag{1-38}$$

where τ_d is the optical fiber time delay. The mode spacing in the optical fiber is defined as the free spectral range (FSR), determined by:

$$FSR = \frac{1}{\tau_d} = \frac{c}{n_F L} \tag{1-39}$$

where c is the speed of light, n_F is the effective refractive index of the optical fiber, and L is the optical fiber length. From Equations 1-38 and 1-39, it can be inferred that the phase noise could be reduced by lengthening the optical fiber distance, but at the same time, the spurious modes are higher and closer, and the selection of a single-mode by the band-pass filter becomes difficult. These non-rejected modes also make an individual contribution of periodic jitter (deterministic), and a trade-off between the phase noise and timing jitter must be reached. In this context, there are different mechanisms for reducing the phase noise of OEOs. A simple way is eliminating the electric amplifier and its white and Flicker phase noise contribution. For this, losses within the loop must be compensated in the optical domain utilizing optical amplifiers [90–92] or by using high power lasers [93, 94].

Another differentiating factor between OEOs is the modulation mechanism and the laser used. Direct laser modulation has demonstrated to be an attractive alternative for the generation of microwave signals that simplifies the architecture of the system through the exclusion of external modulators. Among the most used laser sources are: distribute-feedback (DFB) [83, 95], dual-section distribute-feedback (DL-DFB) [96], micro square laser [97, 98], dual-mode amplified feedback laser (AFL) [99], and vertical-cavity surface-emitting lasers (VCSEL) [15, 100]. This last oscillator called VCSEL based optoelectronic oscillator VBO will be discussed and covered in Chapter 4.

Some applications such as radar systems, software-defined radio, and wireless communications require tunable microwave signals with low phase noise. Due to the difficulty in implementing a selective electric filter with a significant frequency tunable range, numerous authors implement optical filters inside the OEO loop, increasing the complexity and total system cost. Some of them achieve tunable OEOs employing microwave photonic filters (MPF) based on phase-shifted fiber Bragg grating (PS-FBG) [101, 102], or the deamplification of stimulated Brillouin scattering (SBS) [103], fiber Sagnac interferometer [104], injection locking and time delay compensation [105], and external-cavity semiconductor lasers [106].

The optical injection locking technique, addressed in the section 1.1.1.4, is a mechanism suggested by Pantell in 1965 [107] used for increasing the modulation bandwidth and reducing the linewidth of a slave laser injected by a master laser [108]. Through this technique, the reduced bandwidth of some VCSELs has been improved to generate microwave signals at 10 and 12 GHz [109, 110], keeping the OEO architecture. To enhance its applicability, the simultaneous use of OIL and high-order phase modulation sideband has allowed reaching frequencies up to 40 GHz at reduced SSB phase noise (-116 dBc/Hz) [111]. An optically injected Fabry-Perot laser with subharmonic modulation generates a microwave signal at 11.42 GHz and an SSB phase noise of -101 dBc/Hz [112]. Additionally, the dual injection-locked optoelectronic oscillator (DIL-OEO) has shown an ultra-low phase noise and an ultra-low spurious level applying the injection locking concept in the electrical domain to two OEO oscillators (backward and forward) [113–115]. The main limitations of oscillators listed above are the complex and bulky architecture, cost of implementation, and high energy consumption.

Until now, the systems presented in this text have relied on discrete photonic and electronic

devices, which implies low flexibility, high cost, and low applicability in reduced and efficient energy use environments. The development of integrated microwave photonics (IMWP) during the last years [116] has contributed to implementing monolithic integration of several traditional MWP functionalities over different technology platforms such as indium phosphide (InP) and silicon-on-insulator (SOI) [117], or heterogeneous integration to combine different material platforms and take advantage of their strengths [118], reducing the footprint and cost significantly. In this sense, new implementations of OEOs and arbitrary waveform generator (AWG) based on integrated photonics are available in the literature. The first fully monolithically integrated OEO (IOEO) reported in 2018 consists of a print circuit board with the optical and electrical segments packaged [119]. Regarding the optical components, the delay-line is an In-P based spiral-shape optical waveguide of 8.97 mm and significant attenuation of 2 dB/cm. The oscillation frequency depends on the injected current, and consequently, the IOEO has a tunable frequency range from 7.3 GHz to 8.87 GHz with phase noise values around -91 dBc/Hz.

1.3.2. Multi-loop OEO

One of the most representative limitations of OEOs is the level of spurious or non-rejected modes for long delay line lengths. For reducing this level and guarantee a single oscillating mode, it is possible to use a microwave filter with a high Q_f factor (ultra-narrow bandwidth) or to introduce a second fiber length into the OEO cavity.
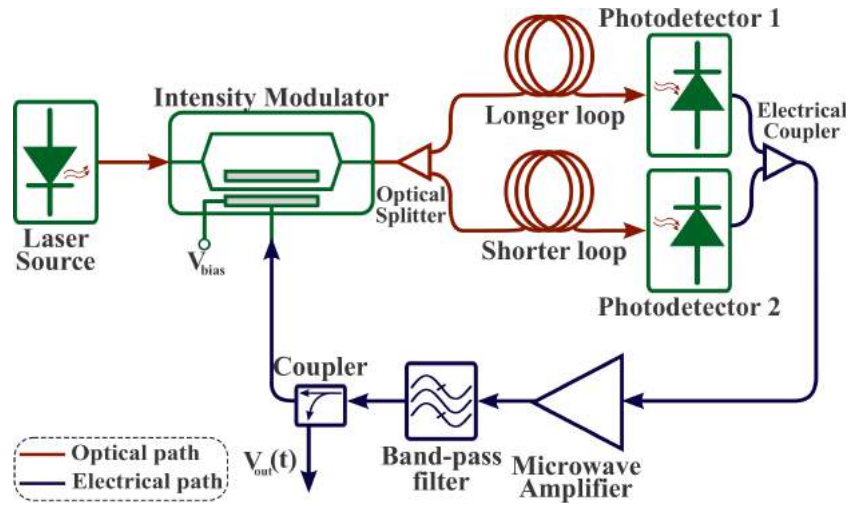
Figure 1-12.: Dual-loop optoelectronic oscillator

A dual-loop optoelectronic oscillator [120, 121], presented in Figure **1-12**, consists of two different length loops: a long loop that sets a high Q factor and a short loop that determines the FSR. The long length loop cannot be a harmonic multiple of the short loop to avoid overlapping modes, but when two modes are closest, they can lock, and the other modes are eliminated. Even though a multi-loop oscillator has high mode suppression, its phase noise

is the average of all loops [53], and in some cases, the phase noise is comparable to the noise of a single OEO [122].

Different authors have implemented and improved phase noise of multi loop OEOs by including all-optical gain [123], a dual-output Mach-Zehnder intensity modulator and a balanced photodetector [124], multicore fiber [125, 126], or phase-shifted fiber Bragg grating [127].

1.3.3. Optical resonator based OEO

Despite the multiple solutions listed in this manuscript and some more available in the literature, delay line based OEO remains an ultra-low phase noise system with bulky and complex implementations. One potential solution is to replace the optical delay line with optical resonators of relatively small size and high-quality factor Q_{opto}. When an optical resonator, such as micro-disk, silica sphere, fiber ring or whispering gallery mode resonator, is used inside an OEO oscillator, the quality factor Q that contributes to the phase noise performance (Equation 1-38 for delay line based OEO) is given by [128]:

$$Q = Q_{opto}\frac{f_0}{\nu_{opto}} \tag{1-40}$$

where ν_{opto} is the optical laser frequency in Hz. Similarly to delay line based OEO, the microwave quality factor is proportional to the oscillation frequency f_0. On the other hand, the FSR depends on the type of resonator and has values ranging from tens of MHz to a few GHz; in this way, some OEOs do not require a microwave filter [129, 130].

One of the main constraints is the dependence between the Q factor and the laser behavior (revealed in the Equation 1-40). For this, the optical resonator based OEOs must be stabilized employing locking techniques, for example, the Pound-Drever-Hall laser stabilization technique [131].

1.4. Optical frequency multipliers

In order to generate microwave signals in higher frequency bands, such as Ka-band (27 - 40 GHz) and W-band (75 - 110 GHz), some authors have designed optical frequency multipliers where a reference frequency can be duplicated [132, 133], quadrupled [134, 135], sextupled [29, 136], and even, octupled [137, 138].

A common factor among many topologies is the use of Mach-Zehnder modulators owing to its non-linear transfer function that allows the generation of different modes carefully selected to generate high-frequency signals in a photodetector (mechanism discussed in section 1.1.1.2) [139, 140].

The number of MZM modulators depends on the mode selection method. For example,

a W-band signal for wireless transmissions can be implemented using only one modulator and a wavelength selective switch (WSS) to select two symmetric subcarriers [141]. Other authors used two modulators polarized at a non-linear point [142,143], or three modulators to octuplicate a reference signal through odd-order sidebands suppression technique and filtering to transmit an orthogonal frequency division multiplexing (OFDM) signal over a fiber optic link [144]. More sophisticated systems include dual-polarization quadrature phase-shift keying (DP-QPSK) modulators composed of two QPSK modulator (each modulator include two MZM sub-modulators) [145].

Notwithstanding the high frequencies achieved by the systems mentioned above, the imminent deterioration of phase noise limits its amplification in other systems. Therefore, some authors have been interested in the OEO as an alternative that can be integrated with optical multiplication techniques. A multimode OEO was proposed in [4] and is illustrated in Figure **1-13**. The system consists of two cascaded MZM modulators biased at the minimum transmission point in order to eliminate even modes and the carrier. The MZM1 modulator generates the first-order sub-carriers, and the MZM2 modulator the third-order sub-carriers. A fiber Bragg grating (FBG) is included within the system to reflect the first-order sub-carriers and to transmit the third order to photodetector two (PD2) where, by heterodyning, a signal equal to six times the reference is generated. For a signal at 24 GHz, the phase noise is -103.6 dBc/Hz at 10 kHz.
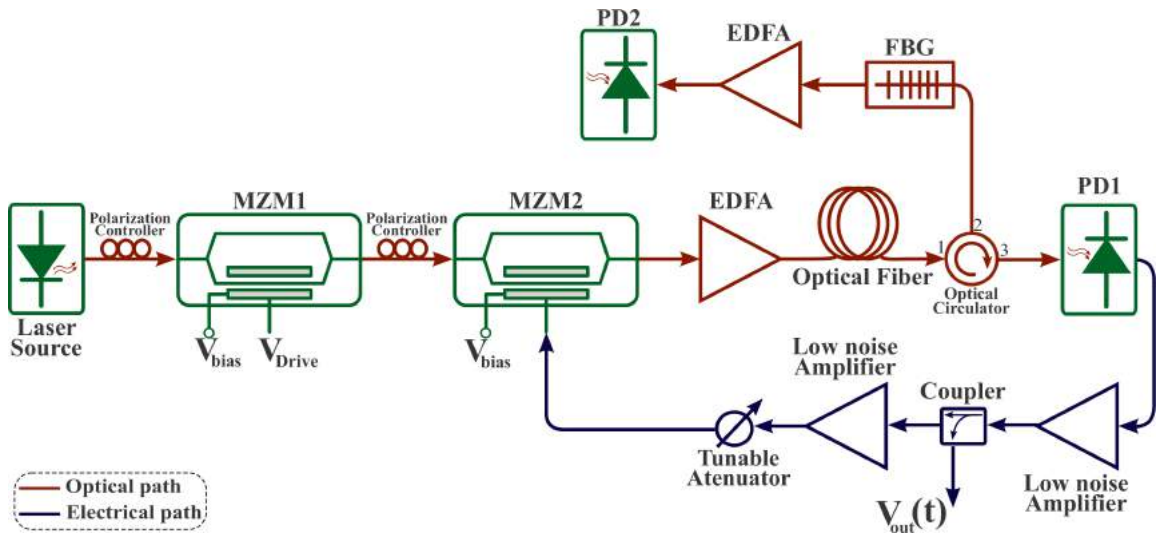
Figure 1-13.: Setup for frequency multiplication based on OEO proposed by [4]

The architecture illustrated in Figure **1-14**, known as harmonic frequency generator (HFG) [146], is another kind of optical frequency multiplier. The polarization of the optical signal emitted by a laser source is controlled by a polarization controller (PC) to ensure maximum transmission to the polarization beam splitter (PBS). Then, the signal is modulated in phase, and it crosses the resonant cavity, in this case, a Faraday mirror (FM), where the counter-propagating and incident waves are orthogonal. The reflected wave passes back through the phase modulator and the PBS in the opposite direction. The signal at port B is the result

of intensity modulation. This signal is detected in a photodetector to recover the resulting harmonics (2nd, 4th, and 6th order) from the reference signal ($V_{RF}(t)$).
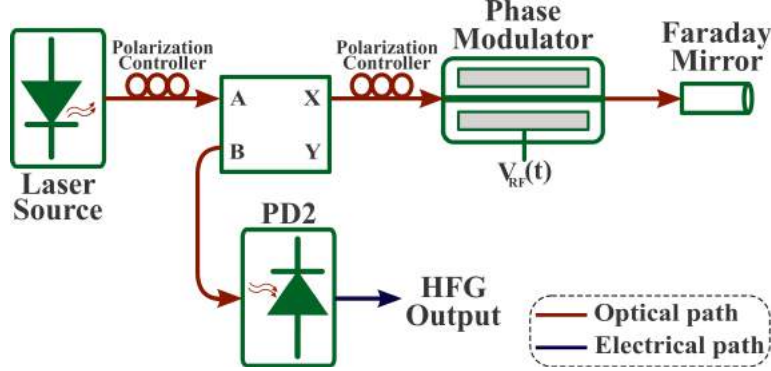
Figure 1-14.: HFG system configuration

1.5. Phase noise performance comparison of optoelectronic oscillators

The Table **1-2** shows some phase noise results of different optoelectronic oscillators addressed in the preceding sections. For each type of implementation, the oscillation frequency f_0 and the SSB phase noise at 10 kHz offset frequency (unless otherwise stated) are specified.

In agreement with the results reported in Table **1-2**, several OEO implementations feature phase noise values lower than -130 dBc/Hz at 10 kHz offset for a 10 GHz carrier. Among them, -160 dBc/Hz is the best phase noise (to our knowledge) obtained by a delay line based OEO; its phase noise value is slightly higher than the values of sapphire oscillators [157] (-165 dBc/Hz, 9 GHz carrier), and lower than dielectric resonator oscillator [158] (-125 dBc/Hz, 10.2 GHz carrier).

As regards the VBO oscillator, its oscillation frequency covers the microwave radio spectrum completely from the S-band to the X-band. Even if its phase noise performance is limited by different factors such as optical coupling (reflections towards the loop when on-chip VCSELs are used), this type of oscillators has demonstrated its potential compared to oscillators that have more bulky architectures and higher energy consumption. In the same way, the oscillation frequency can be increased by using VCSELs with bandwidths higher than 25 GHz [159] and matched electrical accesses. During the development of this thesis, pigtailed VCSELs were used in O and C-band (bands defined by International Telecommunication Union - ITU [160] and also known as long-wavelengths VCSELs); its structure and characterization will be detailed in Chapters 2 and 3.

Table 1-2.: Phase noise performance of several type of optoelectronic oscillators OEO

OEO type	Oscillation frequency f_0 (GHz)	Phase noise (dBc/Hz)	Reference
Delay line based OEO	10	-160 dBc/Hz	[147]
	10	-150 dBc/Hz	[148]
	10	-140 dBc/Hz	[149]
VCSEL based OEO	2.49	-125 dBc/Hz	[109]
	3	-106 dBc/Hz	[150]
	10	-70 dBc/Hz	[151]
	12	-73 dBc/Hz	[152]
Multi-loop OEO	2.5 - 7	-109 dBc/Hz	[153]
	5.5	-119 dBc/Hz	[154]
	10	-140 dBc/Hz	[121]
	15	-118 dBc/Hz	[154]
Resonator based OEO	10	-128 dBc/Hz	[155]
	10	- 95 dBc/Hz	[156]
	10	- 130 dBc/Hz	[129]

1.6. Conclusions

Throughout this chapter, some of the most relevant techniques for microwave signal generation via photonic components were presented. Some straightforward systems are based on two-wave optical heterodination in a photodetector, whereas other more complex systems include several optical modulators capable of adjusting the signal frequency generated from a reference signal. The applicability of microwave signals depends significantly on the frequency and quality. Given the wide frequency range covered and the technological progress in the manufacture of higher bandwidth components, these signals are suitable for wireless and optical telecommunications, data processing, and remote sensing.

The performance of microwave signals can be evaluated both in the frequency domain using phase noise and in the time domain applying statistical tools such as Allan variance. Although the use of each measurement depends on the application in which the microwave signal will be used, phase noise is the most widely used measurement in the scientific literature. The timing jitter is a useful measurement to characterize both clock signals and data streams.

In the last three sections, the optoelectronic oscillator (OEO) architecture and some of its variations used to reduce the phase noise and to eliminate/limit the effect of the non-oscillating modes produced by the resonant cavity were described. Some architectures for frequency multiplication using photonic components were also presented.

The proposed system for microwave signal generation in this work involves an optoelectronic oscillator based on the direct modulation of a vertical-cavity surface-emitting laser (VCSEL). For this reason, the following chapter is dedicated exclusively to VCSELs, their structure, static response, and behavior under large signal modulation conditions.

Chapter 2

Vertical Cavity Surface Emitting Laser - VCSEL

From the first developments of vertical-cavity lasers in the 60s and 70s, the industry of this type of lasers has progressively evolved owing to their benefits over edge-emitting lasers (EEL), their high acceptance in different sectors and applications, and the technological maturity achieved . Two notable advantages are the low threshold current (since quantum wells (QW) are used) and the circular beam profile (easy optical coupling). On the contrary, its low power level has limited its use in applications such as long-haul optical communications.

In terms of emission wavelength, VCSELs can be classified into short-wavelength and long-wavelength VCSELs (LW-VCSEL). LW-VCSEL covers the optical spectrum range defined by the ITU-T for single-mode fiber systems (from 1260 nm to 1675 nm), including the second and third windows named original band (O-band) and conventional band (C-band), respectively. The evolution of LW-VCSELs has been slower than in short-wavelength VCSELs (850 nm and 980 nm) due to technical difficulties to produce mirrors with high reflectivity ($> 99\%$) and a high gain active zone with materials based on ternary and quaternary alloys.

This chapter presents the structure and applications of O and C-band VCSELs employed in the development of this work. According to the structure of the proposed microwave signal generation system, the VCSEL modulation response, the optical pulse generation, and their noise characteristics are also discussed.

2.1. VCSEL structure and manufacturing

The first vertical-cavity laser reported by Melngailis in 1965 was manufactured using a n^+pp^+ doped indium antimonide (InSb) structure [161]. Under pulsed operation (50 ns pulse duration) applied parallel to the emitting direction, the laser wavelength achieved was

5.2 μm at 10 K. In 1979, Prof. Kenichi Iga introduced the first VCSEL at a near-infrared wavelength (1.18 μm) based on GaInAsP/InP alloy driven by 400 ns current pulses at 77 K [162]. Subsequent works from the Tokyo Institute of Technology presented a VCSEL at 1.22 μm using a metallic Au/Zn circular mirror and a threshold current of 160 mA [163,164].

In 1989, the first VCSELs at room temperature and continuous-wave (CW) operation were demonstrated [165]. The laser structure included a GaInAs active zone (formed by a single-quantum-well) and distributed Bragg reflector (DBR) mirrors for achieving a threshold current of 1.5 mA at 983 nm. Then, a VCSEL with an active GaAIAs zone grown by metalorganic chemical vapor deposition (MOCVD) and metallic mirrors Au/SiO$_2$/TiO$_2$/SiO$_2$ reached a threshold current between 28 and 40 mA at 894 nm [166]. In the same year, AT&T Bell Laboratories and Bellcore introduced a 958nm-VCSEL with AlAs/GaAs mirrors grown by molecular beam epitaxy (MBE), reaching a threshold current of 1.3 mA at room temperature [167].

2.1.1. VCSEL structure

The VCSEL is a semiconductor laser diode that emits laser light along a normal to the wafer surface (epitaxial layer). The small length of the optical gain region (given by the active layer thickness) is of the order of ten nanometers to several micrometers and limits the optical gain experienced by the photons inside the cavity. Therefore, to achieve a low threshold condition, mirrors with power reflectivity approaching 100% are needed. These mirrors, known as distributed Bragg reflectors (DBR), are typically implemented by stacking layers with different refractive indexes [168,169]. VCSEL structure is shown in Figure **2-1**.
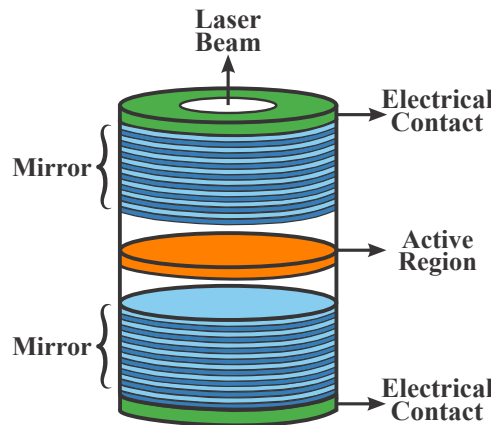
Figure 2-1.: VCSEL structure

Another VCSEL feature associated with the short cavity length is its single-mode behavior since the distance between longitudinal modes is larger than the linewidth of the optical gain spectrum of the active medium. Some transverse modes are excited by the generation of photons from the non-uniform distribution of carriers within the active zone [170]. In this

sense, a trade-off must be made between higher optical power and single-mode behavior. To achieve a single-transverse mode operation, higher-order modes must be eliminated through electrical and optical confinement.

Due to the vertical light emission, one- and two-dimensional VCSEL arrays with a small footprint can be manufactured for sensing [41], parallel optical interconnects [171], and LIDAR applications [172].

Some main features of VCSELs are [173]:

- Low threshold currents smaller than 1 mA, thus minimizing power consumption and simplifying the design of electronic driver circuits.

- Wall-plug efficiency (WPE) larger than 50% [174].

- Excellent digital modulation behavior for data rates nowadays approaching 70 Gbit/s [175].

- High robustness [176].

- Low sensitivity of threshold current and wavelength to temperature variations compared to edge-emitting laser diodes..

- Circular beam profiles with small divergence angles, simplifying the design of beam-shaping optics and the coupling process to optical components.

- Wide ambient operating temperature range exceeding +125 °C.

- Complete testing and device selection on the wafer level, yielding enormous cost reduction compared to edge-emitting laser diodes.

- High mean time between failures (MTBF) [168, 177].

2.1.2. VCSEL manufacturing

Materials, structure, and manufacturing of VCSELs vary according to the required wavelength. For example, the most commonly used materials for short-wavelength VCSELs (SW-VCSEL) are AlGaAs and GaInAs grown on GaAs substrate, whereas for O and C-band VCSELs, the materials are InGaAlAs and InGaAsP on InP substrate [8]. The use of different materials impacts the mirror reflectivity of lasers. In the case of SW-VCSEL around 850 nm, a reflectivity higher than 99% is achieved owing to the high difference between the refractive indexes of a reduced number of GaAs/AlAs layers (from 12 to 15 pairs). In contrast, for a similar reflectivity in LW-VCSEL, more than 40 InGaAsP/InP layers are necessary due to the small difference in refractive indexes, thus introducing high series resistance and optical losses [178].

Consequently, the mirrors of O and C-band VCSEL presented in the 1990s are composed of

several pairs of layers grown on InP and GaAs substrates. In 1993, Baba et al. demonstrated the first near room temperature CW lasing in a 1.3 μm GaInAsP/InP VCSEL using 8.5 pairs of p-doped MgO-Si with Au/Ni/Au metal at the top and six pairs n-doped SiO/Si at the bottom [179]. Likewise, Boucart et al. reported in 1999 a room temperature CW VCSEL emitting at 1.55 μm. The top DBR included 26.5 pairs of n-doped GaAs-AlAs and 50 pairs of n-doped InGaAsP-InP for the bottom mirror [180].

The best approach for VCSELs manufacturing in both optical bands consists of the integration of GaAs-based DBRs and InP-based quantum well active regions by localized wafer fusion. The active region and DBRs are grown independently by epitaxial growth, usually metalorganic vapor phase epitaxy (MOVPE) and molecular beam epitaxy (MBE). Its structure also includes a tunnel junction (TJ) aperture between the active region and one mirror for achieving current and optical confinement [181], reducing the optical absorption, and increasing thermal conductivity of mirrors [178]. These lasers, commonly known as wafer-fused VCSELs, have reached the industrial production stage and proven their reliability [181].

2.1.3. RayCan VCSEL

VCSELs used in this work were manufactured by the Korean company RayCan through epitaxially grown by one-step and vertical-flow low-pressure MOCVD on InP substrate. Figure **2-2** depicts the monolithic structure of 1.3 and 1.5 μm VCSELs. The active region consists of seven pairs of strain-compensated (SC) InAlGaAs quantum wells and, for reducing absorption losses, a C-doped InAlAs-based tunnel junction is positioned between a n-InP layer and the active region [5].
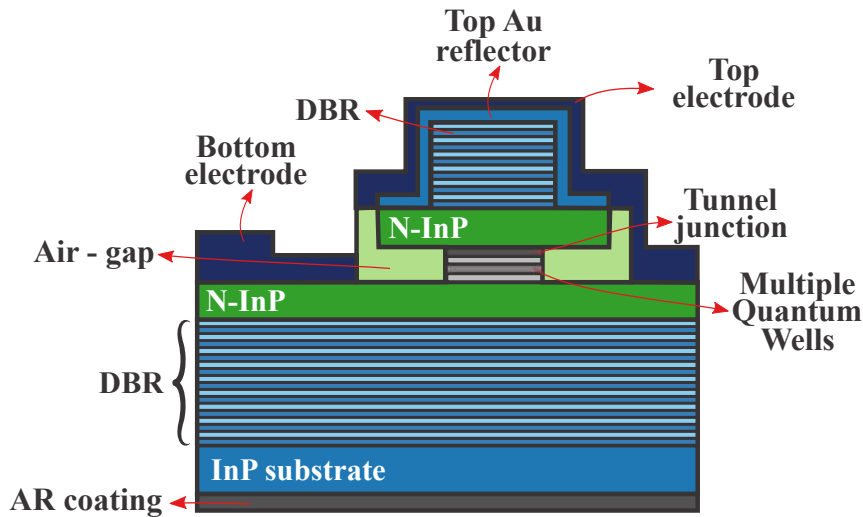
Figure 2-2.: Structure of an all-epitaxial RayCan VCSEL [5].

As stated above, to achieve high reflectivity with InAlGaAs based-DBRs and cover the long-wavelength band, several tens of layers are needed. In this context, for 1.3 μm VCSELs, the

top and bottom DBR are grown as 33 and 50 pairs of InAlGaAs-InAsAs schemes, whereas for 1.55 μm VCSELs, 28 and 38 pairs of undoped-InAlGaAs-InAsAs schemes are needed. An additional Au metal layer is included to increase the reflectivity of top DBRs [5]. Each VCSEL is mounted inside a TO-56 package and its output beam is coupled to an SM optical fiber.

2.2. VCSEL applications

Global data traffic has been continuously growing during the last two decades owing to the high demand for services (such as e-commerce, streaming video, and social networking) and connected devices. This traffic is supported by data centers and has influenced the VCSEL market owing to the vast majority of intra-data center interconnections use VCSEL-based optical multimode transceivers [182, 183]. Since 2014 this market became dynamic thanks to the VCSEL utilization in 3D sensing, LiDAR, and gas sensing [184]. According to Yole Dévelopement [185], VCSEL market revenues will grow five times from 2018 - 2024, whereas the EEL market growth will be only twice for the same period.

VCSEL market can be classified based on materials, applications, type, region, and end-user, among others. Some VCSEL applications are briefly presented below.

2.2.1. Optical communications

At present, VCSELs and parallel fibers are the dominant technology inside the data centers [186]. 850-nm VCSELs have been used in short-reach interconnects (< 300 m) over multimode (MM) fibers because the DBR manufacture at this wavelength is technically less complex. Under direct laser modulation, the fastest VCSEL-based link was reported at 71 Gb/s and a small bit-rate-distance product (7 m MM fiber) [187]. Other authors have demonstrated high-speed VCSEL-based transmitters using advanced modulation formats. For example, an optical link at 60 Gb/s was implemented using 4-pulse-amplitude modulation (PAM) and 200 m optical fiber [188], whereas in [189] the bit-rate achieved was 107.5 Gb/s when multi-band carrierless amplitude-phase modulation (CAP) and 10 m of MM optical fiber were used. Similarly, 980-nm VCSELs have a consistent role in data communications due to their advantages over 850-nm VCSELs, e.g., larger temperature insensitivity, lower chromatic dispersion, and lower transmission loss in the standard OM3 and OM4 MM fiber [41]. To date, 980-nm VCSEL with an error-free performance at 40 Gb/s [190], 44 Gb/s [191], and 50 Gb/s [192] have been demonstrated.

Nowadays, SW-VCSEL manufacture is a mature technology. Nevertheless, the capacity and link reach are limited by transmission losses and dispersion effects (chromatic and modal) in the optical fiber. In this context, data center operators have already started to replace MM fiber with single-mode (SM) fiber and to migrate from parallel optics to wavelength-division multiplexing (WDM) solutions [193]. Single-mode 1.3 and 1.55 μm VCSELs are used for

both short-reach and long-reach interconnects. Two links, 64 Gb/s back-to-back and 50 Gb/s over 15 km SM fiber, were demonstrated using a directly modulated 1.3-μm VCSEL and a feedforward equalizer (FFE) [194]. Similarly, 1.5-μm VCSELs are modulated with different modulation formats (generally PAM-4 and on-off keying OOK) to perform bit rates of 25 Gb/s [195], 40 Gb/s [196], 56 Gb/s [197], and 100 Gb/s [198].

RF-based wireless data transmissions are widely used in indoor and outdoor environments. However, high implementation costs, limited bandwidth, licensed bands, and interference from existing RF systems have driven the development of innovative systems. Optical wireless communications (OWC) consist of data transmission through the propagation of light in the free space. These systems are flexible, easy to install, immune to radio frequency interference, do not need licensed bands, and offer dense spatial reuse [199]. VCSELs in the visible and non-visible spectrum have been used in OWC indoor systems. Figure **2-3** shows a 680-nm VCSEL-Based Li-Fi (light fidelity) system with two-stage injection-locked. VCSEL bandwidth is improved from 5.6 GHz to 26.8 GHz by optical injection. Through PAM4, the bit rate achieved was 56 Gbps for 20-m free-space operation [6]. Similar implementations with three-stage injection-locking at 40 Gbps have been demonstrated using the same visible wavelength and free-space distances of 50 m [200] and 100 m [201].
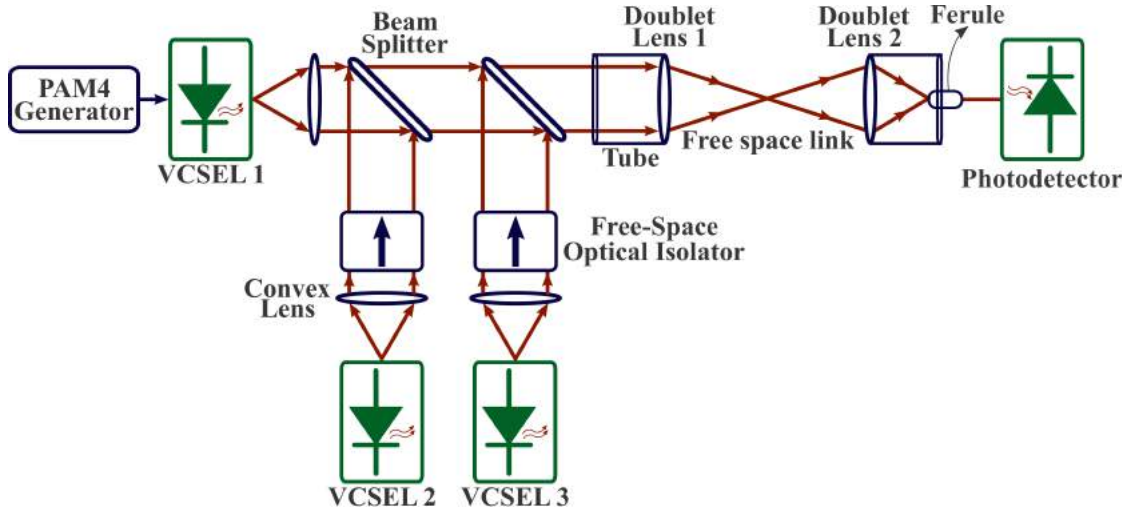
Figure 2-3.: VCSEL-based LiFi transmission setup. Adapted from [6].

Moreover, VCSELs in the non-visible spectrum are also applied for free-space transmissions. In [202], a 100-m FSO link at 64 Gb/s was established with a PAM4 modulated 1.55-μm VCSEL. Under the same principle, a 10-m FSO link at 84 Gb/s was reported in [203] by PAM8 modulation and the use of an optical vestigial sideband (VSB) filter to suppress the linewidth of the optical signal and reduce the fiber dispersion. In both cases, the VCSEL is injected by a DFB laser through an SM fiber optic circulator.

2.2.2. Sensing

The VCSEL implementation in sensing applications gives new dynamics in laser markets. For example, VCSELs are ideal light source for 3D imaging applications due to the possibility of manufacturing 2D VCSEL arrays. VCSELs are preferred over light-emitting diode (LED) for their narrow emission spectrum and the ability for short pulses generation [176]. Additionally, VCSELs feature wall-plug efficiency of slightly higher than 50% [174], minimizing the battery drainage and the self-heating in order to be employed in mobile devices [204]. Apple's iPhone X was the first mobile device to include 3D sensing technology using VCSELs manufactured by Finisar [205] for face identification and proximity sensing. Some VCSEL-based 3D sensing applications are [206]:

- Industrial automation, i.e., gate control, sensing the size and content of containers.

- Home automation by tracking, detecting and identifying individual motion.

- Traffic management for tracking the number of vehicles and distance sensing.

- Entertainment and gaming sector for body gesture monitoring and game control.

- VCSEL-based time of flight (ToF) sensors for robots, vehicles, and household devices.

Besides, VCSELs are used for short-range light detection and ranging (LiDAR) due to their low consumption, high cost-effectiveness, narrow divergence, and good temperature tolerance [207].

2.3. Static and dynamic properties of VCSELs

Direct modulation of VCSELs is the heart of the proposed architecture for microwave signals generation detailed in Chapter 4. Static and dynamic characteristics of directly modulated VCSELs, as well as EEL lasers, can be obtained using a temperature-independent single-mode rate equation model. A model based on rate equations allows describing the dynamic behavior and interaction of carriers and photons inside the optical cavity. Additionally, the model applied to VCSELs gives access to intrinsic physical quantities useful for performing numerical simulations [208].

The VCSEL rate equation system is composed of three differential equations: carrier density $N(t)$ (electrons or holes), photon density $S(t)$, and optical phase $\phi(t)$. The rate equations for a single-mode VCSEL are as follow [209]:

$$\frac{dN(t)}{dt} = \frac{\eta_i I(t)}{qV_{act}} - \left(A + BN(t) + CN^2(t)\right)N(t) - \upsilon_g GS(t) \qquad (2\text{-}1)$$

$$\frac{dS(t)}{dt} = \Gamma\beta BN^2(t) + \Gamma\upsilon_g GS(t) - \frac{S(t)}{\tau_P} \qquad (2\text{-}2)$$

$$\frac{d\phi(t)}{dt} = \frac{\alpha_H \Gamma \upsilon_g a_0}{2} \left(N(t) - N_{tr} \right) \tag{2-3}$$

and the optical gain G is expressed as:

$$G = a_0 \frac{N(t) - N_{tr}}{1 + \epsilon S(t)} \tag{2-4}$$

where η_i is the internal quantum efficiency, I the injected current into the cavity, q the electron charge, V_{act} the active region volume, υ_g the group velocity, β the spontaneous emission coefficient, Γ the longitudinal confinement factor, τ_P the photon lifetime, α_H is the phase-amplitude coupling factor referred also as Henry Factor, a_0 the differential gain coefficient, ϵ the gain compression factor, and N_{tr} the transparency carrier density.

The three terms to the right of Equation 2-1 correspond to the carriers injection (through the injected current I), the non-stimulated, and the stimulated recombinations, respectively. The non-stimulated recombination is the major parasitic carrier loss mechanism [208] and is given by the spontaneous and non-radiative recombination rates, R_{sp} and R_{nr}. These losses are included in the Equation 2-1 through three coefficients: A is the Shockly-Read-Hall non-radiative recombination coefficient, B the radiative recombination coefficient, and C the Auger non-radiative recombination coefficient [210]. The last term represents the carrier loss by the stimulated emission process, which relates the optical gain G and the photon emission into the lasing mode [208].

In the case of Equation 2-2, the term $\Gamma \beta B N(t)^2$ denotes the amount of spontaneous emission involved in the lasing mode. The stimulated recombination contribution is expressed by $\Gamma \upsilon_g G S(t)$ and the photon losses by $S(t)/\tau_P$. Photon lifetime is a time constant that indicates the photons decay owing to the cavity and mirrors losses. Thus, photon lifetime is expressed as $\tau_P^{-1} = \upsilon_g (\alpha_{cav} + \alpha_m)$ where α_{cav} and α_m are the cavity and mirror losses, respectively.

Finally, the non-coupled Equation 2-3 depicts the phenomenon of carrier induced frequency modulation and gives information about the instantaneous frequency $\nu(t)$ of the optical signal ($\nu(t) = \frac{1}{2\pi} \frac{d\phi(t)}{dt}$) [178].

The random nature of the spontaneous emission and other noise sources inside the laser produce carrier and photon fluctuations. These fluctuations impact the amplitude and optical phase of beam laser directly, and their stochastic evolutions can be included in the Equations 2-1 and 2-2 through the Langevin forces ($F_N(t)$ for carrier and $F_S(t)$ for photons fluctuations). For simplicity, noise contributions are not considered in the steady-state and small-signal analysis.

As stated above, the solution of Equations 2-1, 2-2, and 2-3 allows analyzing VCSEL behavior according to its intrinsic parameters. However, there is no analytical solution, and the equations must be solved numerically or by the application of some approximations [208]. Therefore, steady-state and small-signal frequency response solutions are presented and employed to extract VCSELs parameters and to perform large-signal modulation simulations.

2.3.1. Steady-state solutions

Steady-state equations allow determining VCSELs parameters, such as threshold current, steady-state carrier and photon densities, under constant current injection. For this, time derivatives are set to zero ($d / dt = 0$) and different bias current conditions are considered. The steady-state equations are as follow:

$$\frac{\eta_i I}{q V_{act}} - \left(A + BN(t) + CN(t)^2\right) N(t) - v_g GS(t) = 0 \tag{2-5}$$

$$\Gamma \beta BN(t)^2 + \Gamma v_g GS(t) - \frac{S(t)}{\tau_P} = 0 \tag{2-6}$$

Consequently, it is possible to identify the following steady-state solutions:

1. For $I < I_{th}$ and applying an asymptotic approach, i.e., neglecting the spontaneous emission and gain compression ($\Gamma \beta BN(t)^2 = 0$ and $\epsilon S(t) = 0$), Equation 2-5 reveals:

$$I = \frac{q V_{act}}{\eta_i} \left(A + BN + CN^2\right) N \tag{2-7}$$

When the threshold condition is reached and considering the carrier lifetime as $\tau_N^{-1} = A + BN + CN^2$, the threshold current I_{th} corresponds to:

$$I_{th} = \frac{q V_{act}}{\eta_i \tau_N} N_{th} \tag{2-8}$$

At threshold condition, the generation term equals the recombination term and the optical gain can be estimated from Equation 2-6 as:

$$G_{th} = \frac{1}{\Gamma v_g \tau_P} \tag{2-9}$$

2. For $I > I_{th}$, stimulated photons are emitted ($S > 0$) and the carriers stop growing linearly with the current. Due to the equilibrium given by carrier recombination and the injected current, the carrier density tends to N_{th}. Keeping the spontaneous emission and gain compression assumptions, the carrier density is determined using Equation 2-6 as follows:

$$N = N_{tr} + \frac{1}{\tau_P \Gamma v_g a_0} = N_{th} \tag{2-10}$$

Photon density is also obtained by using Equation 2-8 and solving Equation 2-5. The linear relationship of photon density and bias current above the threshold is expressed as:

$$S = \Gamma \tau_P \frac{\eta_i}{q V_{act}} \left(I - I_{th}\right) \tag{2-11}$$

Finally, the optical power output P_{out} from the mirrors can be determined knowing

that $P_{out} = v_g \alpha_m S h\nu V_{cav}$ where $h\nu$ is the energy per photon and V_{cav} the cavity volume. Substituting from Equation 2-11 and using $\Gamma = V_{act}/V_{cav}$ [210], the power output corresponds to:

$$P_{out} = \eta_i \left(\frac{\alpha_m}{\alpha_{cav} + \alpha_m} \right) \frac{h\nu}{q} (I - I_{th}) = \eta_d \frac{h\nu}{q} (I - I_{th}) \qquad (2\text{-}12)$$

where η_d is the differential quantum efficiency.

3. When $I \gg I_{th}$, the photons are generated by stimulated emission and the effect of gain compression should be considered ($S \gg 1/\epsilon$). Neglecting the spontaneous emission, the steady-state equations can be rewritten as:

$$\frac{\eta_i I}{q V_{act}} - \frac{N(t)}{\tau_N} - v_g a_0 \frac{N(t) - N_{tr}}{1 + \epsilon S(t)} S(t) = 0 \qquad (2\text{-}13)$$

$$\Gamma v_g a_0 \frac{N(t) - N_{tr}}{1 + \epsilon S(t)} S(t) - \frac{S(t)}{\tau_P} = 0 \qquad (2\text{-}14)$$

Solving Equation 2-13, the photon density can be expressed as:

$$S = \frac{\eta_i (I - I_{th})}{q V_{act} v_g a_0 (N_{th} - N_{tr}) - \epsilon \eta_i (I - I_{th})} \qquad (2\text{-}15)$$

According to the magnitude of VCSEL parameters $\epsilon \ll v_g a_0$ [211], and therefore Equation 2-15 validates Equation 2-11.

Similarly, the gain compression factor and the transparency carrier density can be derived from Equation 2-13 as follow:

$$\epsilon = \frac{q V_{act} v_g a_0 S (N_{th} - N_{tr}) - \eta_i (I - I_{th})}{S \eta_i (I - I_{th})} \qquad (2\text{-}16)$$

$$N_{tr} = N_{th} - \frac{\eta_i (I - I_{th}) (1 + \epsilon S)}{q V_{act} v_g a_0 S} \qquad (2\text{-}17)$$

2.3.2. Small-signal frequency response

Unlike the steady-state solutions, the small-signal analysis gives additional information about VCSEL dynamical behavior under specific perturbations, such as current modulation. For this purpose, first-order expansion of the rate equations is applied, and the assumption that the changes in the carrier and photon densities away from their steady-state values are small [210].

Firstly, assuming that the VCSEL is biased at $I_0 > I_{th}$ and that the carrier density, photon

density, and the injected current are dynamic variables described as:

$$I(t) = I_0 + \Delta I(t) \tag{2-18}$$

$$N(t) = N_0 + \Delta N(t) \tag{2-19}$$

$$S(t) = S_0 + \Delta S(t) \tag{2-20}$$

where $\Delta I(t) \ll I_0$, $\Delta N(t) \ll N_0$ and $\Delta S(t) \ll S_0$. Considering that $\frac{dN(t)}{dt} = \frac{d\Delta N(t)}{dt}$ and setting $\Delta \dot{N} = \frac{d\Delta N(t)}{dt}$ for all the dynamic variables, Equations 2-1 and 2-2 become:

$$\Delta \dot{N}(I, N, S) = \frac{\partial \dot{N}}{\partial I}\Delta I + \frac{\partial \dot{N}}{\partial N}\Delta N + \frac{\partial \dot{N}}{\partial S}\Delta S \tag{2-21}$$

$$\Delta \dot{S}(N, S) = \frac{\partial \dot{S}}{\partial N}\Delta N + \frac{\partial \dot{S}}{\partial S}\Delta S \tag{2-22}$$

After determining the derivatives for the carrier and photon densities, the linearized equations are:

$$\Delta \dot{N} = \frac{\eta_i}{qV_{act}}\Delta I - \left(\frac{1}{\tau_{\Delta N}} + v_g G_N S_0\right)\Delta N - (v_g G - v_g G_S S_0)\,\Delta S \tag{2-23}$$

$$\Delta \dot{S} = (2\Gamma \beta B N_0 + \Gamma v_g G_N S_0)\,\Delta N - \left(\frac{\Gamma \beta B N_0^2}{S_0} + \Gamma v_g G_S S_0\right)\Delta S \tag{2-24}$$

where G_N represents the differential gain, G_S the gain compression and $\tau_{\Delta N}$ the differential carrier lifetime [210], are expressed as:

$$G_N = \frac{\partial G}{\partial N} = \frac{a_0}{1 + \epsilon S_0} \tag{2-25}$$

$$G_S = -\frac{\partial G}{\partial S} = \frac{\epsilon a_0\,(N_0 - N_{tr})}{(1 + \epsilon S_0)^2} \tag{2-26}$$

$$\frac{1}{\tau_{\Delta N}} = A + 2BN_0 + 3CN_0^2 \tag{2-27}$$

The carrier density can be considered constant at bias currents above the threshold and consequently, the optical gain becomes likewise constant. Using Equation 2-9, Equations 2-23 and 2-24 are rewritten as:

$$\Delta \dot{N} = \frac{\eta_i}{qV_{act}}\Delta I - \left(\frac{1}{\tau_{\Delta N}} + v_g G_N S_0\right)\Delta N - \left(\frac{1}{\Gamma \tau_P} - v_g G_S S_0\right)\Delta S \tag{2-28}$$

$$\Delta \dot{S} = (2\Gamma\beta BN_0 + \Gamma v_g G_N S_0)\, \Delta N - \left(\frac{\Gamma\beta BN_0^2}{S_0} + \Gamma v_g G_S S_0\right)\Delta S \qquad (2\text{-}29)$$

Arranging like terms and defining rate coefficients, the linearized equations can be represented in a matrix form:

$$\frac{d}{dt}\begin{bmatrix} \Delta N \\ \Delta S \end{bmatrix} = \begin{bmatrix} -\gamma_{NN} & -\gamma_{NS} \\ \gamma_{SN} & -\gamma_{SS} \end{bmatrix}\begin{bmatrix} \Delta N \\ \Delta S \end{bmatrix} + \frac{\eta_i}{qV_{act}}\begin{bmatrix} \Delta I \\ 0 \end{bmatrix} \qquad (2\text{-}30)$$

where the rate coefficients are expressed as:

$$\gamma_{NN} = A + 2BN_0 + 3CN_0^2 + v_g G_N S_0 \qquad (2\text{-}31)$$

$$\gamma_{NS} = \frac{1}{\Gamma\tau_P} - v_g G_S S_0 \qquad (2\text{-}32)$$

$$\gamma_{SN} = 2\Gamma\beta BN_0 + \Gamma v_g G_N S_0 \qquad (2\text{-}33)$$

$$\gamma_{SS} = \frac{\Gamma\beta BN_0^2}{S_0} + \Gamma v_g G_S S_0 \qquad (2\text{-}34)$$

For a small-signal analysis, the current modulation can be considered as a small-sinusoidal signal defined as $\Delta I(t) = I_m e^{j\omega t}$. Therefore, the carrier and photon densities vary in the same way as $\Delta N(t) = N_m e^{j\omega t}$ and $\Delta S(t) = S_m e^{j\omega t}$, respectively. Setting $d/dt \to j\omega$, Equation 2-30 becomes:

$$\begin{bmatrix} \gamma_{NN} + j\omega & \gamma_{NS} \\ -\gamma_{SN} & \gamma_{SS} + j\omega \end{bmatrix}\begin{bmatrix} N_m \\ S_m \end{bmatrix} = \frac{\eta_i I_m}{qV_{act}}\begin{bmatrix} 1 \\ 0 \end{bmatrix} \qquad (2\text{-}35)$$

Applying the Cramer's rule, the small-signal carrier and photon densities in terms of the modulation current are [210]:

$$N_m = \frac{\eta_i I_m}{qV_{act}}\frac{\gamma_{SS} + j\omega}{\Lambda} \qquad (2\text{-}36)$$

$$S_m = \frac{\eta_i I_m}{qV_{act}}\frac{\gamma_{SN}}{\Lambda} \qquad (2\text{-}37)$$

where Λ is the determinant of the matrix given by:

$$\begin{aligned} \Lambda &= \gamma_{NN}\gamma_{SS} + \gamma_{NS}\gamma_{SN} + j\omega\left(\gamma_{NN} + \gamma_{SS}\right) - \omega^2 \\ &= \omega_R^2 + j\omega\gamma - \omega^2 \end{aligned} \qquad (2\text{-}38)$$

In Equation 2-38, ω_R is the relaxation resonance pulsation and γ the damping factor. Therefore, the normalized modulation response defined as $H(\omega) = \frac{S_m(\omega)}{I_m(\omega)}\big/\frac{S_m(0)}{I_m(0)}$ [178], corresponds to:

$$H(\omega) = \frac{\omega_R^2}{\omega_R^2 + j\omega\gamma - \omega^2} \qquad (2\text{-}39)$$

The two-pole function $H(\omega)$ in Equation 2-39, presents the typical form of a second-order

system, such as an RLC circuit or a low-pass filter. For a well above threshold operation, the relaxation resonance pulsation can be simplified to [210]:

$$\omega_R^2 \equiv \frac{\upsilon_g a_0 S_0}{\tau_P} \tag{2-40}$$

Replacing Equation 2-11 in Equation 2-40, it is possible to estimate the relaxation resonance frequency f_R as a function of the injected current:

$$f_R = \frac{1}{2\pi} \sqrt{\frac{\eta_i \upsilon_g \Gamma a_0}{q V_{act}}} \sqrt{I - I_{th}} \tag{2-41}$$

Figure **2-4** presents the simulated modulation transfer function for several bias currents when the VCSEL parameters shown in Appendix A are used. At low frequencies, $H(\omega) = 1$ and the frequency response magnitude (S_{21}) grows from 0 to the relaxation resonance frequency. Raising the injected current, both f_R and γ increase, and the relaxation resonance peak is less-marked (higher damping). In all cases, the damped response drops off abruptly after the resonant frequency with a slope of 40 dB/dec.
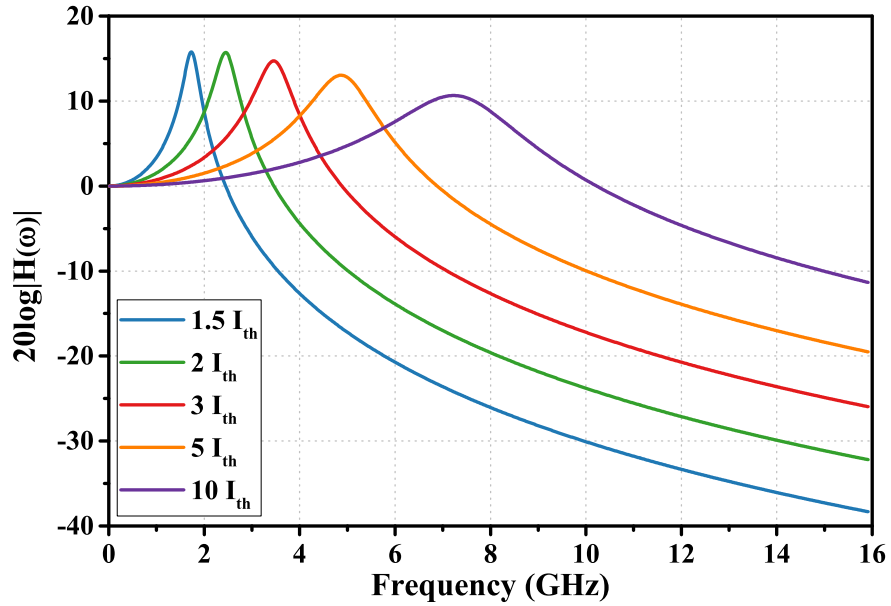
Figure 2-4.: Simulation of modulation transfer function at different bias currents.

2.3.3. Large-signal modulation

Both steady-state and small-signal analysis provide information about laser behavior under specific considerations. However, when the VCSEL is used in digital transmission and optical pulses generation systems, these conditions (modulation index $m \ll 1$) are not satisfied and

nonlinear effects must be considered [212]. Owing to the dynamic and complex large-signal behavior, numerical solutions are introduced using the traditional rate equations.

For large-signal modulation, the optical output waveform depends on the frequency and amplitude of the input signal [213]. For sinusoidal modulation, the optical response takes the form of a narrow pulse followed by a "ringing," which is related to damped oscillations at the relaxation resonance frequency f_R. The main pulse corresponds to the first peak of the relaxation oscillations. As the modulation index increases, the subsequent peaks are strongly suppressed and the output takes the form of a short optical pulse [214]. Figure **2-5** shows the effect of relaxation frequency and peaks apparition when a step-current is applied to laser.
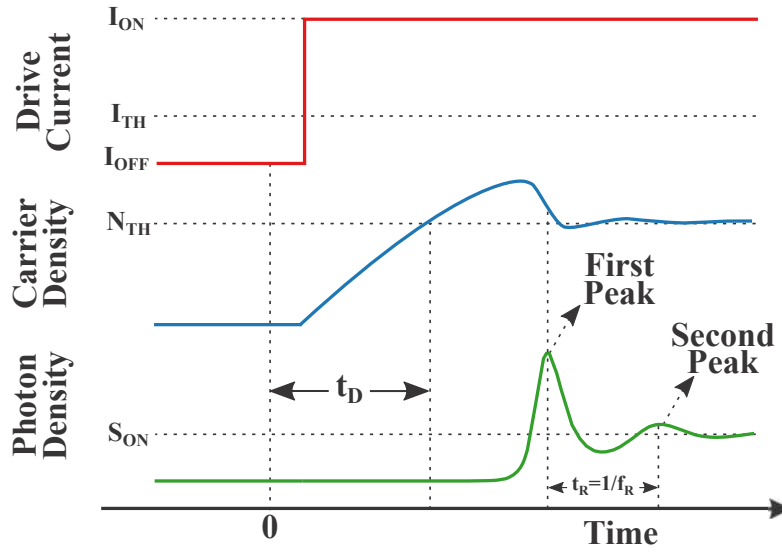
Figure 2-5.: Representation of turn-on delay and relaxation frequency.

Two effects specially analyzed in large-signal modulation are the turn-on delay and the frequency chirp. According to Petermann [215], if a laser diode is biased below the threshold as shown in Figure **2-5**, the turn-on delay t_D is the time between the application of an ideal step-current pulse and the instant when the threshold carrier density is achieved. This time is dominated by the carrier lifetime and is expressed as [216]:

$$t_D = \tau_N \ln \left(\frac{I_{ON} - I_{OFF}}{I_{ON} - I_{th}} \right) \tag{2-42}$$

To avoid this delay time in data transmission systems, lasers are biased slightly above or below the threshold current. Measuring t_D is a delicate process because the carrier lifetime is small (about nanoseconds) and because there are also complementary delays arising from the control systems and the optical and electrical interconnections. In Chapter 3, the carrier lifetime of a C-band VCSEL is estimated by measuring the turn-on delay.

Another effect of direct intensity modulation is the temporal variation of carrier density and

optical phase owing to the amplitude-phase coupling of the laser (Equation 2-3). Optical phase variations involve transient changes in the mode frequency from its steady-state value ν_0 [212]. This phenomenon is known as frequency chirp $\Delta\nu(t)$ (or wavelength chirp). An expression for the laser frequency deviation can be obtained from the solution of the photon density equation and the first-order expansion of the optical gain around the threshold. Thus, two new relationships can be derived as:

$$S(t)\left[\Gamma v_g G - \frac{1}{\tau_P}\right] = \frac{dS(t)}{dt} - \Gamma\beta BN^2(t) \tag{2-43}$$

$$G = G_{th} + G_N\left(N(t) - N_{th}\right) - G_S S(t) \tag{2-44}$$

Using the two equations above, the frequency chirp is determined as [210]:

$$\Delta\nu(t) = \frac{\alpha_H}{4\pi}\left[\frac{1}{S(t)}\frac{dS(t)}{dt} - \frac{\Gamma\beta BN^2(t)}{S(t)} + \Gamma v_g G_S S(t)\right] \tag{2-45}$$

Under large-signal modulation at frequencies on the order of gigahertz or higher, transient chirp is dominant and Equation 2-45 can be reduced to:

$$\Delta\nu(t) = \frac{\alpha_H}{4\pi}\frac{1}{S(t)}\frac{dS(t)}{dt} \tag{2-46}$$

When the injected current varies sinusoidally, the mode frequency shifts periodically, whereas the maximum shift $\Delta\nu_0$ depends on the injected peak current I_m and the factor α_H. The frequency chirp produces the broadening of CW linewidth and limits the performance of digital data transmissions due to the widening of the optical pulses during their propagation. Injection locking and pulse-shape tailoring are techniques to reduce the chirping magnitude [212, 214].

2.3.4. Gain Switching - GS

During the last decades, short optical pulses have been applied in different fields, including THz generation [217], spectroscopy [218], and microscopy [219]. In semiconductor lasers, pulse generation can be performed using mode-locking, Q-switching, or gain switching. The application of the first two methods can be difficult because the laser cavity must be modified by inserting active devices such as an acoustic-optical and intensity modulators, and passive devices such as saturable absorbers. In contrast, gain switching (GS) [17] is the simplest and the most setting flexible method: it is a continuous modification of cavity gain through large-signal modulation (rapid variation of injected carriers).

As stated in the previous section, the photon density (related to the optical output power) of semiconductor lasers exhibits a damped oscillating behavior represented in Figure **2-5** by different spikes spaced at f_R. To generate an ultrashort (picoseconds or femtoseconds

duration) pulse train through GS, the sinusoid or pulse train drive current must be turned off before the occurrence of the second spike. Therefore, the optical pulse train frequency can be modified by merely adjusting the drive repetition rate at values higher than the relaxation frequency f_R.

As an effect of direct modulation and amplitude-phase coupling, the optical pulses with GS are considerably chirped. The nonlinear behavior of the frequency chirp is governed by density variations of injected carriers and the effect of gain compression. The width of the chirped optical pulses can be compressed by a factor of 4-5 by using a compensating fiber dispersion [214].

In order to identify the characteristics of gain switching, rate equations 2-1 - 2-3 are solved numerically. Figure **2-6** shows the optical pulses generated by employing the VCSEL intrinsic parameters listed in Appendix A. The injected current $I(t) = I_0 + I_m cos(2\pi f_m t)$ is adjusted through I_0 from 3 to 5 mA, the amplitude I_m remains constant in 3 mA, f_m is equal to 1 GHz, and $I_{th} = 1$ mA.
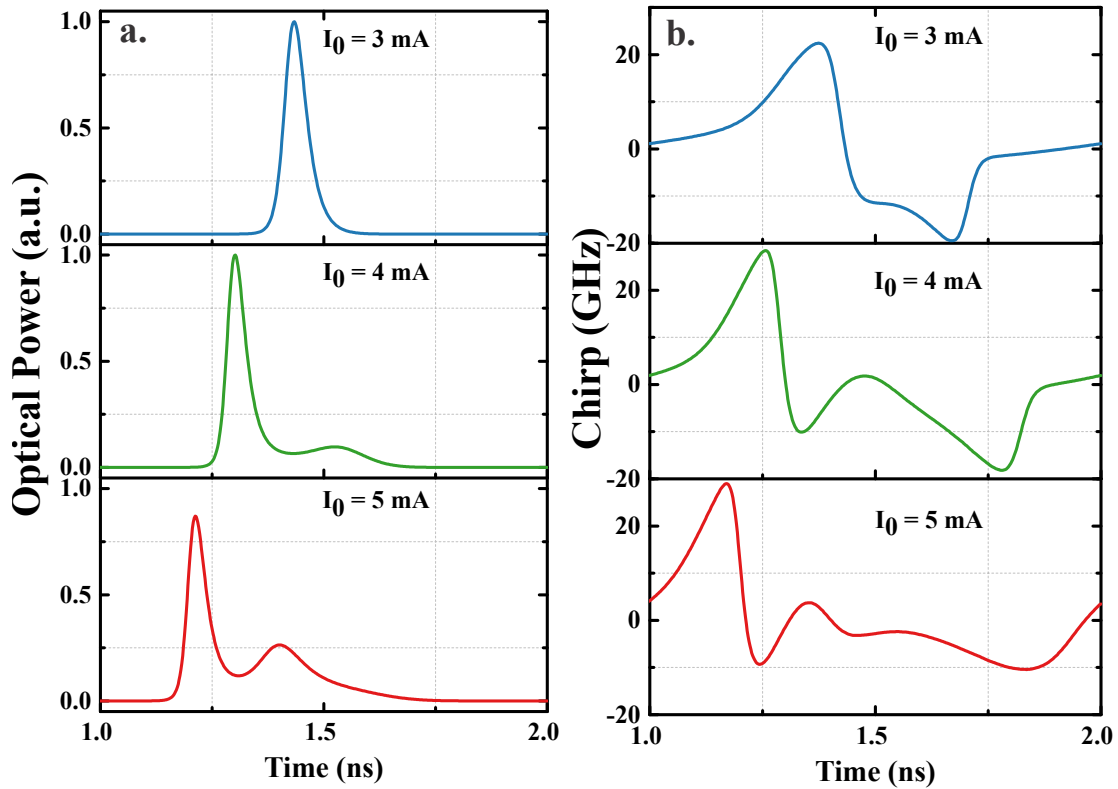
Figure 2-6.: Gain switching simulation **a.** Optical pulse shape **b.** Frequency chirp.

Although the VCSEL is always biased above the threshold $(I_0 > I_{th})$, only the first peak is excited in the case of $I_0 = 3$ mA. In other cases, the pulse includes a bump because the laser is biased above the threshold during the whole cycle and the second relaxation peak is excited. Conversely, the VCSEL response is faster for $I_0 = 5$ mA because the carrier density

threshold is reached earlier. Concerning the frequency chirp, its initial value depends on the number of carriers injected through $I(t)$. The highest positive level occurs when the carrier density begins to decline due to the recombination process (gain compression effect). On the one hand, the pulse width depends on operating parameters such as the bias level I_0, the peak current $I_m^{\max}$, and the photon lifetime τ_P [214]. On the other hand, the peak power is mainly determined by the accumulation speed after the carrier density reaches the threshold [220].

2.4. Electrical modeling of the active zone

Considering the small-signal frequency response developed in Section 2.3.2, the active zone can be modeled through an equivalent electrical circuit. The model detailed below is based on the electrical model proposed by Bacou [8] for LW-VCSEL.

2.4.1. Equivalent circuit equations

In 1983, Tucker introduced the most accepted equivalent electrical scheme [7, 221]. This scheme, shown in Figure **2-7**, has been employed in previous works for modeling a VCSEL at 850 nm [222, 223]. The parallel circuit $R_j C_j$ symbolizes the quantum wells, the series circuit $R_0 L_0$ represents the losses and storage of photons in the optical cavity, and H is the transimpedance of the current-controlled voltage-source.
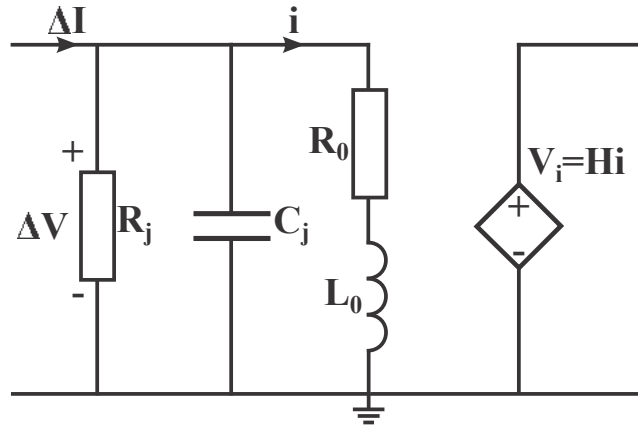
Figure 2-7.: Equivalent electrical scheme of laser cavity [7].

Applying Kirchhoff's circuit laws, the voltage ΔV and the stimulated branch current i are expressed as:

$$\frac{d\Delta V}{dt} = \frac{\Delta I - i}{C_j} - \frac{\Delta V}{R_j C_j} \tag{2-47}$$

$$\frac{di}{dt} = \frac{\Delta V}{L_0} - \frac{R_0}{L_0}i \tag{2-48}$$

where ΔI is the current cavity variations and ΔV is the voltage variation at the active zone terminals. Assuming an exponential V-I relationship, the laser diode current is given by:

$$I = I_{sat}\left[e^{(V/mV_T)} - 1\right] \tag{2-49}$$

where I_{sat} is the saturation current, V_T the thermal voltage, and m the ideality factor. Then, assuming that I_{sat} is negligible compared to I_0, the voltage variation is determined as:

$$\frac{\Delta V}{mV_T} = \frac{\Delta I}{I_0} \tag{2-50}$$

Finally, the relative variation of the carrier density is proportional to the relative variation of the injected current, and the equality of Equation 2-50 becomes:

$$\frac{\Delta V}{mV_T} = \frac{\Delta I}{I_0} = \frac{\Delta N}{N_0} \tag{2-51}$$

2.4.2. Determination of electrical parameters

The development presented below is based on the small-signal analysis and electrical relationships of the previous section. From Equation 2-51, the carrier density evolution is expressed as:

$$\frac{d\Delta N}{dt} = \frac{N_0}{mV_T}\frac{d\Delta V}{dt} \tag{2-52}$$

Under the assumption that carrier density tends to N_{th} above the threshold, the linearized Equation 2-28 can be related to the Equation 2-52 trough:

$$\frac{\eta_i}{qV_{act}}\Delta I - \left(\frac{1}{\tau_{\Delta N}} + v_g G_N S_0\right)\Delta N - \left(\frac{1}{\Gamma\tau_P} - v_g G_S S_0\right)\Delta S = \frac{N_{th}}{mV_T}\left(\frac{\Delta I - i}{C_j} - \frac{\Delta V}{R_j C_j}\right) \tag{2-53}$$

C_j and R_j can be extracted directly as:

$$C_j = \frac{N_{th}qV_{act}}{mV_T\eta_i} \tag{2-54}$$

$$R_j = \frac{1}{C_j}\frac{1}{\left(\frac{1}{\tau_{\Delta N}} + v_g G_N S_0\right)} = \frac{\eta_i mV_T}{N_{th}qV_{act}}\frac{1}{(A + 2BN_{th} + 3CN_{th}^2 + v_g G_N S_0)} \tag{2-55}$$

A third relationship can be established from Equation 2-53:

$$\left(\frac{1}{\Gamma\tau_P} - v_g G_S S_0\right)\Delta S = \frac{N_{th}}{mV_T}\frac{i}{C_j} \tag{2-56}$$

Replacing Equation 2-56 in Equation 2-48 and using the relation for photons density evolution (Equation 2-29):

$$\left(2\Gamma\beta BN_{th} + \Gamma v_g G_N S_0\right)\Delta N - \left(\frac{\Gamma\beta BN_{th}^2}{S_0} + \Gamma v_g G_S S_0\right)\Delta S =$$

$$\frac{N_{th}\Gamma\tau_P}{mV_T C_j\left(1 - \Gamma v_g G_S S_0\tau_P\right)}\left(\frac{\Delta V}{L_0} - \frac{R_0}{L_0}i\right) \tag{2-57}$$

Finally, L_0 and R_0 can be expressed as:

$$L_0 = \frac{\eta_i mV_T\Gamma\tau_P}{N_{th}qV_{act}} \cdot \frac{1}{\left(1 - \Gamma v_g G_S S_0\tau_P\right)\left(2\Gamma\beta BN_{th} + \Gamma v_g G_N S_0\right)} \tag{2-58}$$

$$R_0 = \frac{L_0}{S_0} \cdot \left(\Gamma v_g G_S S_0^2 + \Gamma\beta BN_{th}^2\right) \tag{2-59}$$

2.5. Noise characteristics

So far, the analysis presented in section 2.3 neglects the intrinsic noise process inside the laser, and the carrier and photon densities were considered constants in steady-state. However, the quantum nature of real lasers generates intensity and phase fluctuations [214]. The random carrier and photon recombination produced by the spontaneous emission generates instantaneous variations in their densities. The variations in photon density impact the optical output power, whereas the variations in carrier density modify the output wavelength (finite spectral linewidth) [210].

2.5.1. Intensity noise

As mentioned above, the spontaneous emissions produces output power fluctuations around its steady-state value. Intensity fluctuations are represented in Figure **2-8**.
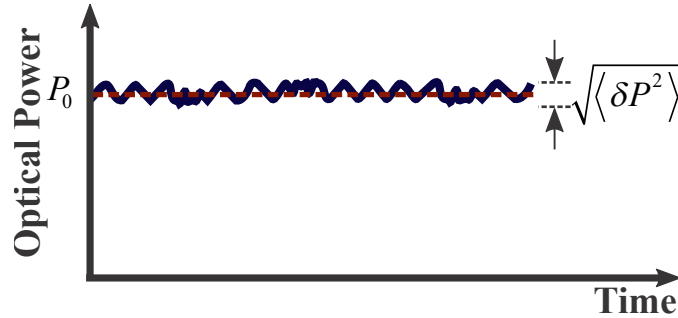
Figure 2-8.: Intensity noise representation of a real laser.

Assuming a noisy laser, its optical power can be expressed as [215]:

$$P(t) = P_0 + \delta P(t) \tag{2-60}$$

where P_0 is the mean optical power ($P_0 = \langle P \rangle$) and $\delta P(t)$ the optical intensity fluctuations. Thereby, the intensity noise is quantified and characterized by the relative intensity noise (RIN) defined as:

$$RIN = \frac{\left\langle \delta P(t)^2 \right\rangle}{P_0^2} \tag{2-61}$$

with $\langle \ \rangle$ the time average. Due to the very low RIN values, this is usually expressed in dB scale and can be normalized to 1-Hz bandwidth. Consequently, RIN corresponds to:

$$RIN \left[\frac{dB}{Hz} \right] = 10\log_{10} \left(\frac{\left\langle \delta P(t)^2 \right\rangle}{P_0^2} \right) - 10\log_{10}(\Delta f) \tag{2-62}$$

where Δf is the noise bandwidth. Likewise, single-sideband RIN is defined in terms of the spectral density of intensity fluctuations $S_{\delta P}$ at ω as [210]:

$$RIN \left[\frac{dB}{Hz} \right] = 10\log_{10} \left(\frac{S_{\delta P}(\omega)}{P_0^2} \right) - 10\log_{10}(\Delta f) \tag{2-63}$$

In this case Δf corresponds to the filter bandwidth of the measurement equipment.

2.5.2. Linewidth and linewidth enhancement factor

In lasing mode, spontaneous emission induces variations of carrier density inside the laser cavity and refractive index of laser materials. From this, the changes in the optical field phase impact the optical quality of the laser through the broadening of its linewidth $\Delta \nu$. In VCSELs and other semiconductor lasers, linewidth is directly proportional to the linewidth enhancement factor α_H [224], and both are desired to be as small as possible.

The enhancement factor represents the relation between the differential refractive index and gain with respect to the carrier concentration inside the laser cavity [225]. α_H is expressed as [226]:

$$\alpha_H = \frac{4\pi}{\lambda} \frac{\partial n / \partial N}{\partial g / \partial N} \tag{2-64}$$

where n is the refractive index, g the gain, and λ the emitting wavelength. From Equation 2-64, α_H exhibits a high dependence on wavelength and laser materials. Consequently, the linewidth can be minimized by using appropriate materials. Employing the enhancement linewidth parameter, the modified linewidth corresponds to [225]:

$$\Delta \nu = \Delta \nu_{ST} \left(1 + \alpha_H^2 \right) \tag{2-65}$$

with $\Delta\nu_{ST}$ the linewidth obtained from the Schawlow-Towns formula [226]. Concerning VCSELs linewidth, their values are higher than EEL lasers due to mirror losses, small cavity size, and better spontaneous emission coupling in the lasing mode [8]. Thus, whereas the linewidth of a VCSEL is of the order of MHz, DFB lasers can reach values of less than 50 kHz [227, 228].

2.5.3. Langevin Approach

Carrier and photon fluctuations can be included into the single-mode rate equations through the Langevin functions [229]. Therefore, Equations 2-1 and 2-2 are rewritten as:

$$\frac{dN(t)}{dt} = \frac{\eta_i I}{qV_{act}} - \left(A + BN(t) + CN(t)^2\right)N(t) - v_g GS(t) + F_N(t) \qquad (2\text{-}66)$$

$$\frac{dS(t)}{dt} = \Gamma\beta BN(t)^2 + \Gamma v_g GS(t) - \frac{S(t)}{\tau_P} + F_S(t) \qquad (2\text{-}67)$$

where $F_N(t)$ and $F_S(t)$ are Langevin white-noise sources that represent the carrier and photon densities variations, respectively. According to the McCumber approach, density changes are associated with a noise impulse of unit integrated intensity [230]. Under this perspective and by using the Wiener-Khintchine theorem, the spectral densities of the Langevin noise sources $\langle F_N^2 \rangle$ and $\langle F_S^2 \rangle$ are expressed in terms of the entering and leaving rates of particles from the electron and photon reservoir as follow:

$$\left\langle F_N^2 \right\rangle = \frac{2}{V_{act}^2}\left(\sum r_n^+ + \sum r_n^-\right) \qquad (2\text{-}68)$$

$$\left\langle F_S^2 \right\rangle = \frac{2}{V_{act}^2}\left(\sum r_s^+ + \sum r_s^-\right) \qquad (2\text{-}69)$$

with r_n^+ and r_s^+ the rate generation of carrier and photons respectively, r_n^- the recombination carrier rate, and r_s^- the absorption and photon losses rate. Employing the steady-state equations 2-5 and 2-6, the spectral densities of Langevin noise sources become [8]:

$$\left\langle F_N^2 \right\rangle = \frac{2\eta_i I_0}{qV_{act}^2} + \frac{4v_g a_0}{V_{act}}\frac{N_{tr}}{1+\epsilon S_0}S_0 \qquad (2\text{-}70)$$

$$\left\langle F_S^2 \right\rangle = \frac{4S_0}{\tau_P V_{act}} + \frac{4\Gamma v_g a_0}{V_{act}}\frac{N_{tr}}{1+\epsilon S_0}S_0 \qquad (2\text{-}71)$$

and the spectral density of exchange between electron and photon densities is given by:

$$\left\langle F_N F_S \right\rangle = -\left[\frac{2S_0}{\tau_P V_{act}} + \frac{4\Gamma v_g a_0}{V_{act}}\frac{N_{tr}}{1+\epsilon S_0}S_0\right] \qquad (2\text{-}72)$$

According to Equations 2-70, 2-71 and 2-72, power densities are constants and depend on the photon density at a given injected current. Figure **2-9** shows the power density evolution of Langevin noise sources functions using the parameters extracted by Bacou [8] for an O-band VCSEL. These results show how noise power rises with an increment in the injected current due to the higher carrier-photon interaction [223].
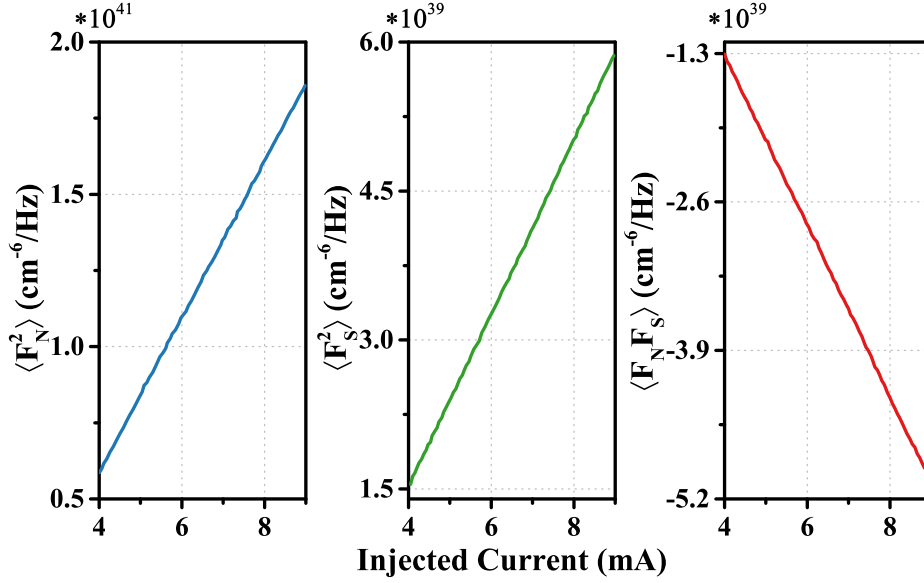
Figure 2-9.: Power density evolution of Langevin noise sources functions [8].

2.5.4. Electrical model of the active zone

Under Markovian assumption, the average of Langevin forces are zero $\langle F_N \rangle = \langle F_S \rangle = 0$, and can be included in the linearized Equations 2-23 and 2-24 as follow [8]:

$$\Delta \dot{N} = \frac{\eta_i}{q V_{act}} \Delta I - \left(\frac{1}{\tau_{\Delta N}} + v_g G_N S_0 \right) \Delta N - \left(v_g G - v_g G_S S_0 \right) \Delta S + F_N(t) \qquad (2\text{-}73)$$

$$\Delta \dot{S} = \left(2\Gamma \beta B N_0 + \Gamma v_g G_N S_0 \right) \Delta N - \left(\Gamma v_g G_S S_0 - \Gamma v_g G + \frac{1}{\tau_P} \right) \Delta S + F_S(t) \qquad (2\text{-}74)$$

By using the electrical model proposed by Harder [229], the noise sources can be included through voltage and current sources, as shown in Figure **2-10**.

By Kirchhoff's circuit laws, the voltage ΔV and the current i correspond to:

$$\frac{d\Delta V}{dt} = \frac{\Delta I - i}{C_j} - \frac{\Delta V}{R_j C_j} + \frac{i_n(t)}{C_j} \qquad (2\text{-}75)$$
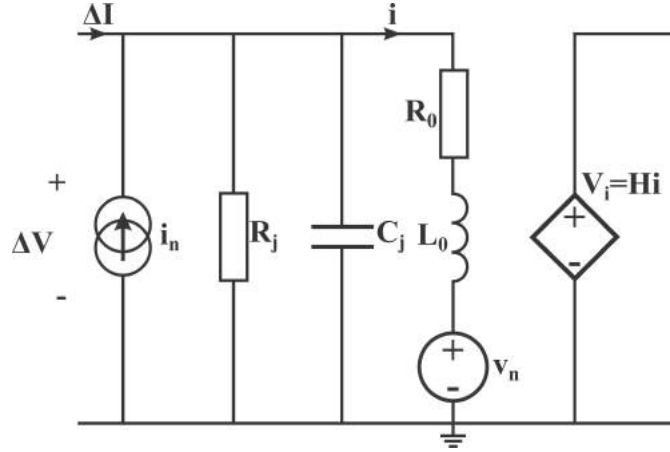
Figure 2-10.: Equivalent electrical scheme of laser cavity including noise sources

$$\frac{di}{dt} = \frac{\Delta V}{L_0} - \frac{R_0}{L_0}i - \frac{v_n(t)}{L_0} \tag{2-76}$$

The voltage and current sources are determined from Equations 2-73 - 2-76 as follow:

$$i_n(t) = \frac{qV_{act}}{\eta_i}F_N(t) \tag{2-77}$$

$$v_n(t) = -\frac{L_0qV_{act}}{\eta_i}\frac{(1 - \Gamma\upsilon_gG_SS_0\tau_P)}{\Gamma\tau_P}F_S(t) \tag{2-78}$$

2.6. Conclusions

As mentioned, long-wavelength VSELs are the central element of the proposed system for the microwave signal generation. These lasers have particular manufacturing characteristics due to the small volume of the active region and the high reflectivity obtained by the growth of several layers on InP and GaAs substrates. Although they have a single-mode behavior, their reduced optical power has limited their use in long haul links using SM fibers. On the contrary, the manufacture of the VCSELs emitting at short wavelengths (SW-VCSEL) evolved quickly, and today they are used in multiple applications.

Direct modulation of VCSELs, as with other semiconductor lasers, produces non-linear effects due to the variation of the carrier density injected into the cavity, the refractive index change, and the amplitude-phase coupling. When the laser is operated under large signal modulation or gain switching condition, negative chirp and linewidth broadening are produced. These two effects are related to the Henry factor, and together with the RIN, provide information about the VCSEL noise processes.

The active region of the VCSEL can be modeled through an electrical circuit and Langevin

functions to represent the carrier and photon fluctuations within the cavity. This model, together with the mathematical development and the experimental characterization, will be employed for the intrinsic parameters extraction in the next chapter.

Chapter 3

Characterization and parameters extraction of VCSELs

Although traditionally short-wavelength VCSELs have been more relevant and developed, long-wavelength VCSELs have gained ground in different applications during the last years. Recently, an InP-based VCSEL emitting at 1.55 μm was demonstrated with a modulation bandwidth in excess of 21 GHz [231]. This phenomenon is originated to the progress in VCSELs manufacture with strained quantum well active regions, tunnel junction, and DBR reflectors. Additionally, VCSELs are an alternative for MWP due to their adaptability with future silicon-based photonic integrated circuits and excellent compatibility with optical injection locking techniques [150].

In this work, O and C-band VCSELs are used for microwave signal generation. In order to verify the overall noise behavior and for design and simulation purposes, each component must be characterized. Different static and dynamic measurements can describe the electrical-optical performance of VCSELs. Additionally, intrinsic parameters of the laser can be extracted employing the equivalent circuit model and the equations developed in Chapter 2.

A complete experimental characterization of VCSELs is presented in this chapter. First, current-power and optical spectrum measurements are shown at different temperature conditions. Then, modulation response measurements and simulations, including the parasitic effects of the electrical access (TO package), are shown. In the same section, turn-on delay measurements for carrier lifetime extraction are included. In the following sections, the characterization is completed through the determination of the linewidth enhancement factor and the relative intensity noise. Finally, a summary of VCSELs parameters and simulations results with these parameters are presented.

3.1. Static characteristics

For the development of this work, RayCan fiber pigtailed VCSELs at 1.3 μm and 1.5 μm were used. The VCSEL structure includes seven pairs of InAlGaAs quantum wells (7 nm thick and 4.5 nm radius [178]), an air gap region for optical and current confinement, a buried tunnel junction (TJ), and DBR mirrors grown with several pairs of InAlGaAs-InAsAs schemes. The laser structure was presented in Section 2.1. Each VCSEL is packaged in a TO-56 can and the optical beam is coupled to an SMF-28 optical fiber.

3.1.1. Optical power and forward voltage

To determine the optical power and forward voltage, each VCSEL is biased at different DC currents and temperature conditions. The experimental setup includes a current source and voltmeter (source measure unit Keithley 2400) and an optical power meter (HP 81520A optical head). Figure **3-1** shows the measured light-current-voltage (L-I-V) curves for both lasers at room temperature.
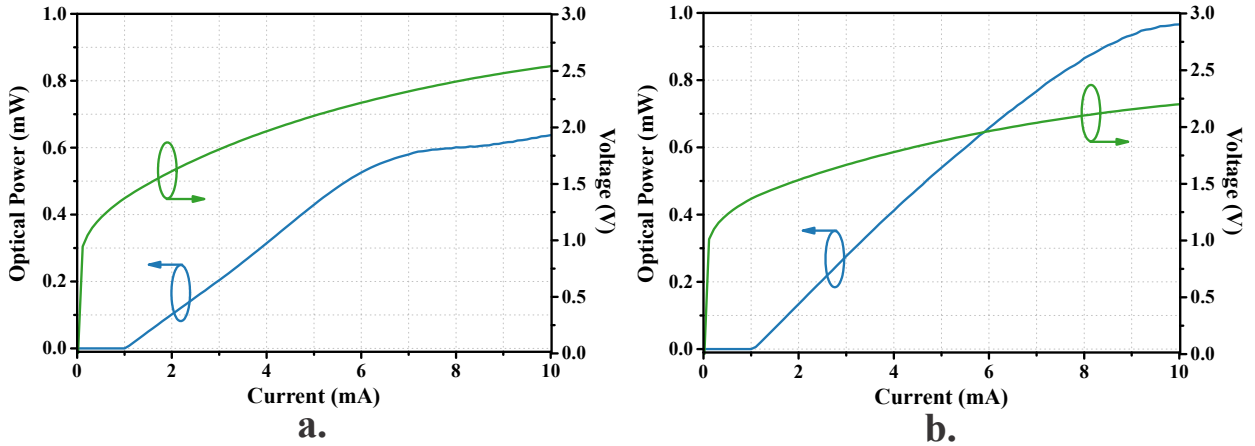
Figure 3-1.: Measured light-current-voltage (L-I-V) curves for **a.** C-band VCSEL **b.** O-band VCSEL.

The threshold currents of C and O-band VCSELs are 0.9 mA and 1 mA, respectively. The bias current used for the microwave signal generator was around 5 mA due to the linearity in this region, the output powers are close, and the wall-plug efficiency can be considered constant in both cases.

3.1.2. Optical spectrum

The optical spectra for both VCSELs were measured using two optical spectrum analyzers (OSA): Yokogawa AQ6370C and Aragon Photonics BOSA400 with spectral resolution of 20

pm and 0.24 pm, respectively. The resulting spectra at room temperature and different bias current are depicted in Figure **3-2**.
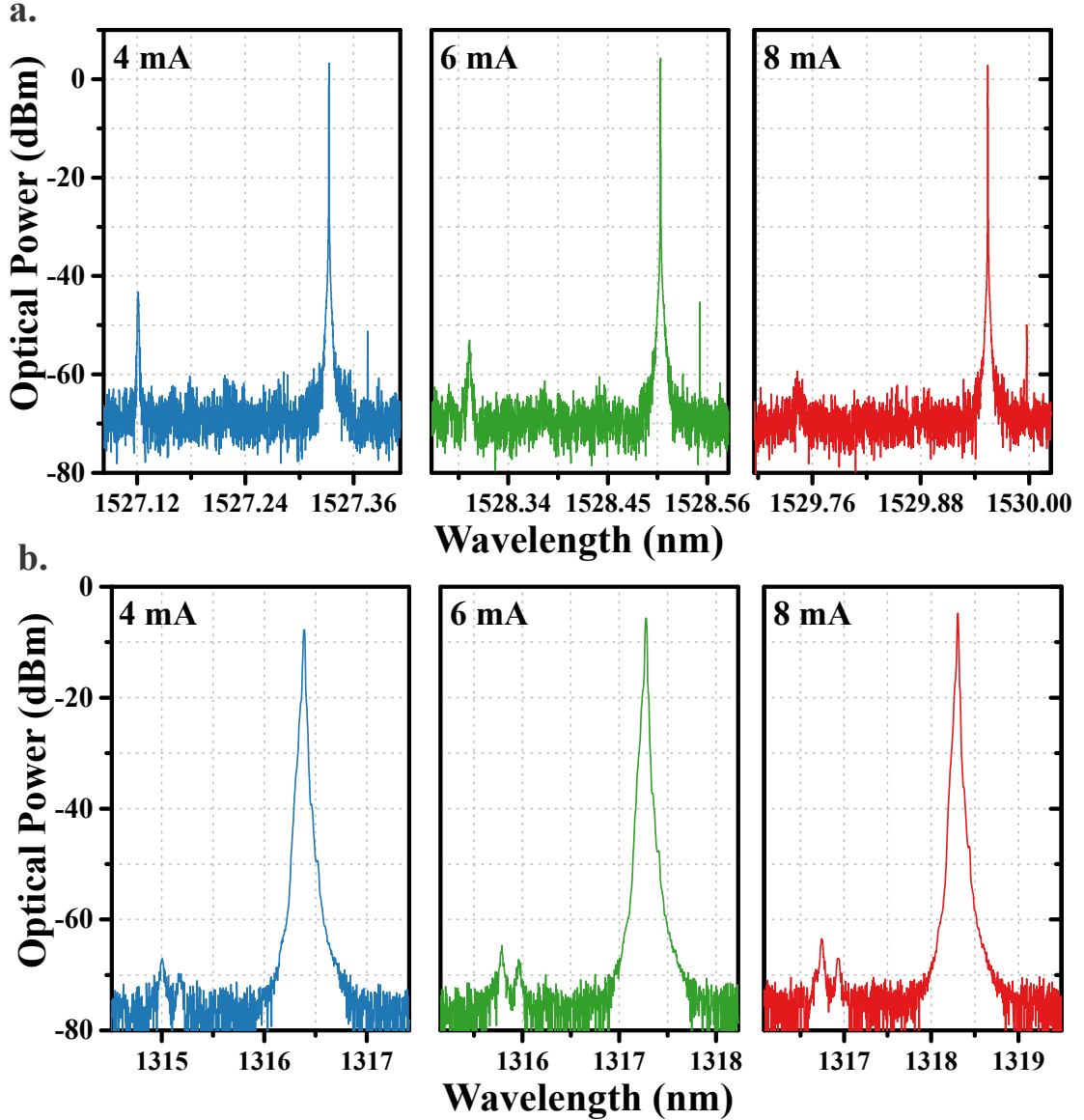
Figure 3-2.: Optical spectra at different bias currents for **a.** C-band VCSEL **b.** O-band VCSEL.

For all measurement conditions, the VCSELs have a single-mode behavior evidenced by one fundamental transverse mode. However, multiple higher-order transverse modes appear as a result of the physical characteristics of the optical cavity (e.g., the tunnel junction diameter). In all cases, the side mode suppression ratio (SMSR) is higher than 40 dB. Assuming a linear dependence between the wavelength and the injected current for bias currents from 3 to 9 mA, the wavelength shifts at a rate of 0.65 nm/mA for the C-band VCSEL and 0.47 nm/mA for the O-band VCSEL.

3.1.3. Influence of the temperature on static characteristics

Static characteristics of VCSELs, as in any semiconductor laser, depend strongly on the physical changes produced by temperature variations inside the cavity. Temperature induces alterations in the refractive index of DBR reflectors and, consequently, the effective optical length of the cavity [232]. Therefore, the longitudinal mode and the lasing wavelength of the VCSEL shift according to the resonance frequency given by the new cavity length. Figure **3-3 a.** presents the wavelength deviation of a C-band VCSEL for three temperature values. The wavelength shifts at a rate of 0.12 nm/°C.
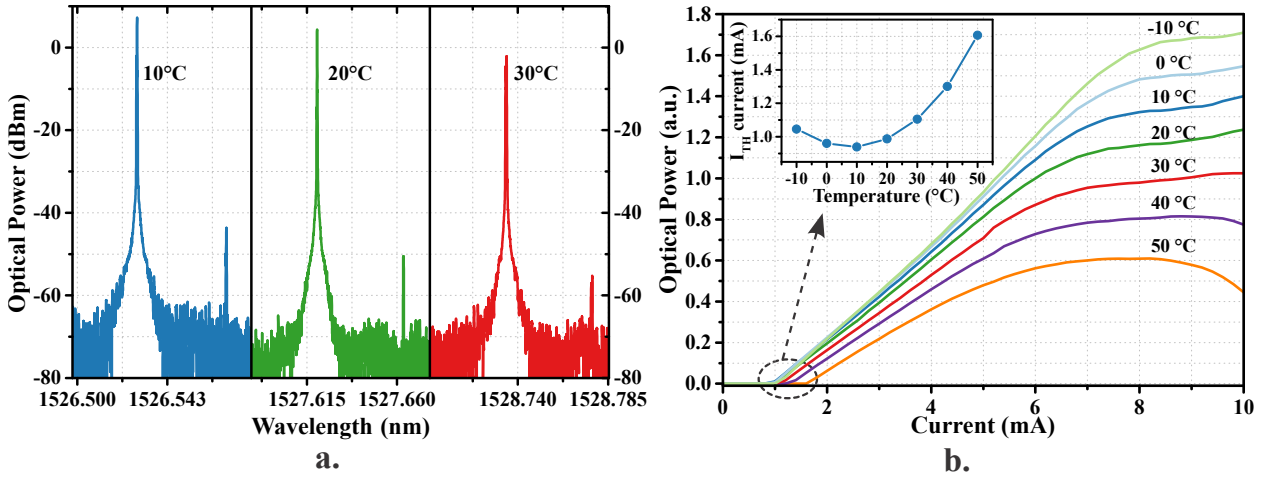
Figure 3-3.: a. Optical spectrum evolution at different temperatures **b.** L-I curves at different temperatures. Inset: threshold current evolution with temperature.

The temperature-dependent laser gain and the carrier leakage out of the active region also produces optical output power variations [233]. Figure **3-3 b.** shows the optical power normalized concerning the emitted power when the injected current is 6 mA at room temperature. The optical power at -10 °C, for bias currents higher than 4 mA, is twice the optical power at 50 °C.

Additionally, the threshold current behavior is strictly governed by the temperature characteristics of VCSELs. The spectral misalignment between the cavity resonance and the temperature-modified peak gain produces threshold current increases. The threshold current evolution exhibits approximately a parabolic shape (as shown the inset of Figure **3-3 b.**) described by the second-order polynomial [234]:

$$I_{th}(T) = \kappa + \zeta(T - T_{\min})^2 \tag{3-1}$$

where κ is the minimum threshold current of the VCSEL and T_{min} is the temperature at which κ occurs due to the spectral alignment of the cavity resonance and peak gain. The coefficient ζ represents the temperature sensitivity and depends on the quantum well design and the effective index of the cavity [234]. For the C-band VCSEL, the lowest threshold

current is 0.94 mA at $T_{min} = 10$ °C.

3.2. Dynamic characteristics

For dynamic measurements, the injected current varies over time in order to understand the VCSEL response to different conditions. The measurements and setups presented in this section allow the extraction of some intrinsic parameters of a C-band VCSEL. Then, these parameters are employed to establish the electrical model elements of its active region.

3.2.1. Turn-on delay - TOD

As stated in section 2.3.3, the turn-on delay t_D is the delay between the application of a current pulse and the beginning of the corresponding optical pulse. This time delay is dominated by the carrier lifetime τ_N and is difficult to measure owing to the additional setup delays and its reduced magnitude (several ns). The procedure consists of applying an electrical pulse to the VCSEL when it is pre-biased below the threshold current. In this way, t_D is determined as the time difference between the electrical applied pulse and the electrical pulse generated by a photodetector connected directly to the VCSEL [8]. Mathematically, the turn-on delay t_D and the carrier lifetime τ_N are related as:

$$t_D = \tau_N \cdot \ln \left(\frac{I_{ON} - I_{OFF}}{I_{ON} - I_{th}} \right) \tag{3-2}$$

where I_{ON} and I_{OFF} are the high and low-level current applied to the laser.

3.2.1.1. Experimental setup

The experimental setup used to measure the turn-on delay is represented in Figure **3-4**. An ultra-high-speed pulse generator is adjusted for delivering a voltage pulse to the VCSEL. The laser is biased at I_{bias} by a current source through the bias T. A VCSEL is mounted on a printed circuit board with a series resistance on which the voltage is monitored to determine the current applied to the VCSEL. This resistance is included due to the impossibility of measuring the current injected using a voltage measure given the dynamic resistance of the VCSEL.

Two considerations must be taken into account for choosing the resistance value:

- Its value must be sufficiently low compared to the dynamic VCSEL resistance for conserving the impedance seen by the generator.

- The value must be high enough for producing an acceptable voltage, given the low currents involved.
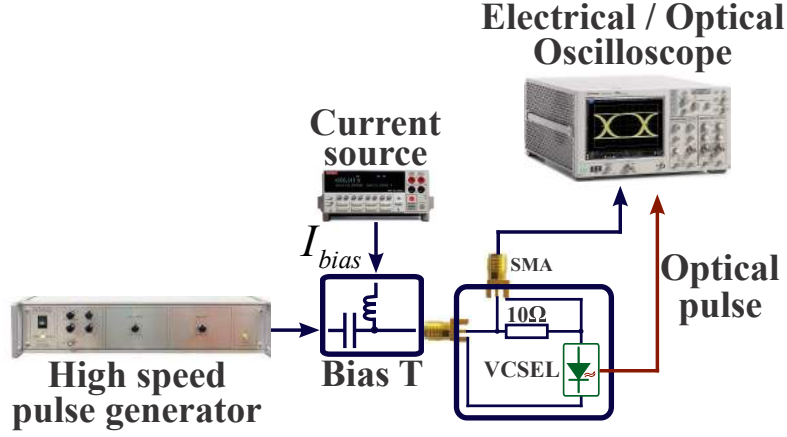
Figure 3-4.: Experimental setup for measuring the turn-on delay t_D.

A calibration process is required for removing the additional delays produced by the electrical and optical connections of the experimental setup. Therefore, the VCSEL is biased above the threshold current for eliminating the turn-on delay. The measured delay, denoted as Δt_{cal}, is 42.84 ns and is represented in Figure **3-5**.
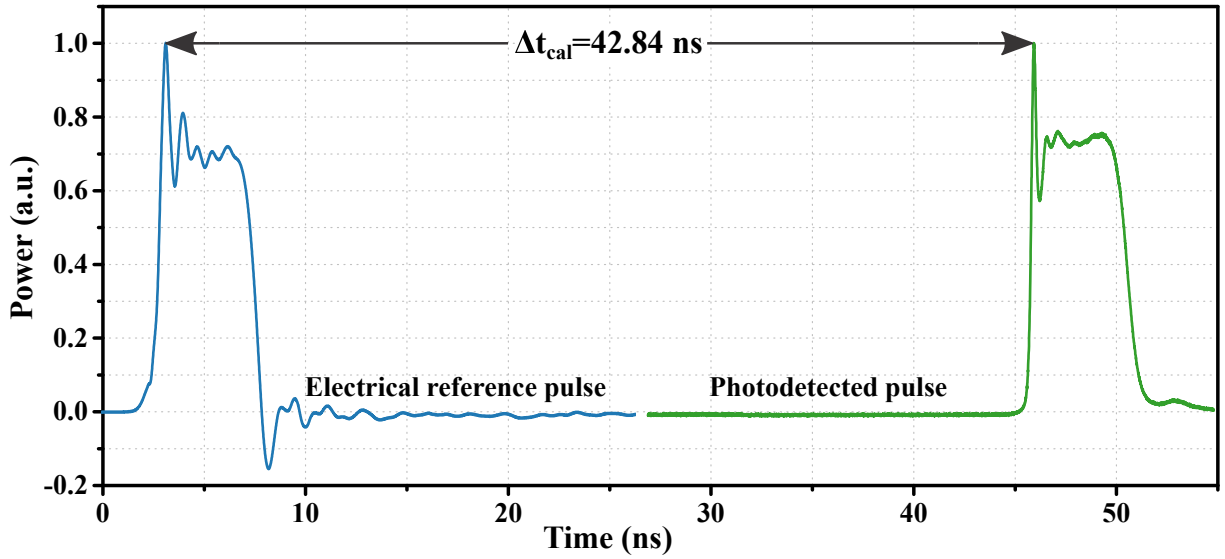
Figure 3-5.: Calibration measurement for $I_{bias} = 1.5 \times I_{th}$.

3.2.1.2. TOD measurements

In order to determine the carrier lifetime, several TOD measurements are performed to guarantee high precision. Therefore, for each bias current I_{bias} ($0 < I_{bias} < I_{th}$), the high pulse level I_{ON} is modified at different values. For example, for $I_{bias} = 0.5 \times I_{th}$, the turn-on delay is 0.53 ns and is illustrated in Figure **3-6 a.**. Figure **3-6 b.** shows the TOD measures
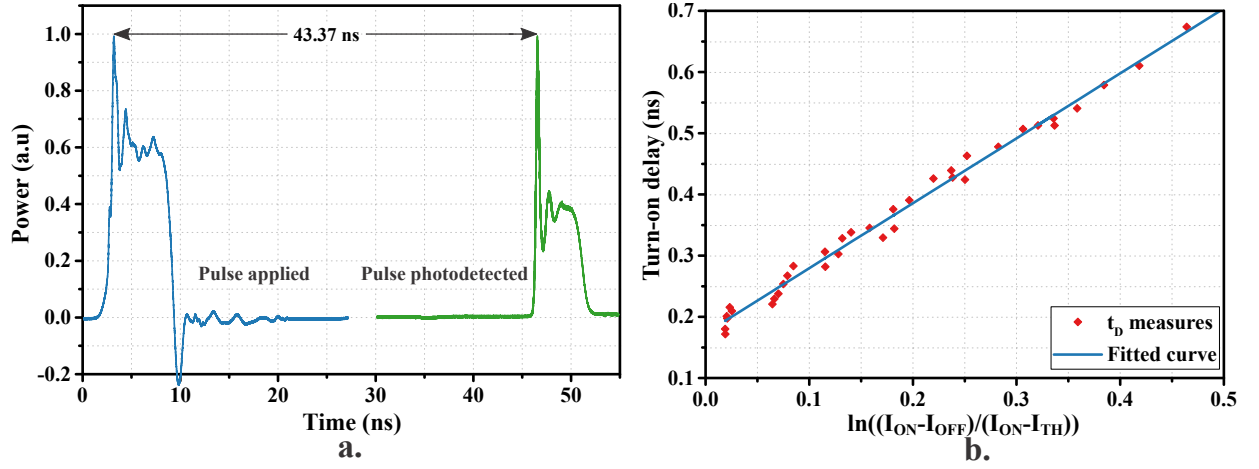
Figure 3-6.: Turn-on delay measurements for: **a.** $I_{bias} = 0.5 \times I_{th}$ **b.** Different I_{bias} values.

against the natural logarithm expressed in equation 3-2 for different I_{bias} and I_{ON} currents. Once a linear polynomial fitting is applied, the carrier lifetime found is $\boldsymbol{\tau_N = 1.06\ ns}$, very close to the value found in [235].

3.2.1.3. Extraction of additional parameters

From τ_N it is possible to determine additional intrinsic parameters through the equations presented in chapter 2. Considering the carrier density at threshold, Equation 2-8 can be rewritten as:

$$N_{th} = \frac{\eta_i \tau_N}{qV_{act}} I_{th} \tag{3-3}$$

Hence, N_{th} can be determined directly, assuming an internal quantum efficiency $\boldsymbol{\eta_i = 0.9}$ and estimating the active region volume with the physical VCSEL descriptions presented in section 3.1. Thus, $\boldsymbol{N_{th} = 3.82 \times 10^{18}\ cm^{-3}}$, and its value is within the values reported in the bibliography for this wavelength and laser structure [178, 236, 237].

The carrier lifetime is also related to the recombination coefficients and threshold carrier density through Equation 3-4. The estimation of these coefficients has a high uncertainty because they depend on the differences in the active layers and the extraction method [178].

$$\tau_N^{-1} = A + BN_{th} + CN_{th}^2 \tag{3-4}$$

The procedure for estimating the coefficients consists of establishing two of them by bibliographic research and then, through Equation 3-4, find the third one. For active regions based on InAlGaAs materials, the non-radiative recombination coefficient A varies in a range from 2×10^7 to $2.7 \times 10^8\ s^{-1}$ [8], and the range for the radiative coefficient B is from 0.2×10^{-10} to $2 \times 10^{-10}\ cm^3 s^{-1}$ [215]. From [238], both coefficients were determined for a VCSEL with similar characteristics to the one used in this work, and they are $\boldsymbol{A = 2.1 \times 10^7}$ $\boldsymbol{s^{-1}}$ and $\boldsymbol{B = 0.9 \times 10^{-10}\ cm^3 s^{-1}}$. Consequently, the Auger recombination coefficient is

$C = 3.96 \times 10^{-29} \; cm^6 s^{-1}$. This value corresponds to the literature [8] and differs slightly from other values [235, 239, 240], mainly due to physical factors such as the active region volume and the assumption of $\eta_i = 0.9$.

3.2.2. VCSEL frequency response

VCSELs, as any semiconductor laser, are directly modulated for data and radio-frequencies transmissions taking advantage of its simple implementation. Laser frequency response gives information about laser behavior when a small signal at different frequencies is applied. This response is especially important for this work because the proposed microwave signal generator is based on VCSEL direct modulation.

3.2.2.1. S-parameter measurements

Generally, the measurements of the intrinsic frequency response of laser diodes include the modulation response of packaging, chip parasitics, and measurement setup elements. Therefore, the laser bandwidth can be obtained only through the extraction of these individual contributions during measurements (when each response is previously determined) or by using simulation tools.

In the case of packaged VCSELs, the main contributions are the TO-56 can leads and the wire bondings to the laser chip. Due to the impossibility of eliminating them during the measurements, the results presented in this section show their influence on the laser frequency response. For this, a vector network analyzer (VNA) and a photodetector are used according to the setup shown in Figure **3-7**. TO-56 leads are directly connected to a bias tee by an SMA connector, and the output laser beam goes to the photodetector (PD) through an optical isolator for avoiding reflexions.
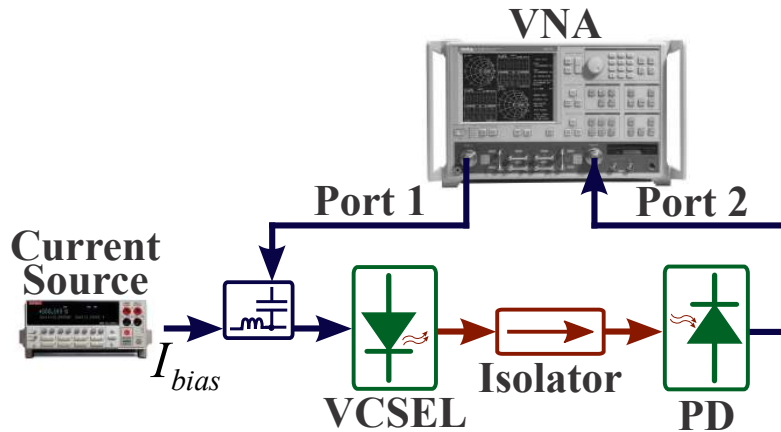
Figure 3-7.: Setup for VCSEL frequency response measurement.

The VCSEL bandwidth is acquired by measuring parameter S_{21} for different bias currents from 2 to 7 mA. Figure **3-8 a.** shows the S_{21} parameter measurements after extracting the photodetector frequency response and normalizing the data to the magnitude at low frequencies. The bandwidth at 3 dB increases with the current injected. There is a bandwidth improvement of 2 GHz (from 2.7 to 4.7 GHz) when the current moves from 2 to 7 mA.
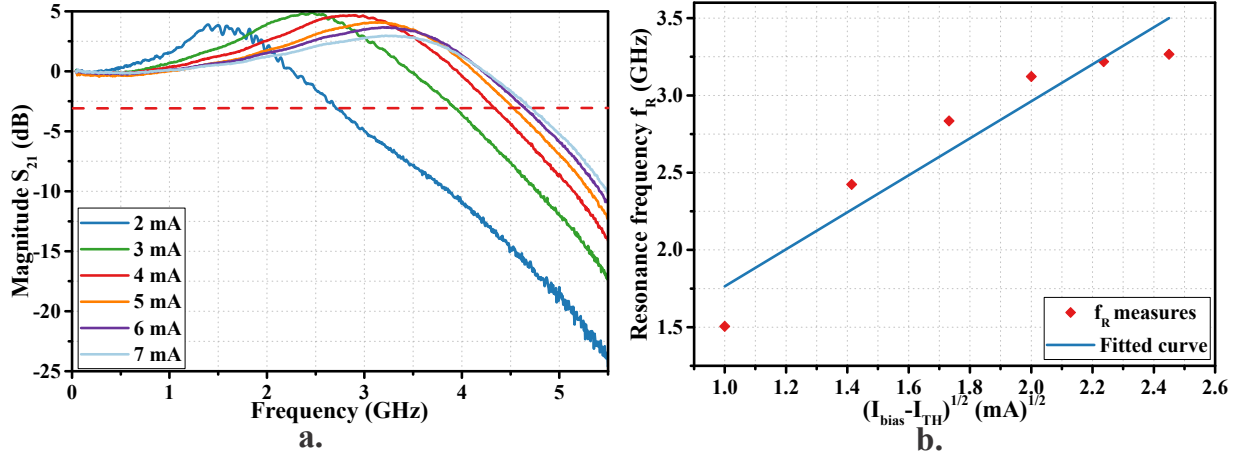
Figure 3-8.: a. S_{21} measurement at different I_{bias} **b.** Squared resonance frequency versus square root of $I_{bias} - I_{th}$.

In all cases, the frequency response presents a bump after reaching the resonance frequency that decreases with a slope greater than -60 dB/dec. This phenomenon is produced by the driver circuits, connections, and packaging employed during the measurements. Despite the frequency response degradation, the resonance frequency f_R for each bias current is certainly identifiable. The relationship between I_{bias} and f_R is expressed in Equation 2-41, rewritten here as:

$$f_R = \frac{1}{2\pi} \sqrt{\frac{\eta_i v_g \Gamma a_0}{q V_{act}}} \sqrt{I_{bias} - I_{th}} \tag{3-5}$$

Figure **3-8 b.** represents the f_R evolution versus the square root of the difference between I_{bias} and I_{th}. Thereby, by fitting the data and assuming $\boldsymbol{v_g = 7.5 \times 10^9 \ cm/s}$ and $\boldsymbol{\Gamma = 0.032}$ [8], the estimated differential gain coefficient is $\boldsymbol{a_0 = 2.85 \times 10^{-16} \ cm^2}$. The differences with values reported in the literature are due to the non-consideration of thermal effects inside the active region for bias currents higher than 5 mA.

3.2.2.2. Equivalent circuit of the electrical access

The electrical access used for S_{21} measurements is modeled through the equivalent circuit shown in Figure **3-9 a.**. This model includes the effects of TO leads connection, TO header parasitics, and bonding wire to the VCSEL chip. Figure **3-9 b.** depicts the mechanical structure of a TO-56 can package used by the manufacturer.
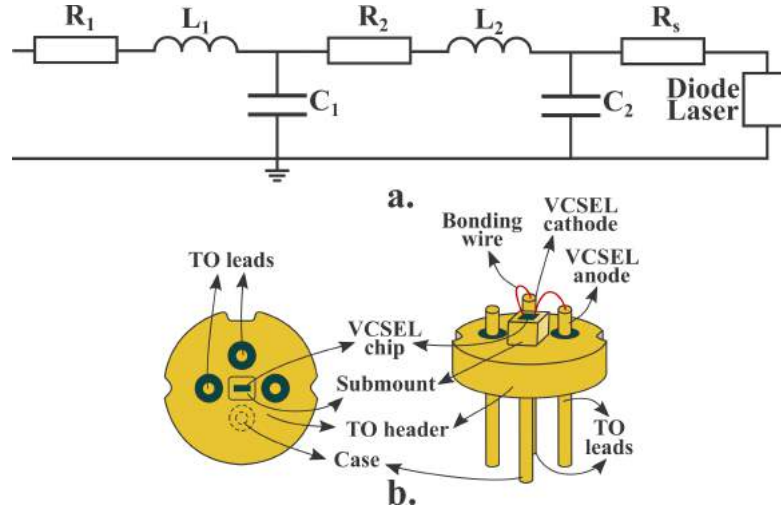
Figure 3-9.: a. Equivalent circuit model of VCSEL electrical access **b.** Mechanical model of TO-56 package.

The electrical circuit model of the electrical access is divided into 3 parts: parasitics induced by the TO leads, bonding wires, and the electrical model of the VCSEL cavity represented in Figure **2-7**. Other models are more detailed [241, 242] and others include the tunnel junction [178]. The TO package leads and fixture are modeled by the resistance R_1 and the inductance L_1, whereas the capacitance C_1 represents the capacitances induced by the TO-header and TO leads. The bonding wires inside the TO packaged are modeled by R_2 and L_2 and their induced capacitance by C_2. According to [178], the resistance R_s model the resistance of semiconductor layers and metal-semiconductor interfaces.

The values of parasitics elements are calculated employing coaxial cable equations. The electrical access is simulated in Advanced Design System (ADS) for fitting the results to the typical S_{11} parameter of a TO-56 package. The values after fitting are shown in Table **3-1**. The parasitic elements are independent of bias current, and they are used in section 3.2.2.4 for extracting the VCSEL response.

Table 3-1.: Parasitic element values of the electrical access model

R_1	L_1	C_1	R_2	L_2	C_2	R_s
3.35 Ω	0.18 nH	0.72 pF	12.64 Ω	4.1 nH	0.52 pF	35 Ω

3.2.2.3. Equivalent circuit of the optical cavity

The equivalent circuit model of the optical cavity presented in Figure **3-10** is based on previous models at 850 nm [222] and 1.55 μm [8]. In this case, the DBR reflectors (top and bottom) are included through the R_{tm}, C_{tm}, R_{bm}, and C_{bm} elements, and the resistance R_e represents the resistance between the electrodes.
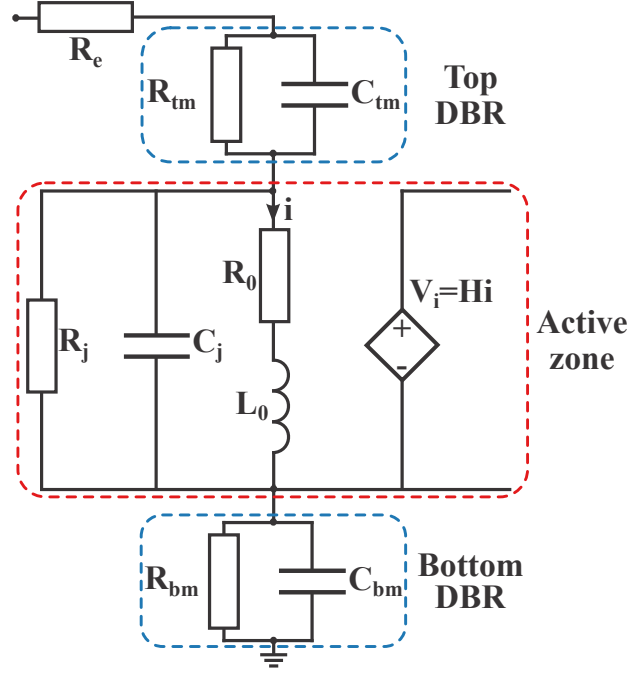
Figure 3-10.: Equivalent circuit model of the optical cavity.

The resonance frequency f_R of the electrical model is governed by the C_j-L_0 interaction, representing the exchange of energy between carriers and photons [221]. Its value is approximately given by:

$$f_R = \frac{1}{2\pi} \left[\frac{1}{C_j L_0} \right]^{1/2} \tag{3-6}$$

Considering the steady state conditions, the carrier density is equal to the threshold carrier density N_{th} for all bias currents higher than I_{th}, and C_j remains constant and can be calculated using Equation 2-54. Thus, $\boldsymbol{C_j = 42.4\ pF}$ when the thermal voltage and the ideality factor are $\boldsymbol{mV_T = 0.05}$ **V** at room temperature. Contrary, L_0 values depend strongly on the bias current and the inverse relationship with the photons density inside the cavity.

In turn, the damping factor ζ is determined by resistors R_j and R_0, which cannot be obtained experimentally. In [211], the authors present a procedure to determine R_j and R_0 using the transfer function of the equivalent electrical circuit of the VCSEL active region. Thereby, both circuit parameters are expressed as [211]:

$$R_j = \frac{R_0 Z_0}{Z_0 C_j L_0 \omega_0^2 - R_0 - Z_0} \tag{3-7}$$

$$\alpha_2 \cdot R_0^2 + \alpha_3 = 0 \tag{3-8}$$

where Z_0 is the characteristic impedance of the VNA, ω_0 is the natural angular frequency,

and the coefficients α_2 and α_3 are defined as:

$$\alpha_2 = 4\zeta^2 Z_0^4 C_j^2 L_0^2 \omega_0^2 + 2Z_0^4 L_0 C_j - 2Z_0^4 L_0^2 C_j^2 \omega_0^2 \tag{3-9}$$

$$\alpha_3 = 2Z_0^4 L_0^3 C_j \omega_0^2 - Z_0^4 L_0^4 C_j^2 \omega_0^4 - Z_0^4 L_0^2 \tag{3-10}$$

Finally, R_j and R_0 are estimated by assuming a damping factor $\zeta = 0.3$ and considering $\omega_0 = \omega_R(1 - 2\zeta^2)^{-1/2}$. Figure **3-11** shows the ADS simulation schematic of VCSEL frequency response using the electrical parameters of the active region and the electrical access model. The elements of the DBR reflectors were taken from [109].

Figure 3-11.: ADS simulation schematic of the VCSEL.

The simulated VCSEL frequency response is compared to the measurements, and the electrical parameters are then fitted. Figure **3-12** depicts the measured and simulated frequency responses when the bias current is 2 mA, 4 mA, and 6 mA. In all cases, the electric model shows a good agreement with the measurements.

The electrical parameters of the VCSEL active region are listed in Table **3-2**. It is worthwhile pointing out that the value of R_0 is small and does not exhibit significant variations in the whole current range. This is mainly because the physical structure of the VCSEL limits the current flow through the DBR reflectors, reducing the optical losses. On the contrary, the resistance R_j decreases when the bias current increases because its value is inversely related to L_0 and ω_0. This trend corresponds well with the bibliography for VCSEL [8] and DFB lasers [221]. Lastly, the increasing behavior of injected carrier is represented by the reduction

Figure 3-12.: Measured and simulated frequency response at different bias currents.

of R_e.

Table 3-2.: Electrical parameters of the optical cavity

I_{bias} (mA)	R_j (Ω)	C_j (pF)	R_0 (Ω)	L_0 (pH)	R_e (Ω)
2	3.69		0.10	186.80	462.16
3	3.09		0.10	94.88	368.42
4	2.64	42.4	0.12	69.01	261.44
5	2.23		0.10	58.24	216.23
6	2.01		0.11	52.52	195.28
7	1.70		0.12	48.14	191.00

3.2.2.4. VCSEL parameter extraction

Once VCSEL cavity parameters have been established, it is possible to determine some additional intrinsic parameters using the mathematical development presented in Chapter 2. The photon density is obtained from Equation 2-55 and is expressed as follows:

$$S = \frac{1 - R_j C_j \left(A + 2B N_{th} + 3C N_{th}^2 \right)}{R_j C_j v_g a_0} \tag{3-11}$$

The photon density evolution shown in Figure **3-13 a.** presents a linear behavior also observed in the light-current curve depicts in Figure **3-1**. This agreement is explained by the direct relationship between the optical output power and the photon density discussed in Section 2.3.

The results obtained from Equation 3-11 allow to determine the gain compression factor and
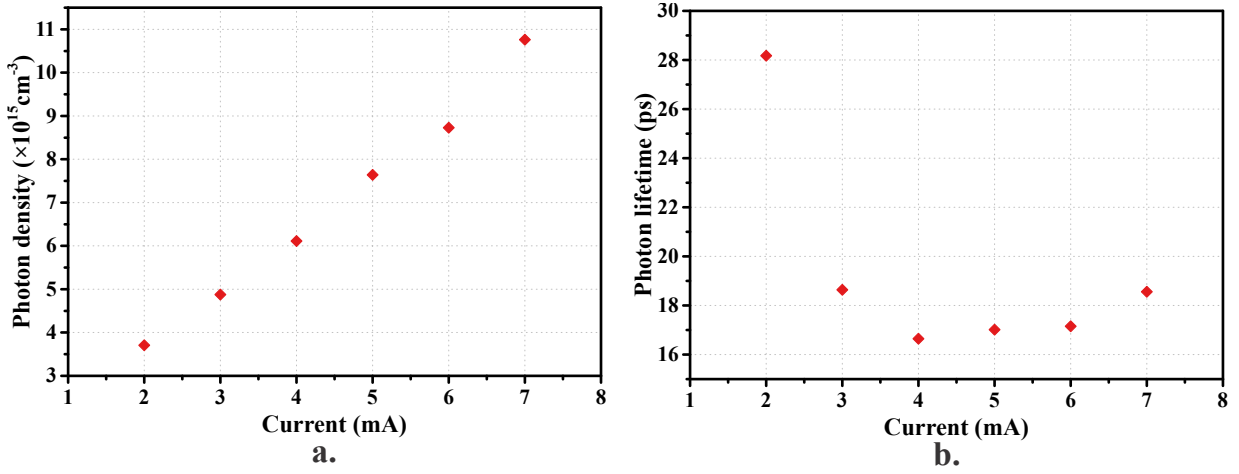
Figure 3-13.: a. Photon density and **b.** photon lifetime evolution as a function of bias current.

the transparency carrier density through Equations 2-16 and 2-17. After optimizing, both parameters are: $\epsilon = 1.57 \times 10^{-17}\ cm^3$ and $N_{tr} = 2.95 \times 10^{18}\ cm^{-3}$.

Similarly, photon lifetime is extracted from Equation 2-58, assuming that the spontaneous emission coefficient is negligible compared to the gain value. Thus, τ_P is defined as:

$$\tau_P = \frac{C_j L_0 v_g \Gamma G_N S}{\Gamma + C_j L_0 \Gamma^2 v_g^2 G_N G_S S^2} \tag{3-12}$$

Due to the absorption losses variations produced by the electron-hole injection at different bias currents [243], the photon lifetime varies as shown in Figure **3-13 b.**. Therefore, the estimated photon lifetime for bias currents higher than 2 mA is $\tau_P = 18.47\ ps$. In [240] the authors found $\tau_P = 19$ ps for the same pigtailed RayCan VCSEL, whereas for an LW-VCSEL manufactured by Vertilas the reported lifetime is 14 ps [235].

3.3. Linewidth enhancement factor

As stated in Chapter 2, the linewidth broadening of semiconductor lasers is originated by the refractive index variations, coming in turn from the amplitude-phase coupling and carrier density fluctuations. The laser linewidth $\Delta\nu$ increases by a factor of $(1 + \alpha_H^2)$ [226], and its linewidth enhancement factor α_H (Henry factor) is defined according to Equation 2-64.

Henry factor can be measured using different techniques available in the literature [8]. The technique used during this work is based on the chromatic dispersion effect of the SM fiber on a modulated optical source [244]. For this purpose, it is essential to know the chromatic dispersion of the optical fiber employed during the measurements.

3.3.1. Measurement of the optical fiber dispersion

Chromatic dispersion is a deterministic phenomenon produced by the different propagation speeds of a light signal traveling in a dispersive medium. In fiber optic-based telecommunications systems, the optical source is a CW laser with a non-zero linewidth. When the source is modulated, its optical spectrum is expanded. Each spectral component propagates at a slightly different speed, causing pulse broadening.

The value of chromatic dispersion depends on the signal wavelength λ and can be expressed as:

$$D(\lambda) = \frac{S_0}{4}\left(\lambda - \frac{\lambda_0^4}{\lambda^3}\right) \tag{3-13}$$

where λ_0 is the zero dispersion wavelength and S_0 the zero dispersion slope. Figure **3-14 a.** shows the dispersion evolution for an SMF-28 Corning fiber taking $\lambda_0 = 1313\,nm$ and $S_0 = 0,086\,ps/(nm^2 \cdot km)$ ($1302\,nm \leq \lambda_0 \leq 1322\,nm$ and $S_0 \leq 0.092\,ps/(nm^2 \cdot km)$). In C-band, the dispersion slope as a function of wavelength corresponds to $\Delta D/\Delta\lambda \simeq 0.055\,ps/(nm^2 \cdot km)$.
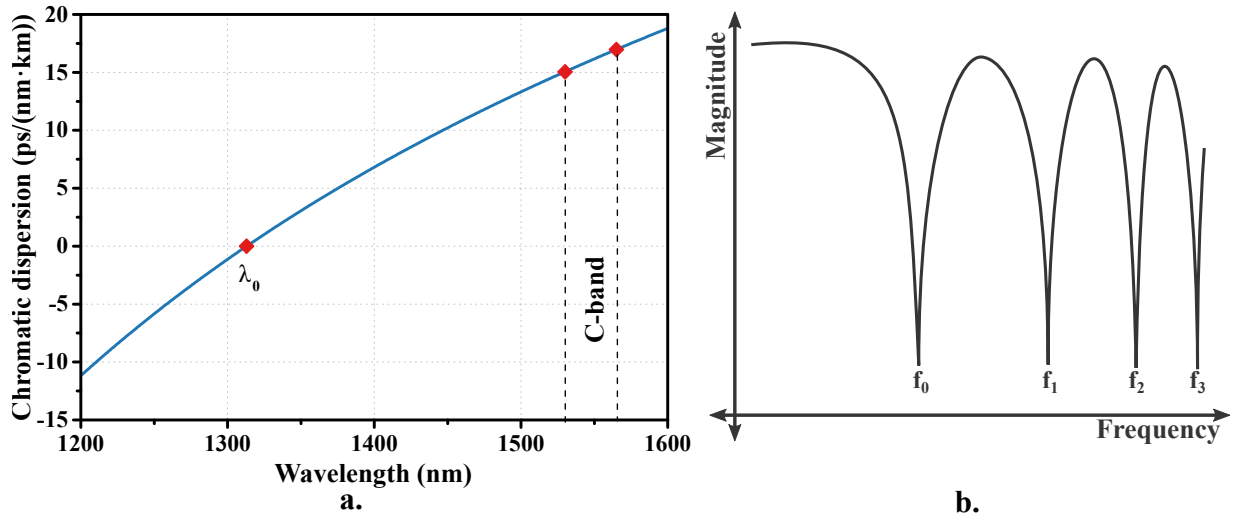
Figure 3-14.: a. Chromatic dispersion evolution of SMF-28 optical fiber **b.** Baseband AM response [9].

The chromatic dispersion modifies the relative phase of modulated signal sidebands. Thereby, the dispersion converts the amplitude modulation into frequency modulation when the optical source is intensity modulated at variable frequency. This effect produces a characteristic baseband AM response form (Figure **3-14 b.**) from which the chromatic dispersion at the wavelength considered can be determined [9]. The resonance frequencies f_u are determined as:

$$f_u^2 L = \frac{c}{2D\lambda_0^2}\left(1 + 2u - \frac{2}{\pi}\arctan(\alpha_H)\right) \tag{3-14}$$

with L the optical fiber length, c the speed of light, λ_0 the source wavelength, and $u =$

$0, 1, 2, 3, \ldots$ are the resonance index. This equation is the result of two simultaneous interferences between the carrier A_0 and the two lateral bands $A_{\pm 1}$ [244]. In Equation 3-14, it is possible to identify a proportionality between the product $f_u^2 L$ and the two unknown parameters, D and α_H. Similarly, two cases are identifiable:

- **Null Henry factor**

  In the particular case where the Henry factor of the source is $\alpha_H = 0$, Equation 3-14 relates the null frequencies and the optical fiber dispersion directly through Equation 3-15 given in [9].

$$f_u = \sqrt{\frac{500c(1 + 2u)}{DL\lambda^2}} \tag{3-15}$$

  with f_u in GHz, D en ps/(nm·km), L in km, and λ_0 in nm.

- **General case**

  The technique described in [244] is applied in the case where $\alpha \neq 0$. Indeed, with this method, the source Henry factor and the fiber dispersion are obtained simultaneously. Several resonance frequencies must be included in the frequency range used in order to achieve good accuracy.

  The trace $f_u^2 L$ as a function of $2u$ gives a straight line whose slope and intercept lead to dispersion and Henry factor. If p_1 and p_2 are, respectively, the slope and the intercept of the linear regression obtained, the dispersion and Henry factor are derived from Equation 3-14 as:

$$D = \frac{c}{2\lambda_0^2 p_1} \cdot 1 \times 10^3 \tag{3-16}$$

$$\alpha = \tan\left[\frac{\pi}{2}\left(1 - \frac{2 D\lambda_0^2}{c} \cdot p_2\right)\right] \tag{3-17}$$

  This method is limited to $-10 < \alpha < +10$ due to the asymptotes of the tangent function close to $\pm\frac{\pi}{2}$.

3.3.1.1. Chromatic dispersion measurement setup

For measuring the chromatic dispersion, an optical source is intensity-modulated at different frequencies generated by a VNA, in order to identify the resonance frequencies. The measurement setup is shown in Figure **3-15**.

First, the VNA is calibrated in transmission frequency response by directly connecting the optical source to the photodetector. Then, a 60.964 km fiber optic is connected to get as many resonance frequencies as possible. The module is composed of a laser source and an intensity modulator. The laser source is modulated through the intensity modulator using the RF signal generated by the VNA. Two different modules were used during this work: iXblue Modbox-VNA and HP 83420A. Although both modules include the same components, the
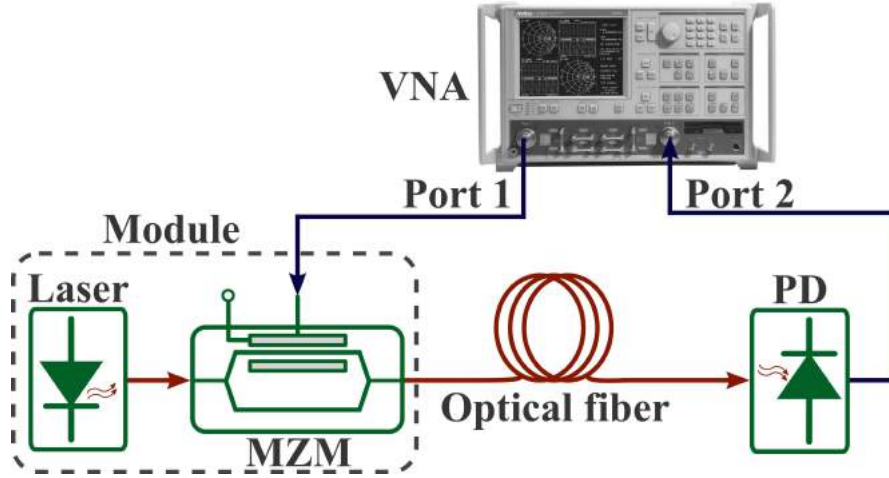
Figure 3-15.: Chromatic dispersion measurement setup.

laser sources are centered at different emitting wavelengths in order to validate the results.

3.3.1.2. Chromatic dispersion measurement results

Figures **3-16 a.** and **b.** show the frequency resonance measurements for a iXblue Modbox-VNA and HP 83420A module, respectively. The main difference between the sources is the bandwidth, hence in the second case, only 3 resonance frequencies are identified. The product trace $f_u^2 \cdot L$ vs. $2u$ and the linear regression for each optical source are depicted in Figures **3-16 c.** and **d.**. Therefore, D and α_H are determined by using the linear regression results and Equations 3-16 and 3-17. The results are summarized in Table **3-3**.

Table 3-3.: Summary results for the two optical sources.

Optical source	Wavelength (nm)	Chromatic dispersion (ps/(nm·km))	α_H
Modbox	1549.72	16.24	0.62
HP 83420A	1554.24	16.48	-1.44

3.3.2. Henry factor of a C-band VCSEL

For VCSELs measurements, the setup presented in Figure **3-15** includes a bias tee to modulate the laser directly. Due to the VCSEL bandwidth, only two resonance frequencies are obtained, as shown in Figure **3-17**.

Since the VCSEL wavelength is 1528.86 nm, the optical fiber dispersion must be adjusted.
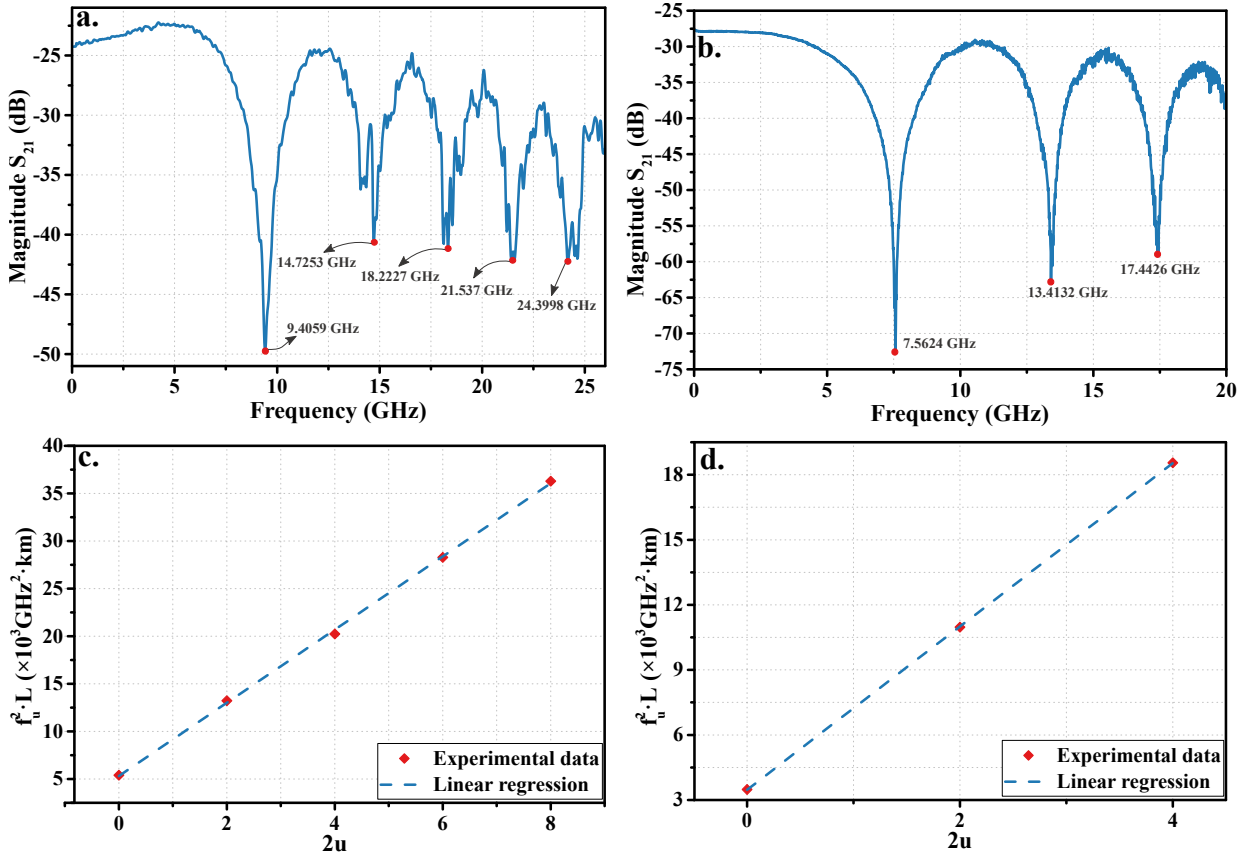
Figure 3-16.: Baseband AM response for **a.** Modbox-VNA **b.** HP 83420A. Product trace $f_u^2 \cdot L$ vs. $2u$ and linear regression for **c.** Modbox-VNA **d.** HP 83420A.

For this, the dispersion slope $\Delta D / \Delta \lambda \simeq 0.055 \, ps/(nm^2 \cdot km)$ is used as:

$$D_{(@1528.86nm)} = D_{(@1549.72nm)} - 0.055 \times (1549.72 - 1528.86) = 15.09 \, ps/(nm \cdot km)$$

Finally, the Henry factor of the VCSEL is calculated by applying Equation 3-14 and the first resonance frequency ($f_0 = 3.2336$ GHz).

$$\alpha_H = \tan \left[\frac{\pi}{2} \left(\frac{c}{2D\lambda_0{}^2} - f_0{}^2 L \right) \right] = 3.06 \tag{3-18}$$

3.4. Relative intensity noise (RIN) in VCSELs

Laser diodes are noisy devices due to the quantum nature of light. The dominant source of noise is spontaneous emission, which produces fluctuations in optical intensity and emission frequency [215]. Relative intensity noise (RIN) characterizes the optical intensity fluctuations and is usually applied as a figure of merit of lasers.
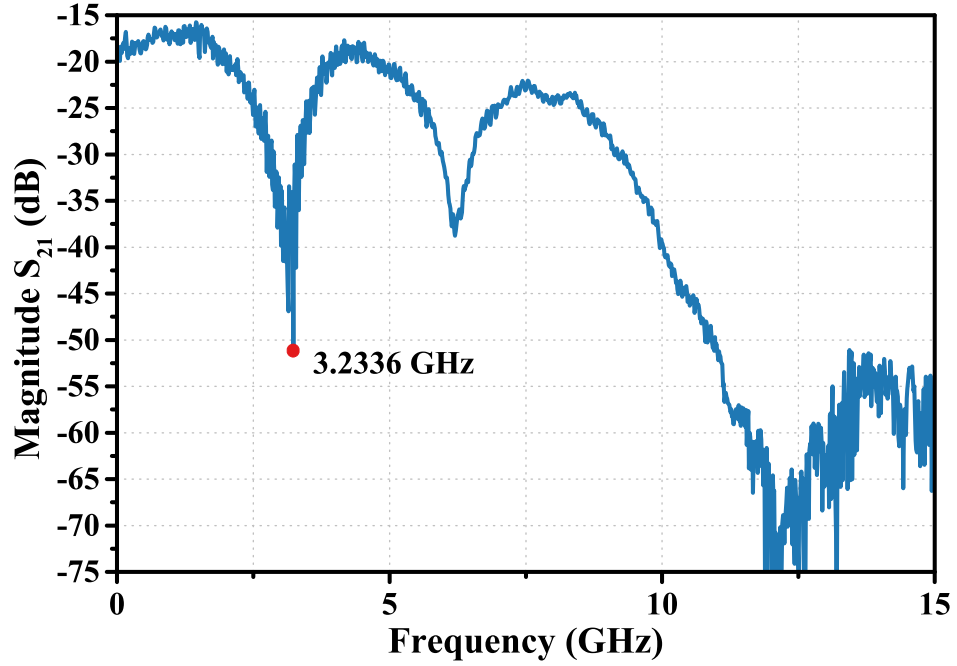
Figure 3-17.: Baseband AM response of C-band VCSEL.

Three parts can be identified in the RIN spectrum. The first one occurs at low frequencies, where the RIN value is reduced. Then, due to the interaction between carrier density and photon density, the RIN grows progressively until reaching its maximum value at a frequency close to the laser relaxation frequency [245]. Finally, the RIN value decreases again for higher frequencies.

As will be seen later, the RIN contributes to the phase noise of the microwave signal generation system. For this reason, the noise of the VCSELs is measured under different bias conditions.

3.4.1. RIN measurement setup

The RIN measurements are performed at high frequencies using the setup shown in Figure **3-18**. Both C and O-band VCSELs are biased at different currents through a bias tee for avoiding DC source noise. The optical reflections are limited by an optical isolator placed at photodetector input. The electrical PD output is connected to a bias tee for monitoring the AC and DC components separately. Since the RIN values may be lower than other noise sources (thermal noise, shot noise, and ESA noise), the photodetector incorporates a G_{RF} gain transimpedance amplifier.

When the laser is on, the noise power measured in the ESA corresponds to the total noise power, i.e., the shot, thermal, and laser noise. Additionally, the amplifier response must be extracted to obtain the response referenced to the photodetector output. Thus, using
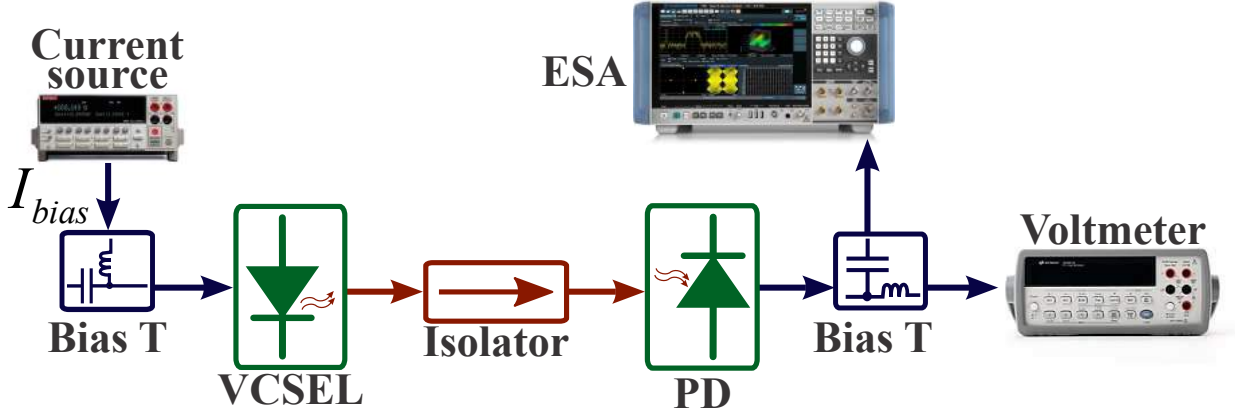
Figure 3-18.: RIN measurement setup.

Equation 2-61, the laser RIN is expressed as:

$$RIN[dB/Hz] = \frac{\frac{\langle \delta V_{on}^2 \rangle - \langle \delta V_{off}^2 \rangle}{G_{RF}^2} - 2q\frac{V_{DC}}{G_{DC}}}{\left(\frac{V_{DC}}{G_{DC}}\right)} \tag{3-19}$$

with $\langle \delta V_{on}^2 \rangle = P_{on}R_{ESA}$, $\langle \delta V_{off}^2 \rangle = P_{off}R_{ESA}$, R_{ESA} the ESA load resistance, V_{DC} the DC voltage photodetected, G_{DC} the DC amplifier gain, and P_{on} and P_{off} the noise power measurement in $dBm \cdot Hz^{-1}$ when the laser is in the on and off state, respectively.

3.4.2. RIN measurements results

Two VCSELs are characterized at room temperature and six different bias currents. Figure **3-19** shows the RIN measurements. From the results, it is possible to identify a definite trend in both cases when the bias current increases. First, the RIN level decreases because the stimulated emission is dominant. Second, the resonance frequency shifts towards higher frequencies in a similar way to the measurements of VCSEL frequency response. Finally, the response after the resonance frequency is more damped.

The resonance frequencies in both cases increase in a nearly linear shape as expected with Equation 3-5. However, the resonant frequency of C-band VCSEL is more sensitive to thermal effects produced inside the active region for bias currents higher than 5 mA. In [109], it was shown that the RIN of C-band VCSELs is more sensitive to temperature variations for low bias currents. This effect is produced by the mode competition inside the cavity derived from the presence of spontaneous emission, and it can be reduced by polarizing the laser at currents higher than 3 mA.

The main differences between VCSELs are the noise level and the resonance frequencies. RIN levels at 1.25 GHz and 2.5 GHz are plotted in Figure **3-20**. For both frequencies, the RIN improves as the bias current increase. At low polarization currents (up to 4 mA), the
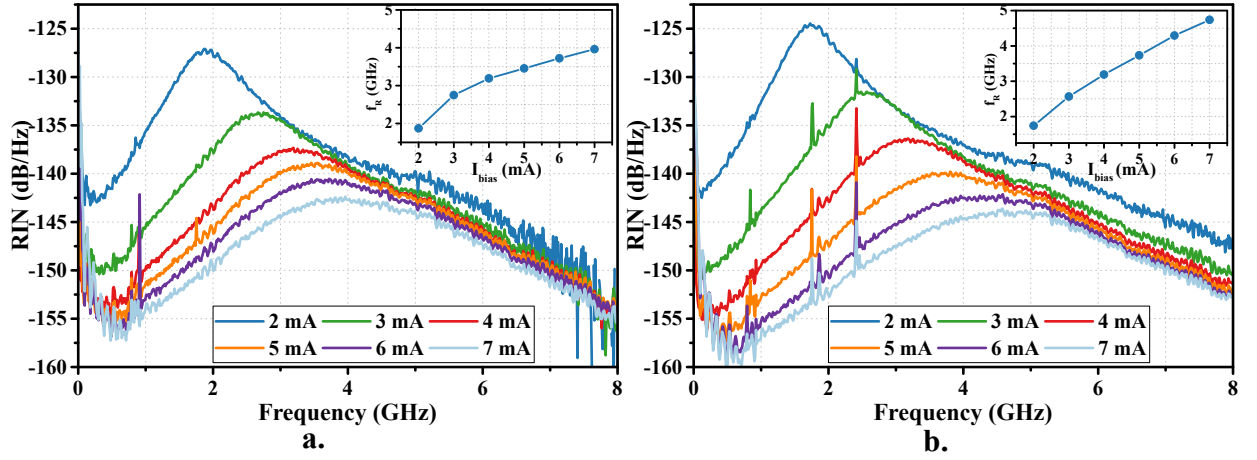
Figure 3-19.: RIN measurement for **a.** C-band VCSEL **b.** O-band VCSEL. Insets show the resonance frequency evolution with bias current.

C-band VCSEL RIN is slightly lower than the O-band VCSEL. After this bias current, the O-band VCSEL noise is the lowest for both frequencies analyzed. This effect, attributed to the active region temperature, limits the RIN improvement of the C-band VCSEL. The RIN is improved by 20.6 dB and 15.7 dB in the whole current range at 1.25 and 2.5 GHz, respectively. For the O-band VCSEL, the RIN enhancements are 26.3 and 19.4 dB at the same two frequencies.
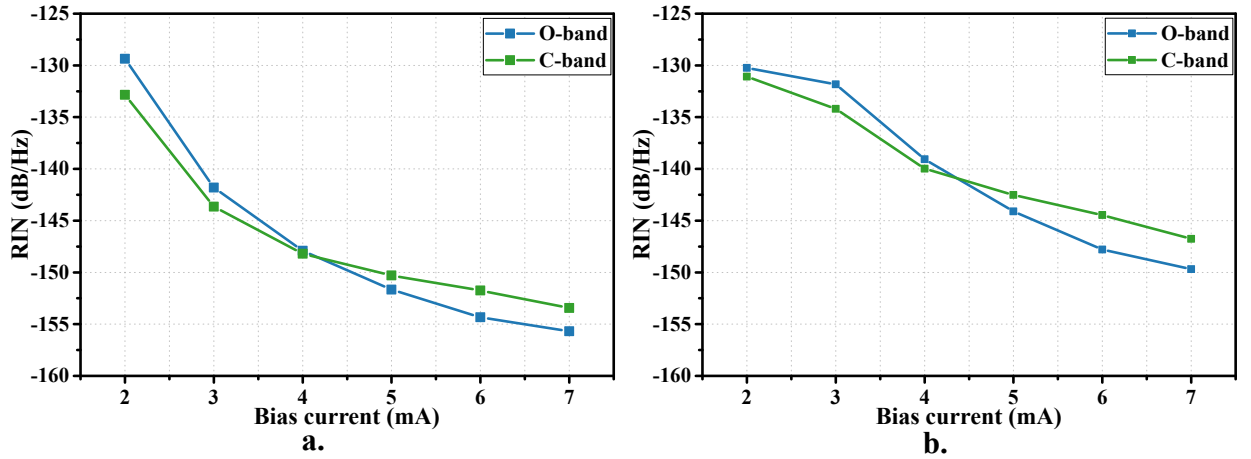
Figure 3-20.: RIN vs. bias current at **a.** 1.25 GHz **b.** 2.5 GHz.

Based on experimental results, the RIN of two lasers, under the same polarization conditions, will equally impact the phase noise of the microwave generation system. Likewise, more accurate RIN measurements can be achieved by adding temperature control and biasing the laser and photodetector with a battery.

3.5. Summary of VCSEL intrinsic parameters extracted

The intrinsic parameters extracted for a C-band VCSEL are presented in Table **3-4**. All listed values are used to simulate the VCSEL behavior under different modulations conditions, and they are also included for the simulation of the proposed microwave signal generator.

Table 3-4.: C-band VCSEL intrinsic parameters extracted

Symbol	Parameter	Value	Units
I_{th}	Threshold current	0.9	mA
τ_N	Carrier lifetime	1.06	ns
η_i	Internal quantum efficiency	0.9	
N_{th}	Threshold carrier density	3.82×10^{18}	cm^{-3}
A	Non-radiative recombination coefficient	2.1×10^7	s^{-1}
B	Radiative recombination coefficient	0.9×10^{-10}	$cm^3 s^{-1}$
C	Auger recombination coefficient	3.96×10^{-29}	$cm^6 s^{-1}$
v_g	Group velocity	7.5×10^9	$cm s^{-1}$
Γ	Longitudinal confinement factor	0.032	
a_0	Differential gain coefficient	2.85×10^{-16}	cm^2
m	Diode ideality factor	2	
ϵ	Gain compression factor	1.57×10^{-17}	cm^3
N_{tr}	Transparency carrier density	2.95×10^{18}	cm^{-3}
τ_P	Photon lifetime	18.47	ps
α_H	Linewidth enhancement factor	3.06	

3.6. VCSEL simulation with the extracted parameters

The intrinsic parameters are used to validate the extraction model by simulating a C-band VCSEL through computer-aided design (CAD) software tools. VPIphotonics Design Suit$^{\text{TM}}$ is a device and layout CAD software based on numerical models used to simulate optical and electrical components simultaneously. Additionally, the active region is also simulated in ADS to compare the VCSEL behavior at different bias currents.

It is worthwhile pointing out that the VCSEL-VPI model, unlike the model presented in this work, is based on a single-mode rate equation model, which includes a temperature-dependent pump current offset to describe self-heating dynamics inside the laser cavity. This model adequately describes the behavior observed during the characterization experiences.

This section presents the simulation results of light-current-voltage behavior, frequency response, RIN, and large-signal modulation.

3.6.1. Optical power and spectrum simulation

VCSEL static performance is evaluated at room temperature thorough the measured and simulated light-current-voltage curves shown in Figure **3-21**. Both simulated optical output power and voltage match firmly with measurements carried out (coefficients of determination R^2 higher than 0.9). The absence of experimental temperature control mainly causes the bias threshold difference.
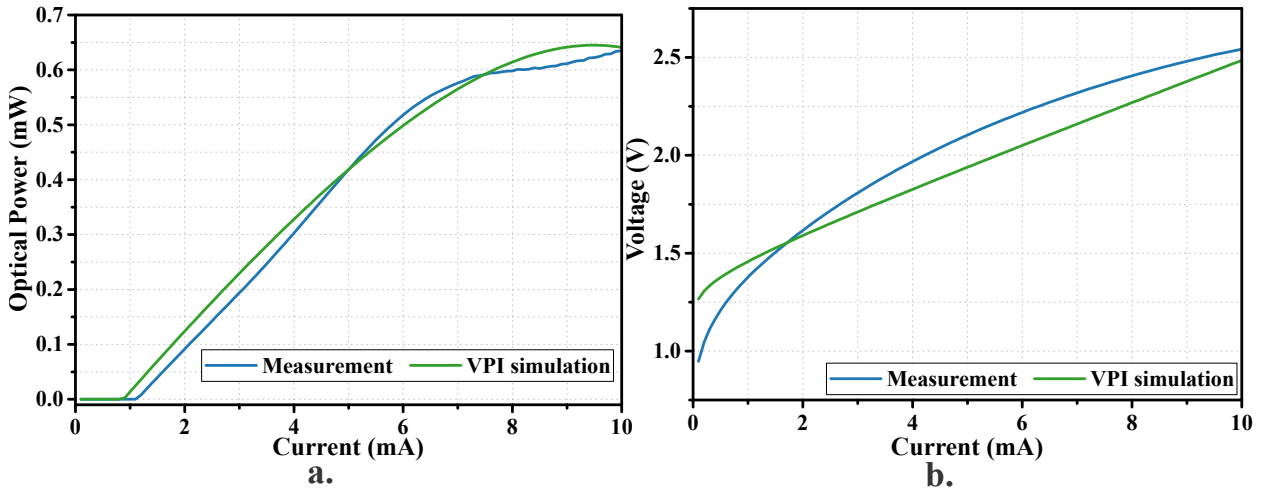
Figure 3-21.: Measured and simulated **a.** Light - current (L-I) **b.** Voltage - current (V-I) curves.

The simulation results prove that the temperature effect on the optical output power and emission wavelength correspond to experimental results obtained in section 3.1. Due to the carrier leakage from the active region at higher temperatures, the simulated optical power decreases, as shown in Figure **3-22 a.**. At the same time, the emission wavelength of Figure **3-22 b.** shifts at a rate of 0.124 nm/°C as effect of cavity length variations.

3.6.2. Frequency response simulation

The simulated frequency responses for 2, 4, and 6 mA are depicted in Figure **3-23**. The resonance frequency peaks are not the same in all cases because the electrical component values were adjusted to the frequency response that includes the TO-can package response. However, both simulations evolve according to the internal temperature effects of the active region for currents higher than 5 mA. Likewise, for high photon densities, the frequency peaks flatten out rapidly owing to the gain compression effect on the f_R and damping factor γ (proportional to ω_R^2). The model developed in Chapter 2 does not consider this effect, but it can be achieved by inserting in Equation 2-40 the differential gain G_N of Equation 2-25.

VCSEL bandwidth in all three cases increases linearly with the resonant frequency according
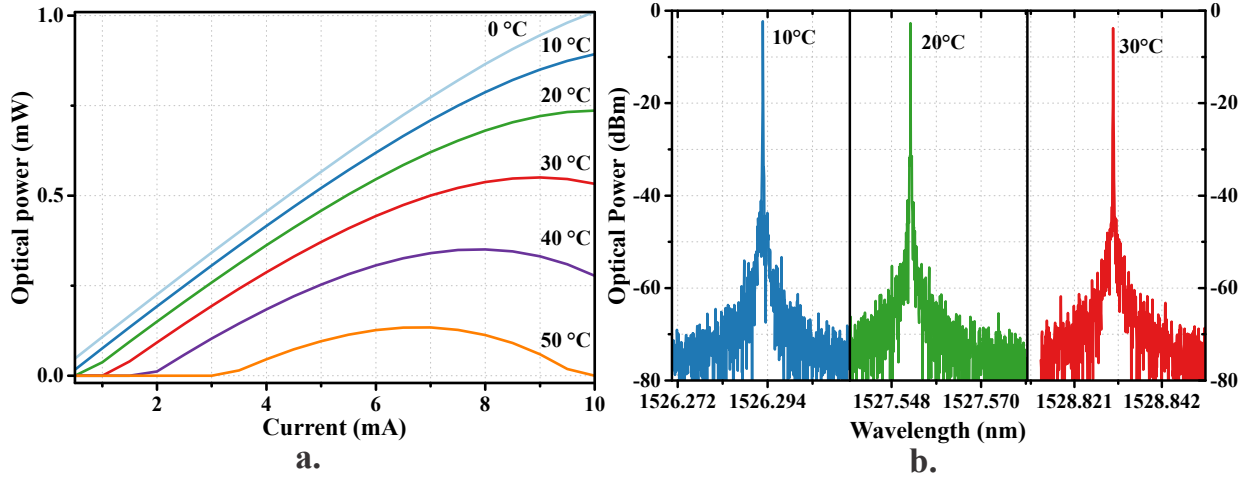
Figure 3-22.: Simulation results of **a.** Light - current (L-I) and **b.** optical spectrum evolution at different temperatures.

to the proportion $f_{3dB} \approx 1.55 \cdot f_R$. This relationship is conserved for the whole current range by the fact that $\gamma/\omega_R < 1$.
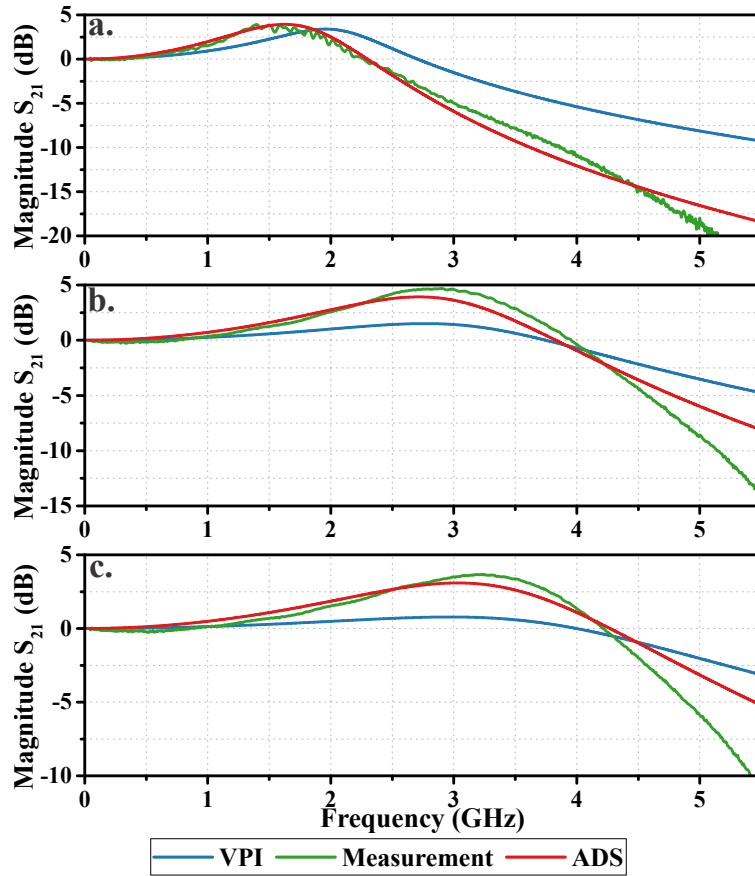
Figure 3-23.: Simulated frequency responses for **a.** 2 mA, **b.** 4 mA, and **c.** 6 mA.

3.6.3. RIN simulations

The RIN at high-frequency is simulated in ADS using the equivalent electrical model of Figure **3-11** and by adding two voltage and current equivalent noise sources. These noise sources represent the carrier and photon density fluctuations. The RIN spectrum plotted in Figure **3-24** shows that the electrical model agrees well with the measurements for all bias currents when the values of the noise sources have been adjusted. Table **3-5** summarizes the values used in the simulations. The curves do not fit for frequencies above 6 GHz due to the influence of VCSEL electrical access. Conversely, the electrical model must be improved in order to obtain a low frequency RIN that corresponds to the 1/f noise found in semiconductor lasers.
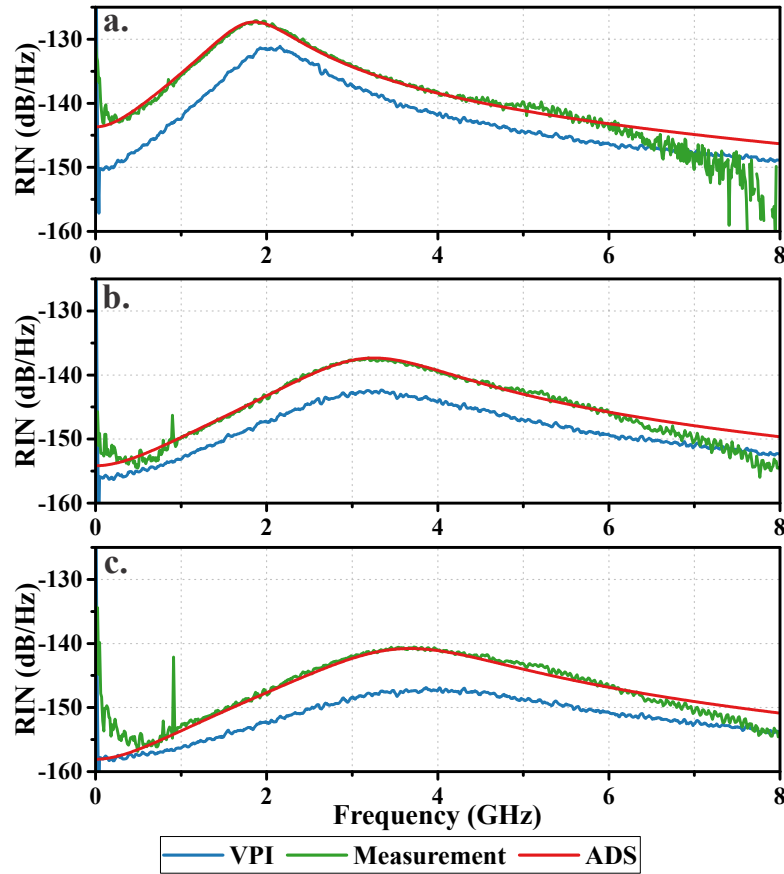
Figure 3-24.: Simulated RIN spectrum for **a.** 2 mA, **b.** 4 mA, and **c.** 6 mA.

As for the VPI simulation, the RIN spectrum is 4 dB lower than measurements for the whole frequency range due to measurement uncertainty and because the extraction of intrinsic parameters was performed assuming values from the literature. The resonance peaks are slightly displaced with respect to the measurement, as it happens for the frequency response. The simulated curves conserve their level difference for frequencies beyond 4 GHz, but both methods must be adjusted for low-frequency simulations.

Table 3-5.: Current and voltage noise source values.

Bias current I_{bias} (mA)	i_n $(pA/\sqrt{Hz})$	v_n $(nV/\sqrt{Hz})$
2	80.92	0.88
4	49.15	0.36
6	27.03	0.36

3.6.4. Gain-switched VCSEL simulations

As mentioned before, optical pulses can be generated, applying the gain switching (GS) technique to a laser. For this, the VCSEL must be directly modulated by an electrical signal at a fixed bias point ($I_{bias} > I_{th}$) and a sinusoidal signal with frequency f_m and amplitude P_m. Figure **3-25** presents the experimentally generated optical pulses and the simulations for $I_{bias} = 5mA$, $f_m = 1.25$ GHz and 2.5 GHz, and $P_m = -2$ dBm. Matlab $^\circledR$ simulations are performed by solving the rate equations numerically.
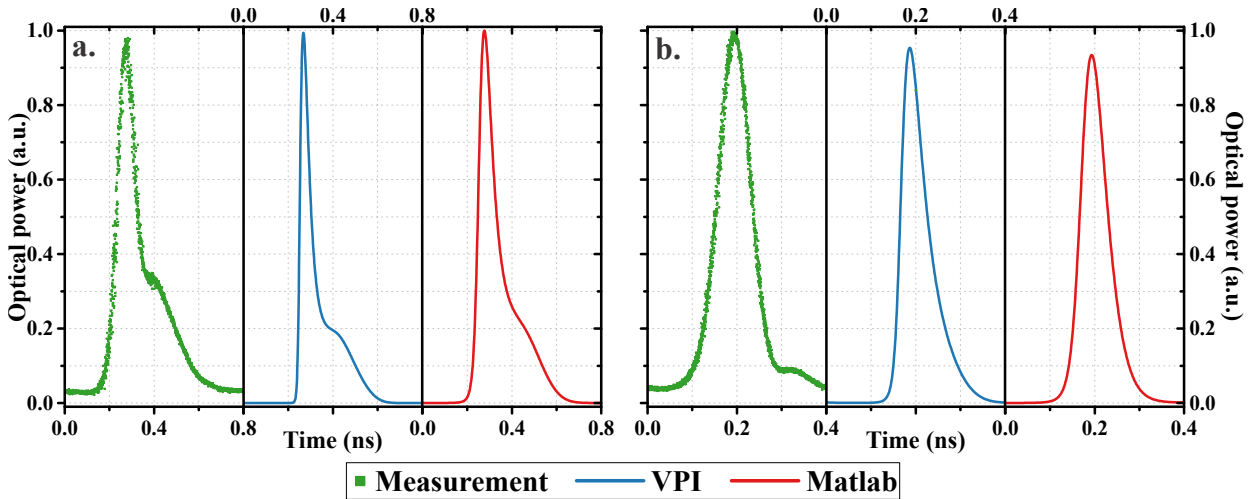
Figure 3-25.: Pulse generated at **a.** 1.25 GHz and **b.** 2.5 GHz.

In the case of $f_m = 1.25$ GHz, the optical pulses include a bump corresponding to the second spike of the relaxation oscillations. The full-width at half-maximum (FWHM) of pulses is lower than 100 ps in all cases, which represents 12.7% of the modulating electrical signal period. For $f_m = 2.5$ GHz, the VCSEL is turned off before the second spike appears and only one pulse is generated during a cycle. The maximum FWHM is 86 ps and it is equivalent to 21.4% of the signal period. Both pulse widths are within the expected values for gain-switched lasers, whose minimum FWHM value is about five times the photon lifetime [246]. Pulse amplitude and FWHM can be improved by adjusting the bias current and driving power P_m. For example, by increasing the power P_m, the pulse peak is higher and the duration is shorter due to the increased reverse current applied. However, above a certain

value, the pulse amplitude decreases abruptly due to the laser response degradation as an effect of the high temperature of the active region [247]. Likewise, relaxation frequencies are eliminated from the pulse shape by increasing the repetition rate. Nevertheless, the pulse amplitude decreases due to the lower frequency response of the VCSEL at high frequency [248].

An undesirable effect of GS is the frequency chirp $\Delta\nu$ produced by the temporal variations of the carriers injected into the active region. The carrier variations modify also the refractive index and the laser frequency. According to Equation 2-46, the chirp of gain-switched lasers can be determined directly from the photon density or the optical power waveform ($P_{opt} \propto S$). The frequency chirp of two pulses at 1.25 GHz is simulated in Matlab by biasing the VCSEL at $I_{bias} = I_0 = 5$ mA and employing two drive signal amplitudes $I_m = 4$ and $I_m = 5$ mA. The carrier density, photon density, and frequency chirp evolution are presented in Figure **3-26**. A more significant number of carriers injected into the active region produce two well identifiable effects. The first is the reduction of FWHM, an effect discussed above. The second is an increment of $\Delta\nu$ in around 10 GHz, due to the new photon density. The time difference between the simulations for different I_m is attributed to the fact that for low I_m values, the injected current is kept longer over the threshold and the lasing condition occurs earlier.
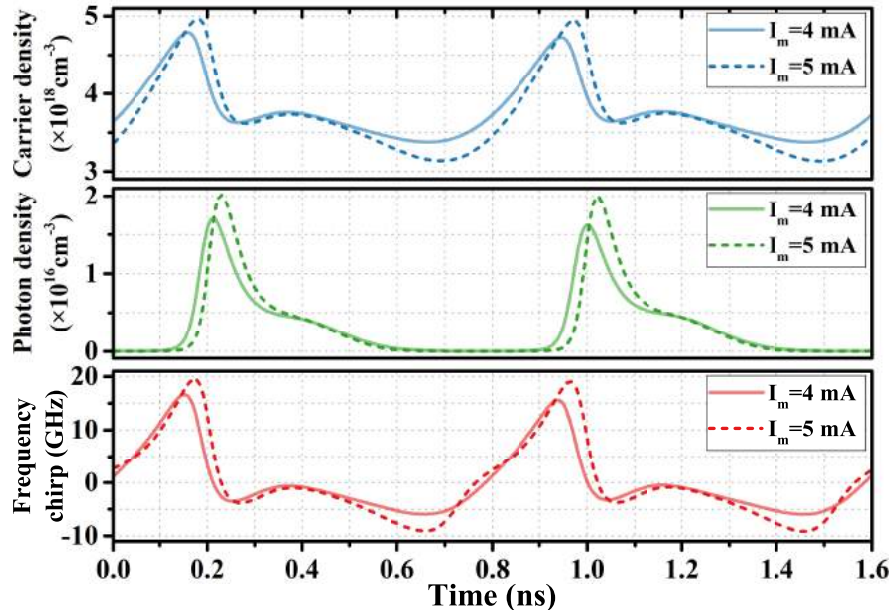
Figure 3-26.: Carrier density, photon density and frequency chirp evolution for $I_m = 4$ mA and $I_m = 5$ mA.

The frequency chirp behavior of GS lasers is non-linear and its temporal evolution is closely related to the evolution of the carrier density (see Figure **3-26**). The transient chirp is dominant during each pulse cycle as an effect of the speedy transitions of the injected current levels. After the appearance of the first peak of the relaxation frequencies, the carrier density

decreases, causing a negative chirp that remains so until the next cycle. This predominantly negative behavior leads to an asymmetric optical spectrum oriented towards the positive frequencies, as shown in Figure **3-27**. Even if the chirp increases with the drive amplitude (broadening of the optical spectrum), the time duration of the negative chirp is reduced. Previous works show that the propagation of the pulse by a positive dispersion fiber produces a reduction of negative chirp and a pulse compression [178].
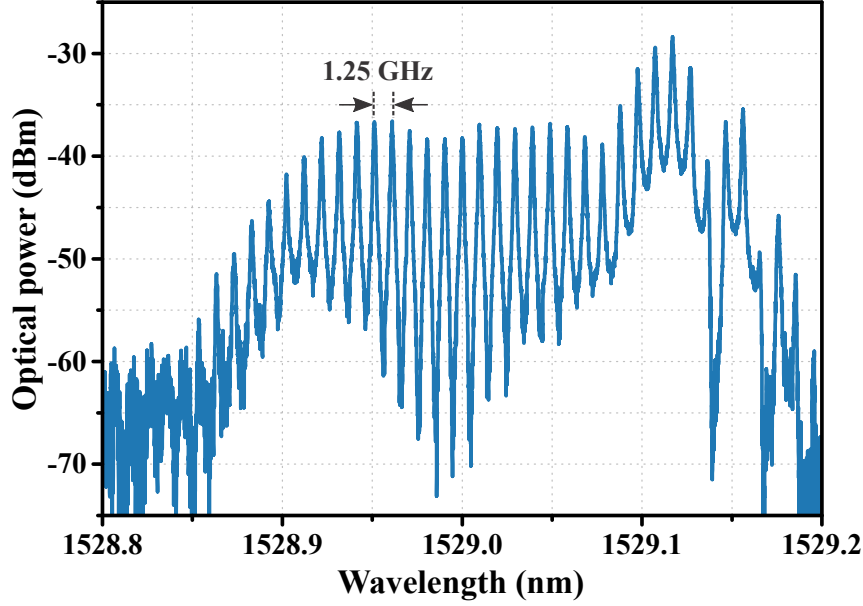
Figure 3-27.: Gain switching optical spectrum at 1.25 GHz.

When a GS optical pulse is photodetected, the electrical spectrum consists of a fundamental component at f_m and multiple equally spaced harmonics. This principle is the basis for the operation of the proposed microwave signal generation system that will be discussed in the next chapter.

3.7. Conclusions

The VCSEL characterization presented in this chapter is based on the theory and equivalent electrical model detailed in Chapter 2. Through this characterization, static characteristics and the temperature influence on the optical power and the emission wavelength were determined. Some intrinsic parameters were estimated by the dynamic characterization using the turn-on delay measurement and the measurement and simulation of the VCSEL frequency response. The enhancement linewidth factor was determined using the optical fiber dispersion method. All the estimated values are within the values reported in the literature.

The intrinsic parameter values found experimentally are used to simulate the VCSEL behavior in different computer-aided design software tools. The simulation results show the

significant influence of the TO-56 package over the VCSEL performance. Although some effects of the package modify the frequency response and the RIN at high frequencies, the resonance frequencies agree well with the simulation results.

The optical pulse generation using gain switching was shown by simulation in VPI and Matlab at two different repetition frequencies: 1.25 GHz and 2.5 GHz. Along with the experimental results, it could be shown that the resonant relaxation frequency of the characterized VCSEL is higher than 1.25 GHz due to the occurrence of a bump in the pulses generated at this frequency. In contrast, the optical pulses at 2.5 GHz include a single peak whose width depends on the lifetime of the photons.

The following chapter presents the proposed system for the generation of microwave signals based on VCSELs. The VCSEL characterization described in this chapter allows to identify the modulation conditions, noise contributions, and the VCSEL performance when it is modulated in a gain switching regime.

Chapter 4

Optoelectronic system for microwave signal generation

Throughout Chapter 1, a comprehensive state of the art of microwave signal generation appropriating optoelectronic systems, their advantages, and performance in terms of phase noise were presented. The optoelectronic oscillator (OEO) reported in the 80s [14, 78] and widely diffused in the 90s [79–81] was discussed in detail, as well as some of its most representative modifications.

A new architectural modification called VCSEL-based optoelectronic oscillator (VBO) was introduced in 2007 [15,16]. This architecture was based on the direct modulation of a VCSEL and the elimination of an external modulator. In this way, the VBO takes advantage of VCSELs, simplifies the architecture, and impacts the energy consumption for the generation of microwave signals. Previous works show the reduction of phase noise thanks to the evolution in the VCSEL manufacture and the use of active devices with lower noise levels [109].

During this chapter, a theoretical approach to VBO architecture is given along with experimental validation for evaluating its performance through phase noise, jitter, and time deviation measurements. Then, an improvement of the VBO architecture is presented for the generation of harmonics without the use of frequency multiplication mechanisms. This architecture, called self-started VCSEL-based harmonic frequency generator (SVHFG), is experimentally characterized. Additionally, a predictive phase noise model is developed and its results are compared with the experimental results.

4.1. VCSEL-based optoelectronic oscillator - VBO

The VCSEL-based optoelectronic oscillator (VBO), illustrated in Figure **4-1**, is a delay-line based and self-feeding ring oscillator. Unlike other OEOs, this oscillator uses a directly modulated VCSEL and a low-loss single-mode glass fiber, which acts as an optical delay-line. Owing to the lower fiber attenuation, long cavity length and high-quality factor Q are possible. The self-sustaining oscillations are initiated by the photodetector noise which is filtered by a band-pass filter (BPF) centered on the oscillation frequency f_0 and then amplified by a microwave amplifier used to compensate loop losses. The generated microwave signal and some reduced spurious modes are extracted through an electrical coupler.
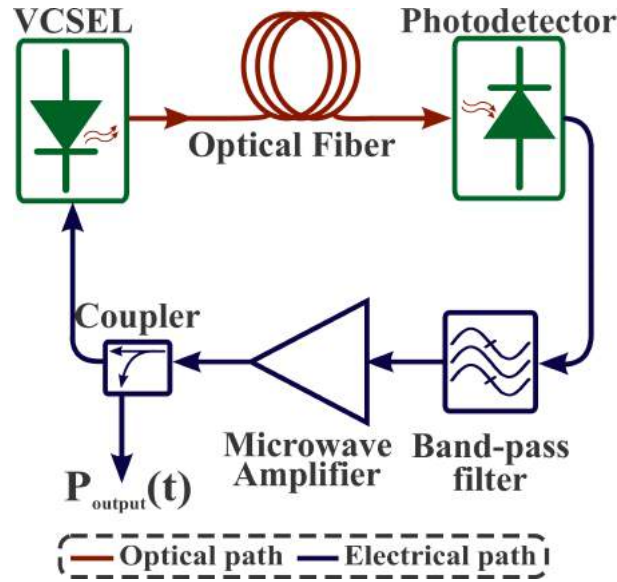
Figure 4-1.: VCSEL-based optoelectronic oscillator architecture.

This oscillator, besides taking advantage of VCSEL features, has a simpler and less expensive architecture because it does not include an external modulator. Power consumption can be reduced due to the low current levels needed to bias the VCSEL. However, given its low optical output power, a higher electrical gain may be required. This simple architecture has proven to be a high spectral purity microwave signal generator and a good alternative for embedded applications (reduced size) [152].

4.1.1. VBO theoretical description

The VBO theoretical description is intended to provide a mathematical development relating the behavior of each loop component to the frequency and oscillation conditions. This analysis should be performed in open and closed-loop, according to [249].

4.1.1.1. Open-loop analysis

When the loop is opened as shown in Figure **4-2**, it is possible to describe the open-loop voltage V_{OL} using the optical power from the VCSEL P_{VCSEL} and the photodetected voltage V_{ph}. Thus, V_{ph} can be denoted as:

$$V_{ph} = \alpha_o \cdot P_{VCSEL} \cdot |H_{VCSEL} \left(2\pi f_0\right)| \cdot \Re \cdot R_{ph} \tag{4-1}$$
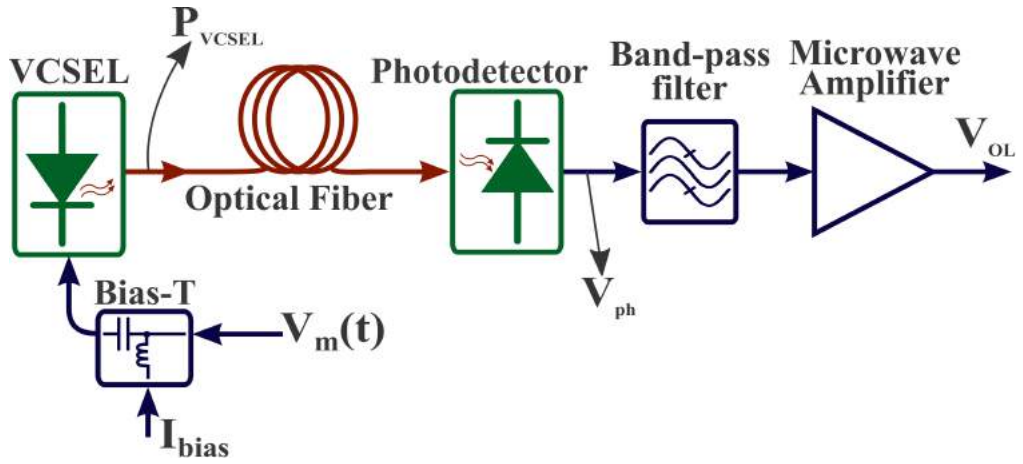
Figure 4-2.: Open-loop VBO diagram.

Considering that the optical output power from the VCSEL under small-signal modulation is $P_{VCSEL} = P_0 + P_m$, and the modulating voltage is $V_m = V_A \cdot \sin\left(2\pi f_0 + \phi\right)$, Equation 4-1 becomes:

$$V_{ph} = \alpha_o \cdot \Re \cdot R_{ph} \left(P_0 + \eta_d \cdot h \cdot \nu \frac{V_A \cdot \sin\left(2\pi f_0 + \phi\right)}{R_d} \cdot |H_{VCSEL}\left(2\pi f_0\right)|\right) \tag{4-2}$$

where:

- α_o represents the optical losses inside the loop, denoted in a complex notation as $\alpha_o = \tilde{\alpha}_o e^{-j\omega\tau_d}$ with τ_d the optical delay time.

- $\Re = \Re_{ph}e^{-j\omega\phi_S}$ is the photodetector responsivity with ϕ_S the phase change caused by the photodetector.

- R_d and R_{ph} are the dynamic resistance of the VCSEL and load photodetector resistance, respectively.

- H_{VCSEL} is the VCSEL frequency response transfer function.

- h is the Planck constant, ν the VCSEL emission frequency, and η_d its differential quantum efficiency.

Then, the electrical signal is filtered and amplified, and the resulting open-loop voltage V_{OL} is expressed as:

$$V_{OL} = \alpha_e \cdot G_A \cdot F \cdot \alpha_o \cdot \Re \cdot R_{ph} \cdot \eta_d \cdot h \cdot \nu \frac{V_A \cdot \sin\left(2\pi f_0 + \phi\right)}{R_d} \cdot |H_{VCSEL}\left(2\pi f_0\right)| \qquad (4\text{-}3)$$

with $\alpha_e = \tilde{\alpha}_e e^{j\phi_e}$ the electrical loop losses, $G_A = \tilde{G}_A e^{j\phi_G}$ the microwave amplifier voltage gain, and $F = \tilde{F} e^{j\phi_F}$ the band-pass filter voltage gain. Defining the open-loop gain as $G_{OL} = V_{OL}/V_m$, from Equation 4-3 is obtained:

$$G_{OL} = \alpha_e \cdot G_A \cdot F \cdot \alpha_o \cdot \Re \cdot R_{ph} \cdot \eta_d \cdot h \cdot \nu \frac{1}{R_d} \cdot |H_{VCSEL}\left(2\pi f_0\right)| \qquad (4\text{-}4)$$

4.1.1.2. Close-loop analysis

The closed-loop VBO shown in Figure **4-3** is composed of the microwave amplifier and the resonant network with a transfer function H_R, which includes all the elements of the open-loop analysis except the microwave amplifier.
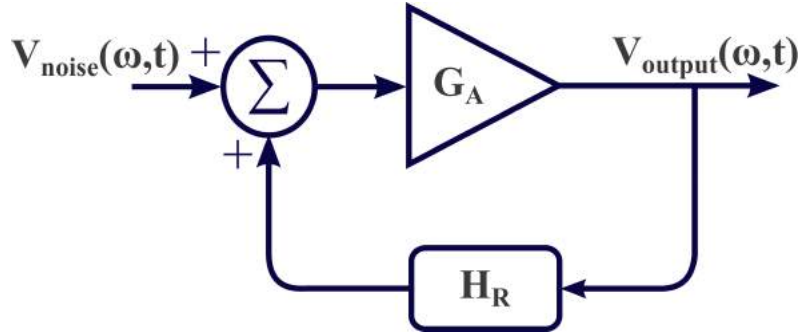
Figure 4-3.: Closed-loop VBO diagram.

V_{noise} is the noise inside the loop and includes all noise sources such as relative intensity noise, thermal noise, and shot noise. As mentioned before, the noise starts the oscillation process together with the constructive feedback originated by the phase coherence of the loop and represented with the positive summing point. The oscillation is achieved when the gain condition of the loop is reached. Taking V_{output} as the output signal voltage, the closed-loop VBO transfer function can be written as:

$$\frac{V_{output}(\omega, t)}{V_{noise}(\omega, t)} = \frac{G_A}{1 - H_R G_A} = \frac{G_A}{1 - G_{OL}} = \frac{\tilde{G}_A e^{j\phi_G}}{1 - \tilde{G}_{OL} e^{-j(\omega\tau + \phi_0)}} \qquad (4\text{-}5)$$

where the τ factor corresponds to the closed-loop time delay and ϕ_0 the open-loop phase.

Finally, the transfer function can be expressed in power terms as:

$$\left| \frac{V_{output}(\omega, t)}{V_{noise}(\omega, t)} \right|^2 = \frac{\tilde{G}_A^2}{1 - \left| \tilde{G}_{OL} \right|^2 - 2 \left| \tilde{G}_{OL} \right| \cos(\omega\tau + \phi_0)} \tag{4-6}$$

4.1.1.3. Oscillation conditions

When the loop is closed and to achieve a sustained self-oscillation, the oscillator must accomplish the gain and phase Barkhausen conditions. Both conditions are denoted as follows:

$$|G_{OL}| = \left| \alpha_e \cdot G_A \cdot F \cdot \alpha_o \cdot \Re \cdot R_{ph} \cdot \eta_d \cdot h \cdot \nu \frac{1}{R_d} \cdot |H_{VCSEL}(2\pi f_0)| \right| = 1 \tag{4-7}$$

$$\omega_0 \tau + \phi_0 = 2k\pi \tag{4-8}$$

with k an integer.

4.1.1.4. Oscillating frequency

The oscillating frequency f_0 is derived from Equation 4-8 and is expressed as:

$$f_0 = \frac{k}{\tau} - \frac{\phi_0}{2\pi\tau} \tag{4-9}$$

The distance between the different oscillation modes is given by the electrical and optical delays inside the loop. This distance, known as the free spectral range (FSR), is determined by:

$$FSR = \frac{1}{\tau} = \frac{1}{\tau_e + \tau_o} = \frac{1}{\tau_e + \frac{n_F L}{c}} \tag{4-10}$$

where τ_e and τ_o are the delay due to the electronic and optical components respectively, L is the optical fiber delay-line length, n_F is the optical fiber refractive index, and c is the speed of light in vacuum. The quality factor Q of the resonant cavity is directly related to the optical delay by $Q = \pi f_0 \tau_o$.

The phase noise of the generated microwave signal is strongly related to the optical fiber length, so when the length increases, the Q factor increases, and the noise is decreased. At the same time, the FSR decreases and the VBO operation will depend on the bandwidth of the band-pass filter, which should be as narrow as possible to allow only one oscillating mode.

4.1.2. VBO experimental characterization

The experimental characterization includes frequency stability measurements in the temporal and frequency domain. For this, several VCSEL-based optoelectronic oscillator experimentations are carried out according to the architecture of Figure **4-1**. Three components are changed in order to verify their impact on phase noise. Two C and O-band VCSELs allow verifying the impact of chromatic dispersion and relative intensity noise (RIN), two cavity filters centered at 1.25 GHz ($BW = 5.25$ MHz) and 2.5 GHz ($BW = 8.1$ MHz), and four SM optical delay lines (1, 2, 3, and 5 km). The VBO setup shown in Figure **4-4** includes an optical isolator to reduce the optical reflections towards the laser and a tunable microwave attenuator to control the electrical power inside the loop. Both VCSELs are not controlled in temperature, but all the experimental measurements were taken inside a temperature-controlled clean room (24 °C).
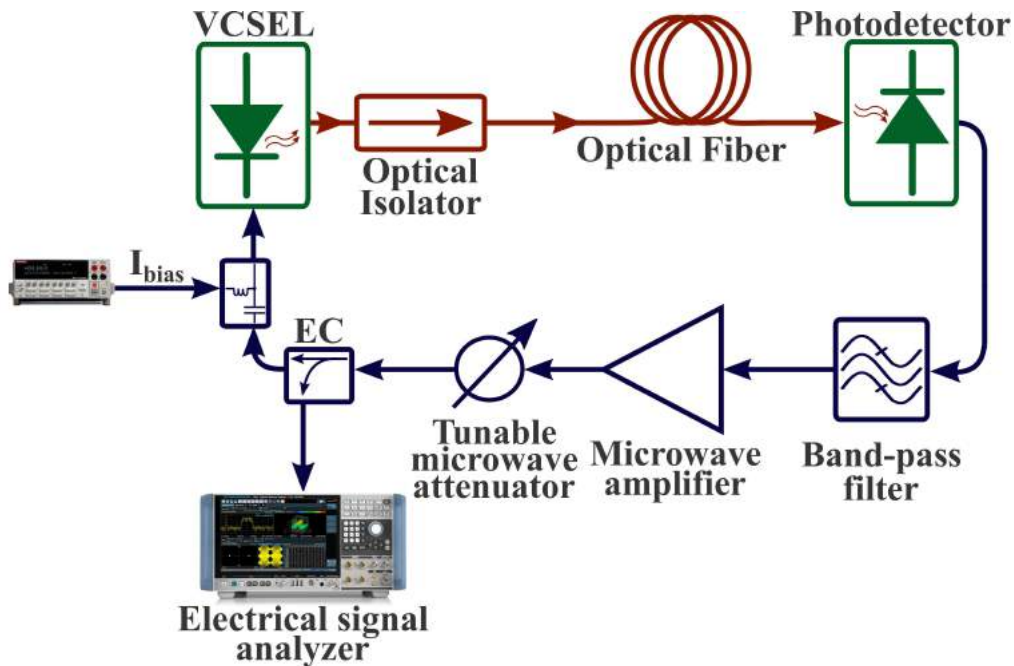
Figure 4-4.: VBO setup implemented.

The phase noise is measured using the direct method with an electrical spectrum analyzer (ESA), whereas for the timing jitter measurements (time interval error), an oscilloscope is employed. For measurement validation purposes, a calibrated phase noise signal was implemented applying frequency modulation (FM) to an ultra-low phase noise source (at different carrier frequencies) with an uniform noise source [10]. The procedure and calibration results are condensed in Appendix B.

4.1.2.1. VBO implementation at 2.5 GHz

Regardless of the laser source, the FSR of the microwave signal varies according to the loop delay, as stated in Equation 4-10. The optical delay, controlled by the SM fiber length, is dominant and determines the FSR and the quality factor Q. The FSR reduction for 4 optical delay line lengths is shown in Figure **4-5**. Although a high Q factor guarantees a lower phase noise, more non-oscillating modes are present within the filter profile. Considering just the optical delay, the calculated and measured FSR are summarized in Table **4-1**. The FSR difference for each delay line corresponds to the fiber length uncertainty and the delay contribution of the electronic components.
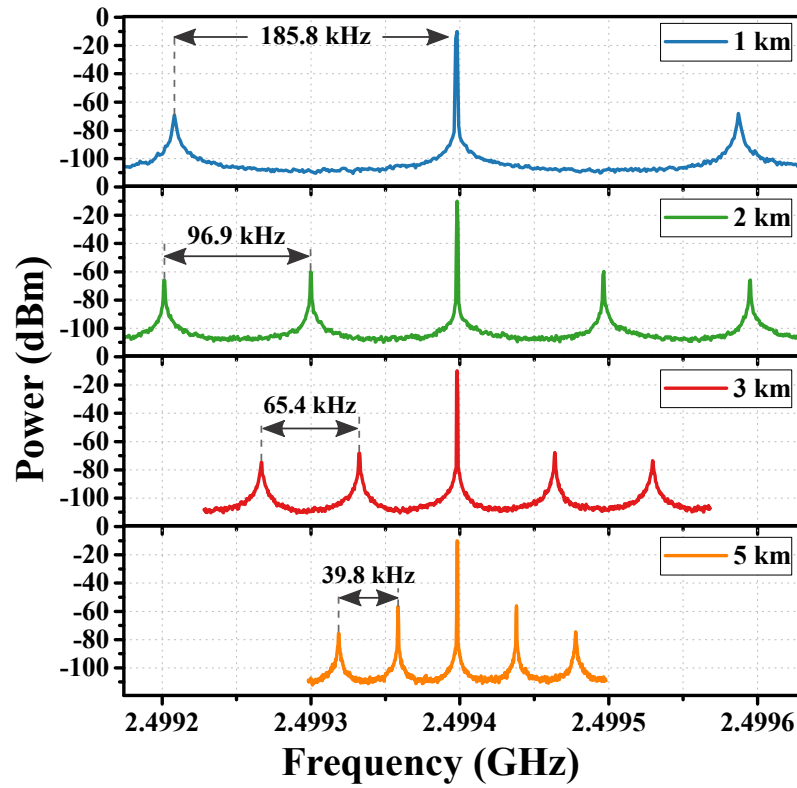
Figure 4-5.: Electrical spectrum at 2.5 GHz for different delay lines using a C-band VCSEL.

Table 4-1.: Calculated and measured FSR.

Optical fiber length (km)	FSR measured (kHz)	FSR calculated (kHz)
1	185.8	200.1
2	96.9	100
3	65.4	66.7
5	39.8	40

In all four cases, the power of the oscillating mode is about -10 dBm. This value is small because the output of the electric coupler is attenuated by 20 dB. Similarly, the power difference with the first non-oscillating mode is over 45 dB in all cases.

The 2.5 GHz VBO phase noise curves are depicted in Figure **4-6**. Both implementations prove the enhancement of phase noise when the optical delay increases. At 10 kHz from the carrier, the phase noise is reduced by 9 dB when the fiber distance is enlarged from 1 km to 5 km. The sharp peaks correspond to the non-oscillating modes generated by the resonant cavity. The phase noise level difference between the optical bands is given by the zero chromatic dispersion of the standard single-mode optical fiber at 1.3 μm. In this sense, the lowest phase noise values are achieved when an O-band VCSEL is used. Independently of the optical fiber length, two noise processes are identified in the phase noise curves. The white phase noise process, located far-from-the-carrier (approximately from 20 kHz), is produced by the white noise of the microwave amplifier. Close-to-the-carrier, the noise curve is governed by the white frequency noise process, which varies at a -20 dB/decade rate as a result of the Leeson effect over the amplifier white noise inside the loop.
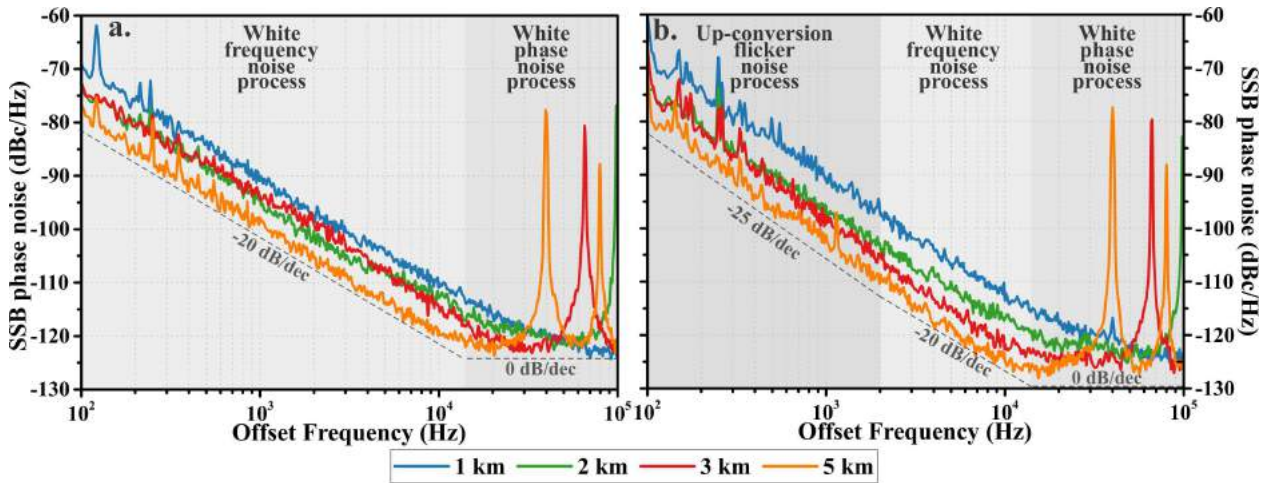
Figure 4-6.: Phase noise at 2.5 GHz for different delay lines using a C-band (**a.**) and an O-band VCSEL (**b.**).

In particular, the phase noise of the O-band VBO presents a third noise process with a slope of -25 dB/dec. This noise is dominated by Rayleigh scattering in the optical fiber. Rayleigh scattering converts the phase variations of the light beam into intensity variations at the output of a long optical fiber [250], then converted into intensity noise in the electrical domain. Due to the non-linearity of the photodetector and microwave amplifier, an amplitude-to-phase noise conversion process takes place inside the loop, generating a degradation of the phase noise of the microwave signal. This scattering has a more significant impact on the O-band than on the C-band, consequently this noise process is not observed in the C-band VBO phase noise curve.

The VBO timing jitter is determined through the time interval error (TIE) measurement of

10.000 microwave signal edges. Figure **4-7** shows the TIE histograms and the estimated standard deviations, assuming a Gaussian distribution for each case. According to the distribution of the samples, the VBO jitter is mostly random, and the standard deviation of the distribution characterizes its mean square root (RMS) value. For both VCSELs, the RMS TIE jitter increases as does the optical fiber length. This phenomenon is caused by the fact that there are additional non-rejected modes, and each one makes an individual contribution of periodic jitter (deterministic). This jitter expands the profile of the Gaussian distribution and thus the RMS jitter. One way to reduce this effect is to use a narrower bandwidth passband filter, to eliminate the contribution of periodic jitter. As expected, the lowest RMS TIE jitters are obtained for the lowest phase noise values, that is, when an O-band VCSEL is used.
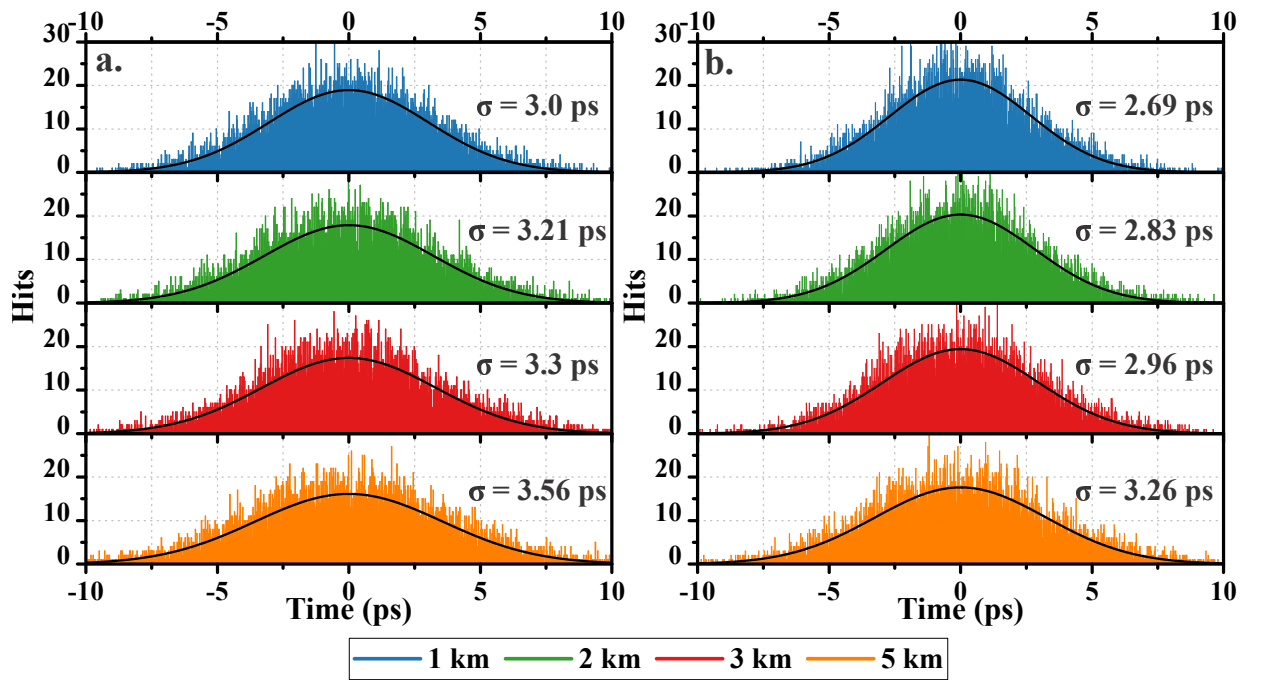
Figure 4-7.: TIE histograms at 2.5 GHz for different delay lines using a C-band (**a.**) and an O-band VCSEL (**b.**).

According to the jitter definitions presented in Chapter 1, the phase noise curves can be integrated and compared with the RMS TIE results. Using Equation 1-37, the phase-jitter and the inverse integrated jitter are determined and plotted in Figure **4-8**. The phase-jitter spectral density varies with the same pattern as the phase noise curve, this implies that the phase-jitter is higher close to the carrier. By definition, jitter values are expected to reduce as the length of the optical fiber increases, because the region under the curve decreases. However, as observed with the TIE histograms, phase-jitter rises due to the individual jitter contributions from the non-oscillating modes. In both cases, the major jitter increment occurs in the region where these modes appear (from 40 kHz to 1 MHz), and then it remains nearly constant up to 100 Hz. The difference in phase noise level gives the initial and final jitter levels between the two implementations (VCSEL at different bands). In the case of

$L = 1$ km, jitter increases during the last 300 Hz (between 100 Hz and 300 Hz) due to the presence of additional phase noise peaks. A particular case occurs when $L = 2$ km in C-band, and is caused by the higher amplitude of the non-oscillating modes during the measurements. It is worth pointing out that the jitter determination is limited by the inaccuracy of the phase noise measurements at frequencies below 1 kHz, typical of the direct measurement method.
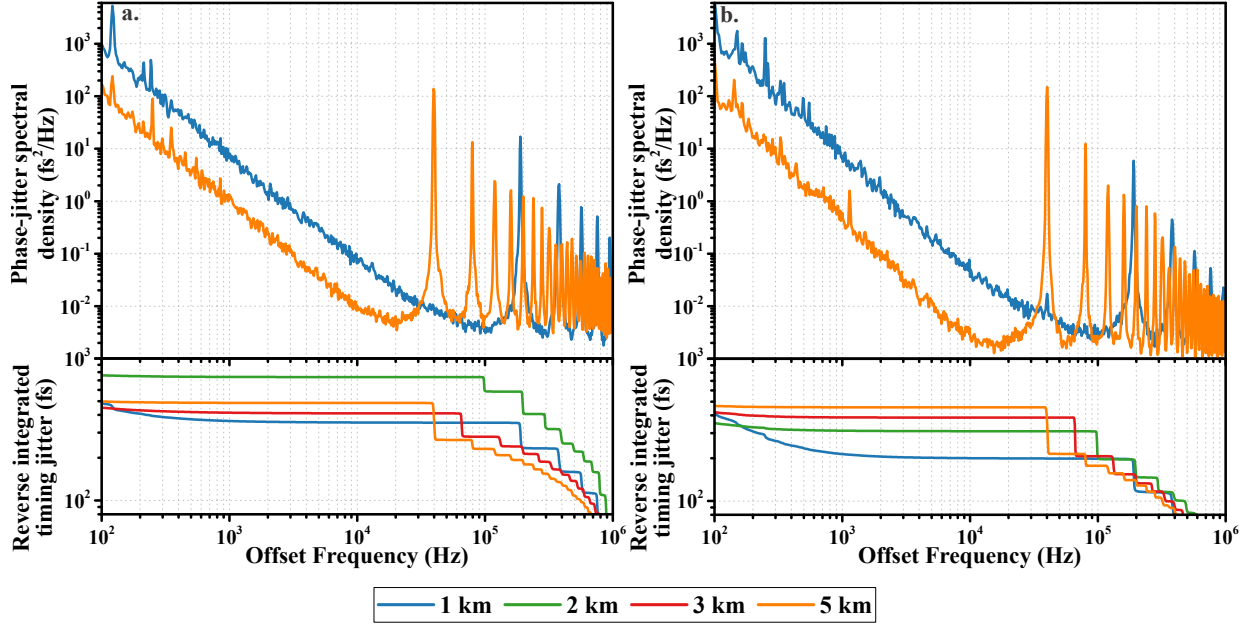
Figure 4-8.: Phase-jitter PSD and inverse integrated jitter at 2.5 GHz for different delay lines using a **a.** C-band **b.** O-band VCSEL.

The results of phase noise (at 10 kHz from the carrier), TIE RMS jitter, and calculated phase-jitter (from 100 Hz to 1 MHz) are summarized in Table **4-2**. Since the phase-jitter is calculated in a specific frequency band and the TIE measurements do not include any filters, the TIE RMS is higher than the phase-jitter in all cases.

Table 4-2.: Summary of 2.5 GHz VBO behavior.

Fiber length (km)	C-band			O-band		
	Phase Noise (dBc/Hz)	TIE RMS jitter (ps)	Phase-jitter calculated (ps)	Phase Noise (dBc/Hz)	TIE RMS jitter (ps)	Phase-jitter calculated (ps)
1	-110	3	0.48	-113.5	2.69	0.43
2	-112.8	3.21	0.46	-117	2.83	0.35
3	-114.5	3.3	0.45	-121.7	2.96	0.43
5	-119	3.56	0.5	-124.8	3.26	0.47

4.1.2.2. VBO implementation at 1.25 GHz

The same optical delays and a C-band VCSEL are used for the implementation of the VBO at 1.25 GHz. This time, the bias conditions of the laser are changed through a 4 to 7 mA bias current sweep in each case. The phase noise measures for $L = 1$ km and $L = 5$ km are shown in Figure **4-9**.
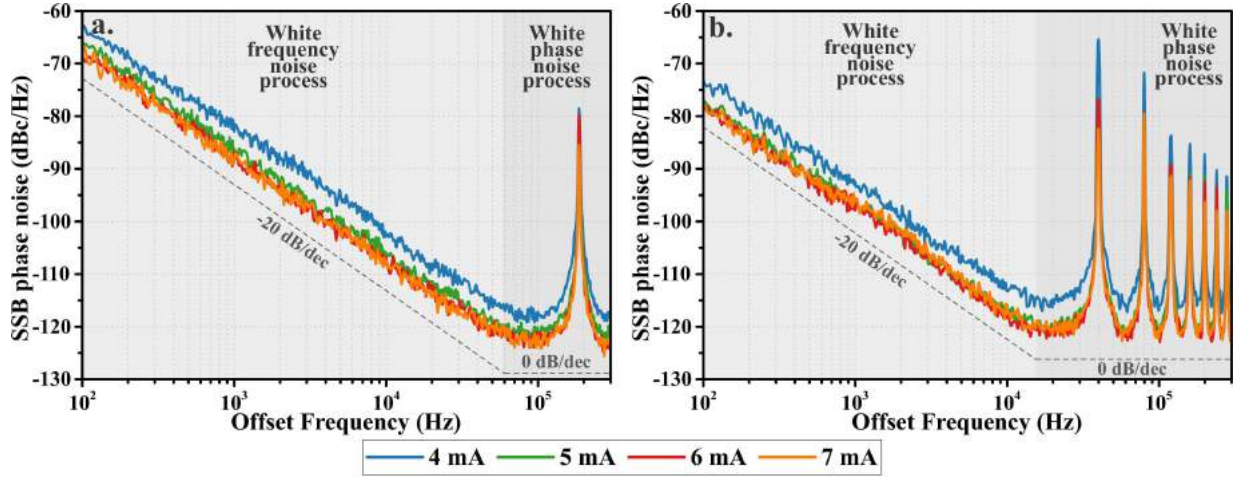
Figure 4-9.: Phase noise at 1.25 GHz for **a.** $L = 1$ km **b.** $L = 5$ km and different bias conditions.

As with 2.5 GHz C-band VBO, white noise processes in frequency and phase are observed in the measured frequency range. Both processes are caused by the Flicker and white noise of the microwave amplifier and the Leeson effect. Under the same polarization conditions, the effect of the resonant cavity is the same as in the 2.5 GHz VBO, i.e., the phase noise is improved by about 9 dB from $L = 1$ km to $L = 5$ km. For the two cases illustrated, the phase noise is improved by 3 dB when the current is increased from 4 to 5 mA. This effect, attributed to the RIN of the C-band VCSEL, appears for all fiber lengths as shown in Figure **4-10**. Although the phase noise improves slightly for $I_{bias} > 5$ mA, the measured values are within the uncertainty range of the measurement method.

The phase noise of the 1.25 GHz VBO is higher than the one of the 2.5 GHz VBO due to the reduction of the resonant cavity Q factor ($Q = \pi f_0 \tau_o$), the difference in the amplifier noise level in both bands, and the power level within the loop.

4.1.2.3. 1.25 GHz VBO thermal characterization

A thermal characterization of the electrical output is performed to validate the applicability of the VBO in changing temperature environments. In this sense, stability measurements are taken in a temperature range between -10 °C and 50 °C. For this characterization, the VBO is entirely introduced into a thermal chamber and exposed to different temperature
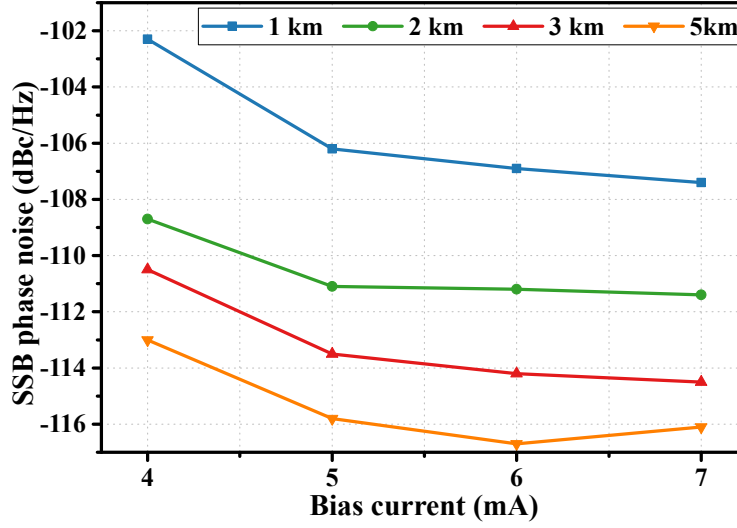
Figure 4-10.: Phase noise at 10 kHz from carrier of the 1.25 GHz VBO at different bias
conditions.

conditions. Two procedures are performed to verify the temperature impact on the power
level inside the loop and the phase noise. The first one consists of setting the temperature at
a constant value during a specific interval of time and measuring the phase noise under the
same oscillation conditions. These conditions are ensured by varying the internal loop power
with a tunable optical coupler left outside the thermal chamber and connected between
the VCSEL and the optical fiber. The bias current and the fiber length are constant for
all processes ($I_{bias} = 6$ mA and $L = 2$ km). Figure **4-11** shows the results for the whole
temperature range after taking 60 measurements every 25 seconds.
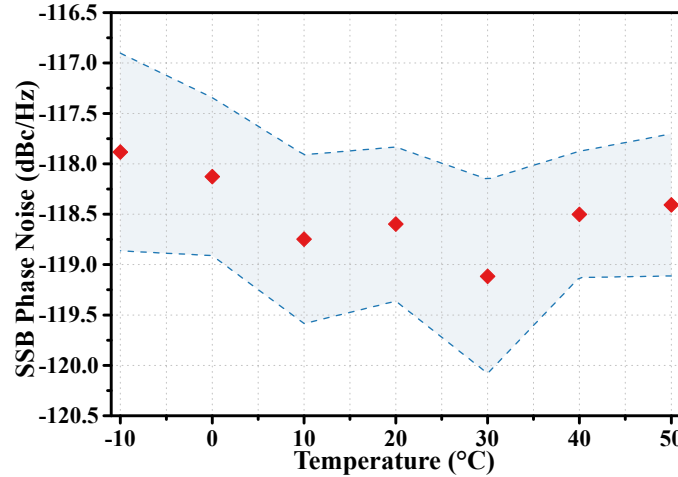
Figure 4-11.: VBO phase noise evolution at different constant temperature conditions.

The error bars in Figure **4-11** are determined by assuming that all noise sources are uncorre-
lated and that the phase noise has a Gaussian distribution. Taking the mean value for each

temperature, the most considerable phase noise variation is 1.5 dB (between -117.75 and -119.25 dBc/Hz). This difference is within the uncertainty calculated for each temperature value. Therefore, it can be concluded that when the power inside the loop is conserved, the phase noise remains constant with temperature variations.

For the second process, the temperature is modified at a constant rate of 1 °C/min from 50 °C to 0 °C and then again up to 50 °C. In this case, the optical coupler is not modified and the electrical peak power, the oscillation frequency, and the phase noise at 10 kHz from the carrier are monitored (4 measurements per minute). The electrical peak power, illustrated in Figure **4-12 a.**, increases by 10 dB when the temperature drops from 50 to 0 °C. This increment is caused by the higher optical power emitted by the VCSEL (as verified in Chapter 2) and the gain drifts of the microwave amplifier. As mentioned, the variations in laser power are associated with temperature-dependent laser gain and the carrier leakage out of the active region at high temperatures. The gain drifts of the amplifier can be compensated by controlling the drain currents and the input power level [251].
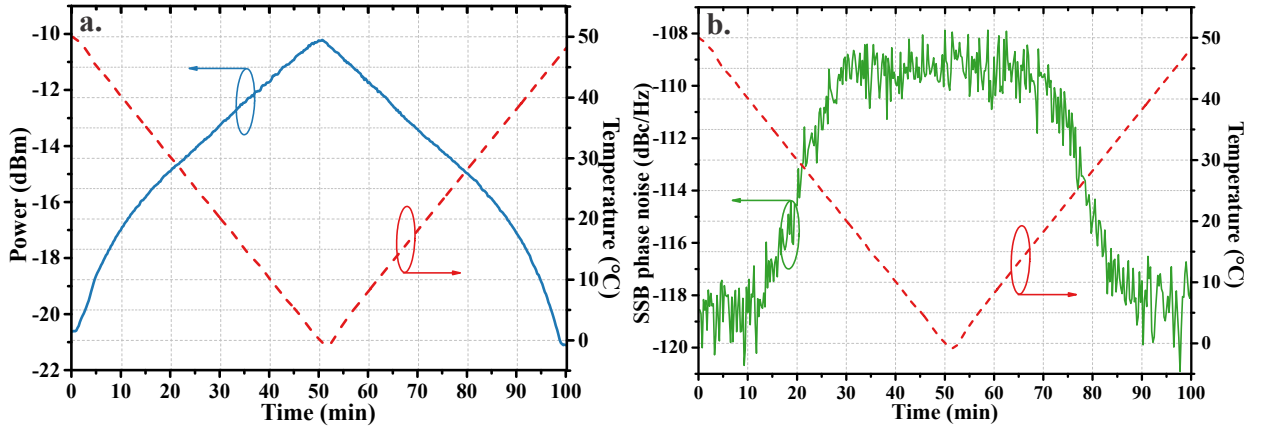
Figure 4-12.: a. Power peak evolution and **b.** phase noise evolution for progressive temperature variations.

The additional loop power produces VCSEL over-modulation and non-linear distortions (e.g., clipping), which deteriorate the VBO performance. As shown in Figure **4-12 b.**, the VBO remains in oscillation condition, even though the phase noise deteriorates dramatically by 10 dB. Both peak power and phase noise return to their initial values when the temperature is raised from 0 to 50 °C.

Another effect of temperature is the enlargement of the optical fiber and the change of its effective refractive index n. These two parameters impact the phase of the optical beam ϕ and consequently, the oscillating frequency f_0. According to the theoretical approach presented in Appendix C, the frequency variation Δf_0 changes as follows:

$$\frac{\Delta f_0}{\Delta T} = f_0 \left(\frac{1}{L} \frac{dL}{dT} + \frac{1}{n} \frac{dn}{dT} \right) \qquad (4\text{-}11)$$

Both L and n vary linearly with the temperature according to relations 4-12 and 4-13 [129], respectively.

$$\Delta L = 0.5 * 10^{-6} \cdot L \cdot \Delta T \tag{4-12}$$

$$\Delta n = 9.2 * 10^{-6} \cdot \Delta T \tag{4-13}$$

Thus, Δf_0 is linear to temperature changes applied to the optical fiber. Figure **4-13** presents the linear trend of f_0 for the temperature range 50 - 0 - 50 °C. The oscillation frequency increases by 505 kHz when the temperature decreases from 50 to 0 °C. For the positive slope of the temperature, the frequency decreases again at the same rate. Thus, the linear variation corresponds to:

$$\left| \frac{\Delta f_0}{\Delta T} \right| = 10.1 \frac{kHz}{°C} = 8.1 \frac{ppm}{°C} \tag{4-14}$$
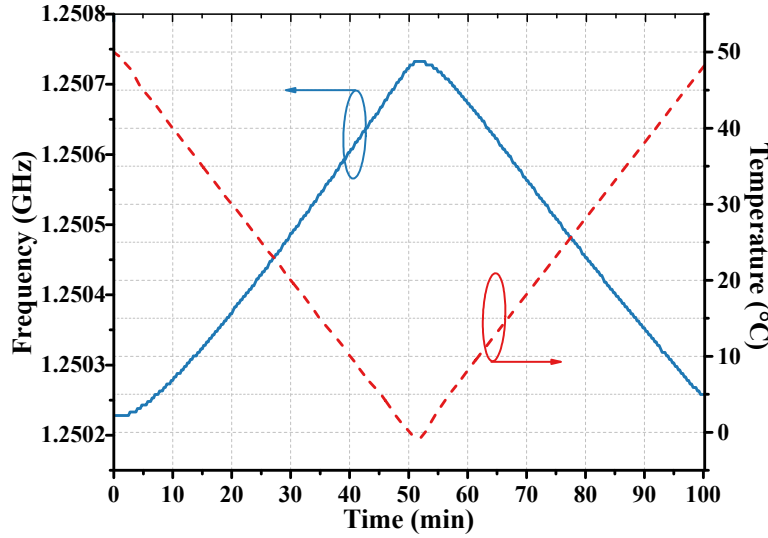
Figure 4-13.: Oscillating frequency f_0 evolution for progressive temperature variations.

Based on the results and comparing them with other oscillator technologies, such as metal cavity and coaxial cable oscillators with thermal stability of 100 ppm/°C [109], the VBO presents an acceptable thermal performance. It is exceeded by quartz oscillators (0.1 ppm/°C) and fiber ring based optoelectronic oscillators (6.8 ppm/°C) [129].

4.2. Self-started VCSEL-based harmonic frequency generator (SVHFG)

As seen in the previous section, directly modulated VCSELs are an alternative to generate low phase noise microwave signals. According to Table **1-2**, the VBO phase noise can

be lower than some multi-loop OEO and resonator-based OEO. VCSEL advantages and the simplicity of the VBO architecture can be used to improve their features, even if the oscillation frequency is limited to the laser bandwidth. Thus, the relatively low oscillation frequencies (4 GHz for LW-VCSEL) relegate VBO suitability to particular applications.

The generation of multiple frequencies (harmonics and sub-harmonics) using optoelectronic devices includes closed-loop systems (discussed in Section 1.4) and different non-linear conversion mechanisms. For example, some optoelectronic mixer architectures include direct laser modulation, semiconductor optical amplifiers, and external electro-optic modulators [252]. In this sense, multiple harmonics can be generated by gain switching applied to semiconductor lasers. Notably, due to the non-linearity of the P-I curve and the low bias currents, gain-switched VCSELs are a low-cost and straightforward alternative for generating harmonics.

The operating principle of the self-started VCSEL-based harmonic frequency generator (SVHFG) conserves the concept of the VBO, i.e., direct modulation of a VCSEL, except it is modulated in gain switching regime (large microwave signal). A gain-switched laser generates an optical pulse train with a pulse-to-pulse time (train periodicity) controlled by the repetition rate f_0 of the drive electrical signal. In the frequency domain, the pulse train corresponds to a frequency comb where f_0 provides the space between modes. By direct photodetection, the optical pulses are converted into an electric pulse train composed of microwave harmonics at $n \times f_0$ frequencies. The driving conditions significantly influence both the quality of the optical comb and the noise level of the microwave harmonics. Indeed, the bias current and the amplitude and frequency of the driving signal have more impact on the performance than the type of laser cavity or other internal laser parameters [253].

4.2.1. SVHFG architecture

The architecture of the SVHFG is illustrated in Figure **4-14**. The optical beam coming from the VCSEL is photodetected and immediately amplified by the microwave amplifier 1. The bandwidth of both the photodetector and the amplifier must be higher than the frequency of the highest order harmonic desired. The microwave harmonics $2f_0$, $3f_0 \ldots nf_0$, are recovered through the electrical coupler 1 (EC1). The variable attenuator and the microwave amplifier 2 ensure the electrical power level to modulate the VCSEL directly in GS condition. The band-pass filter, as in the VBO, is responsible for filtering the fundamental frequency f_0 that can be extracted by the electrical coupler 2 (EC2). Hence, the bandwidth of the amplifier 2 must cover at least the frequency f_0.

The theoretical analysis presented in Section 4.1.1 is still valid for the SVHFG architecture. The gain condition is satisfied by adjusting the variable attenuator, whereas the FSR will be slightly reduced, considering that the electrical delay τ_e is higher due to the additional components. About loop noise, additional factors must be considered due to the contributions of the two microwave amplifiers and the over-modulation of the VCSEL.
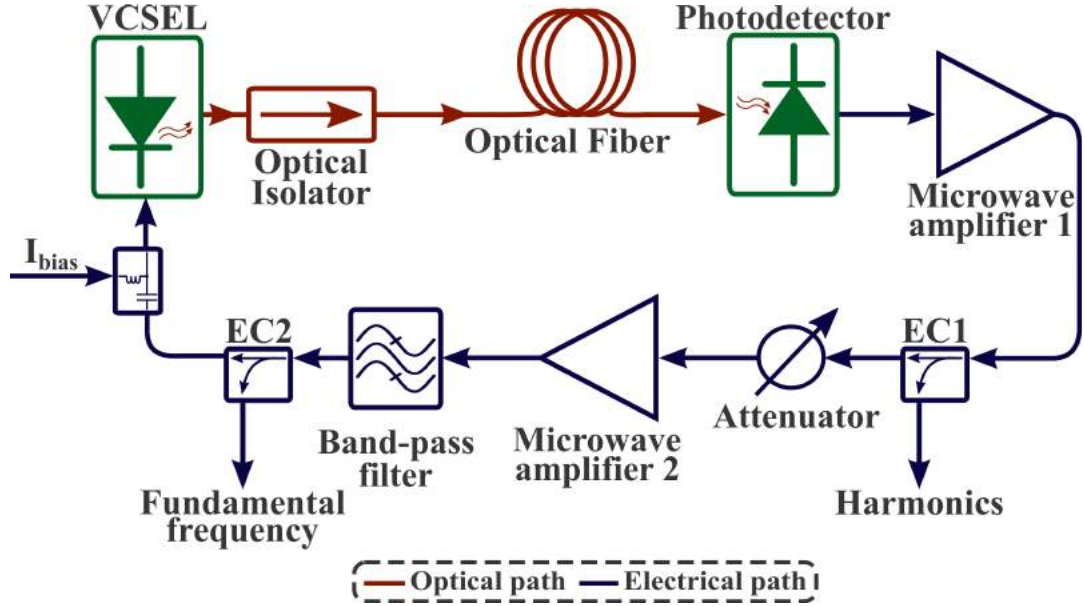
Figure 4-14.: Self-started VCSEL-based harmonic frequency generator architecture.

4.2.2. Predictive phase-noise model

The output signal generated by a real oscillator varies in amplitude and phase due to internal and external noise factors, e.g., the temperature and power supply noise. Rewriting Equation 1-4, the instantaneous output voltage is expressed as:

$$V(t) = [V_0 + \varepsilon(t)] \cos[2\pi f_0 t + \varphi(t)] \tag{4-15}$$

where $\varepsilon(t)$ represents the amplitude fluctuations and $\varphi(t)$ the phase fluctuations. In a real scenario, the oscillator behavior can be mathematically described in terms of the slow-varying complex envelope, as amplitude and phase were decoupled from the oscillation since the resonator relaxation time τ is larger than $1/2\pi f_0$ by a factor of at least 10^2 [254]. In this way, amplitude and phase noise can be analyzed as additive noise phenomena. The noise model developed in this work focuses exclusively on the propagation of phase fluctuations generated by the loop elements.

The SVHFG phase noise can be modeled by the linear feedback system theory proposed by Rubiola [2] for delay-line oscillators, whereby the noise power spectral density includes the noise contributions of the different loop elements and their transfer functions. In the phase noise model, shown in Figure **4-15**, all signals are Laplace transforms of the phase fluctuations. Therefore, $\varphi(s)$ represents the phase fluctuations of the fundamental frequency, $\psi(s)$ are the noise sources further detailed, and B_d and B_f are the transfer function of the delay line and the band-pass filter, respectively.

From the scheme in Figure **4-15**, the phase fluctuations of the fundamental frequency are
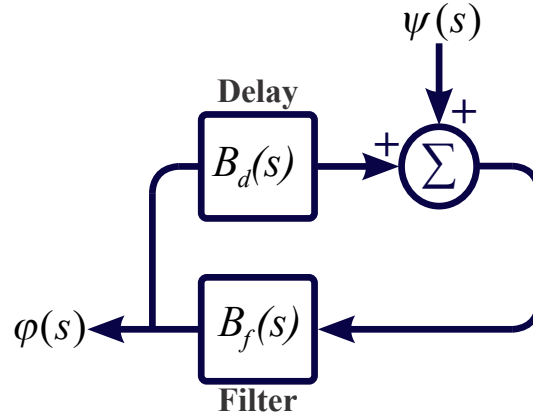
Figure 4-15.: Phase noise model of the SVHFG.

stated as:

$$\varphi(s) = \varphi(s) \cdot B_d(s) \cdot B_f(s) + \psi(s) \cdot B_f(s) \tag{4-16}$$

which leads to:

$$\varphi(s) = \frac{B_f(s)}{1 - B_d(s) \cdot B_f(s)} \cdot \psi(s) = H(s) \cdot \psi(s) \tag{4-17}$$

In the frequency domain, the single-side band power spectral density of the SVHFG phase-noise is given by:

$$S_\varphi(f) = |H(jf)|^2 \cdot S_\psi(f) \tag{4-18}$$

In this way, an expression for phase noise can be obtained by analyzing noise sources $S_\psi(f)$ and the transfer function $H(s)$ separately.

4.2.2.1. Closed-loop transfer function

For the SVHFG, the resonator is comprised of an optical delay line and a band-pass filter tuned at f_0. The phase impulse response in the time domain for the delay and filter are denoted as b_d and b_f respectively and are expressed as [254]:

$$b_d(t) = \delta(t - \tau_d) \tag{4-19}$$

$$b_f(t) = \frac{1}{\tau_f} e^{-\frac{t}{\tau_f}} \tag{4-20}$$

with τ_d the delay time induced by the optical delay line and the electric components ($\tau_d = \tau_e + \tau_o$), and τ_f the filter group delay given by $\tau_f = Q/\pi f_0$. By applying a Laplace transform to b_d and b_f, the transfer function of the feedback loop corresponds to:

$$H(s) = \frac{B_f(s)}{1 - B_d(s) \cdot B_f(s)} = \frac{1}{1 + s\tau_f - e^{-s\tau_d}} \tag{4-21}$$

Therefore, the magnitude squared of the closed-loop transfer function is obtained from Equation 4-21 replacing $s = j\omega$,

$$|H(j\omega)|^2 = \frac{1}{2 - 2\cos\left(\omega\tau_d\right) + \omega^2\tau_f^2 + 2\omega\tau_f\sin\left(\omega\tau_d\right)} \tag{4-22}$$

4.2.2.2. Noise sources

The initial conditions are guaranteed by the optical and electrical components noises, which are injected into the loop through the summing block in Figure **4-15**. Some of these noises are produced by external factors (mechanical and thermal disturbances), whereas others are caused by the intrinsic properties of the component materials and are referred as internal noise sources. The internal noise sources in the SVHFG can be divided into two groups [255]: additive noise generated by random processes, e.g., thermal noise, and multiplicative noise coming from the microwave amplifier and VCSEL frequency noise. Indeed, the power spectral density S_ψ is:

$$S_\psi(f) = S_{add}(f) + S_{mult}(f) \tag{4-23}$$

Each additive noise sources generated by the VCSEL, photodetector, and the optical fiber are represented by a current source in the electrical circuit model in Figure **4-16**. $\langle i_{tot}^2 \rangle$ is the total noise contributions, Z_A is the input impedance of the first amplifier, and Z_{ph} the impedance load of the photodetector.
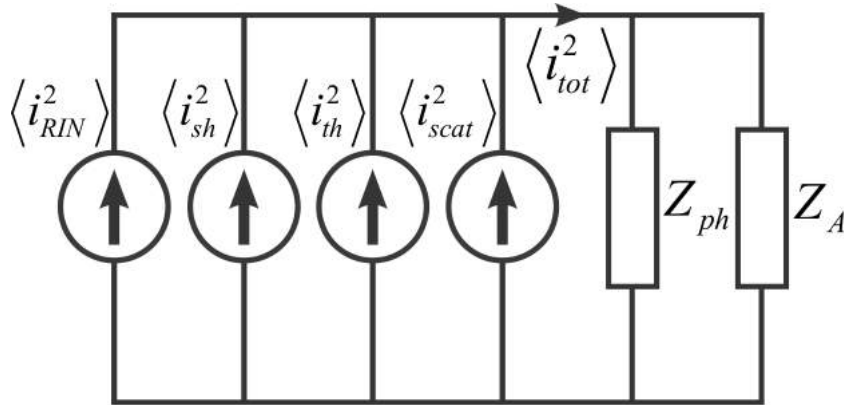
Figure 4-16.: Noise source circuit model.

The total current noise is expressed as:

$$\sqrt{\langle i_{tot}^2 \rangle} = \sqrt{\langle i_{RIN}^2 \rangle + \langle i_{sh}^2 \rangle + \langle i_{th}^2 \rangle + \langle i_{scat}^2 \rangle} \qquad [A/Hz] \tag{4-24}$$

and the current passing through Z_A is:

$$i_A = \sqrt{\langle i_{tot}^2 \rangle} \cdot \frac{Z_{ph}}{Z_A + Z_{ph}} \tag{4-25}$$

Hence, the power spectral density of the additive noise sources referred to the microwave amplifier impedance is defined as:

$$S_{add}(f) = \left\langle i_{tot}^2 \right\rangle \cdot Z_A \cdot \left(\frac{Z_{ph}}{Z_A + Z_{ph}} \right)^2 = \left\langle i_{tot}^2 \right\rangle \cdot Z_{eq} \qquad (4\text{-}26)$$

The additive noise processes included in the model are outlined below.

1. **VCSEL relative intensity noise**
   The VCSEL RIN was addressed in Section 2.5.1 and the measurement results are presented in Section 3.4. The spectrum of laser intensity variations at the photodetector corresponds to:

   $$\left\langle i_{RIN}^2(f) \right\rangle = RIN \cdot i_{ph}^2 \qquad \left[A^2/Hz \right] \qquad (4\text{-}27)$$

   where i_{ph} is the average DC photodetected current and RIN is the VCSEL RIN at the fundamental frequency f_0.

2. **Shot noise**
   The shot noise, originated from the photodetector, is a stationary random process [212] and a wideband noise modeled by a Poisson process [256]. It is produced by the random nature of photon arrivals, which generates a fluctuating current over time. The power spectral density of the photodetector shot noise is proportional to the photodetected current as follows:

   $$\left\langle i_{sh}^2(f) \right\rangle = 2 \cdot q \cdot (i_{ph} + i_{dark}) \qquad \left[A^2/Hz \right] \qquad (4\text{-}28)$$

   where q is the electron charge and i_{dark} is the dark photodetector current (generally negligible).

3. **Thermal (Johnson-Nyquist) noise**
   In any conductor at non-zero temperature, the electrons move randomly, generating a noise current. In the case of the photodetector, this thermal agitation occurs at the load impedance Z_{ph}. This noise current is modeled as a stationary Gaussian random process that is frequency independent [212]. Assuming that Z_{ph} is matched to the load, the power spectral density of the photodetector thermal noise is expressed as [2]:

   $$\left\langle i_{th}^2(f) \right\rangle = \frac{k_B T}{R_{ph}} \qquad \left[A^2/Hz \right] \qquad (4\text{-}29)$$

   with k_B the Boltzman constant and T the absolute temperature.

4. **Intensity-to-phase noise conversion processes**
   The optical fiber produces intensity fluctuations in the optical beam due to its material inhomogeneities [109], non-linearity [257], and connectors mismatch [258]. The intensity noise is converted into microwave phase noise via the amplitude-to-phase noise (AM-PM) conversion in the photodetector [147, 259] and must be considered for the

phase noise analysis.

The stimulated Raman scattering (SRS) and the stimulated Brillouin scattering (SBS) are two non-linear phenomena that occur at high power levels. These two effects are produced by the occurrence of optical and acoustic phonons due to the scattering of a photon to a lower energy photon [212]. SRS and SBS are not considered in this noise analysis because the power emitted by the VCSEL is below the power thresholds for all fiber lengths used.

Rayleigh scattering is caused by microscopic variations in the optical fiber structure, which produce variations in the refractive index. Two phenomena called double Rayleigh backscattering (DRBS), and single Rayleigh backscattering - single reflection (SRBS-SR) [260] are analyzed and represented in Figure **4-17**.
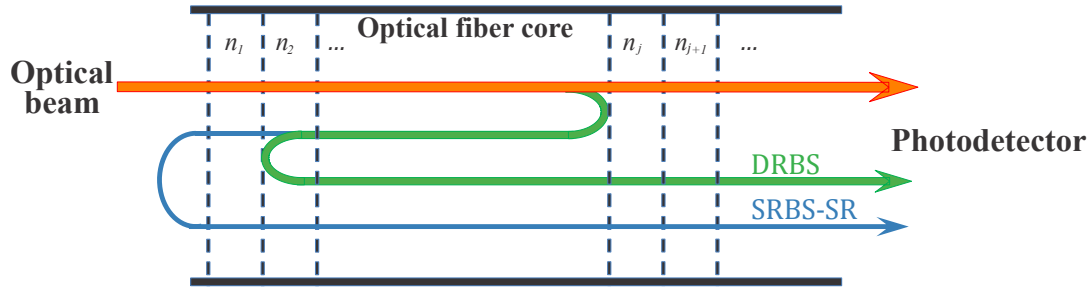
Figure 4-17.: Rayleigh scattering phenomena representation.

Two scattering processes within the fiber generate the double Rayleigh backscattering. The first process reflects some of the incident energy in the backward propagation sense. Then, part of this energy experiments the second scattering process towards the incident beam propagation sense (forward). Due to the noise conversion process, the DRBS is assumed to be a relative noise intensity and is expressed as [261]:

$$RIN_{DRBS}(f) \cong \frac{4S_D^2\alpha_S L_{DRBS}}{\pi\Delta\nu} \cdot \frac{1}{1+(f/\Delta\nu)^2} \qquad [1/Hz] \qquad (4\text{-}30)$$

where S_D is the portion of energy scattered, α_S the Rayleigh coefficient, $\Delta\nu$ the laser linewidth, and f the Fourier frequency. The effective optical fiber length L_{DRBS} is determined as:

$$L_{DRBS} = L - \frac{1-e^{-\alpha L}}{2\alpha} \qquad (4\text{-}31)$$

The second process involves multiple single Rayleigh backscattering (SRBS) followed by a single reflection (SR) at the optical fiber input. The intensity noise produced by this process is:

$$RIN_{SRBS}(f) \cong \frac{4R_P S_D^2\alpha_S L_{SRBS}}{\pi\Delta\nu} \cdot \frac{1}{1+(f/\Delta\nu)^2} \qquad [1/Hz] \qquad (4\text{-}32)$$

with R_P the reflection coefficient at the fiber input and the effective fiber length expressed as:

$$L_{SRBS} = \frac{1 - e^{-\alpha L}}{2\alpha} \tag{4-33}$$

Hence, the power spectral density of intensity noise for both scattering effects is:

$$\left\langle i_{scat}^2(f) \right\rangle = (RIN_{DRBS} + RIN_{SRBS}) \cdot i_{ph}^2 \qquad \left[A^2/Hz\right] \tag{4-34}$$

The two main multiplicative noise processes of the SVHFG are the phase noise of the microwave amplifier and the VCSEL frequency noise to phase noise conversion due to the optical fiber dispersion effect. Assuming that both noise sources are uncorrelated, the power spectral density of the multiplicative noise corresponds to:

$$S_{mult}(f) = S_{amp}(f) + S_{freq}(f) \tag{4-35}$$

1. **Phase noise in microwave amplifiers**
   The power spectral density of the microwave amplifier phase noise includes white and flicker noise [2]. Hence,

$$S_{amp}(f) = b_0 \cdot f^0 + b_{-1} \cdot \frac{1}{f} \tag{4-36}$$

The white noise component is estimated from the equivalent noise spectrum density N and the carrier power P_0 at the amplifier input [68],

$$b_0 = \frac{N}{P_0} = \frac{FkT_0}{P_0} \tag{4-37}$$

with F the noise figure and kT_0 the thermal energy. The SVHFG architecture incorporates two cascade amplifiers, so the Friss formula must be applied and Equation 4-37 becomes:

$$b_0 = \left(F_1 + \frac{F_2 - 1}{A_1^2}\right) \cdot \frac{kT_0}{P_0} \tag{4-38}$$

In contrast, flicker noise is independent of the carrier power at the amplifier input over a wide frequency range. Thus, b_{-1} is constant and its value is related to the size of the amplifier active region and its gain. For microwave amplifiers, b_{-1} is in the range of 10^{-10} (fair quality) to 10^{-14} (best quality) rad^2/Hz [2]. In the case of SVHFG, b_{-1} is given by the sum of the individual contributions b_{-1}^1 and b_{-1}^2 of the two amplifiers.

Equation 4-38 reveals that the level of white noise can be reduced by increasing the power P_0. Due to the direct VCSEL modulation, and assuming a low-loss optical fiber link, the microwave power at the amplifier input can be written as:

$$P_0 = \frac{m^2 \Re^2 P_{bias}^2}{2} \cdot Z_{ph} \parallel Z_A \tag{4-39}$$

where m is the modulation index, $\Re$ the photodetector responsivity, and P_{bias} the

optical power emitted by the VCSEL biased at I_{bias}. Therefore, the phase-noise floor can be reduced through the bias current of the VCSEL and the application of gain switching technique (increasing m).

2. **Laser frequency noise**
   The second multiplicative noise process is produced by the optical delay length fluctuations generated in turn by the laser frequency fluctuations. For the SVHFG, these delay fluctuations are converted into phase fluctuations inside the optical fiber due to the in-phase closed-loop condition. The power spectral density of the phase noise induced by the laser frequency noise is given by [149]:

$$S_{freq}(f) = C_\varphi^2 \cdot S_\nu(f) \tag{4-40}$$

where $S_\nu(f)$ is the power spectral density of the VCSEL frequency noise and the conversion factor C_φ obeys to:

$$C_\varphi = 2\pi \cdot f_0 \cdot \lambda_0^2 \cdot D_\lambda \cdot \frac{L}{c} \tag{4-41}$$

where λ_0 is the VCSEL wavelength and D_λ is the dispersion value of the optical fiber at λ_0. Equation 4-40 reveals that the dispersion conversion of laser frequency noise can deteriorate the SVHFG phase noise performance through the D_λ value. Furthermore, the phase noise can be improved by using dispersion-shifted fibers (DSF) and C-band VCSELs, or O-band VCSELs with standard single-mode fibers (such as SMF-28). To validate the predictive noise model, and since $S_\nu(f)$ was not measured during the development of this work, its power distribution is assumed as an f^{-1} slope flicker noise for the whole observed frequency range [262].

4.2.3. SVHFG experimental characterization

The SVHFG is implemented according to the configuration shown in Figure **4-14**. The microwave amplifier connected to the photodetector has a 38-dB flat gain, a notably wide band from 0.5 to 18 GHz, and a typical noise figure of 3 dB. The frequency band of the second amplifier is from 2 to 4 GHz and 37-dB gain. A cavity filter tuned at 1.25 GHz is used to establish the fundamental frequency. The length of the optical delay line is fixed at 5 km and the bias current at 6 mA for all implementations. An electric circulator is placed between the band-pass filter and the microwave amplifier 2 to eliminate reflections towards the amplifier. The coupled outputs of EC1 and EC2 are attenuated by 10 and 20 dB, respectively. The electric couplers add additional attenuation because their bandwidths (BW_{EC1} = 6 - 18 GHz and BW_{EC2} = 1 - 12.4 GHz) do not cover the whole frequency range of analysis. Finally, a 17 GHz bandwidth fast photodetector and C-band and O-band VCSELs are used.

4.2.3.1. Electrical spectra

The electrical spectra of nine harmonics generated employing different VCSELs is depicted in Figure **4-18**. Even though only the laser sources are modified, the noise level in the case of the C-band VCSEL (see Figure **4-18 a.**) is above the floor noise. This noise increasing is due to the difference in electrical power within the loop. The emission power of the C-band VCSEL is lower than the O-band VCSEL, so to achieve the oscillating condition, it is necessary to compensate the power through the tunable electrical attenuator. In this way, more electrical power directly modulates the laser, consequently reducing the carrier-to-noise ratio (CNR) around the main optical mode. Therefore, an important deterioration of phase noise is expected for these harmonics.
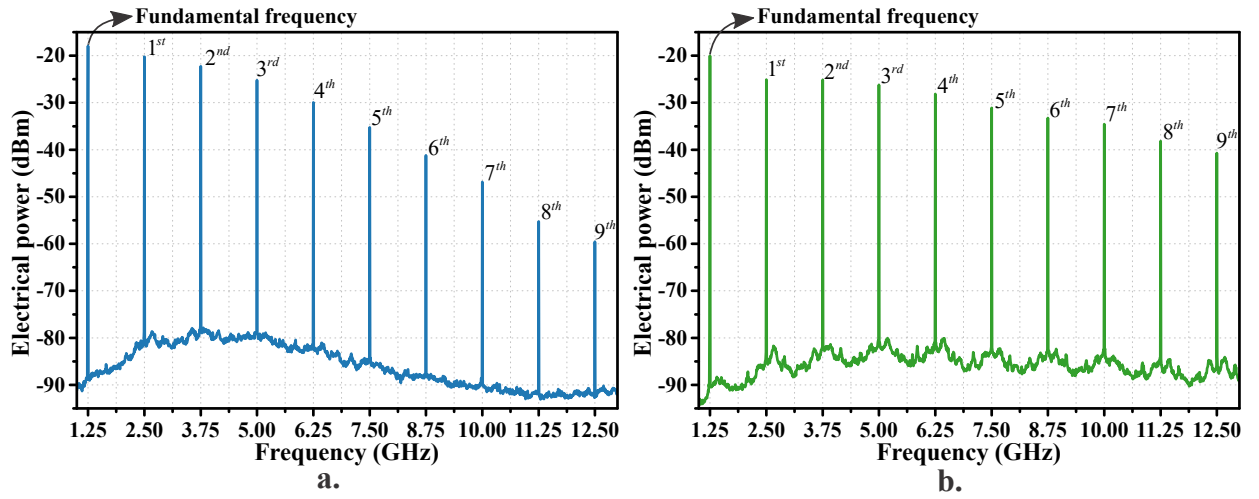
Figure 4-18.: Electrical spectra of the microwave harmonics using **a.** C-band VCSEL **b.** O-band VCSEL.

The power level of all the generated microwave harmonics relative to the fundamental frequency power are summarized in Table **4-3**. As expected, both the fundamental frequency and the first three harmonics of the C-band SVHFG are higher than the O-band SVHFG. This effect occurs because a higher electrical power is required to guarantee the oscillation condition (higher modulation index). From the fourth harmonic, the power of the C-band SVHFG decreases drastically at a rate higher than 4.5 dB per harmonic. In contrast, the O-band SVHFG decreases at a rate lower than 3 dB per harmonic (except for the 8th harmonic). Hence, the carrier power at 12.5 GHz of the O-band implementation is 20 dB higher than the C-band. This performance difference is attributed to the electrical access of the VCSELs and the deterioration of the optical modes at higher modulation powers.

For application purposes, each harmonic can be filtered and amplified with a narrow band-pass filter and a tuned microwave amplifier. Likewise, the power level of the harmonics can be improved by using electrical couplers with less attenuated coupled outputs and a bandwidth adjusted to the required frequencies.

Table 4-3.: Power level of the generated microwave harmonics.

Harmonic	Frequency (GHz)	Power relative to the fundamental (dBc) - C-band SVHFG	Power relative to the fundamental (dBc) - O-band SVHFG
Fundamental	1.25	0	0
1	2.5	-2.2	-5.1
2	3.75	-4.3	-5.1
3	5	-7.2	-6.2
4	6.25	-11.9	-8.2
5	7.5	-17.3	-11.1
6	8.75	-23.2	-13.3
7	10	-28.8	-14.5
8	11.25	-37.3	-18.2
9	12.5	-41.3	-20.7

4.2.3.2. Phase noise of microwave harmonics

The phase noise of the fundamental frequency is shown in Figure **4-19**. The phase noise at 10 kHz from the carrier is -124.7 dBc/Hz in both implementations. According to the slopes of each curve, three noise processes are observed. From right to left, the white phase noise process is present in both cases, appears around 10 kHz to 300 kHz, and corresponds to the contribution of all white noise inside the loop. Then, a slope of -20 dB/dec from 120 Hz and 200 Hz (C and O-band respectively) is the signature of a white frequency noise process and is generated by the Leeson effect on the white noise of the amplifier. The third noise process of -25 dB/dec slope covers the frequencies closest to the carrier from 10 Hz upwards. This noise process is characterized by the up-conversion of the noise generated by Rayleigh scattering, the VCSEL frequency noise, and mainly to the higher flicker noise contribution by the two cascade microwave amplifiers.

As any frequency multiplication method, the phase noise of the microwave harmonics is degraded by a factor of $20 \times logN$, where N is the multiplication factor [146]. The evolution of harmonic phase noise is presented in Figure **4-20**. Both implementations have close phase noise behavior until the third harmonic. After that, the phase noise of the C-band SVHFG deteriorates fast as predicted by the optical CNR reduction and the accelerated decrease in the power level of the harmonics. In the case of the O-band SVHFG, the phase noise degrades logarithmically with an average offset of 4 dB compared to the expected values (red dashed line).

Table **4-4** presents a performance comparison of the carriers generated at 5, 10, and 15 GHz with other optoelectronic oscillator topologies. The results presented include an O-band SVHFG with fundamental frequencies $f_0 = 1.25$ and $f_0 = 2.5$ GHz. For the three selected
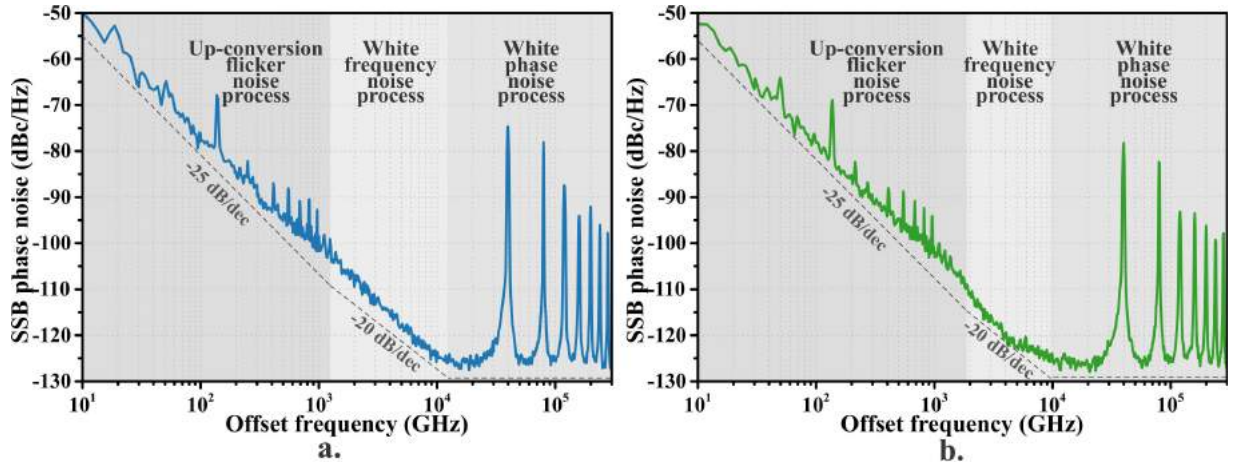
Figure 4-19.: Phase noise of fundamental frequency f_0 using **a.** C-band VCSEL **b.** O-band VCSEL.
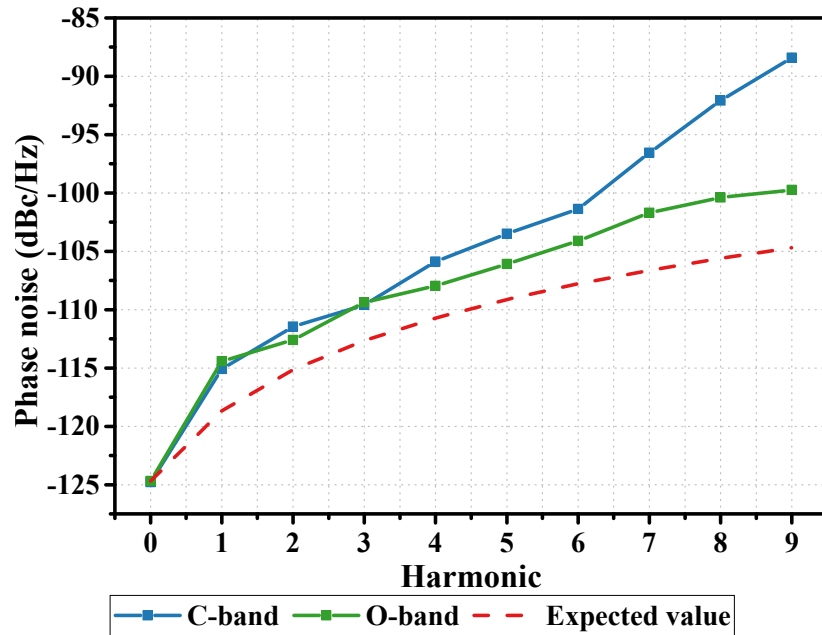
Figure 4-20.: Phase noise evolution of the microwave harmonics.

carriers, the SVHFG performance, in terms of phase noise, is close to other recent implementations available in the literature. For example, at 10 GHz, the phase noise of SVHFG is slightly higher than more complex architectures, which include several loops, different modulation schemes (intensity and phase), and several microwave amplifiers. Besides, the straightforward SVHFG architecture enables the generation of adjustable frequency carriers through an adjustable bandpass filter and microwave amplifiers in the desired bands.

Table 4-4.: SVHFG performance comparison with other OEO topologies.

OEO topology	Oscillation frequency (GHz)	Phase noise @ 10 kHz offset (dBc/Hz)	Modulation	Reference
Dual loop OEO	5.4	-115	External	[263]
SVHFG - $f_0 = 1.25$ GHz	**5**	**-112**	**Direct**	
SVHFG - $f_0 = 2.5$ GHz	**5**	**-117**	**Direct**	
Delay line based OEO	10	-110	Both	[264]
Dual loop OEO	10	-100	External	[265]
Dual loop coupled OEO	10	-90	External	[266]
Resonator based OEO	10	-128	External	[267]
SVHFG - $f_0 = 1.25$ GHz	**10**	**-106**	**Direct**	
SVHFG - $f_0 = 2.5$ GHz	**10**	**-112**	**Direct**	
Multi-loop OEO	15	-118	External	[154]
SVHFG - $f_0 = 2.5$ GHz	**15**	**-104**	**Direct**	

4.2.3.3. Validation of the predictive phase noise model

The predictive phase noise model developed in section 4.2.2 is validated using the parameters shown in Appendix D. Some parameters are obtained from previous component characterizations, such as the VCSEL RIN, whereas other are taken from the component data sheets or the literature. The predicted phase noise of the C-band SVHFG at 1.25 GHz is shown in Figure **4-21**. The measurement and prediction curves agree on the first three noise processes observed in the measurements. The fourth noise process observed in the model is the Flicker frequency noise of -30 dB/dec slope. This process is caused by the Lesson effect of the flicker noise of the amplifier at frequencies below the corner frequency f_c. According to the values b_{-1} and b_0 used by the model, f_c is 470 Hz and the Flicker frequency noise process appears around 200 Hz. It is worth mentioning that this noise process does not appear in any of the measurements due to the low sensitivity of the measurement method at frequencies below 1 kHz. The predicted phase noise level at 10 kHz of the carrier is -128.8 dBc/Hz and the measured value at the same frequency offset is -124.7 dBc/Hz. The 4 dB level difference is due to the characterization measurement inaccuracy and because some parameters are assumed from the literature.

The sharp peaks (non-oscillating modes) at frequencies above 30 kHz of the carrier match well with the peaks measured for a 5 km optical fiber. The level, shape, and distribution of the non-oscillating modes are governed by the resonant cavity delay τ_d and the filter group delay τ_f, which relates the bandwidth and quality factor of the filter (Equation 4-21). The phase noise of SVHFG at different fiber lengths can be predicted by assuming identical electrical and optical conditions, i.e., the same component characteristics and identical electrical and
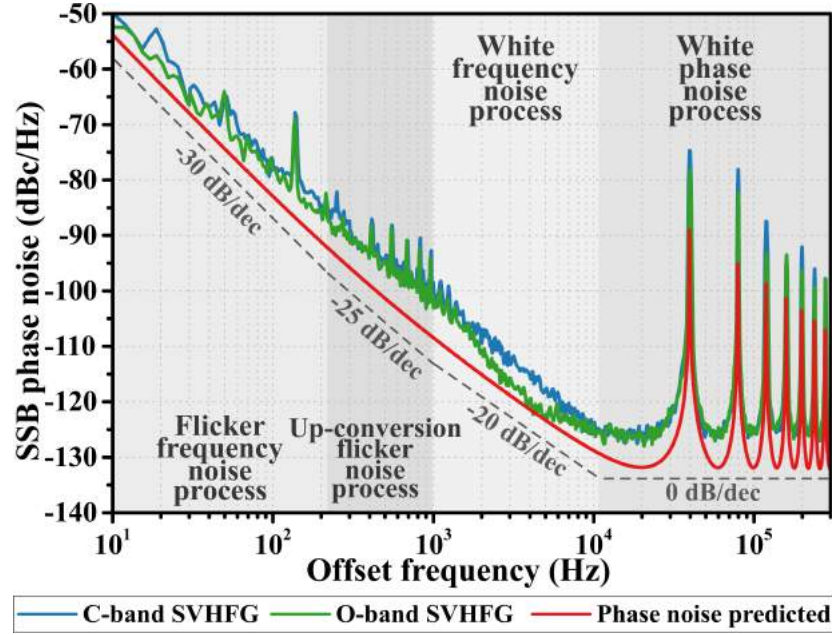
Figure 4-21.: Predicted phase noise of SVHFG at 1.25 GHz.

optical power levels within the loop. Figure **4-22 a.** shows the predicted phase noise for four fiber lengths. As with the VBO, the predicted phase noise deteriorates with the reduction of the fiber length. The predicted phase noise increases by 12 dB when the length is reduced from 5 km to 1 km. This degradation agrees well with the phase noise deterioration of the VBO presented in Figures **4-6** and **4-10**. Additionally, all noise processes remain unchanged over the whole frequency range.

Following the same methodology, the behavior of the SVHFG phase noise can be evaluated when some variables, such as the power input amplifier, the RIN, and the VCSEL frequency noise, are modified. For the input electrical power of the first microwave amplifier, the phase noise is improved by increasing the electrical power, as shown in Figure **4-22 b.**. The predicted phase noise at 10 kHz from the carrier drops from -119 dBc/Hz to -137 dBc for a total power reduction of 20 dB (from -55 dBm to -35 dBm). This improvement is achieved because the far-from-carrier phase noise is dominated by the white noise of the first amplifier, which varies inversely with the input power (Equation 4-37). Concerning the close-to-the-carrier phase noise, higher electrical power produces a higher corner frequency, and the Leeson effect on the amplifier flicker noise is anticipated.

The RIN effect on SVHFG phase noise is depicted in Figure **4-22 c.**. For high-intensity noise levels (-110 dB/Hz), the phase noise close-to and far-from-the-carrier is deteriorated. This deterioration is caused because the RIN contribution exceeds the other noise sources, including the microwave amplifier noise. For low RIN values (< -130 dB/Hz), the phase noise remains unchanged owing to its reduced contribution.

Finally, Figure **4-22 d.** shows the effect of VCSEL frequency noise on phase noise. In
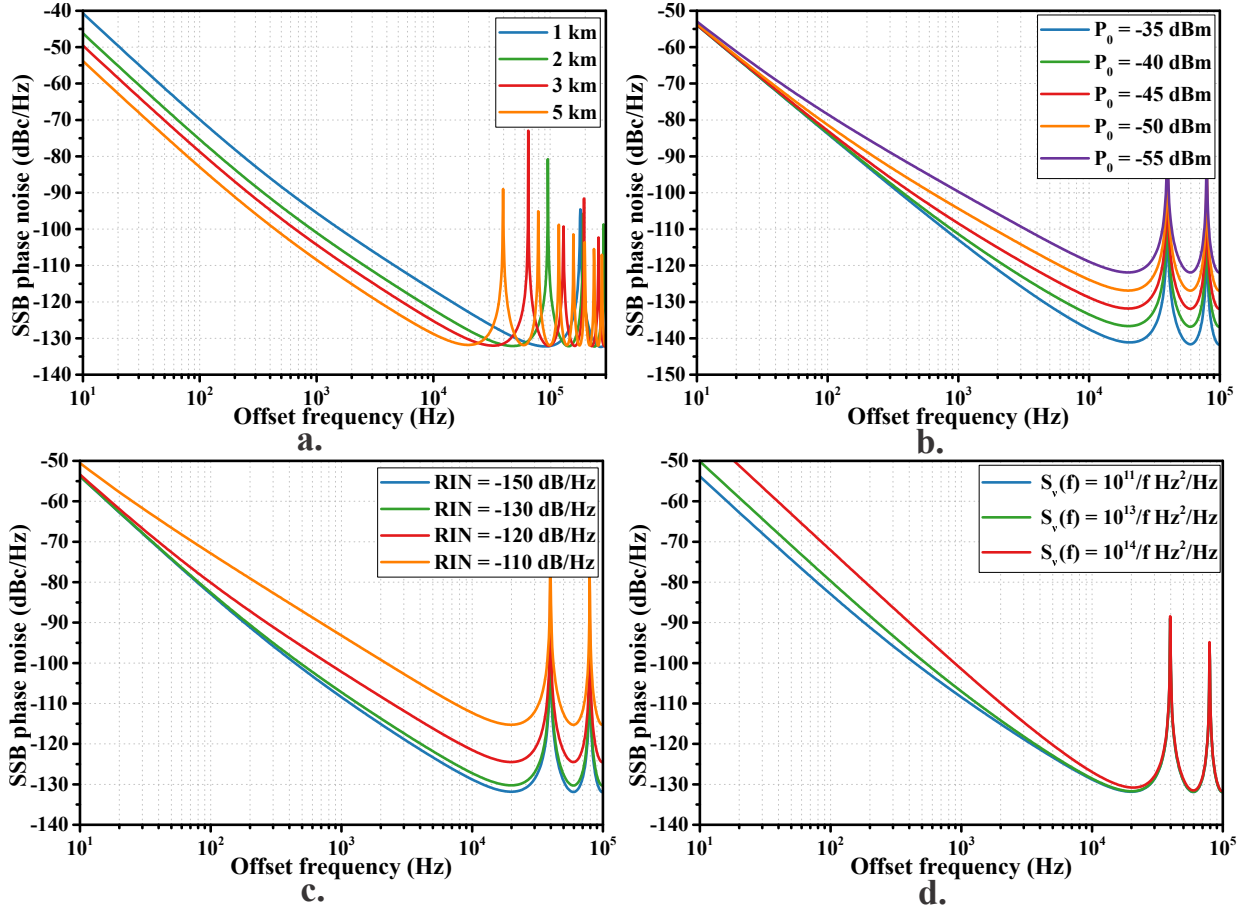
Figure 4-22.: Predicted phase noise by modifying **a.** optical fiber length, **b.** input power of the first microwave amplifier, **c.** VCSEL RIN, and **d.** VCSEL frequency noise.

all cases, the power spectral density of the frequency noise was assumed with a slope of -10 dB/dec. The reduction of the frequency noise from $1 \times 10^{14}/f$ to $1 \times 10^{11}/f$ Hz^2/Hz generates a non-representative improvement of the predicted phase noise of about 1.6 dB. The most outstanding effect occurs close to the carrier because the contribution of frequency noise exceeds the contributions of the RIN and the Leeson effect on the amplifier Flicker noise.

The predictive phase noise model is a tool for the verification or design of closed-loop systems which use a directly modulated laser source. The control of the input electrical power of the first amplifier is a determining factor for the reduction of phase noise. The impact of the white noise of the microwave amplifier is more significant than the optical fiber dispersion and the conversion process of the laser frequency noise. For this reason, the measurements presented for the two optical bands (C-band and O-band) have the same phase noise at 10 kHz from the carrier. Consequently, the SVHFG system can be improved by including a variable optical attenuator to control the input optical power in the photodetector and its output electrical power. This enhancement directly impacts the phase noise of the generated

microwave harmonics, which can be extracted and amplified through the simple use of a tuned filter and a reduced bandwidth microwave amplifier.

4.2.3.4. Time-domain stability

The time-domain stability of the SVHFG is performed using the Allan deviation and the overlapping Allan deviation (definitions presented in Chapter 1). The procedure consists in measuring the fractional frequency every τ seconds with a frequency counter during a specific time. Figure **4-23** shows the two Allan deviations of the fundamental frequency at 1.25 GHz of the C-band SVHFG. The fractional frequencies are measured every second for 60 hours. The confidence intervals are evaluated through a χ^2 distribution and the degrees of freedom are estimated assuming a dominant white frequency noise process ($n = -2$).

Both deviations allow the identification of the same three noise processes. Even though there is an equivalence between the phase noise curves and the Allan deviation, the three processes are not observed in the phase noise curves. This effect is mainly due to the limitations of the phase noise measurement method (direct method via an electrical spectrum analyzer) for frequencies below 100 Hz.
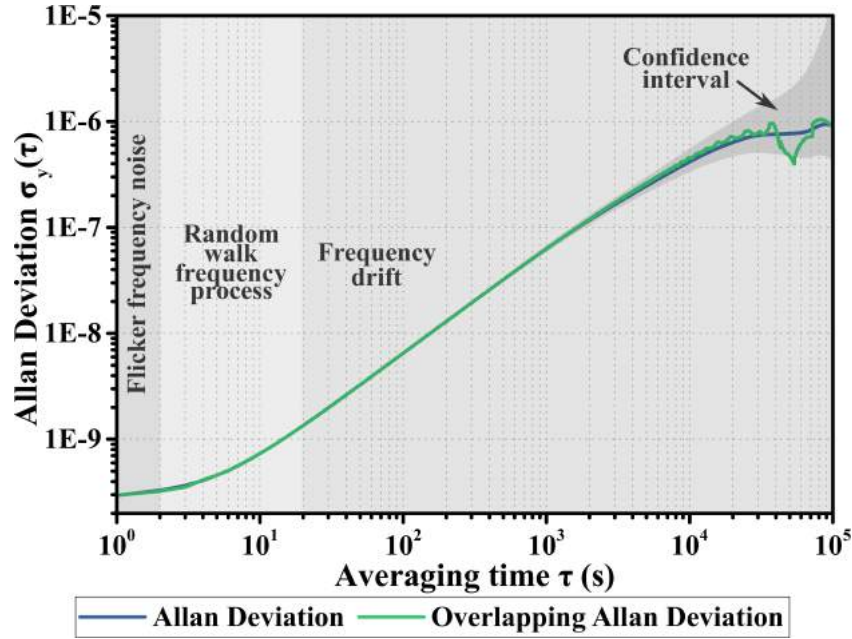
Figure 4-23.: Allan deviation of the O-band SVHFG at 1.25 GHz.

From left to right, the first process is Flicker frequency noise, which is characterized by a 0-slope (τ^0). This noise process vanishes quickly due to the predominant conversion process of the flicker noise from the amplifiers within the loop. The second process, called random walk frequency noise, has a $\tau^{1/2}$ slope and is attributed to the frequency and intensity noise (at low frequencies) of the VCSEL. Finally, frequency drifts have a slope proportional to

τ^1 and are caused by system temperature variations, mechanical vibrations, and aging of components. The gain-switched VCSEL contributes significantly to these frequency drifts owing to the temperature fluctuations of the active zone produced by the fast injection of carriers.

4.2.3.5. Carrier-to-noise measurements

As in any other optoelectronic oscillator, the microwave harmonics generated with the SVHFG can be extracted in both the electrical and optical domains. In the optical case, an optical coupler must be placed between the optical isolator and the optical delay line in the setup shown in Figure **4-14**. The optical pulses generated by the gain switching technique can be distributed through an optical fiber, and then the microwave harmonics can be recovered by a fast photodetector. The quality of these harmonics is affected by the noise contribution of the optoelectronic components included in the optical link. Figure **4-24** shows the setup used to verify the carrier-to-noise ratio (CNR or C/N) of microwave harmonics when C-band optical pulses are transmitted. Due to the reduced power of the VCSEL, the optical pulses are amplified by an erbium-doped fiber amplifier (EDFA) with a gain fixed at 20 dB. Then, a variable optical attenuator (VOA) allows modifying the input power of the photodetector PD2 to evaluate the impact of the input optical power on the electrical noise level.
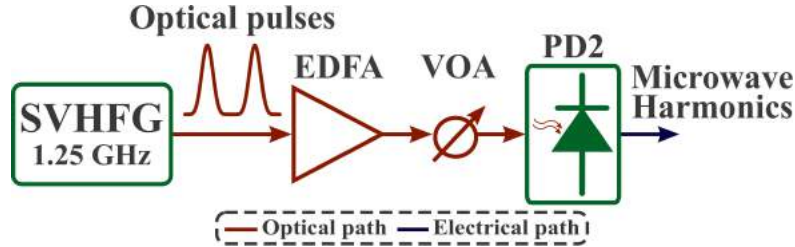
Figure 4-24.: Optical link for the microwave harmonics distribution.

The CNR of the optical link can be expressed as [268]:

$$CNR = \frac{I_{PD2}^2 \cdot (m^2/2)}{\frac{4kT}{R_{ph2}} + 2q \cdot I_{PD2} + RIN \cdot I_{PD2}^2 + \frac{2h\nu \cdot I_{PD2}^2 \cdot F}{P_{in-EDFA}}} \tag{4-42}$$

where I_{PD2} is the photodetected current, RIN is the VCSEL RIN at the frequency f_0, m the modulation index ($m > 0.1$ for large modulation), $4kT/R_{ph2}$ and $2q \cdot I_{PD2}$ are the thermal and shot noise on the photodetector PD2, respectively. The last term of the denominator represents the amplifier-generated excess intensity noise density with F the EDFA noise factor, $P_{in-EDFA}$ the optical power at the amplifier input, and R_{ph2} the load resistance. The noise factor contribution by the variable optical attenuator is zero [269].

For small I_{PD2} values, the floor noise is governed by the thermal noise, whereas for high

currents, the main contribution is given by the intensity noise of the optical amplifier. Thus, the variable attenuator controls both the noise floor level and the power of the fundamental frequency, i.e., the link CNR. Figure **4-25** shows the CNR measurement of the transmitted fundamental frequency and the first three harmonics for five different attenuations.
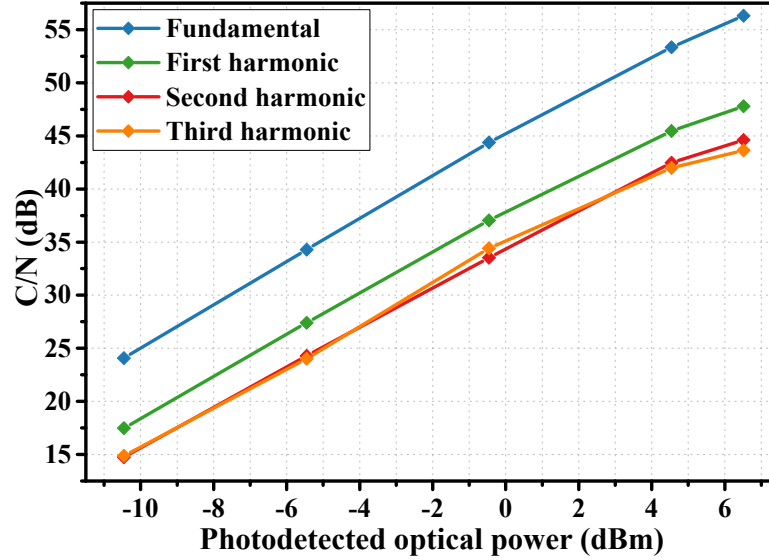
Figure 4-25.: CNR evolution at different photodetected powers.

As expected, the CNR of the fundamental frequency and harmonics is reduced when the photodetected optical power decreases. For all optical powers, the CNR of the fundamental is higher due to the higher power at this frequency (see Figure **4-18**). For both fundamental and harmonic frequencies, a total optical attenuation of 17 dB produces an average CNR deterioration of 30 dB. For harmonics at frequencies higher than 5 GHz, the carrier-to-noise ratio can deteriorate significantly due to the frequency response of the photodetector.

The phase noise floor of the harmonics can be determined from Equation 4-42. As for the CNR, the floor noise is dominated by the thermal noise for low received power and by the RIN laser for high power. In this sense, phase noise can be reduced by increasing the optical input power of the photodetector. Additionally, the performance of the phase noise is affected by the process of amplitude-to-phase conversion in the photodetector. To minimize this non-linear effect, the optical input power must be adjusted in order to reduce the electrical phase fluctuations caused by optical intensity fluctuations [270].

4.3. Conclusions

After introducing a comprehensive state of the art of microwave signal generation using optoelectronic devices in Chapter 1, the VCSEL-based optoelectronic oscillator (VBO) was discussed in detail in this chapter. The theoretical analysis includes open-loop and closed-

loop analysis and oscillation conditions. The VBO performance is experimentally validated for two different oscillation frequencies: 1.25 GHz and 2.5 GHz. In both cases, a phase noise improvement was evidenced by lengthening the optical fiber (resonant cavity). However, it was also proved that the timing jitter (estimated through TIE measurements) increases together with the fiber length due to a higher jitter contribution from additional non-oscillating modes. The phase noise curves are characterized by two noise processes: the white phase noise and the white frequency noise. The white phase noise is dominant far-from-the-carrier and is caused by the white noise of the microwave amplifier. The white frequency noise, with a slope of -20 dB/dec, results from the Leeson effect on the white noise of the amplifier.

Under varying temperature conditions, the VBO can conserve its oscillating condition. However, the phase noise is deteriorated due to the power difference inside the loop, which directly modulates the VCSEL. In contrast, phase noise remains constant under temperature variations as long as the power of the loop is constant.

The system proposed for microwave signal generation, called self-started VCSEL-based harmonic frequency generator (SVHFG), is based on a VCSEL modulated directly in gain switching regime. In the electrical domain, the signal is composed of several harmonics of the fundamental frequency determined by a band-pass filter. The phase noise degradation of the harmonics follows the same principle as any other frequency multiplication system. Frequencies above 10 GHz are reached with phase noise below -100 dBc/Hz.

The SVHFG predictive phase noise model uses a linear feedback system theory and the main additive and multiplicative noise sources. The simulation results agree well with the values obtained experimentally. Using the proposed model, it is possible to design harmonic generation systems according to the physical characteristics of the available optoelectronic components.

Finally, the optical output of the SVHFG is extracted from the system and transmitted through a simple optical transmission system. A photodetector recovers the electrical harmonics after passing through a variable optical attenuator that emulates the losses induced by the optical fiber. The CNR decreases with the optical power received at the photodetector due to the reduced power of each harmonic and the increase in floor noise related to the photodetected current. In terms of phase noise, the transmission system was not validated, but the harmonics are expected to deteriorate quickly due to additional noise sources, such as the amplified spontaneous emission (ASE) of the EDFA amplifier.

The following chapter presents a system for the optical pulse generation using the same principle as the SVHFG. In the frequency domain, the optical pulses correspond to an optical frequency comb, which is used as optical carrier for the transmission of phase and intensity-modulated data.

Chapter 5

Microwave signal generation for optical data transmissions

The generation of short optical pulses through large signal modulation of semiconductor lasers has been widely used since the 1980s. This technique is known as gain switching and was described in Chapter 2. The first gain-switched lasers were edge-emitting lasers at short wavelengths [271]. Subsequently, EE lasers at long wavelengths were used at higher repetition frequencies and shorter pulse durations [272, 273]. In the 90's the technique was applied to SW-VCSELs, and optical pulses of 19 ps and 24 ps duration were obtained at repetition frequencies of 0.5 GHz [274] and 8 GHz [275], respectively. The technological advances in the manufacture of VCSELs at large wavelengths allowed the generation of pulses with a duration of 11.5 ps and 55 ps at repetition frequencies of 10 GHz [248] and 3 GHz [247], respectively. One VCSEL advantage for pulse generation is the reduced size of the active region and, therefore, the small photon lifetime, which impacts the minimum achievable pulse duration.

Even though the GS technique was initially conceived for the generation of short optical pulses, it is currently used for the optical frequency combs (OFC) generation. During the last years, the OFC generation has emerged as a research topic of particular interest with a wide variety of applications such as spectroscopy [276], THz generation [277], LIDAR [278], and optical communications [279, 280]. The GS technique has received special attention over other OFC generation techniques (mode-locking and electro-optic modulation) owing to its high flexibility, easy implementation, and low losses [253]. The frequency combs generated through GS of semiconductor lasers are characterized by high efficiency, high correlation between modes, and good tunability characteristics [281]. The VCSELs have been used for the gain-switched OFC generation owing to their low threshold currents and single-mode transverse emission. Some studies have shown that VCSEL-based OFCs produce energy-efficient and high mode coherence combs [282]. Besides, some authors have described theoretically and experimentally the polarization dynamics of OFCs generated from VCSELs that emit a transverse mode with two orthogonal polarizations [235, 283].

This chapter presents the experimental results of the generation of optical pulses and OFCs using a GS-modulated C-band VCSEL. The optical system output, called self-started VCSEL-based optical frequency comb generator (SVOFC), is used as an optical source for data modulation at different bit rates.

5.1. Self-started VCSEL-based optical frequency comb generator (SVOFC)

The self-started VCSEL-based optical frequency comb generator (SVOFC) allows the optical pulse generation at a repetition frequency f_0 through a closed-loop self-starting system. The resonant cavity system, consists of a single-mode optical fiber with length L, quality factor $Q = \pi \cdot f_0 / FSR$, and free-spectral range $FSR = c/(n_f \cdot L)$ (n_f refractive index). The noise provided by the components initiates the self-sustained oscillation. The optical pulses are generated by direct modulation of a VCSEL in gain-switching condition. The spectral purity of the modulating signal, which can be extracted from the loop just before modulating the VCSEL, is influenced by the quality factor of the resonant cavity. In the time domain, the optical output of the SVOFC consists of optical pulses with amplitude A_p and full-width at half-maximum FWHM. The same optical output in the frequency domain corresponds to an optical frequency comb (OFC).

The OFC generated are characterized by the envelope flatness defined as the ratio of total tones at 10 dB from the highest optical power tone to the total tones at 20 dB,

$$Flatness = \frac{\#\ tones\ at\ 10\ dB}{\#\ tones\ at\ 20\ dB} \tag{5-1}$$

Additionally, the spectral widths at 10 dB Δf_{10} and 20 dB Δf_{20} are also analyzed in order to evaluate the profile widening under different electrical conditions.

The optical characteristics of the OFC depend on the fundamental frequency f_0, the driving signal power, and the bias current of the VCSEL. As with a simple GS system, the f_0 frequency must be carefully selected according to the physical characteristics of the laser and must be higher than the relaxation frequency f_R. In this way, the first spike of the transient relaxation oscillations is guaranteed and, consequently, the reduction of the pulse duration (FWHM).

5.1.1. SVOFC architecture

The architecture of the SVOFC is shown in Figure **5-1**. The VCSEL optical output is connected to an optical isolator to avoid back reflections. The optical pulses are extracted by one arm of a variable ratio optical coupler (VROC) and reinjected into the system by the other arm. Then, the optical pulses are photodetected and microwave harmonics are

generated at frequencies multiples of f_0. The fundamental frequency harmonic is amplified with a microwave amplifier and filtered by a band-pass filter centered at f_0. Finally, the loop is closed with the microwave signal by modulating the VCSEL directly through a bias-tee. The modulating electrical signal can be extracted via an electrical coupler (EC). An electrical attenuator is included to ensure the loop gain and gain switching condition.

The variable-ratio of the VROC allows the optical power adjustment at the photodetector input and consequently, the electrical power at the input of the microwave amplifier. As discussed in Chapter 4, the phase noise floor of the fundamental frequency is dominated by the white noise of the amplifier, which can be reduced by increasing its electrical input power.
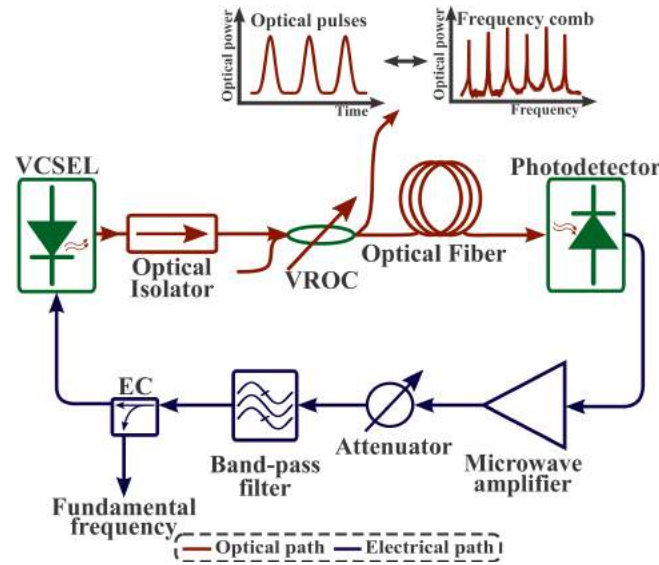
Figure 5-1.: Self-started VCSEL-based optical frequency comb generator architecture.

5.1.2. SVOFC simulations

The C-band SVOFC simulation using a computer-aided design (CAD) software allows verifying the behavior of the generated optical and electrical signals under specific conditions and component characteristics. Figure **5-2** shows the simulation schematic used in VPIphotonics Design Suite$^{\text{TM}}$. The C-band VCSEL is simulated by a single-mode rate equation based VCSEL model configured according to the intrinsic parameters extracted in Chapter 3 and listed in Table **3-4**. The optical fiber consists of an optical delay and a transmission mode Fabry-Perot (FP) filter responsible for the free spectral range and the non-oscillating modes of the electrical signal. For all simulations presented in this section, the non-linear effects of the optical fiber are neglected. The photodetection process is performed with a PIN type photodetector, which includes thermal and shot noise. The amplification stage is divided into two: a first low noise amplifier (LNA) responsible for establishing the white

noise level (dominant noise of the SVOFC white noise process) and the second amplifier of higher gain for establishing the power level required to guarantee the GS regime. The total electrical gain is continuously modified to simulate the electrical power variations generated by the electrical attenuator in the experimental implementations. The white phase noise of both amplifiers was assumed constant at -120 dB/Hz. Finally, the filter is modeled with a fourth-order Bessel filter centered at the desired fundamental frequency. The pulses and the optical spectra are analyzed by an optical analyzer placed at the VCSEL output. The electrical signal is composed of the noise level coming from the first microwave amplifier and the filtered and amplified fundamental frequency. Several simulations are needed to obtain the required electrical power for modulating the VCSEL in GS condition. In this sense, special attention must be considered because, for each simulation, the amplifiers contribute to the floor phase noise level (additive Gaussian white noise).
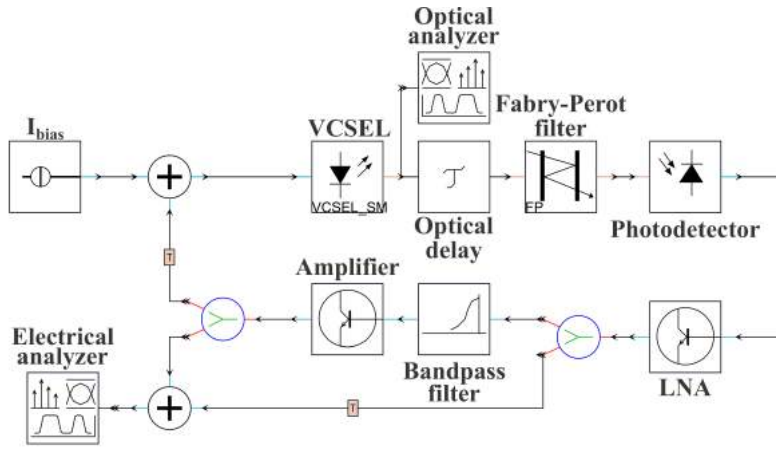
Figure 5-2.: VPI schematic for simulating the C-band SVOFC.

For all simulation cases, the C-band VCSEL is biased at the same current $I_{bias} = 6$ mA. The fundamental frequencies f_0 are selected considering the relaxation resonance frequency of the VCSEL used during the experimental characterization, which is estimated to be $f_R = 2.1$ GHz. Hence, lower ($f_0 = 1.25$ GHz) and higher ($f_0 = 2.5$ GHz) frequencies were considered. The impact of the optical delay line length on the generated signals is adjusted through the FSR of the FP filter and the optical delay time τ_o. For $L = 1$ km, the simulated FSR is 200 kHz and $\tau_o = 5$ μs, whereas for $L = 2$ km, the simulated values are $FSR = 100$ kHz and $\tau_o = 10$ μs. Figure **5-3** shows the normalized waveform of the simulated optical pulses for both optical fiber lengths when $f_0 = 1.25$ GHz. The simulation boundary conditions are set to aperiodic because the laser module generates several blocks (sampled signal) for each simulation run. The aperiodic condition guarantees the visualizers update for each data block. To achieve the GS regime when $FSR = 200$ kHz, it is necessary to compensate for the additional optical losses provided by the FP filter. These losses are caused by the change of the passband width (directly related to FSR) and the temporal analysis of the optical signal using a windowed finite pulse response filter (FIR) for aperiodic conditions. Consequently, the total electrical gain for $FSR = 200$ kHz is 3 dB higher than for $FSR = 100$ kHz.
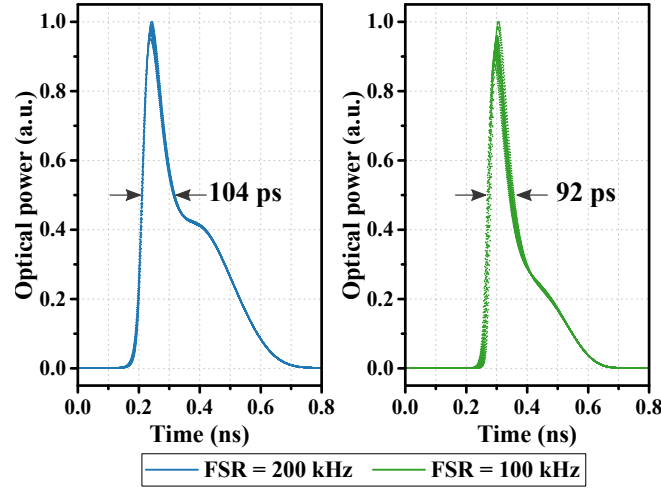
Figure 5-3.: Simulated optical pulses of the C-band SVOFC at 1.25 GHz using $FSR = 200$ kHz and $FSR = 100$ kHz.

The waveform of the two simulated pulses consists of a sharp peak and a variable-amplitude bump. The bump is because the injected carrier density drops off abruptly after the second spike of the transient laser response. This effect can be eliminated by modulating the VCSEL at frequencies higher than the relaxation frequency. The bump amplitude in the case of $FSR = 200$ kHz is more prominent because more recombination processes are performed during each period. Similarly, the FWHM pulse width increases for higher modulating powers, rising from 92 ps to 104 ps. Even though the pulse jitter is not determined, it is evident that the jitter decreases when the electrical power increases. This jitter reduction is produced by the reduction of the turn-on delay distributions at high powers [284]. The behavior of the simulated optical pulses is consistent with the characterization of optical pulses generated when a semiconductor laser is modulated in the GS condition [247, 253].
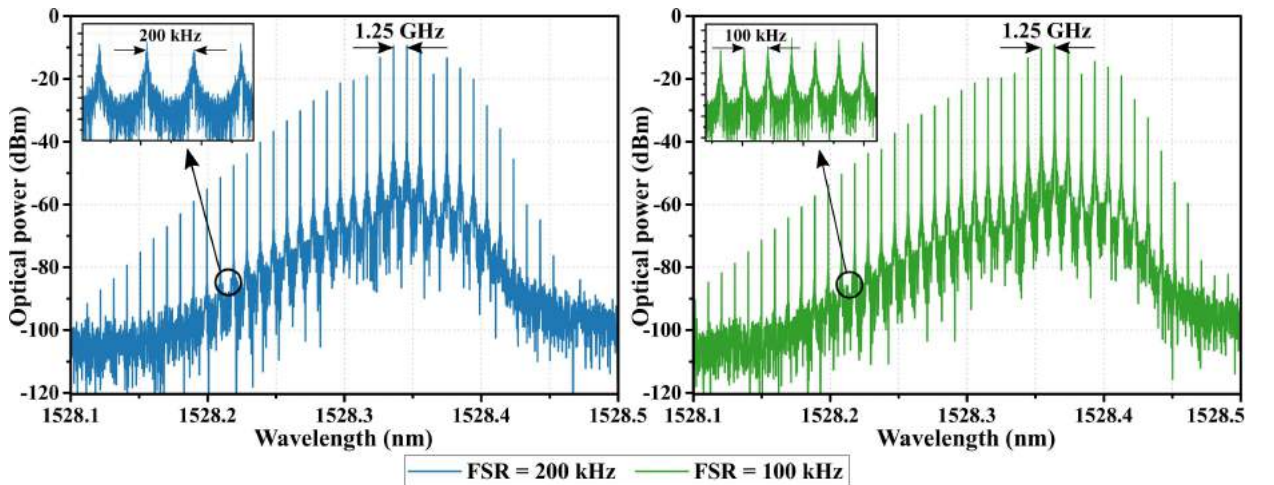
Figure 5-4.: Simulated optical spectra of the C-band SVOFC at 1.25 GHz using $FSR = 200$ kHz and $FSR = 100$ kHz.

Regarding the optical spectra shown in Figure **5-4**, in both cases, the spectrum is asymmetrical around the primary tone with the highest optical power. The distance between the secondary tones corresponds to the fundamental frequency $f_0 = 1.25$ GHz. The spectral width at 30 dB from the primary tone is 21.2 GHz and 23.5 GHz for $FSR = 200$ kHz and $FSR = 100$ kHz, respectively. Considering the spectral asymmetry and the decreasing power of the secondary tones, the flatness of the two optical frequency combs is low (0.58 on average). Figure **5-4** insets show the effect of the resonant cavity on the modulated optical signal. In each case, a frequency sub-comb is observed with a distance between tones equal to the FSR value. This recognition can only be performed in a simulation environment because there are no commercially available optical spectrum analyzers with a small resolution (some kHz).

When $f_0 = 2.5$ GHz and $FSR = 100$ kHz, the optical pulse depicted in Figure **5-5 a.** consists of the first spike and its FWHM width is 78 ps. The reduction of the pulse duration compared to the 1.25 GHz SVOFC is caused by the faster decrease of the carrier density and the absorption of the photons inside the active region. The optical spectrum of the OFC shown in Figure **5-5 b.** is wider (63 GHz at 30 dB) and flatter (0.8) than the case of 1.25 GHz SVOFC.
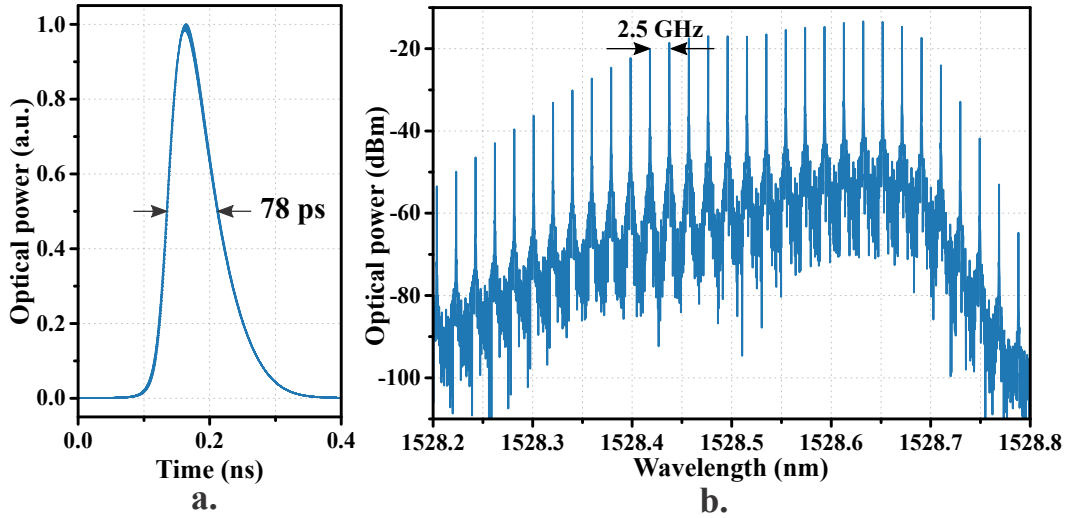
Figure 5-5.: a. Optical pulse and **b.** optical spectrum of the simulated C-band SVOFC at 2.5 GHz.

Through the simulation results, it is demonstrated that the optical output features of the SVOFC depend directly on the electrical power and the frequency of the modulating signal. Sharper pulses and flatter OFCs are obtained at modulation frequencies higher than the laser relaxation frequency.

Finally, the fundamental frequency of the 1.25 GHz SVOFC is analyzed using its spectrum (Figure **5-6 a.**) and phase noise (Figure **5-6 b.**) for the two FSR values. The electrical spectra consist of a power oscillation mode dominant over non-oscillating modes spaced according to the selected FSR. The power levels are -8.7 dBm and -5.2 dBm for $FSR = 200$

and $FSR = 100$ kHz, respectively. As expected, the phase noise at 10 kHz from the carrier is improved by 13 dB when the FSR passes from 200 kHz (-116 dBc/Hz) to 100 kHz (-129 dBc/Hz). Figure **5-6 b.** shows that the white noise processes are at the same level due to the white noise is contributed by the microwave amplifiers. The phase noise close-to-the-carrier can be determined more accurately by increasing the sample rate and the time window of the simulation.
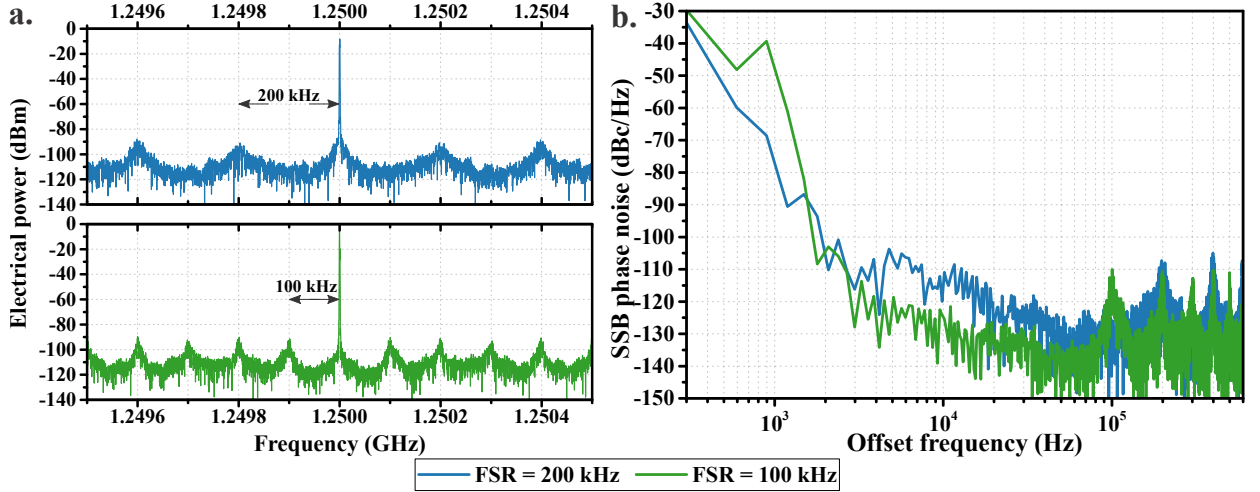
Figure 5-6.: a. Electrical spectra and **b.** simulated SSB phase noise of the C-band SVOFC at 1.25 GHz.

5.1.3. SVOFC experimental characterization

The SVOFC is implemented according to the architecture depicted in Figure **5-1**. The optical pulses generated using C-band and O-band VCSELs are characterized with a 8.5-GHz bandwidth oscilloscope (Keysight DCA-X 86100D). The optical coupler (F-CPL Newport) allows a very precise adjustment of the coupling ratio from 0 to 100%. The resonant cavity consists of different single-mode SMF-28e+ optical fiber lengths. A photodetector with 17 GHz bandwidth and 0.94 A/W responsivity is used. The gain of the wideband amplifier is 38 dB. Considering the VCSEL bandwidth and the relaxation resonance frequency, two cavity filters tuned at 1.25 GHz and 2.5 GHz are included. The optical frequency combs are characterized with a high resolution (10 MHz) Brillouin optical spectrum analyzer (BOSA) (Aragon Photonics BOSA 400). The spectral quality of the fundamental frequency is measured by an electrical spectrum analyzer ESA (R&S FSW50).

5.1.3.1. Optical pulses

The optical pulse waveforms at a repetition frequency of 1.25 GHz and an optical fiber length of 1 km are presented in Figure **5-7**. The bias current I_{bias} is ranged from 5 mA

to 8 mA for each VCSEL. The optical coupler generates supplementary attenuations to the O-band implementation, leading to a difference in pulse amplitudes. In both cases, the pulse amplitude increases with I_{bias} until it reaches a maximum point, 6 mA for the C-band SVOFC and 8 mA for the O-band SVOFC. When the bias current increases, the power inside the loop increases as well, and therefore the VCSEL is modulated with a higher peak-to-peak current. After reaching the maximum point, the bias current and the modulating microwave signal produce a heating effect of the active region [285] that degrades the laser response and reduces the pulse optical power.
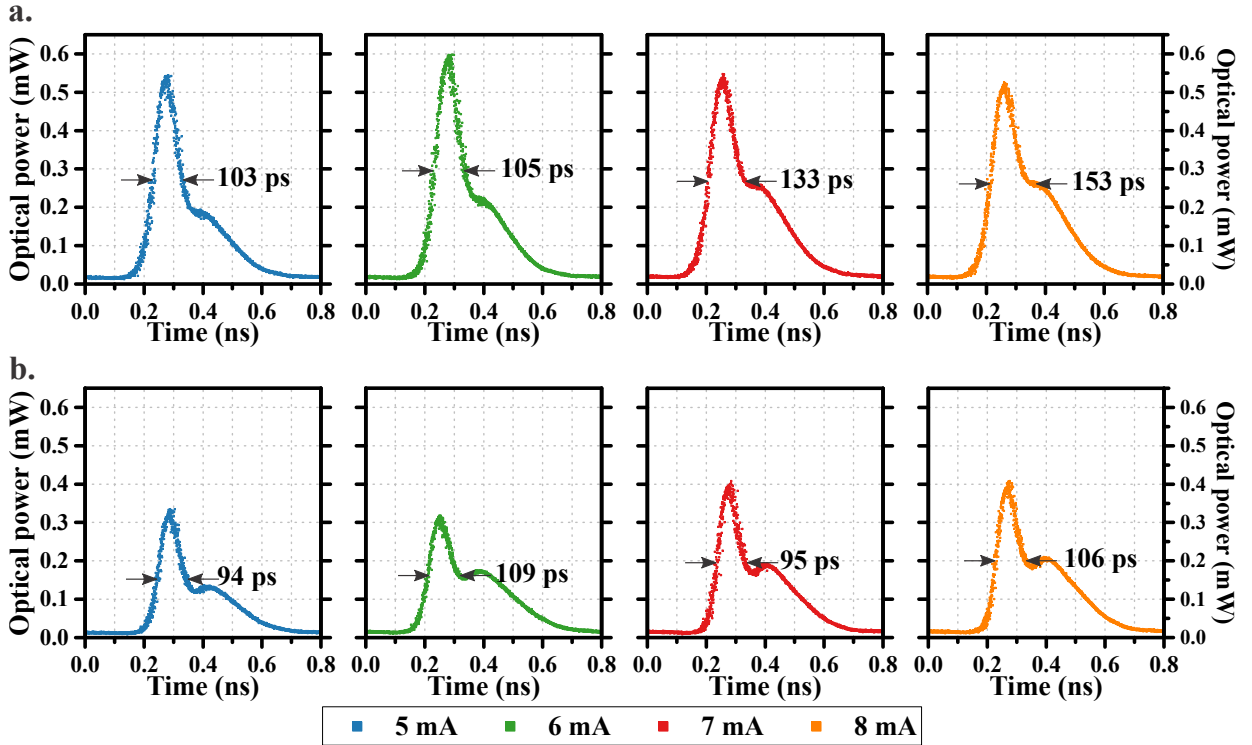
Figure 5-7.: Optical pulses at 1.25 GHz using **a.** C-band **b.** O-band VCSEL.

The waveform of all pulses includes a bump corresponding to the second peak of the transient relaxation response. The bump amplitude increases at higher bias currents because the total current applied per period is above the threshold for a longer time. In other words, the lasing process is turned off after the occurrence of the second spike, and consequently, the pulse is widening. This effect is most evident in the C-band SVOFC case (Figure **5-7 a.**) since the FWHM rises by 50 ps from 5 mA to 8 mA. Even though the second spike of the O-band SVFOC is more pronounced (Figure **5-7 b.**), the higher pulse amplitude results in a stable FWHM. When the optical fiber length is 2, 3, and 5 km, the power inside the loop must be adjusted through the VROC to conserve the gain switching and oscillating condition. In this process, the pulse waveform is preserved, but the amplitude and width are modified according to the electrical power level set to achieve oscillation.

The time interval error (TIE) of the optical pulses is measured and decomposed into random

(RJ) and deterministic jitter (DJ) through an oscilloscope. The number of samples is set at 10,000 rising edges to guarantee the same measurement conditions. The RJ evolution for different polarization current values is presented in Figure **5-8**. The statistics shown (mean value and standard deviation) are determined from several measurements for different optical fiber lengths. In the C-band SVOFC (Figure **5-8 a.**), the RJ decreases due to the reduction of the turn-on delays produced in turn by the higher I_{bias} and modulating power levels [247]. From $I_{bias} = 8$ mA, the RJ rises owing to thermal effects in the cavity. The average RJ value of the O-band SVOFC (Figure **5-8 b.**) shows a linear trend throughout the current range since the VCSEL response (frequency and optical power output) is preserved for high bias currents. Despite the described differences and the measurement uncertainty, the RJ of both implementations varies between 2.2 ps and 4.5 ps.
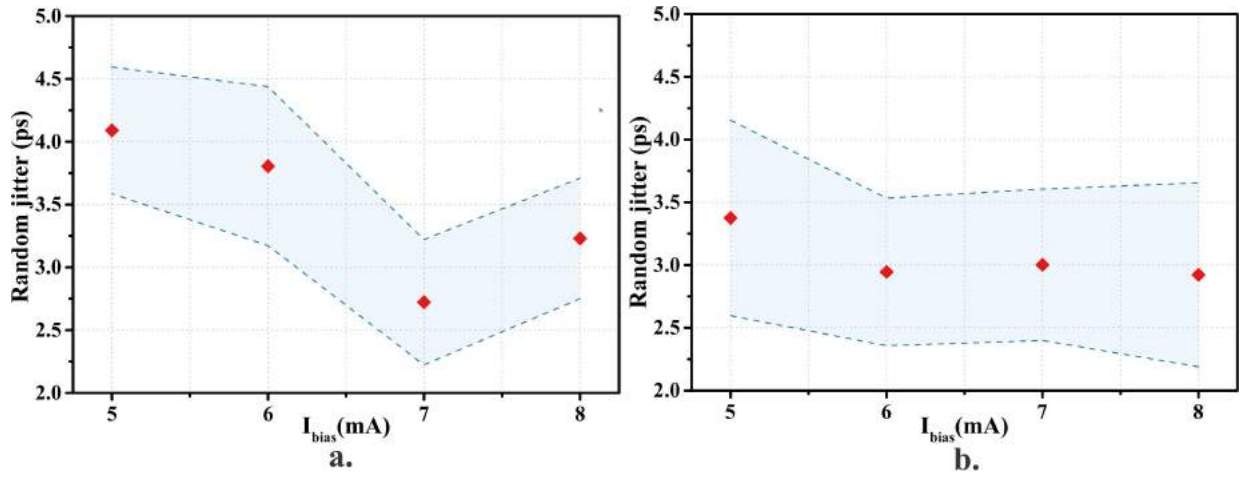
Figure 5-8.: Random jitter of optical pulses at 1.25 GHz using **a.** C-band **b.** O-band VCSEL.

The normalized waveforms of the optical pulses generated at 2.5 GHz and different fiber lengths are depicted in Figure **5-9**. For this repetition frequency, the polarization current is fixed at 6 mA for both VCSELs. The photodetected power for each implementation is fixed through the VROC, and thereby the modulating signal power is constant. Unlike the 1.25-GHz optical pulses, the 2.5-GHz pulses are composed only by the first spike of the transient response because the lasing action is turned off before the occurrence of the second spike. Under constant electrical conditions (I_{bias} and modulating power), the pulse width remains constant for each VCSEL and is independent of the optical fiber length. The slight difference between the C-band SVOFC pulse duration (85 ps) and the O-band SVOFC (76 ps) is attributed to the difference of VCSEL photon lifetimes.

The TIE histograms of the optical pulses obtained at 2.5 GHz for four optical fiber lengths using a C-band VCSEL are plotted in Figure **5-10**. Each histogram includes 100,000 samples taken under the same electrical loop conditions. In all cases, the jitter clearly shows a Gaussian behavior, which allows estimating the RMS random jitter by its standard deviation. Even though the value for $L = 3$ km is higher (3.44 ps), the RMS RJ can be considered

a.

b.
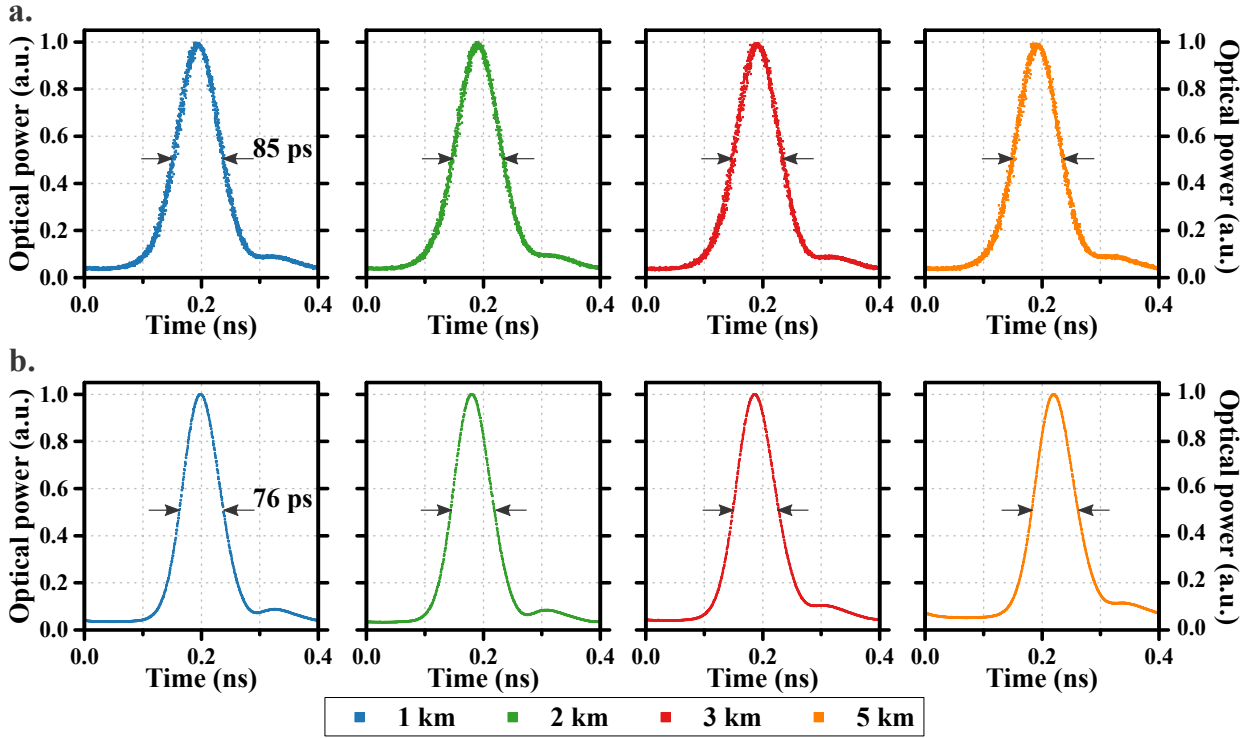
Figure 5-9.: Optical pulses at 2.5 GHz using **a.** C-band **b.** O-band VCSEL.

constant in all cases with an average value of 3.1 ps. The same behavior is observed for the O-band SVOFC, with an average value of 2.4 ps. Smaller RMS RJ values can be obtained by measuring 10,000 samples, as indicated in the JEDEC 65B standard [286].
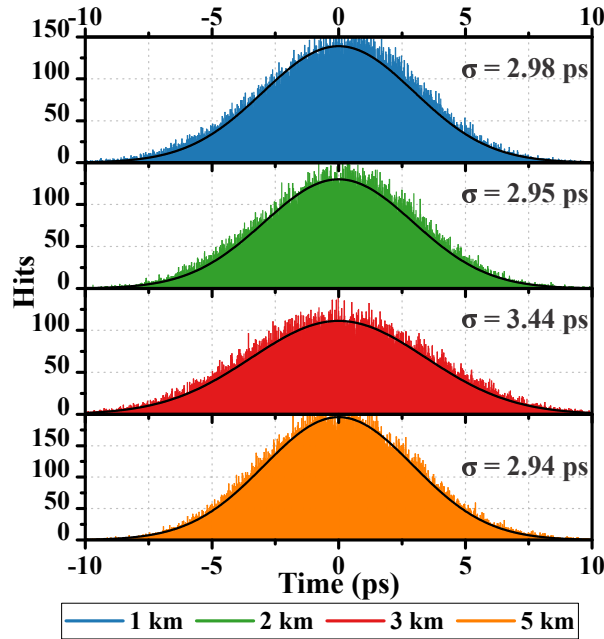
Figure 5-10.: TIE histograms of optical pulses at 2.5 GHz using a C-band VCSEL.

The implemented SVOFCs show that the optical pulse features depend on the physical characteristics of the VCSEL, such as the active region volume and the photon lifetime, and on the electrical conditions applied to modulate the laser in GS condition. The implementation results agree well with the behavior observed in the VPI simulations. This agreement is achieved because the VCSEL model is based on the rate equations that consider the thermal effects inside the active region. Additionally, the simulated VCSEL module is configured with the intrinsic parameters of the VCSEL used in the experimental characterization.

5.1.3.2. Optical frequency combs

Figure **5-11** presents the optical spectra of the pulses generated by the C-band SVOFC at 1.25 GHz for a fixed fiber length ($L = 1$ km) and different bias conditions (pulses presented in Figure **5-7**). The spectra have an asymmetric envelope with a marked decrease at higher wavelengths (right side) and suppressed tones. This spectrum asymmetry is induced by the frequency chirp of the large-signal modulation (amplitude-phase coupling of the laser). Tone suppression is induced by the effect of the frequency modulation (FM) produced either by the effect of carrier density modulation or by temperature variations [287].
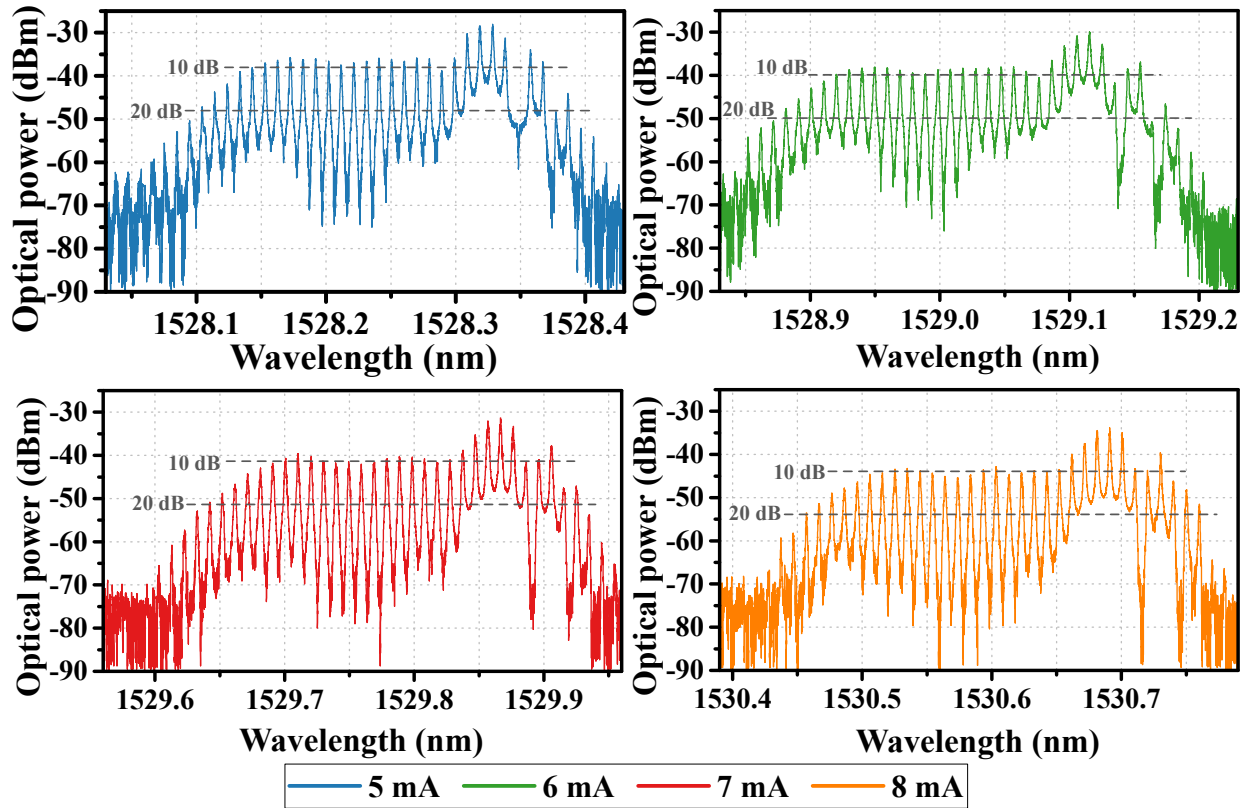
Figure 5-11.: Optical spectra of the C-band SVOFC at 1.25 GHz and different I_{bias} currents.

The optical spectra width measured at 30 dB from the highest power is 42 GHz ($\sim$ 0.33 nm) for all the implementations. This spectral width is constant since the electrical power used to modulate the VCSEL varies slightly. For lower electrical powers, adjusted through a variable electrical attenuator, the spectral width of the frequency comb decreases, whereas for higher powers, the width is enlarged until it reaches the maximum. Although a wider optical frequency comb may be desired, high electrical powers can lead the SVOFC into a frequency doubling status [288], deteriorating system performance in the optical and electrical domains.

The combs generated from the SVOFC are characterized according to their flatness using Equation 5-1 and to the 10 dB and 20 dB spectral width (Δf_{10} and Δf_{20}). Table **5-1** summarizes the results of the C-band SVOFC with $L = 1$ km. The OFC flatness deteriorates from 0.75 to 0.42 as an effect of the increasing electrical power inside the loop caused by the bias current augmentation from 5 mA to 8 mA. This deterioration is attributed to the "vanishing" of secondary tones in the middle of the comb profile. The Δf_{10} and Δf_{20} do not vary representatively because the tones at the edges are conserved. Even if a 0.75 flatness is achieved, the SVOFC performance at 1.25 GHz is limited by the effect of the frequency chirp.

Table 5-1.: Summary of optical frequency combs generated by the C-band SVOFC at 1.25 GHz and $L = 1$ km.

I_{bias} (mA)	# tones at 10 dB	# tones at 20 dB	Flatness	Δf_{10}	Δf_{20}
5	21	28	0.75	27.47	36.22
6	21	29	0.72	28.82	37.55
7	13	30	0.43	26.30	36.19
8	13	31	0.42	26.23	38.78

The C-band SVOFC at 1.25 GHz was also implemented using different fiber lengths and bias currents. The evolution of the flatness, Δf_{10}, and Δf_{20} are presented in Figure **5-12**. Concerning the flatness (Figure **5-12 a.**), all 3 cases do not overcome the value obtained by $L = 1$ km (0.75 for $I_{bias} = 5$ mA). Although the highest flatness values are achieved at 5 and 6 mA, two flatnesses below 0.3 occur at 6 and 7 mA owing to the lower number of tones in the first 10 dB span. This tone reduction is caused by the lower modulating electrical power (about 2 dB below) required to ensure the oscillating condition and controlled by the tunable electrical attenuator and the VROC. The Δf_{10} spectral width depicted in Figure **5-12 b.**, varies between 21.2 and 28.7 GHz for all the I_{bias} values and fiber lengths, excluding the two values for which the spectral width is reduced by the low modulating electrical power ($L = 3$ km and $L = 5$ km). Finally, the Δf_{20} spectral width (Figure **5-12 c.**) ranges from 28.9 GHz to 37.5 GHz, except for $L = 5$ km and $I_{bias} = 7$ mA where Δf_{20} is 22.46 GHz.

The evolution of the SVOFC features at 1.25 GHz will depend on the electrical modulation conditions of the VCSEL. Therefore, by controlling the photodetected optical power and the modulating electrical power, it is possible to improve the profile flatness and enhance the
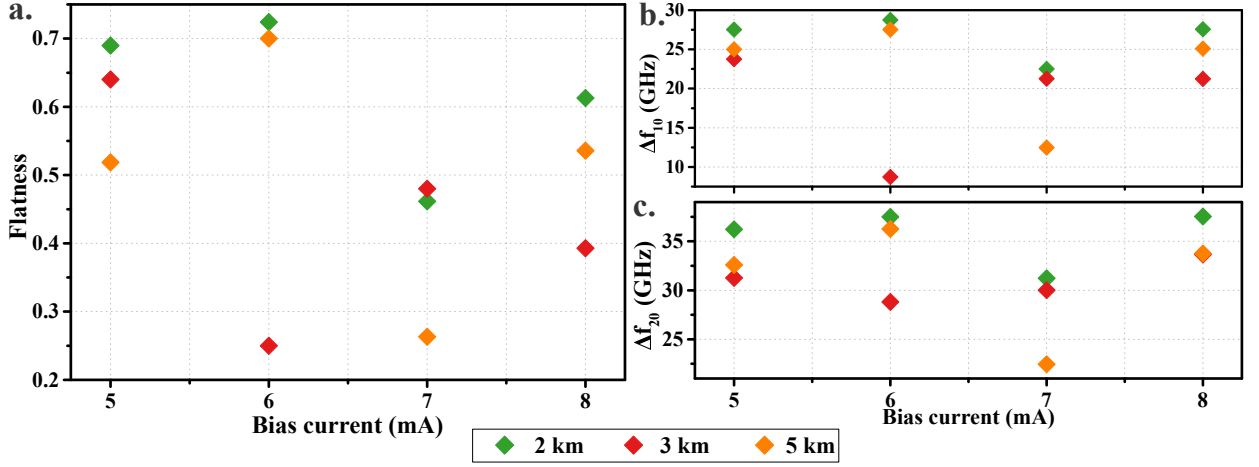
Figure 5-12.: a. Flatness, **b.** Δf_{10}, and **c.** Δf_{20} evolution of the C-band SVOFC using different fiber lengths and bias currents.

Δf_{10} and Δf_{20} spectral widths for a constant fundamental frequency (repetition frequency) f_0.

Figure **5-13** shows the optical spectra of the C-band SVOFC at 2.5 GHz and a constant I_{bias}. Although the comb envelope remains asymmetrical, the mid-tones are not suppressed. The spectral width is 50 GHz measured at 30 dB from the peak power for all fiber lengths. This value is constant because the electrical modulation conditions are guaranteed to be the same. The non-suppression and the modulation conditions result in a flatter profile in comparison to the one obtained for the C-band SVOFC at 1.25 GHz. Table **5-2** condensates the performance of the OFCs generated. The flatness in all four cases is higher than 0.84, exceeding the performance of the C-band SVOFC at 1.25 GHz (Table **5-1**). The highest difference between the Δf_{10} spectral widths is 2.5 GHz, whereas for Δf_{20} is 5 GHz. It means that the highest variation is given by the occurrence of two supplementary tones when $L = 1$ km and $L = 3$ km. Additionally, the CNR measured in a 10 dB span is higher than 25 dB in all cases, whereas at 1.25 GHz implementation, several tones do not exceed a CNR of 15 dB (Figure **5-11**).

It has been experimentally demonstrated that the performance of the optical frequency comb generated with the SVOFC is related to the bias current, the modulating electrical power, and the repetition frequency determined by the band-pass filter. For frequencies close to the VCSEL relaxation frequency f_R, the OFC envelope is less flat owing to the tone suppression during the first 10 dB span (8 suppressed tones). In contrast, for higher frequencies, the spectral width of the envelope is constant and its profile is flatter. It is worth pointing out the importance of controlling the electrical conditions inside the loop to guarantee better performance. Hence, when the polarization current increases, the modulating electrical power must increase to deplete the carriers and enhance the photon absorption in the cavity [253]. A wider comb is obtained by increasing the electrical loop power. After reaching the broadest spectral width, non-linear effects appear, such as the frequency doubling operation. These effects must be minimized to avoid deterioration of the electrical SVOFC performance.
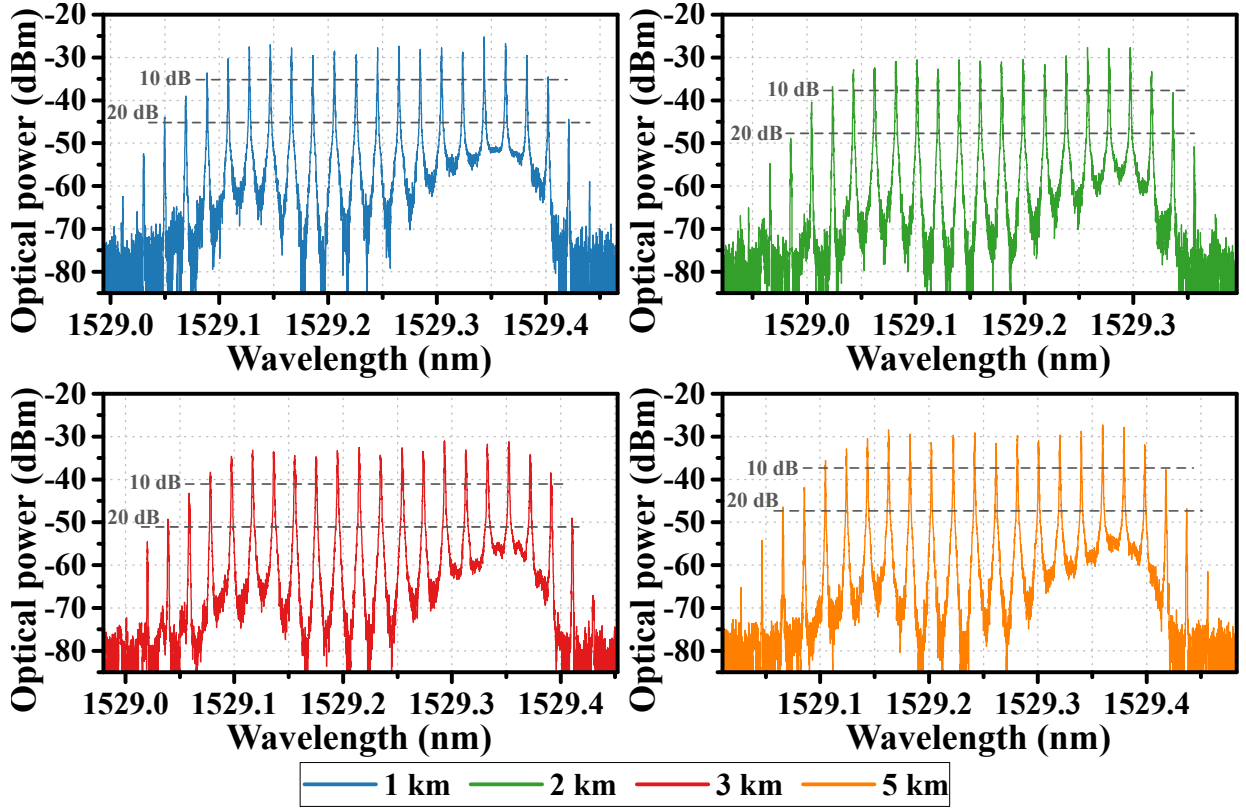
Figure 5-13.: Optical spectra of the C-band SVOFC at 2.5 GHz and different fiber lengths.

Table 5-2.: Summary of optical frequency combs generated by the C-band SVOFC at 2.5 GHz.

Fiber length (km)	# tones at 10 dB	# tones at 20 dB	Flatness	Δf_{10}	Δf_{20}
1	17	20	0.85	40.18	47.60
2	16	18	0.89	37.60	42.57
3	17	20	0.85	40.12	47.61
5	16	19	0.84	37.63	45.12

5.1.3.3. Spectral purity of fundamental frequency

The spectral purity of the fundamental frequency f_0 is determined by measuring the phase noise for four optical fiber lengths. Figure **5-14** shows the phase noise of the C-band and O-band SVOFC at 1.25 GHz for $L = 1$ km and $L = 5$ km. For $L = 1$ km (Figure **5-14 a.**), the curves overlap over most of the observed frequency range, and the phase noise at

10 kHz from the carrier is -115 dBc/Hz. This curve superposition shows that the optical fiber dispersion (zero in O-band) does not impact the SVOFC phase noise behavior. The four slopes illustrated in Figure **5-14 a.** correspond to four noise processes produced by additive and multiplicative noise contributed by the system components. From right to left, the white phase noise is the first process and is governed by the white noise of the microwave amplifier (if the other noise source contributions are lower, such as the VCSEL RIN at the oscillation frequency). With a -20 dB/dec slope, the white frequency noise process is caused by the Leeson effect on the white noise of the microwave amplifier. The phase noise curve is followed by a noise process with a slope of -25 dBc/Hz, caused by multiplicative noises (e.g., the VCSEL frequency noise and the VCSEL RIN at low frequencies) and the Rayleigh scattering contribution. The last process is the Flicker frequency noise and results from the Leeson effect on the amplifier flicker noise at frequencies below its corner frequency f_c.
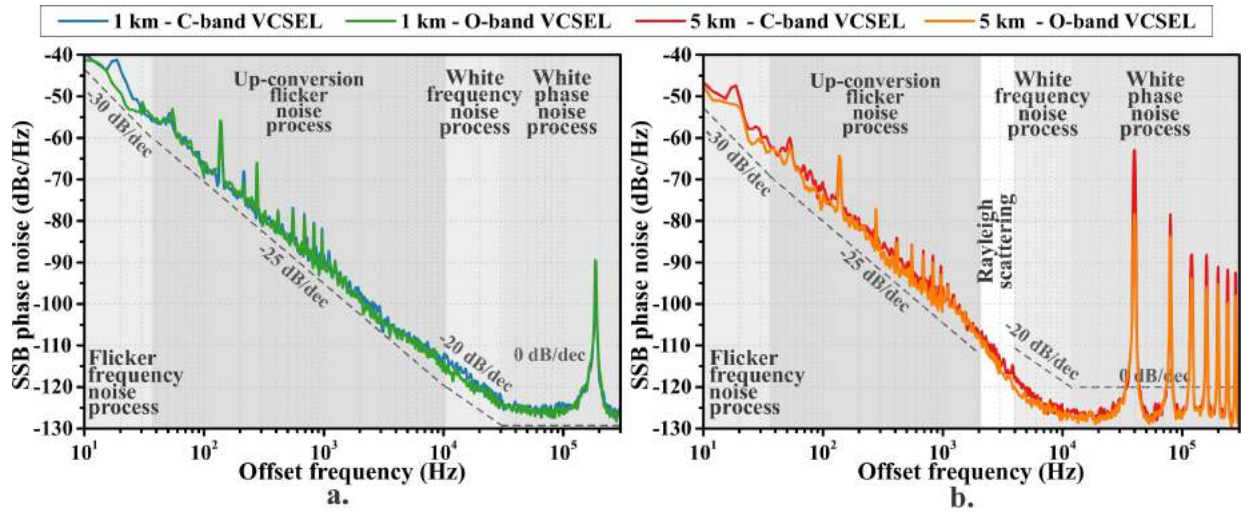
Figure 5-14.: Phase noise curves of the fundamental frequency at 1.25 GHz for **a.** $L = 1$ km, **b.** $L = 5$ km.

In the case of $L = 5$ km, Figure **5-14 b.**, the phase noise is improved by about 12 dB as an effect of the quality factor Q of the resonant cavity. Thus, the phase noise at 10 kHz from the carrier is -126 dBc/Hz and -127 dBc/Hz for the C-band SVOFC and O-band SVOFC, respectively. Non-oscillating modes are closer to the carrier (FSR reduction when fiber increases), resulting in higher RMS phase jitter. The same four noise processes are identified in the curves. Nevertheless, between 2 and 4 kHz, there is a pronounced transition generated by the higher Rayleigh scattering effect in long optical fibers.

The SVOFC phase noises at 1.25 GHz and 2.5 GHz for the four fiber lengths are summarized in Table **5-3**. From the best of our knowledge, these phase noise values are the lowest reported for carriers at both frequencies using direct VCSEL modulation. The values in Table **5-3** also overcome the values presented in Chapter 4. The difference with previous implementations is the use of a variable optical coupler to adjust the electrical power received by the microwave amplifier. By increasing the electrical input power, the white noise of the

amplifier is reduced, and at the same time, the floor phase noise of the system is reduced. At 1.25 GHz, the phase noise of the C-band SVOFC is reduced by 9 dB compared to the VBO results presented in section 4.1.2, whereas at 2.5 GHz the reduction is 7 dB on average (except for $L = 5$ km).

Table 5-3.: Phase noise performance summary of fundamental frequency at 1.25 GHz and 2.5 GHz.

| Fiber length (km) | 1.25 GHz | | 2.5 GHz |
	C-band	O-band	C-band
1	-115.0	-115.0	-116.0
2	-119.2	-121.0	-119.4
3	-123.7	-125.0	-122.7
5	-126.3	-127.8	-121.3

5.2. Optical data transmissions

Due to the growth of the Internet and mobile users, several telecommunication sectors face infrastructure challenges to support the increasing data flows. In this sense, service providers have deployed networks based on guided and unguided media. Data transmissions over optical fiber are widely used today thanks to the reduced attenuations achieved (below 0.2 dB/km for SMF in C-band [289]) and the efficient use of the medium through techniques such as wavelength division multiplexing (WDM). Although significant transmission rate improvements have been achieved using intensity modulation and direct detection (IM/DD), coherent detection has attracted notable interest in recent years. The coherent detection, together with digital signal processing (DSP), has allowed the development and application of advanced optical modulation formats to increase the channel capacity beyond 100 Gb/s [183].

At the same time, the optical wireless communications (OWC) have become a promising alternative for wireless transmissions due to its wide bandwidth and its applicability in environments where radio waves are forbidden [290]. The long-range OWC communications, also known as free-space optical (FSO) communication, include terrestrial and satellite links such as ground-to-satellite, satellite-to-ground, and satellite-to-satellite links. Unlike radio frequency communications, FSO communications do not require spectrum licensing, are safer, more straightforward to develop, and have lower power consumption [291, 292].

In FSO systems, the on-off keying (OOK) modulation is the most implemented modulation scheme due to its simplicity [293, 294]. However, the differential phase-shift keying (DPSK) modulation is preferred to OOK modulation owing to the 3 dB sensitivity improvement and the reduction of the peak power to mitigate non-linear effects [295, 296]. Although DPSK requires more complex and costly implementation, theoretical studies show that it is a prominent modulation for inter-satellite communications [297]. To improve the receiver sensitivity

and to provide flexible multi-rate capabilities, efficient pulse shaping at the transmitter must be guaranteed [295]. For both modulation formats, the pulse shaping process (Figure **5-15**) in non-return-to-zero (NRZ) format is performed by using an optical intensity modulator driven by uncoded data (OOK) or coded data (DPSK).
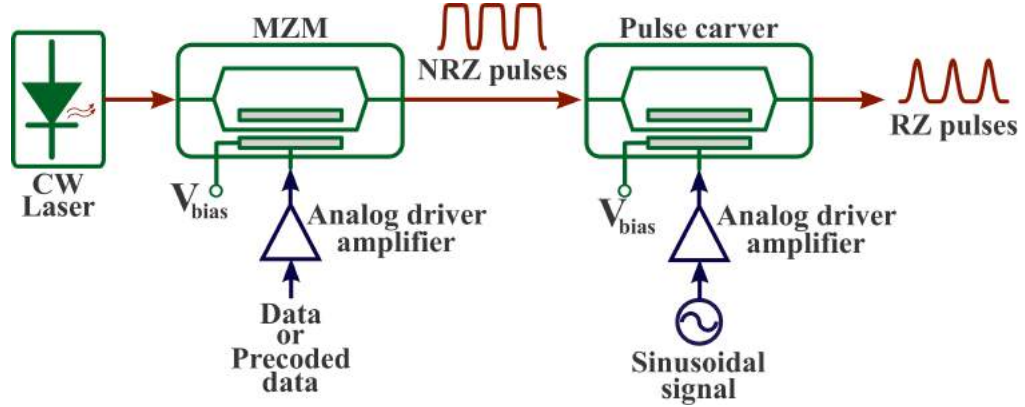
Figure 5-15.: Pulse shaping setup for NRZ and RZ pulses generation.

To generate return-to-zero (RZ) pulses, the NRZ optical pulse duration must be reduced by including a second intensity modulator called pulse carver (PC), as shown in Figure **5-15**. The duty cycle (pulse FWHM relative to symbol period) of the RZ pulses is controlled by the bias point of the PC, the frequency and amplitude of the sinusoidal drive signal [298]. For example, a 33% duty cycle is obtained when the bias point is set at the maximum transmission point, the amplitude of the drive signal is twice the V_π voltage, and its frequency is half the data bit rate. Although the spectral width of the optical signal in RZ format is wider than in NRZ, the RZ pulses have superior performance and higher tolerance to polarization variations during propagation [299].

The use of two intensity modulators implies a higher energy consumption due to the power supplies and the electrical amplifiers needed to guarantee the required electrical power of the driven signals. In this sense, the optical and electrical outputs of the SVOFC can be applied in the pulse shaping process to eliminate one of the intensity modulators, synchronize the system in the two domains and to produce optical pulses with duty cycles lower than 33%. The experimental results of the SVOFC application in a data transmission system are presented in this section. Similarly, the results when only the optical output is used to generate pulsed RZ-OOK and RZ-DPSK modulations are also included.

5.2.1. 1.25 Gb/s pulsed RZ-OOK modulation

As mentioned above, the pulsed RZ-OOK modulation is performed by two Mach-Zehnder intensity modulators (MZM) driven by the data signal and a sinusoidal signal (Figure **5-15**). Two driver amplifiers are used to ensure the required excursion of the transfer function.

Hence, to achieve NRZ-OOK modulation, the first modulator must be biased at the quadrature bias point $(V_{\pi/2})$ and the peak-to-peak voltage of the applied data signal must be equal to V_π. The RZ pulsed data with 50% duty cycle are obtained from the PC modulator submitted to the same polarization conditions. The frequency of the applied sinusoidal signal must be equal to the data bit rate, and its peak-to-peak voltage must be equal to V_π.
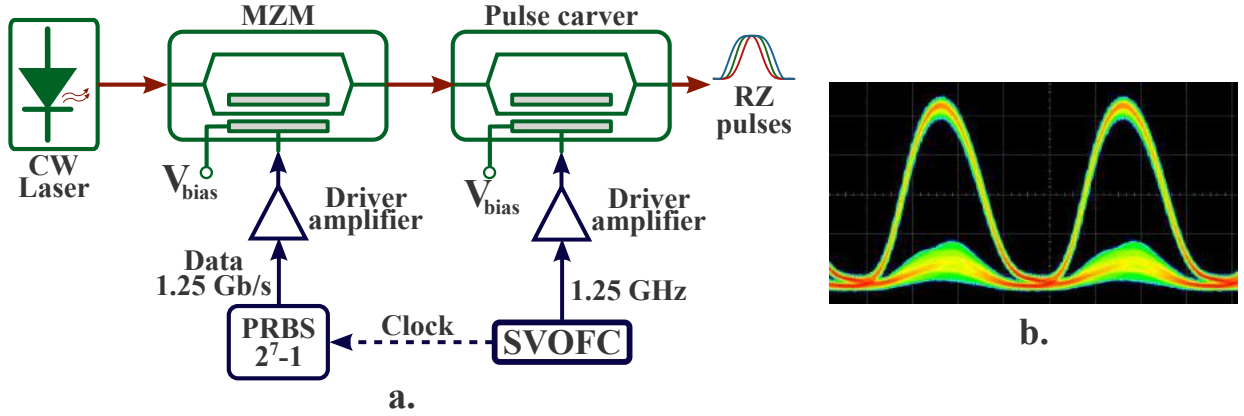
Figure 5-16.: a. Transmitter setup for RZ pulses generation, **b.** Eye diagram of the 50 %
       RZ pulses generated.

The transmitter setup for RZ-OOK modulation with a 50% duty cycle is shown in Figure **5-16 a.**. The electrical output of the C-band SVOFC at 1.25 GHz is used as a pseudo-random binary sequence (PRBS) clock to generate data at 1.25 Gb/s and as a sinusoidal signal for the PC modulator. In this way, the electrical signals and optical pulses generated are synchronized with the fundamental frequency of the SVOFC. The eye diagram of the optical pulses generated with a 50 % duty cycle is presented in Figure **5-16 b.**. The experimental duty cycle is 47 % when the optical time delay length is $L = 1$ km. Although the optical pulses were not characterized in terms of timing jitter, it is expected that jitter will increase with the deterioration of the sinusoidal signal stability and the jitter transferred by the PRBS (from the SVOFC).

The experimentally validated system is limited to 50% duty cycle because to generate RZ-OOK pulses with 33 % and 67 % duty cycles, the sinusoidal signal frequency must be half the transfer rate (625 MHz).

5.2.2. Pulsed RZ-OOK and RZ-DPSK modulation with lower duty cycles

The optical pulses generated by the C-band SVOFC at 1.25 GHz have a narrow duration (about 100 ps), which corresponds to duty cycles of less than 20% for data transmission at 1.25 Gb/s. Consequently, these pulses can be employed as an optical carrier to modulate the data generated by a PRBS with a $2^7 - 1$ pattern length. The proposed transmitter

setup is presented in Figure **5-17**. The SVOFC electrical output synchronizes the PRBS generator and the data pre-coder for the DPSK modulation. The MZM modulator is biased at the minimum transmission point, whereas the driver amplifier guarantees a peak-to-peak voltage equal to $2 \cdot V_\pi$. An electrical or optical phase shifter must be placed in the electrical or optical path to compensate for the phase offset produced by the connections and the data generation and coding processes.
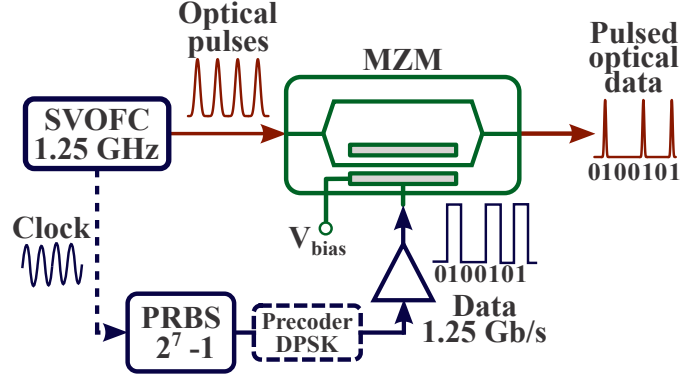
Figure 5-17.: Transmitter setup for 1.25 Gb/s pulsed RZ-OOK and RZ-DPSK data generation.

The DPSK modulation includes two basic operations: differential coding and phase-shift keying [300]. The differential coding avoids error propagation that may occur by differential decoding at the receiver [298] and is performed by an one-bit-delay XNOR logic gate. The phase change is accomplished by the voltage excursion applied to the intensity modulator. Thus, when a 1-bit is applied, the voltage reaches a maximum transfer point, whereas for a 0-bit, the immediately preceding maximum transfer point is reached. The shifting between these two points produces a π radians phase change and ensures the same optical power level for each bit. Table **5-4** shows an example of data coding and transmitted optical phase.

Table 5-4.: Data sequence coded for DPSK modulation.

Data sequence		1	1	0	1	0	0	1	0
Differentially encoded data	1	1	1	0	0	1	0	0	1
Transmitted optical phase	π	π	π	0	0	π	0	0	π

Figure **5-18 a.** shows the eye diagram of the optical pulses generated by the C-band SVOFC. The RMS jitter is 6.4 ps, 16% duty cycle, and 14.6 dB extinction ratio (ER). When RZ-OOK modulation is applied (Figure **5-18 b.**), the optical jitter increases to 10 ps, and the ER is reduced by 2 dB. The increase in jitter is caused by the jitter transfer from the electrical data [301] and the optical phase variations induced by extrinsic sources to the MZ modulator (e.g., temperature and mechanical stress) [302]. The ER reduction is due to the insertion loss of the modulator. In the case of the RZ-DPSK modulation depicted in Figure **5-18 c.** , the jitter obtained is 10 ps, $ER = 11.7$ dB, and 19% duty cycle. The eye diagram of

the RZ-DPSK pulses shows that a pulse is transmitted in all time periods, a characteristic behavior of this modulation type.
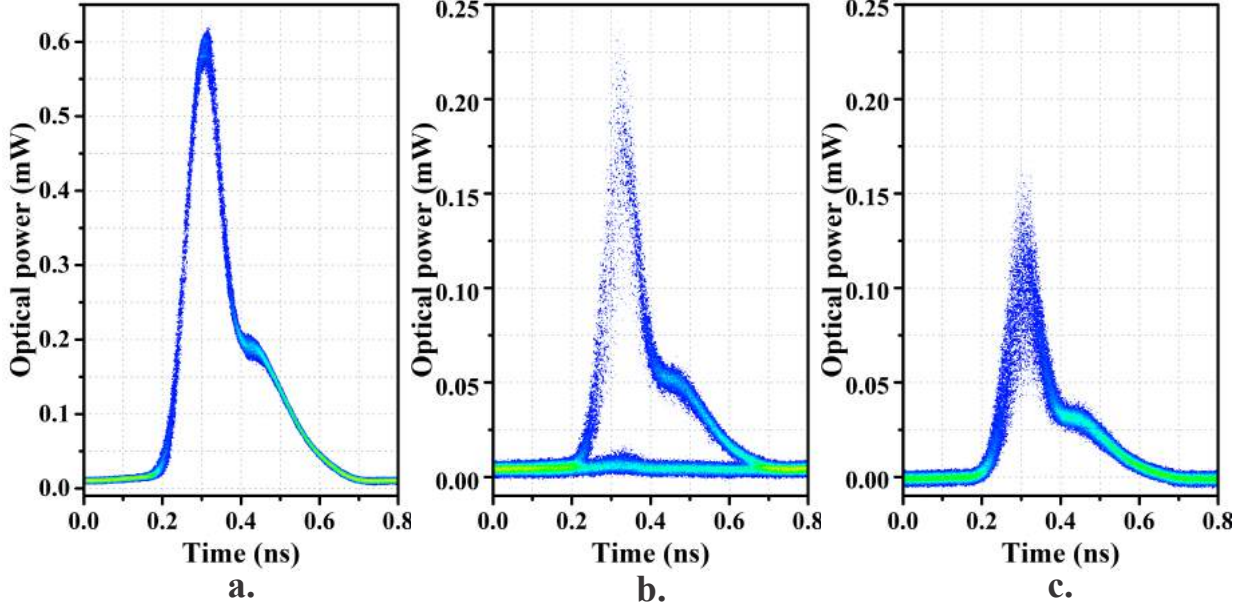
Figure 5-18.: Eye diagrams of the **a.** SVOFC optical output pulses, **b.** pulsed RZ-OOK optical data, and **c.** pulsed RZ-DPSK optical data.

Even though the proposed transmitter setup shows a suitable amplitude behavior, the phase of the RZ-DPSK pulses changes due to the phase variations induced by the gain switching condition of the SVOFC. Consequently, the amplitude-phase coupling of the laser limits the applicability of the optical output in phase modulations.

5.2.3. Optical intensity modulation at different bit rates

The optical output of the C-band SVOFC at 1.25 GHz can be used as an optical carrier when intensity modulation at different bit rates is applied. As shown in Figure **5-19**, the optical pulses are modulated through an MZ modulator by the data generated through a bit error rate tester (BERT) with a constant pattern length of $2^7 - 1$. The modulated signal is then amplified by a 20-dB erbium-doped fiber amplifier (EDFA) and distributed through an optical switch (OS) to different characterization equipment. The electrical spectrum is measured by an electrical spectrum analyzer connected to the photodetector electrical output.

Initially, two transfer rates at 155.52 Mb/s and 622.08 Mb/s below the SVOFC repeat rate are used. In time domain (Figure **5-20 a.**), the modulated signal consists of easily identifiable 0-bits, and 1-bits formed by multiple optical pulses at 1.25 GHz. From the optical spectrum of each modulation (Figure **5-20 b.**), it can be identified that the data is carried by each
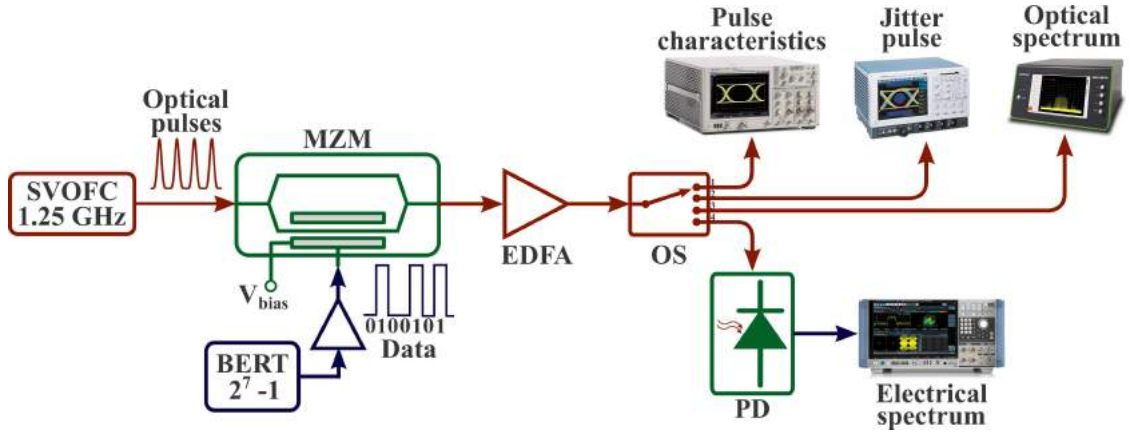
Figure 5-19.: Transmitter setup for optical data transmissions at different bit rates.

tone of the optical frequency combs coming from the SVOFC. In this way, the optical data can be recovered by filtering out a tone (sub-carrier) which satisfies specific characteristics, such as the power level. As expected, the optical spectrum also reveals that the spectral width of each tone enlarges as the modulation transfer rate increases.
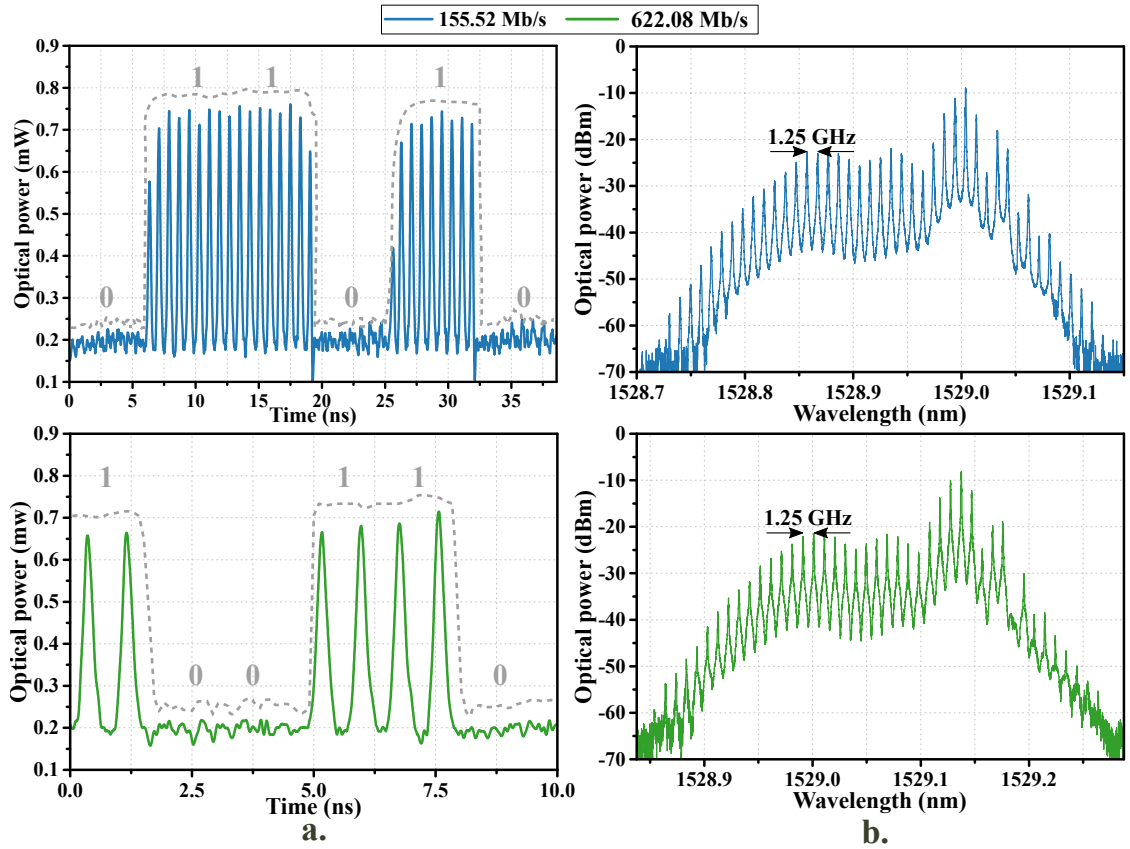
Figure 5-20.: Pulsed optical modulation output in **a.** time domain and **b.** frequency domain at 155.52 Mb/s and 622.08 Mb/s.

The modulated data is recovered into the electrical domain by a photodetector connected back-to-back (B2B). The photodetected electrical spectra for 155.52 Mb/s and 622.08 Mb/s transfer rates are shown in Figures **5-21 a.** and **b.**, respectively. In both cases, the spectrum is composed of the baseband signal and several electrical carriers at frequencies equal to $n \times f_0$. Each electrical carrier transports the optically modulated data (insets in Figure **5-21**). The data stream can be recovered directly with a low pass filter adjusted to the bit rate or by a frequency down-conversion process (using an electric mixer). A narrow-bandwidth band-pass filter recovers an electric carrier at a frequency equal to $n \times f_0$. The phase noise of each carrier depends on the phase noise of the fundamental frequency and the intrinsic deterioration of the frequency multiplication process. The proposed modulation
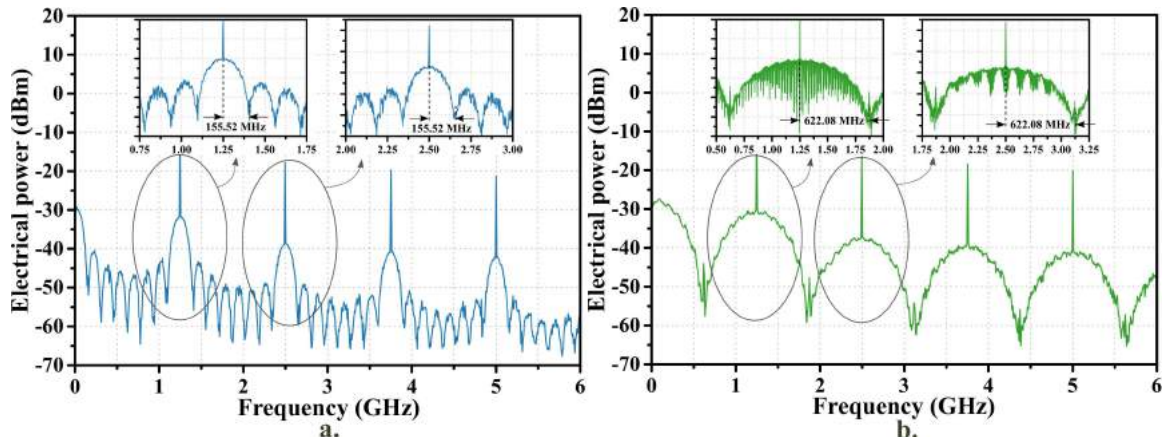
Figure 5-21.: Electrical signal photodetected at **a.** 155.52 Mb/s and **b.** 622.08 Mb/s. Insets: zoom on the first and second harmonic.

scheme allows the joint distribution of carriers and electrical data to remote units using optical fiber. Once in the electrical domain, the data can be retransmitted using the equally spaced electrical carriers.

When the bit rate is equal to the fundamental frequency, pulsed RZ-OOK modulation is obtained again. The ER of the SVOFC pulses can be determined from the eye diagram shown in Figure **5-22 a.**. Therefore, for a high-level power equal to 183 μW and 5 μW for the low level, the ER is 15.6 dB. Likewise, the ER of the RZ-OOK pulses (Figure **5-22 b.**) is estimated to be 15 dB. The RMS jitter increases slightly (compared to the results in section 5.2.2) from 3.4 ps to 4.5 ps. This small variation is caused by the higher performance of the electrical signal used to modulate the optical carrier. To obtain a lower initial optical jitter, the electrical power inside the SVOFC loop is augmented. This power increase yields a widening of the optical pulses due to the stronger stimulation of the second spike of the VCSEL relaxation response. The duty cycle of unmodulated pulses is 26%, whereas after optical modulation, it is 28%. These results show that the optical modulation quality is impacted by the electrical data signal quality [301]. The optical spectrum of the modulated data, presented in Figure **5-22 c.**, is composed of the different tones from the optical frequency comb. Owing to the widening of the optical spectrum as an effect of the pulsed modulation, the signal-to-noise ratio of each tone is reduced to approximately 13 dB

(around 20 dB when the bit rate is 155.52 and 622.08 Mb/s). The optical spectrum around the maximum power agrees well with the spectrum of 33% and 50% RZ-OOK modulations.
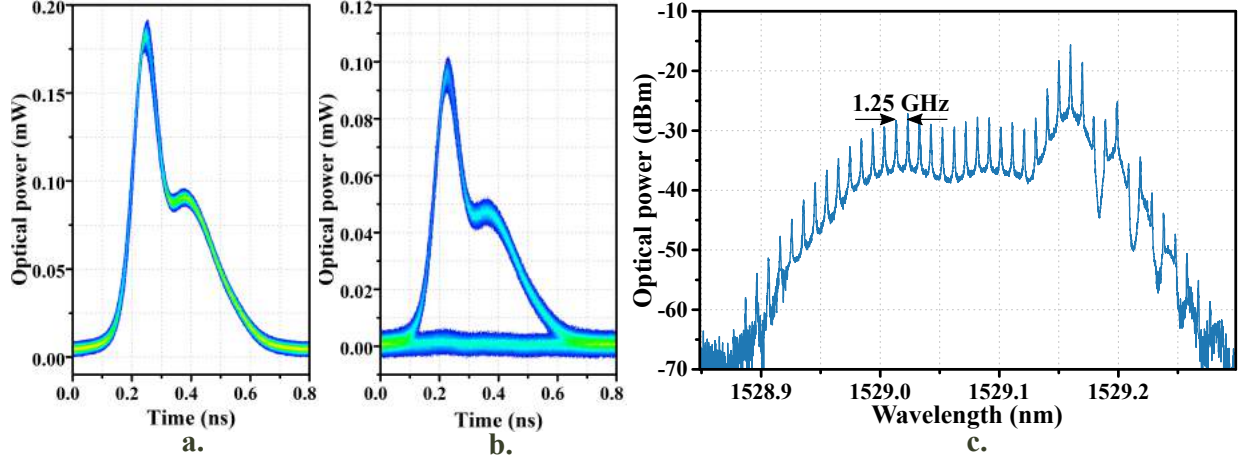
Figure 5-22.: Eye diagrams of the **a.** 1.25-GHz SVOFC optical output and **b.** pulsed RZ-OOK optical data. **c.** Optical spectrum of the RZ-OOK data.

Figure **5-23** shows the SBB phase noise curves of the fundamental frequency and 3 recovered harmonics on the receiver side. The frequency distance between the oscillating mode and the non-oscillating modes is 39.8 kHz and corresponds to the FSR produced by 5 km of optical fiber used in the C-band SVOFC. The phase noise at 10 kHz from the fundamental frequency carrier is -121.2 dBc/Hz. The phase noise of the harmonic n is deteriorated by $20 \times log(n)$ dB from the fundamental frequency noise. The measured and theoretical phase noise of the recovered harmonics are summarized in Table **5-5**. The difference between the measured and theoretical values is owed to the non-flat optical spectrum and the non-linearity of the photodetector frequency response. The phase noise of the fundamental frequency measured at the electrical output of the SVOFC is -125.8 dBc/Hz. The phase noise deterioration of the two fundamental frequencies is 4.6 dB and is caused by additional noise sources such as amplified spontaneous emission (ASE) and the increased shot noise due to the higher photodetected optical power.

Table 5-5.: Measured and theoretical phase noise of the transmitted harmonics.

Harmonic	Frequency (GHz)	Measured phase noise (dBc/Hz)	Theoretical phase noise (dBc/Hz)
1	1.25	-121.2	-121.2
2	2.5	-113	-115.2
3	3.75	-108	-111.7
4	5	-105	-109.2
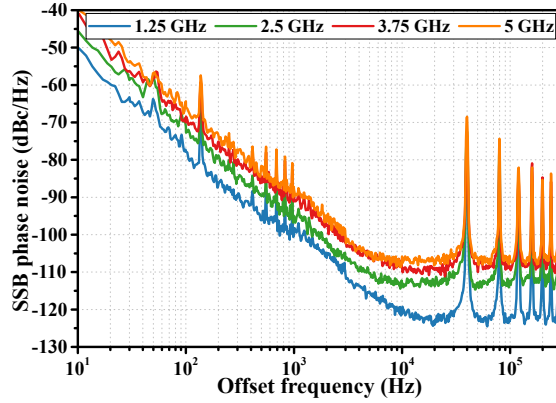
Figure 5-23.: Phase noise curves of the fundamental frequency and 3 harmonics recovered at the photodetector.

Under the same principle, the C-band SVOFC at 2.5 GHz is used for 1.25 Gb/s optical data transmission according to the configuration shown in Figure **5-24**. The transmitter modulates the optical pulse coming from the SVOFC with a data stream generated by a BERT at 1.25 Gb/s. The modulated optical signal is sent to the receiver via an optical variable attenuator to adjust the received optical power (P_{in}). On the receiver side, a 20-dB gain EDFA amplifier and a PIN photodetector are used. A low-pass filter with a $0.75 \times bit$ $rate$ cutoff frequency, filters the baseband data to estimate the bit error rate (BER).
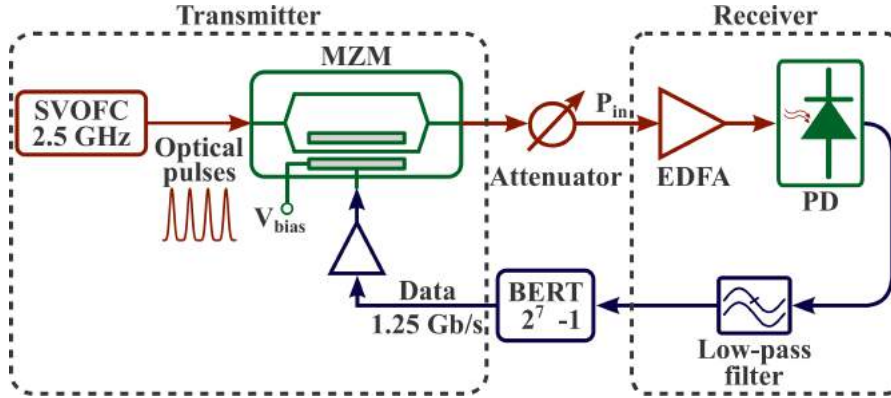
Figure 5-24.: Transceiver setup for 1.25 Gb/s pulsed OOK data transmission.

The eye diagrams of the filtered electrical data for different received optical powers are shown in Figure **5-25**. The average eye width is 276 ps for input powers higher than -30 dBm. Below this power, the eye diagram is closed, and widths below 190 ps are obtained. Similarly, the signal-to-noise ratio (SNR) decreases from 6 to values lower than 5 for $P_{in} < -30$ dBm. The eye width is significantly affected by the high RMS jitter value (around 88 ps). This jitter level is attributed to the superposition of the non-oscillating modes of the SVOFC fundamental frequency over each data spectral component (equally separated spectral lines). Table **5-6** summarizes the characteristics determined from the measured eye diagrams. The results of the NRZ-OOK modulation using the VCSEL as a CW laser source and the SVOFC

with two different optical fiber length ($L = 1$ km and $L = 2$ km) are included in this table. Even though the 1.25 Gb/s NRZ-OOK link has a better performance for all received optical power levels, all three links deteriorate from powers below -30 dBm. It is worth pointing out that the eye width of the pulsed RZ-OOK links ($\sim$ 280 ps) is much smaller than the NRZ-OOK link ($\sim$ 660 ps) due to the higher RMS jitter contribution.
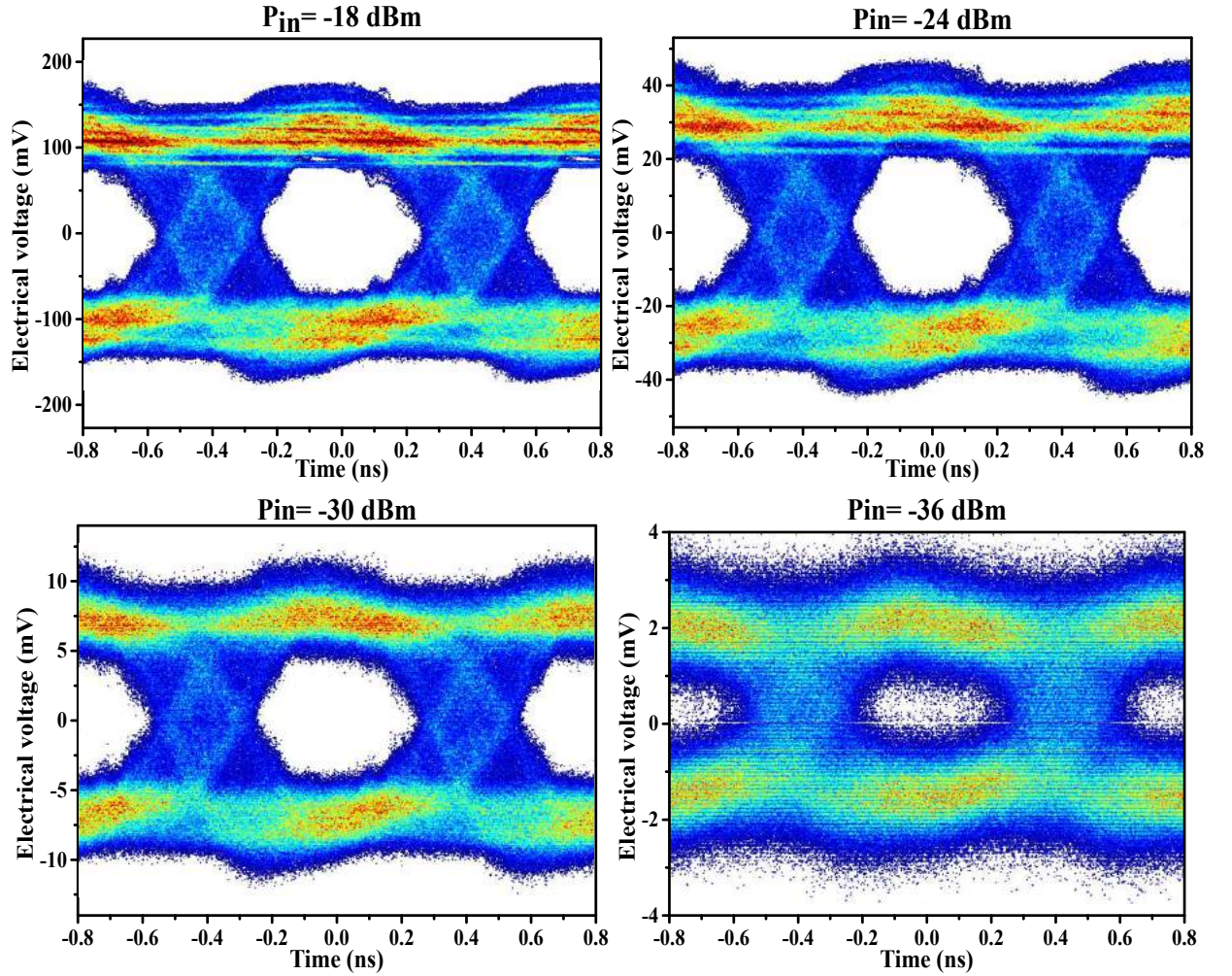
Figure 5-25.: Eye diagram of the electrical data at different received optical powers.

The BER measured for the three optical links are plotted in Figure **5-26**. For P_{in} higher than -33 dBm, the measured BER is above 10^{-9} and are not included in the figure. In all three cases, the BER deteriorates dramatically following the same pattern, from 10^{-8} for $P_{in} = -33$ dBm to $BER = 10^{-3}$ when $P_{in} = -36$ dBm. Previous work shows that using RZ-OOK pulsed modulation (33%, 50%, and 67% duty cycles) the link performance is improved by enhancing the receiver sensitivity ($BER = 10^{-9}$ achieved with lower P_{in} values) [299]. This effect is not evidenced during the tests owing to the periodic jitter added by the joint transmission of the electrical carrier (including the non-oscillating modes) and the data stream. However, the performance of the proposed system equals the NRZ-OOK

Table 5-6.: Summary of the measured parameters of the NRZ-OOK and pulsed RZ-OOK links.

P_{in} (dBm)	RMS jitter (ps)			SNR			Eye width (ps)		
	NRZ-OOK	$L=1$ km	$L=2$ km	NRZ-OOK	$L=1$ km	$L=2$ km	NRZ-OOK	$L=1$ km	$L=2$ km
-27	21	88	89	7	6	6	681	275	273
-30	23	87	88	6	6	6	669	280	279
-33	30	92	91	6	5	5	624	255	256
-36	58	102	126	4	4	3	455	187	48

link performance under the same modulation conditions because the BER values are very close for different optical power at the receiver input.
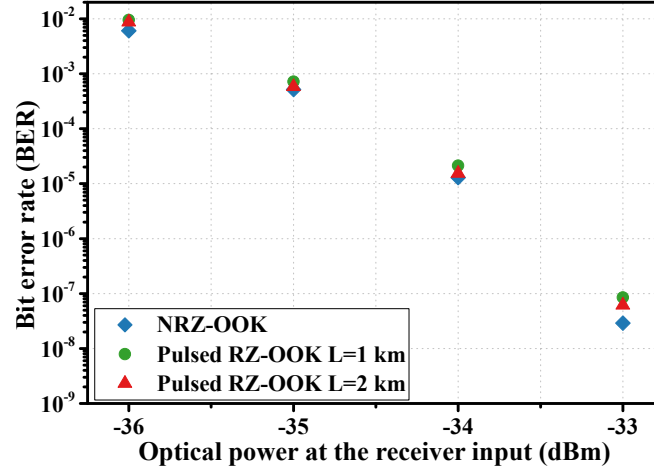
Figure 5-26.: Bit error rates measured for pulsed RZ-OOK and NRZ-OOK links.

The system performance can be improved by using a booster amplifier at the emission side and/or an LNA and an optical filter at the reception (the PIN should also be replaced by an avalanche photodiode APD). In any case, a trade-off between bit rate, performance and noise must be considered.

5.3. Conclusions

In this chapter, the generation of optical frequency combs using a closed-loop system called self-started VCSEL-based optical frequency comb generator (SVOFC) was presented. The VCSEL is directly modulated in gain switching regime. A microwave signal is generated simultaneously at the fundamental frequency defined by a band-pass filter, and its spectral purity is related to the optical fiber length used.

Initially, the C-band SVOFC is simulated numerically in VPIPhotonics Design Suite$^{\text{TM}}$. The parameters of the C-band VCSEL were set according to the intrinsic parameters extracted experimentally in Chapter 3. Both the optical delay and the Fabry-Perot FP effect of the optical fiber were included with a fixed time delay and an FP filter (the free spectral range can be adjusted). Through the simulation, it was possible to verify that the OFC flatness and the pulse shape are strongly related to the frequency and power of the electrical signal inside the loop. When the fundamental frequency is higher than the relaxation frequency of the laser, the pulse waveform is closer to a Gaussian shape, and the OFC flatness increases. The FSR of the FP filter is reflected in the non-oscillating modes of the electrical microwave signal.

The simulation results are validated by implementing the SVOFC using C and O-band VCSELs and two fundamental frequencies at 1.25 GHz and 2.5 GHz. The pulse width varies according to the modulating electrical power and is limited by the photon lifetime. Similarly, the timing jitter of the pulses can be improved by reducing the turn-on delay through increasing the electrical power inside the loop. At 1.25 GHz and using a C-band VCSEL, the shortest pulse duration achieved was 103 ps (13% of cycle time) and the highest flatness was 0.75. At 2.5 GHz, the best metrics were 85 ps (21% of cycle time) and flatness above 0.84 in all the implementations.

Finally, the SVOFC is used for optical data modulation at different bit rates. Using the electric output of the SVOFC, a 50 % RZ transmitter at 1.25 Gb/s was demonstrated. To reduce the duty cycle, it is necessary to halve the SVOFC microwave frequency. A second transmitter for 1.25 Gb/s pulsed RZ-OOK and RZ-DPSK was proposed. In this case, the optical pulses generated by the SVOFC at 1.25 GHz are modulated by a data signal synchronized with the electrical output of the SVOFC. Although the optical intensity of the modulated pulses corresponds well with the two modulation schemes, the transmitter is limited for DPSK due to the optical phase shift of the pulses coming from the SVOFC. The same principle is applied to the modulation of bit rates lower than the fundamental frequency of the SVOFC. For 155.52 Mb/s and 622.08 Mb/s bit rates, data is optically transmitted over each of the OFC tones. After being photodetected, the data can be retransmitted at microwave frequencies multiple of 1.25 GHz. When the bit rate equals the fundamental frequency, the performance of the transmitter in terms of BER is equal to that of a 1.25 Gb/s NRZ-OOK transmitter. This behavior is due to the jitter of the recovered data, caused by the transmission of the microwave carriers together with the optically modulated data.

Conclusions and Future work

Conclusions

This thesis manuscript presents the theoretical and experimental results conducted as part of an international joint supervision agreement between the Universidad Nacional de Colombia and the Institut Supérieur de l'Aéronautique et de l'Espace ISAE-SUPAERO. The main objectives of this research were the exploration of optical techniques for microwave signal generation, and the design and implementation of an optoelectronic system based on VCSEL to be integrated into telecommunication applications.

A complete and detailed state of the art of microwave signal generation using optoelectronic systems and optoelectronic oscillators was presented. Even though almost forty years have passed since the first OEO architecture, different authors continue researching its structure and proposing new topologies that preserve the initial concept but include new components in order to reduce the phase noise while increasing the oscillation frequency. This interest is supported by the increasing use of microwave signals (millimeter and THz) in different applications and the growing need to use unexplored or uncovered frequency bands.

Although there are currently different mechanisms for determining the stability of signals in the frequency and time domain, there is no standard for unifying definitions and measurement methods. In this document, the most commonly used definitions in the literature were detailed and used to characterize the systems implemented experimentally. In the specific case of telecommunications, the measurement standardization would facilitate the interoperability processes.

Considering that the proposed system for microwave signal generation is based on VCSEL and its applicability in a data transmission application had to be verified, VCSELs emitting at telecom optical wavelengths were selected, specifically in C and O-band. Although the technology of manufacturing VCSELs at 850 nm can now be considered mature, the manufacture of long-wavelength VCSELs has evolved gradually, due to the technical difficulties of constructing highly reflective mirrors. However, the insertion of the tunnel junction has improved the electrical and optical confinement inside the laser cavity and boosted its use

in a wide range of applications.

In order to identify and simulate the behavior of the C-band VCSEL used in the proposed system, a theoretical-experimental procedure was proposed to extract its intrinsic parameters. Firstly, the process is based on a mathematical model that allows, from the VCSEL rate equations, to analyze the laser performance in the steady-state when different bias conditions are assumed. Supplementary relations were established by relating the intrinsic parameters and the components of the equivalent electrical circuit. The second step included a complete experimental characterization through static and dynamic measurements of the packaged VCSEL and the simulation of the equivalent circuit to determine the maximum number of VCSEL parameters. Finally, the extraction process was validated through the simulation and comparison of C-band VCSEL measurements, including the RIN, by using the Langevin approach. The applied procedure agrees well with the experimental results and showed that the VCSEL bandwidth is limited to 4 GHz, whereas the resonance frequency is affected by temperature effects inside the active zone for higher bias current. Although the package was included in the simulations with an electrical circuit, its effect on the VCSEL bandwidth is not decisive because its cutoff frequency is higher than 4 GHz.

The VCSEL based optoelectronic oscillator architecture was theoretically described and implemented at two oscillation frequencies (1.25 GHz and 2.5 GHz) using the characterized C-band VCSEL and an O-band VCSEL to verify the effect of fiber dispersion on phase noise. The lowest phase noise at 10 kHz from the carrier (-124 dBc/Hz) was obtained when the O-band VCSEL is used with 5-km optical fiber at 2.5 GHz. One of the most remarkable features of the VBO is its capacity to maintain the oscillating condition when the whole system is exposed to a temperature variation between 0 and 50 degrees Celsius. Therefore, the VBO performance and thermal robustness make it a straightforward alternative for on-board systems.

The self-started VCSEL-based harmonic frequency generator (SVHFG) is a closed-loop system capable of generating multiple microwave harmonics by modulating a VCSEL in gain switching regime. By implementing two SVHFG, it was verified that the lowest phase noise at 10 kHz offset from the fundamental frequency at 1.25 GHz was -124.7 dBc/Hz. The system noise processes are governed by the noise generated by the two cascaded amplifiers. With this system, it was possible to generate a carrier at 15 GHz and phase noise -104 dBc/Hz; this performance is close to the one obtained by more complex optoelectronic systems.

A predictive phase noise model was proposed and validated with the experimental results. The model uses the feedback system theory and considers the additive and multiplying noise sources coming from the system components. By comparing the phase noise curves, the model accuracy and the impact of the resonator quality factor, the RIN, the input power of the first amplifier, and the VCSEL frequency noise on the phase noise were verified. This model can be employed for the design of closed-loop systems in which a directly modulated laser is included.

To verify the system applicability, the optical output of the self-started VCSEL-based optical frequency comb generator (SVOFC) was used as an optical carrier for amplitude-modulated

data transmission. Through the simulation and implementation, it was demonstrated that the characteristics of the optical pulses generated with gain-switched VCSELs depend on the SVOFC fundamental frequency, the power inside the loop, and the bias current. Similarly, the profile of the optical frequency combs depends on the electrical characteristics of the system. It was also proved that the OFC profile is flatter when the SVOFC fundamental frequency is higher than the VCSEL relaxation frequency. Thanks to the use of the variable-ratio coupler and the adjustment of the electrical power at the microwave amplifier input, the phase noise -127.8 dBc/Hz at 10 kHz offset is the lowest reported, as far as we know, for a 1.25 GHz carrier using a directly modulated VCSEL.

The data transmission at different bit rates was demonstrated experimentally using the SVOFC electrical output to synchronize the data generation equipment and its optical output as an input to an external modulation system. When bit rates are lower than the SVOFC fundamental frequency, each OFC tone behaves as an optical carrier, and data can be recovered by direct detection. When the bit rate and the frequency are equal, pulsed optical data was generated using an OOK and DPSK modulation scheme. Although the intensity behavior validates the use of the SVOFC pulses for DPSK modulation, the pulse phase varies as an effect of the VCSEL direct modulation inside the SVOFC. The deterministic jitter added by the simulated transmission of data and carrier (fundamental frequency), led to the performance of the pulsed RZ-OOK transmitter being equal to that obtained for an NRZ-OOK transmitter.

Future work

Although the two systems proposed for the generation of harmonics and optical frequency combs are entirely operational, the quality of the signals in the electrical and optical domains can be improved. The injection locking (IL) technique can be applied in order to reduce the jitter of the optical pulses and the phase noise of the fundamental frequency as a consequence of RIN reduction. The optical phase behavior of the pulses generated using the IL technique must be analyzed and measured. Depending on the results, the SVOFC optical pulses could be used for the generation of pulsed optical data using phase modulation schemes such as DPSK and QPSK. Similarly, the negative chirp of the optical pulses can be compensated by replacing the optical fiber used with a negative dispersion optical fiber.

As demonstrated in this work, temperature fluctuations can significantly impact the phase noise of the electrical signal. In this sense, a thermal control over the VCSEL, the optical fiber, and the microwave amplifiers must be implemented to guarantee a specific operating point. As for the VCSEL, the temperature control serves to mitigate the heating effects of the active region for large I_{bias} values. When the SVOFC system is applied for data transmission, the thermal control must be extended to the intensity modulator, together with a bias control to ensure the selected bias point. In this way, the optical jitter transfer due to extrinsic factors is restricted.

During the development of this research, the implementation of VBO using on-chip VCSELs was explored to achieve higher oscillation frequencies. In the case of 850-nm VCSEL, the optical coupling was performed with multimode optical fiber, and the VBO was operational at 10 GHz and 12 GHz. For C-band VCSELs, the complex optical coupling with SM fiber limited the implementation. It is recommended to continue exploring these lasers in order to demonstrate the VBO integration potential and to enhance its applicability. Besides, the VCSEL-to-VCSEL injection is an attractive integration solution, which also allows increasing the bandwidth of the injected VCSEL.

As for the intrinsic parameter extraction from the VCSEL, the procedure can be improved by using a temperature-dependent single-mode rate equation model and ensuring an impedance coupling between the electrical access of the VCSEL and the driver circuit in the frequency range of interest.

Although the predictive phase noise model presented is accurate, a better approximation can be obtained by including the Flicker noise of the photodetector and the VCSEL RIN at low frequencies. This adjusted model would allow a more accurate prediction when a specific phase noise near the carrier is required.

Finally, the SVHFG system can be used for the subharmonic generation by applying the gain switching technique until the period-doubling status is achieved. Thus, the system increases its applicability, for example, in pulse shaping of reduced duty cycle optical data that requires two frequencies: one frequency equal to the bit rate and half of this frequency for the pulse carver modulator.

Appendix A

VCSEL Intrinsic Parameters

VCSEL parameters listed in Table **A-1** correspond to an LW-VCSEL at 1.3 μm.

Table A-1.: VCSEL parameters from [8]

Parameter	Value	Units
η_i	0.8	
υ_g	7.7×10^9	cm/s
Γ	0.032	
A	1.1×10^8	s^{-1}
B	1×10^{-10}	cm^3/s
C	3.57×10^{-29}	cm^6/s
β	1×10^{-5}	
ϵ	2.2×10^{-17}	cm^3
a_0	4.8×10^{-16}	cm^2
N_{tr}	3.24×10^{18}	cm^{-3}
τ_P	6.4	ps
α_H	3.5	

Threshold current was set at 1 mA, whereas the photon density was determined for each bias current using Equation 2-11.

Appendix B

Electrical spectrum analyzer (ESA) calibration

The calibration of the electrical spectrum analyzer aims to validate the phase noise measurements made during this work, besides determining the floor noise at the working frequencies.

Even if the directly measured phase noise method is the simplest, different factors limit the measurement accuracy. Some of these factors are listed below:

- IF filter bandwidth (RBW), relative to noise bandwidth.

- Type of IF and form factor.

- Local oscillator stability - residual FM.

- Local oscillator stability and noise sidebands.

- The analyzer detector response introduces an error.

- Logarithmic amplifier response of the analyzer to noise.

B.1. Equipment

To calibrate the ESA, a signal with a calibrated phase noise and constant slope of -20 dB/decade is generated using an FM modulated generator with uniform noise [10]. The device is described in Figure **B-1**.

To ensure accuracy, the synthesizer noise without frequency modulation must be at least 10 dB less than the desired calibrated noise, at the desired offset frequency. Thus, the manipulation was performed with a Rohde & Schwarz synthesizer model SMA100B, equipped with option B711. Table **B-1** compares the phase noise speculations at 1 GHz of both equipments. The generator is about 10 dB below ESA for all offset values.
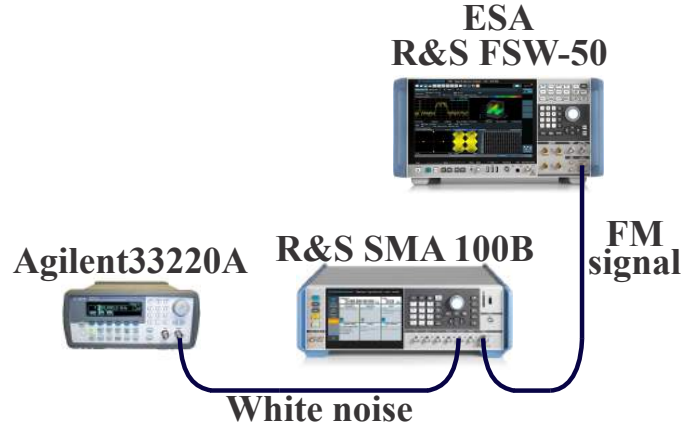
Figure B-1.: Experimental setup.

Table B-1.: Spectral purity: typical values at 1 GHZ of SSB phase noise for FSW-50 and SMA 100B (from datasheets).

Offset	FSW-50	SMA 100B
10 Hz	-90 dBc/Hz	$\simeq$ -106 dBc/Hz
100 Hz	-116 dBc/Hz	$\simeq$ -120 dBc/Hz
1 kHz	-132 dBc/Hz	$\simeq$ -140 dBc/Hz
10 kHz	-140 dBc/Hz	$\simeq$ -152 dBc/Hz
100 kHz	-143 dBc/Hz	$\simeq$ -153 dBc/Hz
1 MHz	-149 dBc/Hz	$\simeq$ -163 dBc/Hz
10 MHz	-156 dBc/Hz	$\simeq$ -165 dBc/Hz

B.2. Operating principle

The SMA100B synthesizer provides a sinusoidal signal at frequency f_c, written as follows:

$$C(t) = A_0 \cdot \cos(\omega_c t) \tag{B-1}$$

with A_0 the amplitude and $\omega_c = 2\pi f_0$ the angular frequency. This signal is frequency-modulated by an external source (generator Agilent 33220A):

$$C_m(t) = A_0 \cdot \cos\left[\omega_c t + m \cdot \sin\left(\omega_m t\right)\right] \tag{B-2}$$

where $\omega_m = 2\pi f_m$ is the modulating frequency and m is the modulation index defined as:

$$m = \frac{kV_m}{f_m} = \frac{\Delta f}{f_m} \tag{B-3}$$

where k is the sensitivity in Hz/V (adjusted in the R&S synthesizer configuration) and Δf is the frequency deviation. The modulating noise amplitude establishes the frequency deviation and, therefore, the phase noise level shown in table **B-2**. For example, for a deviation of 500

Table B-2.: Standard phase noise [10].

FM noise deviation	1 Hz	10 Hz	100 Hz	1kHz	10 kHz	100 kHz
			Offset			
5 Hz	-60	-80	-100	-120	-140	-160
16 Hz	-50	-70	-90	-110	-130	-150
50 Hz	-40	-60	-80	-100	-120	-140
158 Hz	-30	-50	-70	-90	-110	-130
500 Hz	-20	-40	-60	-80	-100	-120
1.58 kHz	-10	-30	-50	-70	-90	-110
5 kHz	0	-20	-40	-60	-80	-100
15.8 kHz	10	-10	-30	-50	-70	-90
50 kHz	20	0	-20	-40	-60	-80

Hz, the phase noise at 10 kHz from the carrier is -100 dBc/Hz, whereas it is -120 dBc/Hz for a deviation of 50 Hz. The synthesizer - noise generator combination must now be calibrated to find the voltage values to produce the deviation values given in table **B-2**.

B.3. Calibration process

B.3.1. Verification of frequency deviation

The objective is to determine the amplitude required to produce a given frequency deviation. To do this, the modulator is a sine fixed at 10 kHz. The synthesizer is set to the chosen frequency, i.e., 1.25 GHz in the example.

$$V_c = A_c \sin(2\pi f_c \cdot t) \tag{B-4}$$

with A_c the amplitude (here 0.32 V for $P = 0$ dBm) and $f_c = 1,25\,GHz$ the frequency of the signal. According to Equations B-2 and B-3, $m = 2.41$ corresponds to the 1er zero of the 0th-order Bessel function. For this index, the carrier is suppressed.

Finally, to achieve this state (i.e., 10.49 dBm), the Agilent generator must be adjusted at $V_m = 2.117$ V peak-to-peak.

B.3.2. Noise source adjustment

The goal is to determine the configuration of the Agilent 33220A noise source to provide the same 10.49 dBm power. This is achieved using the ESA and its Band Power marker

function. A power of 10.47 dBm is measured between 0 and 40 MHz (see Figure) for a value of $5.9\,V_{pk-pk}$ set on the source (loaded at $50\,\Omega$).
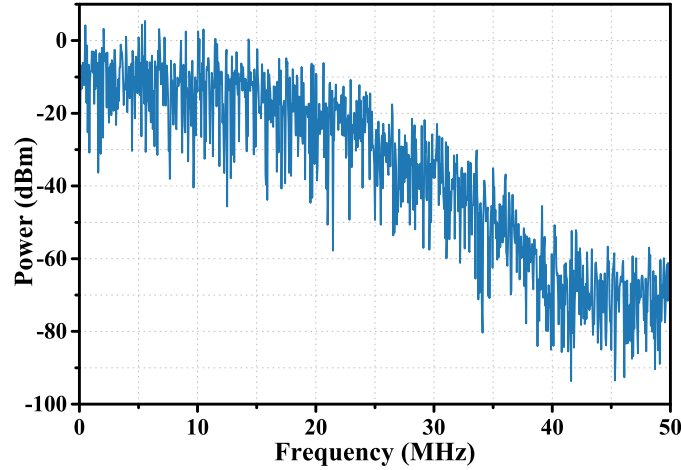
Figure B-2.: Noise spectrum produced by the Agilent 33220A source.

B.3.3. Verification of unmodulated synthesizer phase noise

First, the unmodulated R&S synthesizer phase noise is verified at different carrier frequencies: 1.25 GHz, 2.5 GHz, 10 GHz, 12 GHz and 15 GHz. Figure **B-3** shows the results at 1.25 GHz.
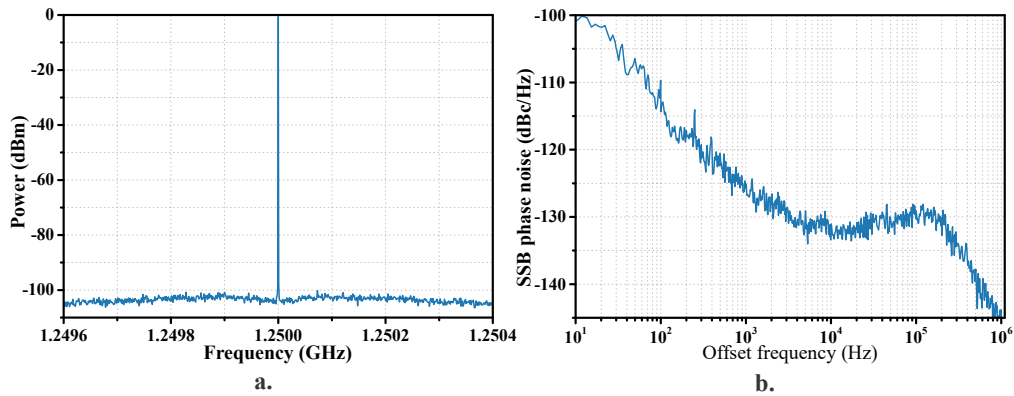
Figure B-3.: Synthesizer R&S SMA100B at 1.25 GHz (P = 0 dBm) - **a.** Spectrum and **b.** phase noise without modulation.

These values can be compared to the 1 GHz manufacturer data reported in the Table **B-1**. At the other frequencies, the synthesizer phase noise is much lower than the ESA.

B.3.4. Generation of phase noise references

Now, the FM modulation capabilities of the synthesizer to generate the desired frequency deviations (Figure **B-4**) is used, according to the values given in Table **B-2**. The "standard" phase noise obtained exhibits a slope of -20 dB/decade. Figure **B-5** shows the results at 1.25 GHz and different Δf values.
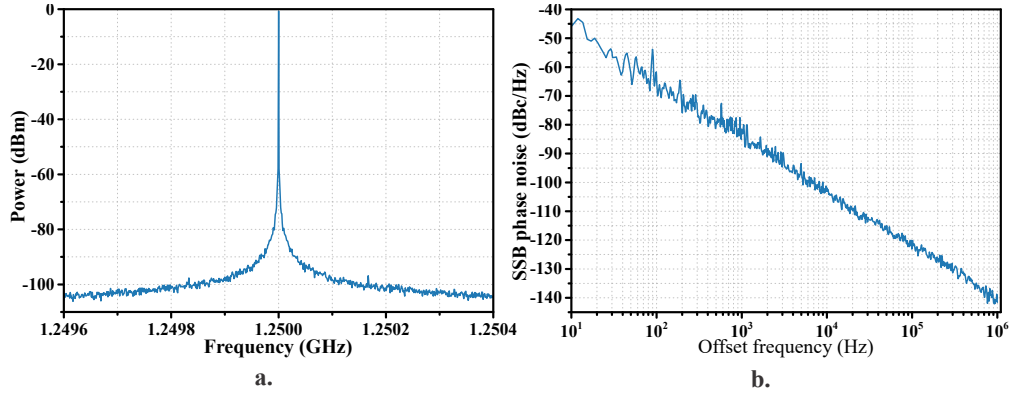
Figure B-4.: Synthesizer R&S SMA100B at 1.25 GHz (P = 0 dBm) - **a.** Spectrum and **b.** phase noise with $\Delta f = 500$ Hz.
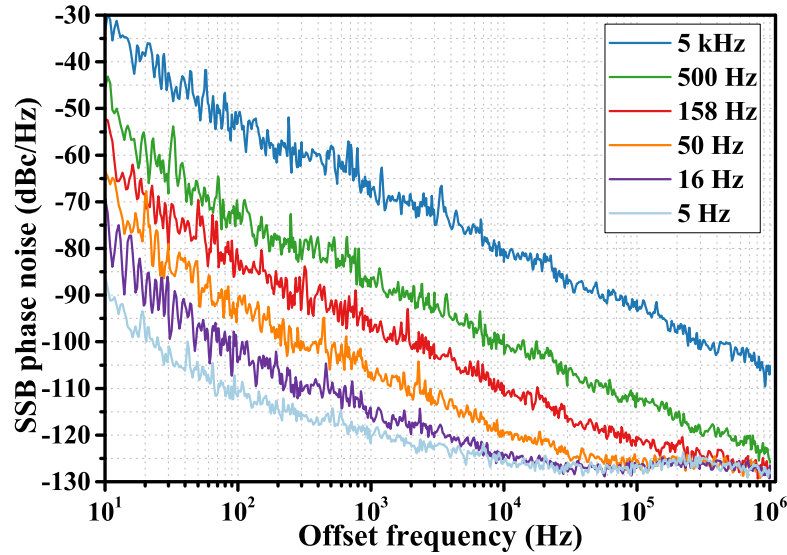
Figure B-5.: Standard phase noises.

Starting from the top curve (500 Hz deviation, phase noise = -100 dBc/Hz @10 kHz), the measured phase noise decreases, indicating that the ESA is capable of measuring it. Then, starting from the 158 Hz deviation, one begins to reach the measurement floor of the instrument for offsets above 100 kHz.

At 10 kHz from the carrier, the -120 dBc/Hz expected for the 50 Hz deviation is well measured, whereas only -125 dBc/Hz is measured instead of the -130 dBc/Hz expected at 16 Hz deviation. At a frequency of 1.25 GHz, the FSW-50 measurement floor can, therefore, be estimated to be approximately -125 dBc/Hz at 10 kHz from the carrier frequency.

B.4. ESA configuration

The measurements presented have been obtained with the following ESA settings:

- Offset: Start = 10 Hz; Stop = 1 MHz

- Sweep formard = ON (sweep from the carrier)

- RBW = 10 %

- AVG count: 3

- Multiplier = OFF

- Sweep mode: I/Q FFT

- I/Q window = Blackman-Harris

Appendix C

Thermal perturbations in optical fibers

When an optical fiber is subjected to thermal stress, the optical beam that passes through it undergoes physical changes. The most critical parameter for this work is the variation of the optical phase. The following is an analysis of the temperature effect on the optical phase and its incidence on the photodetected electrical frequency [257].

The occurrence of three effects causes the optical phase variation. The first one is the fiber length L variation due to the thermal contraction or expansion. The second effect is the variation of the effective refractive index n due to fiber bending, which modifies the diameter D.

The optical phase ϕ inside the optical fiber is expressed as:

$$\phi = \beta L \tag{C-1}$$

whit β is the optical fiber line phase constant (wave number). The optical phase shift $\Delta\phi$ under thermal stress involves the lengthening of L and the diameter and refractive index variations. This relation is stated as:

$$\Delta\phi = \beta L + L\Delta\beta \tag{C-2}$$

where the diameter and refractive index variations are expressed as:

$$L\Delta\beta = L\frac{d\beta}{dn}\Delta n + L\frac{d\beta}{dD}\Delta D \tag{C-3}$$

Considering a optical fiber without coating, the diameter can be neglected and the equation C-2 becomes:

$$\frac{\Delta\phi}{L} = \beta\frac{\Delta L}{L} + \frac{d\beta}{dn}\Delta n \tag{C-4}$$

If the optical signal is amplitude modulated at frequency f_0, the phase variation induced in the optical fiber will impact the photodetected phase signal. To obtain an expression that

relates the optical phase and the photodetected phase, the electric wave number β_e is used:

$$\beta_e = \frac{2\pi f_0 n}{c} \tag{C-5}$$

and

$$\frac{d\beta_e}{dn} = \frac{\beta_e}{n} \tag{C-6}$$

Therefore, the electrical phase shift is determined by:

$$\frac{\Delta\phi}{L} = \beta_e \left(\frac{\Delta L}{L} + \frac{\Delta n}{n} \right) \tag{C-7}$$

Now, the phase shift can be expressed as a function of the temperature effects as:

$$\frac{\Delta\phi}{\Delta T \cdot L} = \beta_e \left(\frac{1}{L}\frac{dL}{dT} + \frac{1}{n}\frac{dn}{dT} \right) \tag{C-8}$$

and hence, the relative phase variation induced by a temperature change is written as:

$$\frac{\Delta\phi}{\Delta T \cdot \phi} = \frac{1}{L}\frac{dL}{dT} + \frac{1}{n}\frac{dn}{dT} \tag{C-9}$$

Using Equation 4-9, the photodetected frequency shift Δf_0 can be expressed as function of the optical phase shift and the optical delay τ (given by the optical fiber),

$$\frac{\Delta f_0}{\Delta\tau} = \frac{k}{\tau^2} = \frac{f_0}{\tau} \tag{C-10}$$

The frequency fluctuation relative to the phase fluctuation due to thermal perturbation is given by:

$$\frac{\Delta f_0}{\Delta T} = \frac{c}{2\pi L n}\frac{\Delta\phi}{\Delta T} \tag{C-11}$$

Replacing Equation C-8 into C-11, Δf_0 becomes:

$$\frac{\Delta f_0}{\Delta T} = f_0 \left(\frac{1}{L}\frac{dL}{dT} + \frac{1}{n}\frac{dn}{dT} \right) \tag{C-12}$$

The expression C-12 is only valid for fibers without a coating. For a coated optical fiber, the thermal expansion of the coating material and its mechanical influence give additional temperature constraints.

Appendix D

Parameters used in the predictive phase noise model

The parameters listed in Table **D-1** were used to predict the phase noise of the self-started VCSEL-based harmonic frequency generator (SVHFG).

Table D-1.: Parameters used to predict the phase noise

Name	Parameter	Value	Units
Center frequency of filter		1.250143	GHz
Filter bandwidth		2.021873	MHz
Optical fiber dispersion (C-band)	D_λ	17	$ps/(nm \cdot km)$
Rayleigh coefficient	α_S	3.2×10^{-2}	km^{-1}
Scattering coefficient	S_D	10^{-3}	
Attenuation coefficient	α	0.2	dB/km
Reflection coefficient	R_P	-40	dB
Photodetector impedance	R_{ph}	100	Ω
Amplifier input impedance 1	Z_A	50	Ω
Amplifier noise figure 1	NF_1	5	dB
Amplifier gain 1	A_1	38	dB
Amplifier noise figure 2	NF_2	5	dB
Amplifier Flicker noise 1	b_{-1}^1	-100 [2]	$dB \times rad^2/Hz$
Amplifier Flicker noise 2	b_{-1}^2	-100 [2]	$dB \times rad^2/Hz$

Bibliography

[1] R. J. Steed, L. Ponnampalam, M. J. Fice, C. C. Renaud, D. C. Rogers, D. G. Moodie, G. D. Maxwell, I. F. Lealman, M. J. Robertson, L. Pavlovic, L. Naglic, M. Vidmar, and A. J. Seeds, "Hybrid Integrated Optical Phase-Lock Loops for Photonic Terahertz Sources," *IEEE Journal of Selected Topics in Quantum Electronics*, vol. 17, pp. 210–217, jan 2011.

[2] E. Rubiola, *Phase Noise and Frequency Stability in Oscillators*. The Cambridge RF and Microwave Engineering Series, Cambridge: Cambridge University Press, 2008.

[3] N. Da Dalt and A. Sheikholeslami, *Understanding Jitter and Phase Noise: A Circuits and Systems Perspective*. Cambridge: Cambridge University Press, 2018.

[4] Y. Teng, Y. Chen, B. Zhang, J. Li, L. Lu, Y. Zhu, and P. Zhang, "Generation of Low Phase-Noise Frequency-Sextupled Signals Based on Multimode Optoelectronic Oscillator and Cascaded Mach-Zehnder Modulators," *IEEE Photonics Journal*, vol. 8, no. 4, pp. 1–8, 2016.

[5] M. Park, O. Kwon, W. Han, K. Lee, S. Park, and B. Yoo, "All-epitaxial InAlGaAs-InP VCSELs in the 1.3-1.6-μm wavelength range for CWDM band applications," *IEEE Photonics Technology Letters*, vol. 18, no. 16, pp. 1717–1719, 2006.

[6] H. H. Lu, C. Y. Li, H. W. Chen, C. M. Ho, M. T. Cheng, Z. Y. Yang, and C. K. Lu, "A 56 Gb/s PAM4 VCSEL-Based LiFi Transmission with Two-Stage Injection-Locked Technique," *IEEE Photonics Journal*, vol. 9, no. 1, pp. 1–8, 2017.

[7] R. S. Tucker and D. J. Pope, "Microwave Circuit Models of Semiconductor Injection Lasers," *IEEE Transactions on Microwave Theory and Techniques*, vol. 31, pp. 289–294, mar 1983.

[8] A. Bacou, *Caractérisation et modélisation optoélectronique de VCSELs à grande longueur d'onde pour sous-ensembles optiques intégrés*. PhD thesis, Université de Toulouse, 2008.

[9] D. Derickson, *Fiber Optic Test and Measurement.* Hewlett-Packard professional books, Prentice Hall PTR, 1998.

[10] K. Gheen, "Phase Noise Measurements Methods and Techniques," Tech. Rep. Application Note, Agilent Technologies, 2012.

[11] "3GPP TS 38.101-2: NR; User Equipment (UE) radio transmission and reception; Part 2: Range 2 Standalone."

[12] T. Nitsche, C. Cordeiro, A. B. Flores, E. W. Knightly, E. Perahia, and J. C. Widmer, "IEEE 802.11ad: directional 60 GHz communication for multi-Gigabit-per-second Wi-Fi [Invited Paper]," *IEEE Communications Magazine*, vol. 52, no. 12, pp. 132–141, 2014.

[13] D. Jäger, "Traveling-wave optoelectronic devices for microwave and optical applications," in *Proceedings of the Progress in Electromagnetics Research Symposium (PIERS)*, p. 327, 1991.

[14] A. Neyer and E. Voges, "Nonlinear electrooptic oscillator using an integrated interferometer," *Optics Communications*, vol. 37, no. 3, pp. 169–174, 1981.

[15] M. Varón Durán, A. Le Kernec, and J.-C. Mollier, "Opto-microwave source using a harmonic frequency generator driven by a VCSEL-based ring oscillator," in *Proceedings of the European Microwave Association*, vol. 3, pp. 248–253, EUMA European Microwave Association, 2007.

[16] A. Hayat, M. Varón, A. Bacou, A. Rissons, and J. C. Mollier, "2.49 GHz low phase-noise optoelectronic oscillator using 1.55μm VCSEL for avionics and aerospace applications," in *2008 IEEE International Meeting on Microwave Photonics jointly held with the 2008 Asia-Pacific Microwave Photonics Conference*, (Gold Coast, Qld, Australia), pp. 98–101, 2008.

[17] K. Y. Lau, "Gain switching of semiconductor injection lasers," *Applied Physics Letters*, vol. 52, no. 4, pp. 257–259, 1988.

[18] C. H. Lee, *Microwave Photonics, Second Edition.* Taylor & Francis, 2013.

[19] A. J. Seeds and K. J. Williams, "Microwave Photonics," *J. Lightwave Technol.*, vol. 24, no. 12, pp. 4628–4641, 2006.

[20] J. Yao, "A Tutorial on Microwave Photonics," *Photonics Society Newsletter*, vol. 26, no. 3, pp. 4–12, 2012.

[21] J. Capmany and D. Novak, "Microwave photonics combines two worlds," *Nature Photonics*, vol. 1, no. 6, pp. 319–330, 2007.

[22] S. Iezekiel, *Microwave Photonics: Devices and Applications.* Wiley - IEEE, John Wiley & Sons, 2009.

[23] A. Wootten and A. R. Thompson, "The Atacama Large Millimeter/Submillimeter Array," *Proceedings of the IEEE*, vol. 97, no. 8, pp. 1463–1471, 2009.

[24] P. E. Dewdney, P. J. Hall, R. T. Schilizzi, and T. J. L. W. Lazio, "The Square Kilometre Array," *Proceedings of the IEEE*, vol. 97, no. 8, pp. 1482–1496, 2009.

[25] K. P. Jackson, S. A. Newton, B. Moslehi, M. Tur, C. C. Cutler, J. W. Goodman, and H. Shaw, "Optical fiber delay-line signal processing," *IEEE Transactions on Microwave Theory and Techniques*, vol. MTT-33, no. 3, pp. 193–210, 1985.

[26] X. Zou, X. Liu, W. Li, P. Li, W. Pan, L. Yan, and L. Shao, "Optoelectronic oscillators (OEOs) to sensing, measurement, and detection," *IEEE Journal of Quantum Electronics*, vol. 52, no. 1, pp. 1–16, 2016.

[27] U. Gliese, T. N. Nielsen, S. Nørskov, and K. E. Stubkjær, "Multifunctional Fiber-Optic Microwave Links Based on Remote Heterodyne Detection," *IEEE Transactions on Microwave Theory and Techniques*, vol. 46, no. 5, pp. 458–468, 1998.

[28] G. Qi, J. Yao, J. Seregelyi, S. Paquet, and C. Bélisle, "Optical Generation and Distribution of Continuously Tunable Millimeter-Wave Signals Using an Optical Phase Modulator," *J. Lightwave Technol.*, vol. 23, no. 9, pp. 2687–2695, 2005.

[29] S. Pan and J. Yao, "Tunable Subterahertz Wave Generation Based on Photonic Frequency Sextupling Using a Polarization Modulator and a Wavelength-Fixed Notch Filter," *IEEE Transactions on Microwave Theory and Techniques*, vol. 58, no. 7, pp. 1967–1975, 2010.

[30] H. Kiuchi, T. Kawanishi, M. Yamada, T. Sakamoto, M. Tsuchiya, J. Amagai, and M. Izutsu, "High Extinction Ratio Mach Zehnder Modulator Applied to a Highly Stable Optical Signal Generator," *IEEE Transactions on Microwave Theory and Techniques*, vol. 55, no. 9, pp. 1964–1972, 2007.

[31] L. R. Hofer, D. B. Schaeffer, C. G. Constantin, and C. Niemann, "Bias Voltage Control in Pulsed Applications for Mach Zehnder Electrooptic Intensity Modulators," *IEEE Transactions on Control Systems Technology*, vol. 25, no. 5, pp. 1890–1895, 2017.

[32] J. Snoddy, Y. Li, F. Ravet, and X. Bao, "Stabilization of electro-optic modulator bias voltage drift using a lock-in amplifier and a proportional-integral-derivative controller in a distributed Brillouin sensor system," *Appl. Opt.*, vol. 46, pp. 1482–1485, mar 2007.

[33] K. Balakier, M. J. Fice, L. Ponnampalam, A. J. Seeds, and C. C. Renaud, "Monolithically Integrated Optical Phase Lock Loop for Microwave Photonics," *Journal of Lightwave Technology*, vol. 32, pp. 3893–3900, oct 2014.

[34] L. Goldberg, H. F. Taylor, J. F. Weller, and D. M. Bloom, "Microwave Signal Generation with Injection-Locked Laser-Diodes," *Electronics Letters*, vol. 19, no. 13, pp. 491–493, 1983.

[35] L. A. Johansson and A. J. Seeds, "Generation and Transmission of Millimeter-Wave Data-Modulated Optical Signals Using an Optical Injection Phase-Lock Loop," *J. Lightwave Technol.*, vol. 21, no. 2, p. 511, 2003.

[36] C. Muñoz, J. Coronel, J. Chamorro, A. Rissons, and M. Varón, "Microwave signal generation with optical injection locking," in *Latin America Optics and Photonics Conference, (Optical Society of America, 2016)*, 2016.

[37] R. Zhou, T. Shao, M. D. Gutierrez Pascual, F. Smyth, and L. P. Barry, "Injection Locked Wavelength De-Multiplexer for Optical Comb-Based Nyquist WDM System," *IEEE Photonics Technology Letters*, vol. 27, no. 24, pp. 2595–2598, 2015.

[38] C.-Y. Lin, Y.-C. Chi, C.-T. Tsai, H.-Y. Wang, H.-Y. Chen, M. Xu, G.-K. Chang, and G.-R. Lin, "Millimeter-Wave Carrier Embedded Dual-Color Laser Diode for 5G MMW oF Link," *J. Lightwave Technol.*, vol. 35, no. 12, pp. 2409–2420, 2017.

[39] X. Li, *Body Matched Antennas for Microwave Medical Applications.* PhD thesis, Karlsruher Institut für Technologie KIT, 2013.

[40] C. Li, M. R. Tofighi, D. Schreurs, and T.-S. J. Horng, *Principles and Applications of RF/Microwave in Healthcare and Biosensing.* Elsevier Science, 2016.

[41] Y. Liu, C. Hu, Y. Dong, B. Xu, W. Zhan, and C. Sun, "Geometric accuracy of remote sensing images over oceans: The use of global offshore platforms," *Remote Sensing of Environment*, vol. 222, pp. 244–266, 2019.

[42] J. A. Nanzer, *Microwave and Millimeter-wave Remote Sensing for Security Applications.* Artech House, 2012.

[43] T. Nagatsuma, S. Hisatake, M. Fujita, H. H. N. Pham, K. Tsuruda, S. Kuwano, and J. Terada, "Millimeter-Wave and Terahertz-Wave Applications Enabled by Photonics," *IEEE Journal of Quantum Electronics*, vol. 52, pp. 1–12, jan 2016.

[44] J. Yao, "Microwave photonics for 5G," in *Broadband Access Communication Technologies XIII*, vol. 10945, pp. 8–16, 2019.

[45] T. Berceli and P. R. Herczfeld, "Microwave Photonics - A Historical Perspective," *IEEE Transactions on Microwave Theory and Techniques*, vol. 58, pp. 2992–3000, nov 2010.

[46] X. Xu, J. Wu, T. G. Nguyen, T. Moein, S. T. Chu, B. E. Little, R. Morandotti, A. Mitchell, and D. J. Moss, "Photonic microwave true time delays for phased array antennas using a 49 GHz FSR integrated optical micro-comb source," *Photon. Res.*, vol. 6, no. 5, pp. B30–B36, 2018.

[47] P. Zheng, C. Wang, X. Xu, J. Li, D. Lin, G. Hu, R. Zhang, B. Yun, and Y. Cui, "A Seven Bit Silicon Optical True Time Delay Line for Ka-Band Phased Array Antenna," *IEEE Photonics Journal*, vol. 11, no. 4, pp. 1–9, 2019.

[48] Z. Tang, F. Zhang, and S. Pan, "60-GHz RoF System for Dispersion-Free Transmission of HD and Multi-Band 16QAM," *IEEE Photonics Technology Letters*, vol. 30, no. 14, pp. 1305–1308, 2018.

[49] Y. Tian, K. Lee, C. Lim, and A. Nirmalathas, "60 GHz Analog Radio-Over-Fiber Fronthaul Investigations," *Journal of Lightwave Technology*, vol. 35, pp. 4304–4310, oct 2017.

[50] Y.-H. Hung, J.-H. Yan, K.-M. Feng, and S.-K. Hwang, "Photonic microwave carrier recovery using period-one nonlinear dynamics of semiconductor lasers for OFDM-RoF coherent detection," *Opt. Lett.*, vol. 42, no. 12, pp. 2402–2405, 2017.

[51] Y. Tong, C. Chow, G. Chen, C. Peng, C. Yeh, and H. K. Tsang, "Integrated Silicon Photonics Remote Radio Frontend (RRF) for Single-Sideband (SSB) Millimeter-Wave Radio-Over-Fiber (ROF) Systems," *IEEE Photonics Journal*, vol. 11, no. 2, pp. 1–8, 2019.

[52] Y.-C. Chi and G.-R. Lin, "Optoelectronic Oscillators," in *Wiley Encyclopedia of Electrical and Electronics Engineering* (J. Webster, ed.), pp. 1–12, 2016.

[53] P. Devgan, "A Review of Optoelectronic Oscillators for High Speed Signal Processing Applications," *ISRN Electronics*, vol. 2013, pp. 1–16, 2013.

[54] T. von Lerber, S. Honkanen, A. Tervonen, H. Ludvigsen, and F. Küppers, "Optical clock recovery methods: Review (Invited)," *Optical Fiber Technology*, vol. 15, no. 4, pp. 363–372, 2009.

[55] H. Tsuchida, "Simultaneous Prescaled Clock Recovery and Serial-to-Parallel Conversion of Data Signals Using a Polarization Modulator-Based Optoelectronic Oscillator," *Journal of Lightwave Technology*, vol. 27, no. 17, pp. 3777–3782, 2009.

[56] H. Tsuchida, "Subharmonic Optoelectronic Oscillator," *IEEE Photonics Technology Letters*, vol. 20, no. 17, pp. 1509–1511, 2008.

[57] S. Pan and J. Yao, "Optical Clock Recovery Using a Polarization-Modulator-Based Frequency-Doubling Optoelectronic Oscillator," *Journal of Lightwave Technology*, vol. 27, no. 16, pp. 3531–3539, 2009.

[58] Q. Wang, L. Huo, Y. Xing, D. Wang, X. Chen, C. Lou, and B. Zhou, "Gaussian-like dual-wavelength prescaled clock recovery with simultaneous frequency-doubled clock recovery using an optoelectronic oscillator," *Optics Express*, vol. 22, no. 3, pp. 2798–2806, 2014.

[59] L. Huo, Q. Wang, and C. Lou, "Multifunctional Optoelectronic Oscillator Based on Cascaded Modulators," *IEEE Photonics Technology Letters*, vol. 28, no. 4, pp. 520–523, 2016.

[60] J. Lasri, P. Devgan, Renyong Tang, and P. Kumar, "Ultra-low timing jitter 40 Gb/s

clock recovery using a novel electroabsorption-modulator-based self-starting optoelectronic oscillator," in *The 16th Annual Meeting of the IEEE Lasers and Electro-Optics Society, 2003. LEOS 2003.*, vol. 1, pp. 390–391, oct 2003.

[61] J. Lasri, P. Devgan, Renyong Tang, and P. Kumar, "Ultralow timing jitter 40-Gb/s clock recovery using a self-starting optoelectronic oscillator," *IEEE Photonics Technology Letters*, vol. 16, pp. 263–265, jan 2004.

[62] P. Wu and J. Ma, "BPSK optical mm-wave signal generation by septupling frequency via a single optical phase modulator," *Optics Communications*, vol. 374, pp. 69–74, 2016.

[63] Y. Chi and G. Lin, "A Q-Factor Enhanced Optoelectronic Oscillator for 40-Gbit/s Pulsed RZ-OOK Transmission," *IEEE Transactions on Microwave Theory and Techniques*, vol. 62, no. 12, pp. 3216–3223, 2014.

[64] J. Rutman, "Characterization of phase and frequency instabilities in precision frequency sources: Fifteen years of progress," *Proceedings of the IEEE*, vol. 66, no. 9, pp. 1048–1075, 1978.

[65] "IEEE Standard Definitions of Physical Quantities for Fundamental Frequency and Time Metrology—Random Instabilities," *IEEE Std 1139-2008*, pp. c1–35, feb 2009.

[66] J. A. Barnes, A. R. Chi, L. S. Cutler, D. J. Healey, D. B. Leeson, T. E. McGunigal, J. A. Mullen, W. L. Smith, R. L. Sydnor, R. F. C. Vessot, and G. M. R. Winkler, "Characterization of Frequency Stability," *IEEE Transactions on Instrumentation and Measurement*, vol. IM-20, no. 2, pp. 105–120, 1971.

[67] D. B. Leeson, "A simple model of feedback oscillator noise spectrum," *Proceedings of the IEEE*, vol. 54, no. 2, pp. 329–330, 1966.

[68] E. Rubiola and V. Giordano, "On the 1/f frequency noise in ultra-stable quartz oscillators," *IEEE Transactions on Ultrasonics, Ferroelectrics, and Frequency Control*, vol. 54, no. 1, pp. 15–22, 2007.

[69] J. Rutman, "Instabilite de frequence des oscillateurs (Frequency instability of oscillators)," *L'Onde Electrique*, vol. 52, no. 11, pp. 480–487, 1972.

[70] D. W. Allan, "Statistics of atomic frequency standards," *Proceedings of the IEEE*, vol. 54, no. 2, pp. 221–230, 1966.

[71] W. Riley and D. A. Howe, *Handbook of Frequency Stability Analysis.* National Institute of Standards and Technology (NIST), U.S. Department of Commerce, NIST Special Publication 1065, 2008.

[72] D. W. Allan and J. A. Barnes, "A Modified "Allan Variance" with Increased Oscillator Characterization Ability," in *Proceedings of the 35th Annual Frequency Control Symposium*, pp. 470–475, 1981.

[73] S. Bregni, *Synchronization of Digital Telecommunications Networks.* JohnWiley & Sons, 2002.

[74] "IEEE Draft Standard for Jitter and Phase Noise," *IEEE P2414*, p. 40, apr 2019.

[75] International Telecommunication Union (ITU), "ITU-T Recommendation G.810 (08/96), Definitions and Terminology for Synchronization Networks," 1996.

[76] Tektronix, "Understanding and Characterizing Timing Jitter: Primer," October 2003.

[77] JEDEC Solid State Technology Association, "Standard JESD65B, Definition of Skew Specifications for Standard Logic Devices," 2003.

[78] A. Neyer and E. Voges, "High-frequency electro-optic oscillator using an integrated interferometer," *Applied Physics Letters*, vol. 40, no. 1, pp. 6–8, 1982.

[79] X. S. Yao and L. Maleki, "High frequency optical subcarrier generator," *Electronics Letters*, vol. 30, no. 18, pp. 1525–1526, 1994.

[80] X. S. Yao and L. Maleki, "A novel photonic oscillator," in *The Telecommunications and Data Acquisition Report*, pp. 32–43, 1995.

[81] X. S. Yao and L. Maleki, "Optoelectronic microwave oscillator," *J. Opt. Soc. Am. B*, vol. 13, no. 8, pp. 1725–1735, 1996.

[82] X. S. Yao and L. Maleki, "Optoelectronic oscillator for photonic systems," *IEEE Journal of Quantum Electronics*, vol. 32, no. 7, pp. 1141–1149, 1996.

[83] H. Sung, X. Zhao, E. K. Lau, D. Parekh, C. J. Chang-Hasnain, and M. C. Wu, "Optoelectronic Oscillators Using Direct-Modulated Semiconductor Lasers Under Strong Optical Injection," *IEEE Journal of Selected Topics in Quantum Electronics*, vol. 15, no. 3, pp. 572–577, 2009.

[84] L. Huang, Q. Yu, L. Deng, S. Fu, M. Tang, P. P. Shum, and D. Liu, "Widely tunable optoelectronic oscillator using phase modulation to intensity modulation conversion and a heterogeneous multicore fiber," in *2017 Opto-Electronics and Communications Conference (OECC) and Photonics Global Conference (PGC)*, pp. 1–3, 2017.

[85] Y. Shao, X. Han, Q. Ye, B. Zhu, Y. Dai, C. Wang, and M. Zhao, "Low Power RF Signal Detection Using a High Gain Tunable OEO based on Equivalent Phase Modulation," *Journal of Lightwave Technology*, p. 1, 2019.

[86] T. Sakamoto, T. Kawanishi, and M. Izutsu, "Optoelectronic oscillator using a LiNbO3 phase modulator for self-oscillating frequency comb generation," *Optics letters*, vol. 31, pp. 811–813, mar 2006.

[87] Z. Tang, S. Pan, D. Zhu, R. Guo, Y. Zhao, M. Pan, D. Ben, and J. Yao, "Tunable Optoelectronic Oscillator Based on a Polarization Modulator and a Chirped FBG," *IEEE Photonics Technology Letters*, vol. 24, no. 17, pp. 1487–1489, 2012.

[88] T. Wu, C. Zhang, H. Huang, J. Li, S. Fu, and K. Qiu, "Triangular waveform genera-tion based on polarization modulated optoelectronic oscillator," in *2017 International Topical Meeting on Microwave Photonics (MWP)*, pp. 1–4, oct 2017.

[89] A. Liu, J. Liu, J. Dai, Y. Dai, F. Yin, J. Li, Y. Zhou, and K. Xu, "High-rate and low-jitter optical pulse generation based on an optoelectronic oscillator using a cascaded polarization modulator and phase modulator," in *2017 16th International Conference on Optical Communications and Networks (ICOCN)*, pp. 1–3, 2017.

[90] C. W. Nelson, A. Hati, D. A. Howe, and W. Zhou, "Microwave Optoelectronic Oscil-lator with Optical Gain," in *2007 IEEE International Frequency Control Symposium Joint with the 21st European Frequency and Time Forum*, pp. 1014–1019, 2007.

[91] P. S. Devgan, V. J. Urick, J. F. Diehl, and K. J. Williams, "Improvement in the Phase Noise of a 10 GHz Optoelectronic Oscillator Using All-Photonic Gain," *Journal of Lightwave Technology*, vol. 27, no. 15, pp. 3189–3193, 2009.

[92] P. S. Devgan, V. J. Urick, J. D. McKinney, and K. J. Williams, "A Low-Jitter Master-Slave Optoelectronic Oscillator Employing All-Photonic Gain," in *2007 Interntional Topical Meeting on Microwave Photonics*, pp. 70–73, oct 2007.

[93] W. Loh, S. Yegnanarayanan, J. Klamkin, S. M. Duff, J. J. Plant, F. J. O'Donnell, and P. W. Juodawlkis, "Amplifier-free slab-coupled optical waveguide optoelectronic oscillator systems," *Optics Express*, vol. 20, no. 17, pp. 19589–19598, 2012.

[94] W. Zhou, O. Okusaga, C. Nelson, D. Howe, and G. Carter, "10 GHz dual loop opto-electronic oscillator without RF-amplifiers," in *Optoelectronic Integrated Circuits X*, vol. 6897, pp. 199–204, International Society for Optics and Photonics, SPIE, 2008.

[95] J. Cho, H. Kim, and H. Sung, "Reduction of Spurious Tones and Phase Noise in Dual-Loop OEO by Loop-Gain Control," *IEEE Photonics Technology Letters*, vol. 27, no. 13, pp. 1391–1393, 2015.

[96] J. Cho and H. Sung, "Simple Optoelectronic Oscillators Using Direct Modulation of Dual-Section Distributed-Feedback Lasers," *IEEE Photonics Technology Letters*, vol. 24, no. 23, pp. 2172–2174, 2012.

[97] M. Liao, J. Xiao, Y. Huang, H. Weng, J. Han, Z. Xiao, and Y. Yang, "Tunable Opto-electronic Oscillator Using a Directly Modulated Microsquare Laser," *IEEE Photonics Technology Letters*, vol. 30, no. 13, pp. 1242–1245, 2018.

[98] M.-L. Liao, Y.-Z. Huang, H.-Z. Weng, J.-Y. Han, Z.-X. Xiao, J.-L. Xiao, and Y.-D. Yang, "Narrow-linewidth microwave generation by an optoelectronic oscillator with a directly modulated microsquare laser," *Optics letters*, vol. 42, pp. 4251–4254, nov 2017.

[99] B. Pan, D. Lu, L. Zhang, and L. Zhao, "A Widely Tunable Optoelectronic Oscillator Based on Directly Modulated Dual-Mode Laser," *IEEE Photonics Journal*, vol. 7,

no. 6, pp. 1–7, 2015.

[100] H. Hasegawa, Y. Oikawa, and M. Nakazawa, "A 10-GHz optoelectronic oscillator at 850 nm using a single-mode VCSEL and a photonic crystal fiber," *IEEE Photonics Technology Letters*, vol. 19, no. 19, pp. 1451–1453, 2007.

[101] W. Li and J. Yao, "A Wideband Frequency Tunable Optoelectronic Oscillator Incorporating a Tunable Microwave Photonic Filter Based on Phase-Modulation to Intensity-Modulation Conversion Using a Phase-Shifted Fiber Bragg Grating," *IEEE Transactions on Microwave Theory and Techniques*, vol. 60, no. 6, pp. 1735–1742, 2012.

[102] B. Yang, X. Jin, X. Zhang, S. Zheng, H. Chi, and Y. Wang, "A Wideband Frequency-Tunable Optoelectronic Oscillator Based on a Narrowband Phase-Shifted FBG and Wavelength Tuning of Laser," *IEEE Photonics Technology Letters*, vol. 24, pp. 73–75, jan 2012.

[103] H. Peng, Y. Xu, X. Peng, X. Zhu, R. Guo, F. Chen, H. Du, Y. Chen, C. Zhang, L. Zhu, W. Hu, and Z. Chen, "Wideband tunable optoelectronic oscillator based on the deamplification of stimulated Brillouin scattering," *Opt. Express*, vol. 25, no. 9, pp. 10287–10305, 2017.

[104] S. E. Hosseini, A. Banai, and F. X. Kärtner, "Tunable Low-Jitter Low-Drift Spurious-Free Transposed-Frequency Optoelectronic Oscillator," *IEEE Transactions on Microwave Theory and Techniques*, vol. 65, no. 7, pp. 2625–2635, 2017.

[105] Z. Fan, Q. Qiu, J. Su, and T. Zhang, "Tunable low-drift spurious-free optoelectronic oscillator based on injection locking and time delay compensation," *Opt. Lett.*, vol. 44, no. 3, pp. 534–537, 2019.

[106] C. Chang, M. J. Wishon, D. Choi, J. Dong, K. Merghem, A. Ramdane, F. Lelarge, A. Martinez, A. Locquet, and D. S. Citrin, "Tunable X-Band Optoelectronic Oscillators Based on External-Cavity Semiconductor Lasers," *IEEE Journal of Quantum Electronics*, vol. 53, no. 3, pp. 1–6, 2017.

[107] R. Pantell, "The laser oscillator with an external signal," *Proceedings of the IEEE*, vol. 53, no. 5, pp. 474–477, 1965.

[108] A. Hayat, A. Bacou, A. Rissons, J. C. Mollier, V. Iakovlev, A. Sirbu, and E. Kapon, "Long Wavelength VCSEL-by-VCSEL Optical Injection Locking," *IEEE Transactions on Microwave Theory and Techniques*, vol. 57, no. 7, pp. 1850–1858, 2009.

[109] J. Coronel, *Injection Locked VCSEL Based Oscillator - ILVBO*. PhD thesis, Universidad Nacional de Colombia and Institut Superieur de l'Aeronautique et de l'Espace, 2016.

[110] J. F. Coronel, M. Varon, and A. Rissons, "Phase noise analysis of a 10-GHz optical injection-locked vertical-cavity surface-emitting laser-based optoelectronic oscillator," *Optical Engineering*, vol. 55, no. 9, pp. 1 – 4, 2016.

[111] M. Shi, L. Yi, and W. Hu, "High-Resolution Brillouin Optoelectronic Oscillator Using High-Order Sideband Injection-Locking," *IEEE Photonics Technology Letters*, vol. 31, no. 7, pp. 513–516, 2019.

[112] Y. Zhang, Y. Xia, J. Zou, Z. Zhang, S. Zhang, J. Yuan, and Y. Liu, "Modulator-free optoelectronic oscillator based on an optically injected semiconductor laser," in *Semiconductor Lasers and Applications VIII* (N. H. Zhu and W. H. Hofmann, eds.), vol. 10812, pp. 39–44, International Society for Optics and Photonics, SPIE, 2018.

[113] Weimin Zhou and G. Blasche, "Injection-locked dual opto-electronic oscillator with ultra-low phase noise and ultra-low spurious level," *IEEE Transactions on Microwave Theory and Techniques*, vol. 53, no. 3, pp. 929–933, 2005.

[114] O. Okusaga, W. Zhou, E. Levy, M. Horowitz, G. Carter, and C. Menyuk, "Experimental and simulation study of dual injection-locked OEOs," in *2009 IEEE International Frequency Control Symposium Joint with the 22nd European Frequency and Time forum*, pp. 875–879, 2009.

[115] O. Okusaga, E. J. Adles, E. C. Levy, W. Zhou, G. M. Carter, C. R. Menyuk, and M. Horowitz, "Spurious mode reduction in dual injection-locked optoelectronic oscillators," *Opt. Express*, vol. 19, pp. 5839–5854, mar 2011.

[116] D. Marpaung, C. Roeloffzen, R. Heideman, A. Leinse, S. Sales, and J. Capmany, "Integrated microwave photonics," *Laser & Photonics Reviews*, vol. 7, no. 4, pp. 506–538, 2013.

[117] R. Maram, S. Kaushal, J. Azaña, and L. R. Chen, "Recent Trends and Advances of Silicon-Based Integrated Microwave Photonics," *Photonics*, vol. 6, no. 1, pp. 1–40, 2019.

[118] D. Marpaung, J. Yao, and J. Capmany, "Integrated microwave photonics," *Nature Photonics*, vol. 13, pp. 80–90, 2019.

[119] J. Tang, T. Hao, W. Li, D. Domenech, R. Baños, P. Muñoz, N. Zhu, J. Capmany, and M. Li, "Integrated optoelectronic oscillator," *Optics Express*, vol. 26, no. 9, pp. 12257–12265, 2018.

[120] X. S. Yao, L. Maleki, Yu Ji, G. Lutes, and Meirong Tu, "Dual-loop opto-electronic oscillator," in *Proceedings of the 1998 IEEE International Frequency Control Symposium*, pp. 545–549, 1998.

[121] X. S. Yao and L. Maleki, "Multiloop optoelectronic oscillator," *IEEE Journal of Quantum Electronics*, vol. 36, pp. 79–84, jan 2000.

[122] D. Eliyahu and L. Maleki, "Low phase noise and spurious level in multi-loop opto-electronic oscillators," in *IEEE International Frequency Control Symposium and PDA Exhibition Jointly with the 17th European Frequency and Time Forum*, pp. 405–410, 2003.

[123] K. Mikitchuk, A. Chizh, and S. Malyshev, "Double-Loop All-Optical Gain Optoelectronic Oscillator with Low Phase Noise and Spurs Level," in *2018 International Topical Meeting on Microwave Photonics (MWP)*, pp. 1–4, oct 2018.

[124] F. Fan, J. Hu, W. Zhu, Y. Gu, X. Han, and M. Zhao, "Dual-loop optoelectronic oscillator based on a compact balanced detection scheme," *Optical Engineering*, vol. 56, no. 2, pp. 1–6, 2017.

[125] L. Huang, L. Deng, S. Fu, M. Tang, M. Cheng, M. Zhang, and D. Liu, "Stable and Compact Dual-Loop Optoelectronic Oscillator Using Self-Polarization-Stabilization Technique and Multicore Fiber," *Journal of Lightwave Technology*, vol. 36, pp. 5196–5202, nov 2018.

[126] S. García and I. Gasulla, "Experimental demonstration of multi-cavity optoelectronic oscillation over a multicore fiber," *Optics Express*, vol. 25, pp. 23663–23668, oct 2017.

[127] Y. Shao, X. Han, Y. Bing, M. Li, Y. Gu, and M. Zhao, "Polarization multiplexed dual-loop OEO based on a phase-shifted fiber bragg grating," in *2017 International Topical Meeting on Microwave Photonics (MWP)*, pp. 1–4, oct 2017.

[128] P. H. Merrer, H. Brahimi, and O. Llopis, "Optical techniques for microwave frequency stabilization : Resonant versus delay line approaches and related modelling problems," in *2008 International Topical Meeting on Microwave Photonics jointly held with the 2008 Asia-Pacific Microwave Photonics Conference*, pp. 146–149, 2008.

[129] K. Saleh, *High spectral purity microwave sources based on optical resonators.* PhD thesis, Université de Toulouse, 2012.

[130] Z. Abdallah, *Microwave sources based on high quality factor resonators; Modeling, Optimization and Metrology.* PhD thesis, Université Toulouse 3 Paul Sabatier, 2016.

[131] R. W. P. Drever, J. L. Hall, F. V. Kowalski, J. Hough, G. M. Ford, A. J. Munley, and H. Ward, "Laser phase and frequency stabilization using an optical resonator," *Applied Physics B*, vol. 31, no. 2, pp. 97–105, 1983.

[132] L. Wang, N. Zhu, W. Li, and J. Liu, "A Frequency-Doubling Optoelectronic Oscillator Based on a Dual-Parallel Mach-Zehnder Modulator and a Chirped Fiber Bragg Grating," *IEEE Photonics Technology Letters*, vol. 23, pp. 1688–1690, nov 2011.

[133] X. Liu, W. Pan, X. Zou, D. Zheng, L. Yan, and B. Luo, "Frequency-Doubling Optoelectronic Oscillator Using DSB-SC Modulation and Carrier Recovery Based on Stimulated Brillouin Scattering," *IEEE Photonics Journal*, vol. 5, no. 2, 2013.

[134] D. Zhu, S. Liu, D. Ben, and S. Pan, "Frequency-Quadrupling Optoelectronic Oscillator for Multichannel Upconversion," *IEEE Photonics Technology Letters*, vol. 25, no. 5, pp. 426–429, 2013.

[135] D. Zhu, S. Pan, and D. Ben, "Tunable Frequency-Quadrupling Dual-Loop Optoelec-

tronic Oscillator," *IEEE Photonics Technology Letters*, vol. 24, no. 3, pp. 194–196, 2012.

[136] A. Chiba, Y. Akamatsu, and K. Takada, "RF Frequency Sextupling Utilizing a Single Mach-Zehnder Optical Modulator possessing external-load RF terminals," in *Conference on Lasers and Electro-Optics*, p. SF1G.8, Optical Society of America, 2016.

[137] Y. Zhang and S. Pan, "Experimental demonstration of frequency-octupled millimeter-wave signal generation based on a dual-parallel Mach-Zehnder modulator," in *2012 IEEE MTT-S International Microwave Workshop Series on Millimeter Wave Wireless Technology and Applications*, pp. 1–4, 2012.

[138] M. Hasan and T. J. Hall, "A photonic frequency octo-tupler with reduced RF drive power and extended spurious sideband suppression," *Optics & Laser Technology*, vol. 81, pp. 115–121, 2016.

[139] Y. Fu, X. Zhang, B. Hraimel, T. Liu, and D. Shen, "Mach-Zehnder: A Review of Bias Control Techniques for Mach-Zehnder Modulators in Photonic Analog Links," *IEEE Microwave Magazine*, vol. 14, pp. 102–107, nov 2013.

[140] Y. Gao, A. Wen, Q. Yu, N. Li, G. Lin, S. Xiang, and L. Shang, "Microwave Generation With Photonic Frequency Sextupling Based on Cascaded Modulators," *IEEE Photonics Technology Letters*, vol. 26, no. 12, pp. 1199–1202, 2014.

[141] X. Li, J. Yu, Z. Zhang, J. Xiao, and G.-K. Chang, "Photonic vector signal generation at W-band employing an optical frequency octupling scheme enabled by a single MZM," *Optics Communications*, vol. 349, pp. 6–10, 2015.

[142] Z. Zhu, S. Zhao, X. Li, K. Qu, and T. Lin, "Photonic generation of versatile frequency-doubled microwave waveforms via a dual-polarization modulator," *Optics Communications*, vol. 384, pp. 1–6, 2017.

[143] X. Chen, L. Xia, and D. Huang, "Generalized study of microwave frequency multiplication based on two cascaded MZMs," *Optik*, vol. 127, no. 8, pp. 4061–4067, 2016.

[144] H. Zhou, Z. Zheng, and Q. Wan, "Radio over fiber system carrying OFDM signal based on optical octuple frequency technique," *Optics Communications*, vol. 349, pp. 54–59, 2015.

[145] Y. Gao, A. Wen, W. Jiang, D. Liang, W. Liu, and S. Xiang, "Photonic Microwave Generation With Frequency Octupling Based on a DP-QPSK Modulator," *IEEE Photonics Technology Letters*, vol. 27, pp. 2260–2263, nov 2015.

[146] P. O. Hedekvist, B. . Olsson, and A. Wiberg, "Microwave harmonic frequency generation utilizing the properties of an optical phase Modulator," *Journal of Lightwave Technology*, vol. 22, no. 3, pp. 882–886, 2004.

[147] D. Eliyahu, D. Seidel, and L. Maleki, "RF Amplitude and Phase-Noise Reduction of

an Optical Link and an Opto-Electronic Oscillator," *IEEE Transactions on Microwave Theory and Techniques*, vol. 56, no. 2, pp. 449–456, 2008.

[148] O. Okusaga, J. P. Cahill, A. Docherty, C. R. Menyuk, W. Zhou, and G. M. Carter, "Suppression of Rayleigh-scattering-induced noise in OEOs," *Optics Express*, vol. 21, pp. 22255–22262, sep 2013.

[149] K. Volyanskiy, Y. K. Chembo, L. Larger, and E. Rubiola, "Contribution of Laser Frequency and Power Fluctuations to the Microwave Phase Noise of Optoelectronic Oscillators," *Journal of Lightwave Technology*, vol. 28, no. 18, pp. 2730–2735, 2010.

[150] M.-E. Belkin, L. Belkin, A. Loparev, A.-S. Sigov, and V. Iakovlev, "Long Wavelength VCSELs and VCSEL-Based Processing of Microwave Signals," in *Optoelectronics - Materials and Devices*, ch. 6, Rijeka: IntechOpen, 2015.

[151] K. Koizumi, M. Yoshida, and M. Nakazawa, "A 10-GHz Optoelectronic Oscillator at 1.1 μm Using a Single-Mode VCSEL and a Photonic Crystal Fiber," *IEEE Photonics Technology Letters*, vol. 22, no. 5, pp. 293–295, 2010.

[152] J. Coronel, C. D. Muñoz, M. Varón, F. Destic, A. Rissons, V. Rodrigues, and K. Bougueroua, "X-band and Ku-band VCSEL-based optoelectronic oscillators using on-chip laser," *Optical Engineering*, vol. 58, no. 7, pp. 1–4, 2019.

[153] Y. Shao, X. Han, M. Li, Q. Liu, and M. Zhao, "Microwave Downconversion by a Tunable Optoelectronic Oscillator Based on PS-FBG and Polarization-Multiplexed Dual loop," *IEEE Transactions on Microwave Theory and Techniques*, vol. 67, no. 5, pp. 2095–2102, 2019.

[154] G. Charalambous, G. K. M. Hasanuzzaman, A. Perentos, and S. Iezekiel, "High-Q wavelength division multiplexed optoelectronic oscillator based on a cascaded multi-loop topology," *Optics Communications*, vol. 387, pp. 361–365, 2017.

[155] K. Saleh, O. Llopis, and G. Cibiel, "Optical Scattering Induced Noise in Fiber Ring Resonators and Optoelectronic Oscillators," *Journal of Lightwave Technology*, vol. 31, no. 9, pp. 1433–1446, 2013.

[156] P.-H. Merrer, K. Saleh, O. Llopis, S. Berneschi, F. Cosi, and G. N. Conti, "Characterization technique of optical whispering gallery mode resonators in the microwave frequency domain for optoelectronic oscillators," *Applied Optics*, vol. 51, no. 20, pp. 4742–4748, 2012.

[157] E. N. Ivanov and M. E. Tobar, "Low phase-noise sapphire crystal microwave oscillators: current status," *IEEE Transactions on Ultrasonics, Ferroelectrics, and Frequency Control*, vol. 56, no. 2, pp. 263–269, 2009.

[158] M. Regis, O. Llopis, B. Van Haaren, R. Plana, A. Gruhle, J. Rayssac, and J. Graffeuil, "Ultra low phase noise C and X band bipolar transistors dielectric resonator oscillators," in *Proceedings of the 1998 IEEE International Frequency Control Symposium*

(Cat. No.98CH36165), pp. 507–511, 1998.

[159] M. Feng, C. Wu, and N. Holonyak, "Oxide-Confined VCSELs for High-Speed Optical Interconnects," *IEEE Journal of Quantum Electronics*, vol. 54, no. 3, pp. 1–15, 2018.

[160] International Telecommunication Union, *Optical Fibres, Cables and Systems*. Handbooks on Standardization, 2010.

[161] I. Melngailis, "Longitudinal Injection-Plasma laser of InSb," *Applied Physics Letters*, vol. 6, no. 3, pp. 59–60, 1965.

[162] H. Soda, K. Iga, C. Kitahara, and Y. Suematsu, "GaInAsP/InP Surface Emitting Injection Lasers," *Japanese Journal of Applied Physics*, vol. 18, no. 12, pp. 2329–2330, 1979.

[163] Y. Motegi, H. Soda, and K. Iga, "Surface-emitting GaInAsP/InP injection laser with short cavity length," *Electronics Letters*, vol. 18, no. 11, pp. 461–463, 1982.

[164] H. Soda, Y. Motegi, and K. Iga, "GaInAsP/InP surface emitting injection lasers with short cavity length," *IEEE Journal of Quantum Electronics*, vol. 19, no. 6, pp. 1035–1041, 1983.

[165] Y. H. Lee, J. L. Jewell, A. Scherer, S. L. McCall, J. P. Harbison, and L. T. Florez, "Room-temperature continuous-wave vertical-cavity single-quantum-well microlaser diodes," *Electronics Letters*, vol. 25, no. 20, pp. 1377–1378, 1989.

[166] F. Koyama, S. Kinoshita, and K. Iga, "Room-temperature continuous wave lasing characteristics of a GaAs vertical cavity surface-emitting laser," *Applied Physics Letters*, vol. 55, no. 3, pp. 221–222, 1989.

[167] J. L. Jewell, A. Scherer, S. L. McCall, Y. H. Lee, S. Walker, J. P. Harbison, and L. T. Florez, "Low-threshold electrically pumped vertical-cavity surface-emitting microlasers," *Electronics Letters*, vol. 25, no. 17, pp. 1123–1124, 1989.

[168] T. Numai, *Fundamentals of Semiconductor Lasers*. Springer Series in Optical Sciences, Springer Japan, 2014.

[169] P. Moser, *Energy-Efficient VCSELs for Optical Interconnects*. Springer Theses, Springer International Publishing, 2015.

[170] C. J. Chang-Hasnain, J. P. Harbison, G. Hasnain, A. C. Von Lehmen, L. T. Florez, and N. G. Stoffel, "Dynamic, polarization, and transverse mode characteristics of vertical cavity surface emitting lasers," *IEEE Journal of Quantum Electronics*, vol. 27, no. 6, pp. 1402–1409, 1991.

[171] P. Westbergh, J. S. Gustavsson, and A. Larsson, "VCSEL Arrays for Multicore Fiber Interconnects With an Aggregate Capacity of 240 Gb/s," *IEEE Photonics Technology Letters*, vol. 27, no. 3, pp. 296–299, 2015.

[172] M. E. Warren, D. Podva, P. Dacha, M. K. Block, C. J. Helms, J. Maynard, and R. F. Carson, "Low-divergence high-power VCSEL arrays for lidar application," in *Vertical-Cavity Surface-Emitting Lasers XXII*, vol. 10552, pp. 72–81, International Society for Optics and Photonics, SPIE, 2018.

[173] R. Michalzik, *VCSELs: Fundamentals, Technology and Applications of Vertical-Cavity Surface-Emitting Lasers.* Springer Series in Optical Sciences, Springer Berlin Heidelberg, 2012.

[174] R. Jager, M. Grabherr, C. Jung, R. Michalzik, G. Reiner, B. Weigl, and K. J. Ebeling, "57% wallplug efficiency oxide-confined 850 nm wavelength GaAs VCSELs," *Electronics Letters*, vol. 33, no. 4, pp. 330–331, 1997.

[175] Z. Tan, C. Yang, Y. Zhu, Z. Xu, K. Zou, F. Zhang, and Z. Wang, "A 70 Gbps NRZ optical link based on 850 nm band-limited VCSEL for data-center intra-connects," *Science China Information Sciences*, vol. 61, no. 8, 2018.

[176] H. Moench, S. Gronenborn, X. Gu, R. Gudde, M. Herper, J. Kolb, M. Miller, M. Smeets, and A. Weigl, "VCSELs in short-pulse operation for time-of-flight applications," in *Vertical-Cavity Surface-Emitting Lasers XXII*, vol. 10552, pp. 82–88, SPIE, 2018.

[177] G. Drake, W. S. Fernando, R. W. Stanek, and D. G. Underwood, "Modulator based high bandwidth optical readout for {HEP} detectors," *Journal of Instrumentation*, vol. 8, no. 02, 2013.

[178] A. Consoli, *Short Pulse Generation From Semiconductor Lasers: Characterization, Modeling And Applications.* PhD thesis, Universidad Politécnica de Madrid, 2011.

[179] T. Baba, Y. Yogo, K. Suzuki, F. Koyama, and K. Iga, "Near room temperature continuous wave lasing characteristics of GaInAsP/InP surface emitting laser," *Electronics Letters*, vol. 29, no. 10, pp. 913–914, 1993.

[180] J. Boucart, C. Starck, F. Gaborit, A. Plais, N. Bouche, E. Derouin, L. Goldstein, C. Fortin, D. Carpentier, P. Salet, F. Brillouet, and J. Jacquet, "1-mW CW-RT monolithic VCSEL at 1.55 μm," *IEEE Photonics Technology Letters*, vol. 11, no. 6, pp. 629–631, 1999.

[181] A. Mereuta, A. Caliman, P. Wolf, A. Sirbu, V. Iakovlev, D. Ellafi, A. Rudra, D. Bimberg, and E. Kapon, "Long wavelength VCSELs made by wafer fusion," in *2016 IEEE Photonics Conference (IPC)*, pp. 337–338, oct 2016.

[182] J. A. Tatum, D. Gazula, L. A. Graham, J. K. Guenter, R. H. Johnson, J. King, C. Kocot, G. D. Landry, I. Lyubomirsky, A. N. MacInnes, E. M. Shaw, K. Balemarthy, R. Shubochkin, D. Vaidya, M. Yan, and F. Tang, "VCSEL-Based Interconnects for Current and Future Data Centers," *Journal of Lightwave Technology*, vol. 33, no. 4, pp. 727–732, 2015.

[183] A. Willner, *Optical Fiber Telecommunications VII.* Elsevier, 2019.

[184] P. Boulay and P. Mukish, "VCSELS - Technology, Industry and market trends - Market & Technology report," 2018.

[185] P. Mukish, P. Boulay, and M. Vallo, "Status of the solid-state ligthing source industry 2019 - Market & Technology Report," 2019.

[186] Q. Cheng, M. Bahadori, M. Glick, S. Rumley, and K. Bergman, "Recent advances in optical technologies for data centers: a review," *Optica*, vol. 5, pp. 1354–1370, nov 2018.

[187] D. M. Kuchta, A. V. Rylyakov, F. E. Doany, C. L. Schow, J. E. Proesel, C. W. Baks, P. Westbergh, J. S. Gustavsson, and A. Larsson, "A 71-Gb/s NRZ Modulated 850-nm VCSEL-Based Optical Link," *IEEE Photonics Technology Letters*, vol. 27, no. 6, pp. 577–580, 2015.

[188] J. M. Castro, R. Pimpinella, B. Kose, P. Huang, B. Lane, K. Szczerba, P. Westbergh, T. Lengyel, J. S. Gustavsson, A. Larsson, and P. A. Andrekson, "Investigation of 60 Gb/s 4-PAM Using an 850 nm VCSEL and Multimode Fiber," *Journal of Lightwave Technology*, vol. 34, no. 16, pp. 3825–3836, 2016.

[189] R. Puerta, M. Agustin, Ł. Chorchos, J. Toński, J. R. Kropp, N. Ledentsov, V. A. Shchukin, N. N. Ledentsov, R. Henker, I. T. Monroy, J. J. V. Olmos, and J. P. Turkiewicz, "Effective 100 Gb/s IM/DD 850-nm Multi- and Single-Mode VCSEL Transmission Through OM4 MMF," *Journal of Lightwave Technology*, vol. 35, no. 3, pp. 423–429, 2017.

[190] P. Moser, J. A. Lott, G. Larisch, and D. Bimberg, "Impact of the Oxide-Aperture Diameter on the Energy Efficiency, Bandwidth, and Temperature Stability of 980-nm VCSELs," *Journal of Lightwave Technology*, vol. 33, no. 4, pp. 825–831, 2015.

[191] P. Wolf, P. Moser, G. Larisch, W. Hofmann, and D. Bimberg, "High-Speed and Temperature-Stable, Oxide-Confined 980-nm VCSELs for Optical Interconnects," *IEEE Journal of Selected Topics in Quantum Electronics*, vol. 19, no. 4, p. 1701207, 2013.

[192] G. Larisch, P. Moser, J. A. Lott, and D. Bimberg, "Impact of Photon Lifetime on the Temperature Stability of 50 Gb/s 980 nm VCSELs," *IEEE Photonics Technology Letters*, vol. 28, pp. 2327–2330, nov 2016.

[193] G. Kanakis, N. Iliadis, W. Soenen, B. Moeneclaey, N. Argyris, Kalavrouziotis, D. Spiga, and H. Bakopoulos, P. Avramopoulos, "High-Speed VCSEL-Based Transceiver for 200 GbE Short-Reach Intra-Datacenter Optical Interconnects," *Applied sciences*, vol. 9, no. 12, p. 2488, 2019.

[194] M. Verplaetse, L. Breyne, C. Neumeyr, T. D. Keulenaer, W. Soenen, X. Yin, P. Ossieur, G. Torfs, and J. Bauwelinck, "DSP-free and real-time NRZ transmission of 50Gb/s

over 15km SSMF and 64Gb/s back-to-back with a 1.3u m VCSEL," in *Optical Fiber Communication Conference Postdeadline Papers*, Optical Society of America, 2018.

[195] M. Muller, W. Hofmann, A. Nadtochiy, A. Mutig, G. Böhm, M. Ortsiefer, D. Bimberg, and M. Amann, "1.55 um high-speed VCSELs enabling error-free fiber-transmission up to 25 Gbit/s," in *22nd IEEE International Semiconductor Laser Conference*, pp. 156–157, 2010.

[196] J. Luo, B. Wu, Y. Ma, A. Daly, C. Neumeyr, Z. Feng, H. Segawa, and M. Ortsiefer, "40-Gb/s 10-Krn SSMF Transmission Using Directly PAM4 Modulation of 1.5 um 10 GHz VCSEL," in *2016 Asia Communications and Photonics Conference (ACP)*, pp. 1–3, nov 2016.

[197] F. Karinou, C. Prodaniuc, N. Stojanovic, M. Ortsiefer, A. Daly, R. Hohenleitner, B. Kögel, and C. Neumeyr, "Directly PAM-4 Modulated 1530-nm VCSEL Enabling 56 Gb/s/ λ Data-Center Interconnects," *IEEE Photonics Technology Letters*, vol. 27, no. 17, pp. 1872–1875, 2015.

[198] R. Rodes, J. Estaran, B. Li, M. Muller, J. B. Jensen, T. Gruendl, M. Ortsiefer, C. Neumeyr, J. Rosskopf, K. J. Larsen, M. . Amann, and I. T. Monroy, "100 Gb/s single VCSEL data transmission link," in *OFC/NFOEC*, pp. 1–3, 2012.

[199] A. Malik and P. Singh, "Free Space Optics: Current Applications and Future Challenges," *International Journal of Optics*, 2015.

[200] C. Li, H. Lu, T. Lu, W. Tsai, B. Chen, C. Chu, C. Wu, and C. Liao, "A 100m/40Gbps 680-nm VCSEL-based LiFi transmission system," in *2016 Conference on Lasers and Electro-Optics (CLEO)*, pp. 1–2, 2016.

[201] W. Tsai, H. Lu, C. Li, T. Lu, C. Liao, C. Chu, and P. Peng, "A 50-m/40 Gb/s 680-nm VCSEL-Based FSO Communication," *IEEE Photonics Journal*, vol. 8, no. 2, pp. 1–8, 2016.

[202] H.-H. Lu, C.-Y. Li, C.-M. Ho, M.-T. Cheng, X.-Y. Lin, Z.-Y. Yang, and H.-W. Chen, "64 Gb/s PAM4 VCSEL-based FSO link," *Optics Express*, vol. 25, pp. 5749–5757, mar 2017.

[203] Y. Wang, H. Lu, C. Li, P. Chew, Y. Jheng, W. Tsai, and X. Huang, "A High-Speed 84 Gb/s VSB-PAM8 VCSEL Transmitter-Based Fiber-IVLLC Integration," *IEEE Photonics Journal*, vol. 10, pp. 1–8, oct 2018.

[204] J. Skidmore, "Semiconductor Lasers for 3-D Sensing," *Opt. Photon. News*, vol. 30, no. 2, pp. 26–33, 2019.

[205] J. Pozo and E. Beletkaia, "VCSEL Technology in the Data Communication Industry," *PhotonicsViews*, vol. 16, no. 6, pp. 21–23, 2019.

[206] A. Solanki and A. Nayyar, *Green Building Management and Smart Automation.* Ad-

vances in Civil and Industrial Engineering, IGI Global, 2019.

[207] F. Zhao, H. Jiang, and Z. Liu, "Recent development of automotive LiDAR technology, industry and trends," in *Eleventh International Conference on Digital Image Processing (ICDIP 2019)*, vol. 11179, pp. 1132–1139, SPIE, 2019.

[208] A. Mutig, *High Speed VCSELs for Optical Interconnects*. PhD thesis, Technical University of Berlin, 2011.

[209] C. J. O'Brien, M. L. Majewski, and A. D. Rakic, "A Critical Comparison of High-Speed VCSEL Characterization Techniques," *Journal of Lightwave Technology*, vol. 25, no. 2, pp. 597–605, 2007.

[210] L. A. Coldren and S. W. Corzine, *Diode Lasers and Photonic Integrated Circuits*. Wiley Series in Microwave and Optical Engineering, Wiley, 1 ed., 1995.

[211] A. Bacou, A. Hayat, V. Iakovlev, A. Syrbu, A. Rissons, J. C. Mollier, and E. Kapon, "Electrical modeling of long-wavelength VCSELs for intrinsic parameters extraction," *IEEE Journal of Quantum Electronics*, vol. 46, no. 3, pp. 313–322, 2010.

[212] G. P. Agrawal, *Fiber-optic Communication Systems*. Wiley series in microwave and optical engineering, Wiley-Interscience, 2002.

[213] R. S. Tucker, "High-Speed Modulation of Semiconductor Lasers," *IEEE Transactions on Electron Devices*, vol. 32, no. 12, pp. 2572–2584, 1985.

[214] G. P. Agrawal and N. K. Dutta, *Semiconductor Lasers*. Van Nostrand Reinhold, 1993.

[215] K. Petermann, *Laser Diode Modulation and Noise*. Kluwar Academic Publishers, 1988.

[216] R. W. Dixon and W. B. Joyce, "Generalized expressions for the turn-on delay in semiconductor lasers," *Journal of Applied Physics*, vol. 50, no. 7, pp. 4591–4595, 1979.

[217] S. Vidal, J. Degert, J. Oberlé, and E. Freysz, "Femtosecond optical pulse shaping for tunable terahertz pulse generation," *Journal of the Optical Society of America B*, vol. 27, no. 5, pp. 1044–1050, 2010.

[218] K. J. Mohler, B. J. Bohn, M. Yan, G. Mélen, T. W. Hänsch, and N. Picqué, "Dual-comb coherent Raman spectroscopy with lasers of 1-GHz pulse repetition frequency," *Optics letters*, vol. 42, no. 2, pp. 318–321, 2017.

[219] Y. Kusama, Y. Tanushi, M. Yokoyama, R. Kawakami, T. Hibi, Y. Kozawa, T. Nemoto, S. Sato, and H. Yokoyama, "7-ps optical pulse generation from a 1064-nm gain-switched laser diode and its application for two-photon microscopy," *Optics Express*, vol. 22, pp. 5746–5753, mar 2014.

[220] B. Li, C. Sun, Y. Ling, H. Zhou, and K. Qiu, "Step-Pulse Modulation of Gain-Switched Semiconductor Pulsed Laser," *Applied sciences*, vol. 9, no. 602, 2019.

[221] R. Tucker and I. Kaminow, "High-frequency characteristics of directly modulated In-GaAsP ridge waveguide and buried heterostructure lasers," *Journal of Lightwave Technology*, vol. 2, no. 4, pp. 385–393, 1984.

[222] A. Rissons, *Caractérisation et modélisation optoélectronique de diodes laser à cavité verticale émettant par la surface (VCSEL).* PhD thesis, École National Supériuer de l'Aeronautique et de l'Espace, 2003.

[223] J. Perchoux, *Caractérisation et modélisation du bruit d'intensité de VCSELs (Al-GaAs) et de son influence sur le bruit de phase des liaisons opto-hyperfréquences.* PhD thesis, École National Supériuer de l'Aeronautique et de l'Espace, 2005.

[224] J. Singh, *Semiconductor Optoelectronics: Physics and Technology.* Electrical engineering series, McGraw-Hill, 1995.

[225] S. F. Yu, *Analysis and Design of Vertical Cavity Surface Emitting Lasers.* Wiley Series in Lasers and Applications, Wiley, 2003.

[226] C. Henry, "Theory of the linewidth of semiconductor lasers," *IEEE Journal of Quantum Electronics*, vol. 18, no. 2, pp. 259–264, 1982.

[227] T. Septon, S. Gosh, A. Becker, V. Sichkovskyi, F. Schnabel, A. Rippien, J. P. Reithmaier, and G. Eisenstein, "Narrow Linewidth InAs/InP Quantum Dot DFB Laser," in *2019 Optical Fiber Communications Conference and Exhibition (OFC)*, pp. 1–3, 2019.

[228] K. Kasai, M. Nakazawa, M. Ishikawa, and H. Ishii, "8 kHz linewidth, 50 mW output, full C-band wavelength tunable DFB LD array with self-optical feedback," *Optics Express*, vol. 26, pp. 5675–5685, mar 2018.

[229] C. Harder, J. Katz, S. Margalit, J. Shacham, and A. Yariv, "Noise equivalent circuit of a semiconductor laser diode," *IEEE Journal of Quantum Electronics*, vol. 18, no. 3, pp. 333–337, 1982.

[230] D. E. McCumber, "Intensity Fluctuations in the Output of cw Laser Oscillators. I," *Phys. Rev.*, vol. 141, pp. 306–322, jan 1966.

[231] S. Spiga, W. Soenen, A. Andrejew, D. M. Schoke, X. Yin, J. Bauwelinck, G. Boehm, and M. Amann, "Single-Mode High-Speed 1.5-μm VCSELs," *Journal of Lightwave Technology*, vol. 35, no. 4, pp. 727–733, 2017.

[232] B. Tell, K. F. Brown-Goebeler, R. E. Leibenguth, F. M. Baez, and Y. H. Lee, "Temperature dependence of GaAs-AlGaAs vertical cavity surface emitting lasers," *Applied Physics Letters*, vol. 60, no. 6, pp. 683–685, 1992.

[233] P. V. Mena, J. J. Morikuni, S. . Kang, A. V. Harton, and K. W. Wyatt, "A simple rate-equation-based thermal VCSEL model," *Journal of Lightwave Technology*, vol. 17, no. 5, pp. 865–872, 1999.

[234] C. Chen, P. O. Leisher, A. A. Allerman, K. M. Geib, and K. D. Choquette, "Temperature Analysis of Threshold Current in Infrared Vertical-Cavity Surface-Emitting Lasers," *IEEE Journal of Quantum Electronics*, vol. 42, pp. 1078–1083, oct 2006.

[235] A. Quirce, C. de Dios, A. Valle, L. Pesquera, and P. Acedo, "Polarization Dynamics in VCSEL-Based Gain Switching Optical Frequency Combs," *Journal of Lightwave Technology*, vol. 36, no. 10, pp. 1798–1806, 2018.

[236] C. W. Wilmsen, L. A. Coldren, and H. Temkin, *Vertical-Cavity Surface-Emitting Lasers: Design, Fabrication, Characterization, and Applications.* Cambridge Studies in Modern Optics, Cambridge University Press, 2001.

[237] L. A. Coldren, S. W. Corzine, and M. L. Mashanovitch, *Diode Lasers and Photonic Integrated Circuits.* Wiley Series in Microwave and Optical Engineering, John Wiley & Sons, 2 ed., 2012.

[238] A. Consoli, J. Arias, J. M. Tijero, F. J. L. Hernández, and I. Esquivias, "Electrical characterization of long wavelength VCSELs with tunnel junction," in *Vertical-Cavity Surface-Emitting Lasers XV*, vol. 7952, pp. 73–82, International Society for Optics and Photonics, SPIE, 2011.

[239] J. Minch, S. H. Park, T. Keating, and S. L. Chuang, "Theory and experiment of In/sub 1-x/Ga/sub x/As/sub y/P/sub 1-y/ and In/sub 1-x-y/Ga/sub x/Al/sub y/As long-wavelength strained quantum-well lasers," *IEEE Journal of Quantum Electronics*, vol. 35, no. 5, pp. 771–782, 1999.

[240] P. Pérez, A. Valle, I. Noriega, and L. Pesquera, "Measurement of the Intrinsic Parameters of Single-Mode VCSELs," *Journal of Lightwave Technology*, vol. 32, no. 8, pp. 1601–1607, 2014.

[241] C. Chen, N. H. Zhu, S. J. Zhang, and Y. Liu, "Characterization of Parasitics in TO-Packaged High-Speed Laser Modules," *IEEE Transactions on Advanced Packaging*, vol. 30, no. 1, pp. 97–103, 2007.

[242] M.-C. Lin, *The Study of 10-40 Gb/s High-Speed Laser Module Based on Coaxial-Type Packages.* PhD thesis, National Sun Yat-Sen University, 2008.

[243] B. R. Bennett, R. A. Soref, and J. A. Del Alamo, "Carrier-induced change in refractive index of InP, GaAs and InGaAsP," *IEEE Journal of Quantum Electronics*, vol. 26, pp. 113–122, jan 1990.

[244] F. Devaux, Y. Sorel, and J. F. Kerdiles, "Simple measurement of fiber dispersion and of chirp parameter of intensity modulated light emitter," *Journal of Lightwave Technology*, vol. 11, no. 12, pp. 1937–1940, 1993.

[245] R. Hui and M. S. O'Sullivan, *Fiber Optic Measurement Techniques.* Electronics & Electrical, Elsevier/Academic Press, 2009.

[246] K. Y. Lau, "Short-pulse and high-frequency signal generation in semiconductor lasers," *Journal of Lightwave Technology*, vol. 7, no. 2, pp. 400–419, 1989.

[247] A. Consoli, I. Esquivias, F. J. Lopez Hernandez, J. Mulet, and S. Balle, "Characterization of Gain-Switched Pulses From 1.55-um VCSEL," *IEEE Photonics Technology Letters*, vol. 22, no. 11, pp. 772–774, 2010.

[248] K. Koizumi, M. Yoshida, and M. Nakazawa, "10-GHz 11.5-ps Pulse Generation From a Single-Mode Gain-Switched InGaAs VCSEL at 1.1 um," *IEEE Photonics Technology Letters*, vol. 21, pp. 1704–1706, nov 2009.

[249] M. Varon, *Étude et réalisation d'un oscillateur opto-microonde à base de VCSEL pour la génération harmonique de signaux microondes*. PhD thesis, Institut Supérieur de l'Aéronautique et de l'Espace, 2008.

[250] S. Wu, A. Yariv, H. Blauvelt, and N. Kwong, "Theoretical and experimental investigation of conversion of phase noise to intensity noise by Rayleigh scattering in optical fibers," *Applied Physics Letters*, vol. 59, no. 10, pp. 1156–1158, 1991.

[251] K. Yamauchi, Y. Iyama, M. Yamaguchi, Y. Ikeda, S. Urasaki, and T. Takagi, "X-band MMIC power amplifier with an on-chip temperature-compensation circuit," *IEEE Transactions on Microwave Theory and Techniques*, vol. 49, no. 12, pp. 2501–2506, 2001.

[252] M. E. Belkin, L. M. Belkin, A. V. Loparev, V. Iakovlev, G. Suruceanu, A. Mereuta, A. Caliman, A. Sirbu, and E. Kapon, "Microwave-band optoelectronic frequency converters based on long wavelength VCSELs," in *2011 IEEE International Conference on Microwaves, Communications, Antennas and Electronic Systems (COMCAS 2011)*, pp. 1–5, nov 2011.

[253] A. Rosado, A. Pérez-Serrano, J. M. G. Tijero, Á. Valle, L. Pesquera, and I. Esquivias, "Experimental study of optical frequency comb generation in gain-switched semiconductor lasers," *Optics & Laser Technology*, vol. 108, pp. 542–550, 2018.

[254] E. Rubiola and R. Brendel, "A generalization of the Leeson effect," FEMTO-ST Institute, 2010.

[255] O. Lelièvre, V. Crozatier, P. Berger, G. Baili, O. Llopis, D. Dolfi, P. Nouchi, F. Goldfarb, F. Bretenaker, L. Morvan, and G. Pillet, "A Model for Designing Ultralow Noise Single- and Dual-Loop 10-GHz Optoelectronic Oscillators," *Journal of Lightwave Technology*, vol. 35, pp. 4366–4374, oct 2017.

[256] D. Derickson and M. Muller, *Digital Communications Test and Measurement: High-speed Physical Layer Characterization*. Modern Semiconductor Design, Prentice Hall, 2008.

[257] M. Kaba, *Etude Approfondie et Realisation d'un Oscillateur Opto-Microondes por Applications Fibreés à 1550 nm*. PhD thesis, École National Supériuer de l'Aeronautique

et de l'Espace, 2003.

[258] J. L. Gimlett and N. K. Cheung, "Effects of phase-to-intensity noise conversion by multiple reflections on gigabit-per-second DFB laser transmission systems," *Journal of Lightwave Technology*, vol. 7, no. 6, pp. 888–895, 1989.

[259] J. P. Cahill, W. Zhou, and C. R. Menyuk, "Additive phase noise of fiber-optic links used in photonic microwave-generation systems," *Appl. Opt.*, vol. 56, pp. B18—-B25, jan 2017.

[260] V. Kalavally, I. D. Rukhlenko, M. Premaratne, and T. Win, "Multipath Interference in Pulse-Pumped Fiber Raman Amplifiers: Analytical Approach," *Journal of Lightwave Technology*, vol. 28, no. 18, pp. 2701–2707, 2010.

[261] A. Yariv, H. Blauvelt, and S. . Wu, "A reduction of interferometric phase-to-intensity conversion noise in fiber links by large index phase modulation of the optical beam," *Journal of Lightwave Technology*, vol. 10, no. 7, pp. 978–981, 1992.

[262] F. Gruet, A. Al-Samaneh, E. Kroemer, L. Bimboes, D. Miletic, C. Affolderbach, D. Wahl, R. Boudot, G. Mileti, and R. Michalzik, "Metrological characterization of custom-designed 894.6 nm VCSELs for miniature atomic clocks," *Opt. Express*, vol. 21, pp. 5781–5792, mar 2013.

[263] G. Charalambous, G. K. M. Hasanuzzaman, A. Perentos, and S. Iezekiel, "Optoelectronic recirculating delay line implementation of a high-q optoelectronic oscillator," in *2017 International Topical Meeting on Microwave Photonics (MWP)*, pp. 1–4, oct 2017.

[264] Y. Cheng, J. Yan, and S. Zhao, "Self-Oscillating Parametric Optical Frequency Comb Generation Using an Electroabsorption Modulated Laser-Based Optoelectronic Oscillator," *IEEE Photonics Journal*, vol. 11, no. 4, pp. 1–9, 2019.

[265] H. Du, R. Guo, H. Peng, Y. Xu, and Z. Chen, "Tunable Optical Comb Generation Utilizing an Optoelectronic Oscillator Based on Stimulated Brillouin Scattering," in *2018 Asia Communications and Photonics Conference (ACP)*, pp. 1–3, oct 2018.

[266] F. Fan, J. Hu, W. Zhu, J. Wang, Y. Gu, X. Han, Z. Wu, and M. Zhao, "Tunable optoelectronic oscillator based on coupled double loops and stimulated brillouin scattering," in *2017 International Topical Meeting on Microwave Photonics (MWP)*, pp. 1–3, oct 2017.

[267] K. Saleh, P. H. Merrer, O. Llopis, and G. Cibiel, "Optoelectronic oscillator based on fiber ring resonator: Overall system optimization and phase noise reduction," in *2012 IEEE International Frequency Control Symposium Proceedings*, pp. 1–6, 2012.

[268] V. Auroux, A. Fernandez, O. Llopis, P. H. Merrer, and A. Vouzellaud, "Microwave phase noise properties of optical links involving small signal and gain saturated optical amplifiers," in *2014 European Frequency and Time Forum (EFTF)*, pp. 381–383, 2014.

[269] D. M. Baney, P. Gallion, and R. S. Tucker, "Theory and Measurement Techniques for the Noise Figure of Optical Amplifiers," *Optical Fiber Technology*, vol. 6, no. 2, pp. 122–154, 2000.

[270] G. Cibiel, M. Regis, E. Tournier, and O. Llopis, "AM noise impact on low level phase noise measurements," *IEEE Transactions on Ultrasonics, Ferroelectrics, and Frequency Control*, vol. 49, no. 6, pp. 784–788, 2002.

[271] C. Lin, P. L. Liu, T. C. Damen, D. J. Eilenberger, and R. L. Hartman, "A Simple Picosecond Pulse Generation Scheme for Injection Lasers," in *Electronics Letters* (C. V. Shank, R. Hochstrasser, and W. Kaiser, eds.), vol. 16, (Berlin, Heidelberg), pp. 30–33, Springer Berlin Heidelberg, 1980.

[272] H. Liu, M. Fukazawa, Y. Kawai, and T. Kamiya, "Gain-switched picosecond pulse (<10 ps) generation from 1.3 mu m InGaAsP laser diodes," *IEEE Journal of Quantum Electronics*, vol. 25, no. 6, pp. 1417–1425, 1989.

[273] I. H. White, D. F. G. Gallagher, and M. Osinski, "Erratum: Direct streak-camera observation of picosecond gain-switched optical pulses from a 1.5 μm semiconductor laser," *Electronics Letters*, vol. 21, no. 8, pp. 359–, 1985.

[274] P. Pepeljugoski, J. Lin, J. Gamelin, M. Hong, and K. Y. Lau, "Ultralow timing jitter in electrically gain-switched vertical cavity surface emitting lasers," *Applied Physics Letters*, vol. 62, no. 14, pp. 1588–1590, 1993.

[275] G. Hasnain, J. M. Wiesenfeld, T. C. Damen, J. Shah, J. D. Wynn, Y. H. Wang, and A. Y. Cho, "Electrically gain-switched vertical-cavity surface-emitting lasers," *IEEE Photonics Technology Letters*, vol. 4, pp. 6–9, jan 1992.

[276] I. Coddington, N. Newbury, and W. Swann, "Dual-comb spectroscopy," *Optica*, vol. 3, no. 4, pp. 414–426, 2016.

[277] A. R. Criado, C. de Dios, E. Prior, G. H. Döhler, S. Preu, S. Malzer, H. Lu, A. C. Gossard, and P. Acedo, "Continuous-Wave Sub-THz Photonic Generation With Ultra-Narrow Linewidth, Ultra-High Resolution, Full Frequency Range Coverage and High Long-Term Frequency Stability," *IEEE Transactions on Terahertz Science and Technology*, vol. 3, no. 4, pp. 461–471, 2013.

[278] I. Coddington, W. Swann, L. Nenadovic, and N. Newbury, "Rapid and precise absolute distance measurements at long range," *Nature Photonics*, vol. 3, pp. 351–356, 2009.

[279] M. Imran, P. M. Anandarajah, A. Kaszubowska-Anandarajah, N. Sambo, and L. Potí, "A Survey of Optical Carrier Generation Techniques for Terabit Capacity Elastic Optical Networks," *IEEE Communications Surveys Tutorials*, vol. 20, no. 1, pp. 211–263, 2018.

[280] J. He, F. Long, R. Deng, J. Shi, M. Dai, and L. Chen, "Flexible multiband OFDM ultra-wideband services based on optical frequency combs," *IEEE/OSA Journal of*

Optical Communications and Networking, vol. 9, no. 5, pp. 393–400, 2017.

[281] A. Quirce, C. de Dios, A. Valle, and P. Acedo, "VCSEL-Based Optical Frequency Combs Expansion Induced by Polarized Optical Injection," *IEEE Journal of Selected Topics in Quantum Electronics*, vol. 25, pp. 1–9, nov 2019.

[282] A. Criado, C. de Dios Fernandez, E. P. Cano, M. Ortsiefer, P. Meissner, and P. Acedo, "VCSEL-Based Optical Frequency Combs: Toward Efficient Single-Device Comb Generation," *IEEE Photonics Technology Letters*, vol. 25, pp. 1981–1984, oct 2013.

[283] E. Prior, C. De Dios, M. Ortsiefer, P. Meissner, and P. Acedo, "Understanding VCSEL-Based Gain Switching Optical Frequency Combs: Experimental Study of Polarization Dynamics," *Journal of Lightwave Technology*, vol. 33, pp. 4572–4579, nov 2015.

[284] P. K. Pepeljugoski, D. M. Cutrer, and K. Y. Lau, "Parametric dependence of timing jitter in gain switched semiconductor lasers," *Applied Physics Letters*, vol. 63, no. 26, pp. 3556–3558, 1993.

[285] J. M. Wiesenfeld, G. Hasnain, J. S. Perino, J. D. Wynn, R. E. Leibenguth, Y. . Wang, and A. Y. Cho, "Gain-switched GaAs vertical-cavity surface-emitting lasers," *IEEE Journal of Quantum Electronics*, vol. 29, no. 6, pp. 1996–2005, 1993.

[286] JEDEC Solid State Technology Association, "JEDEC Standard JESD65B Definition of Skew Specifications for Standard Logic Devices," 2003.

[287] S. Kobayashi, Y. Yamamoto, M. Ito, and T. Kimura, "Direct frequency modulation in AlGaAs semiconductor lasers," *IEEE Journal of Quantum Electronics*, vol. 18, no. 4, pp. 582–595, 1982.

[288] W. Jian, Q. Ji-Fang, and L. Jin-Tong, "Period-Doubling in 10 GHz Gain-Switched DFB Laser Diode," *Chinese Physics Letters*, vol. 24, pp. 2852–2854, sep 2007.

[289] Y. Tamura, H. Sakuma, K. Morita, M. Suzuki, Y. Yamamoto, K. Shimada, Y. Honma, K. Sohma, T. Fujii, and T. Hasegawa, "Lowest-ever 0.1419-dB/km loss optical fiber," in *2017 Optical Fiber Communications Conference and Exhibition (OFC)*, pp. 1–3, 2017.

[290] K. Wang, C. Gong, D. Zou, and Z. Xu, "Turbulence Channel Modeling and Non-Parametric Estimation for Optical Wireless Scattering Communication," *Journal of Lightwave Technology*, vol. 35, no. 13, pp. 2746–2756, 2017.

[291] R. K. Singh, Karmeshu, and S. Kumar, "A Novel Approximation for K Distribution : Closed-Form BER Using DPSK Modulation in Free-Space Optical Communication," *IEEE Photonics Journal*, vol. 9, no. 5, pp. 1–14, 2017.

[292] X. Liu, "Free-Space Optics Optimization Models for Building Sway and Atmospheric Interference Using Variable Wavelength," *IEEE Transactions on Communications*, vol. 57, no. 2, pp. 492–498, 2009.

[293] M. R. Bhatnagar, Z. Ghassemlooy, S. Zvanovec, M.-a. Khalighi, and M. M. Abadi, "Quantized Feedback-Based Differential Signaling for Free-Space Optical Communication System," *IEEE Transactions on Communications*, vol. 64, no. 12, pp. 5176–5188, 2016.

[294] M. T. Dabiri and S. M. S. Sadough, "Generalized Blind Detection of OOK Modulation for Free-Space Optical Communication," *IEEE Communications Letters*, vol. 21, no. 10, pp. 2170–2173, 2017.

[295] A. K. Majumdar and J. C. Ricklin, *Free-Space Laser Communications: Principles and Advances.* Optical and Fiber Communications Reports, Springer New York, 2010.

[296] C. Wree, C. P. Collier, S. Lane, A. Turney, B. Armentrout, C. Wree, C. P. Collier, S. Lane, J. Yates, N. Francis, and A. Joshi, "Ten Gb/s optically pre-amplified RZ-systems with very large link losses," *Proc. SPIE*, vol. 7091, 2008.

[297] Y. Liu, S. Zhao, Z. Gong, R. Hou, and R. Qiang, "Gamma radiation impact on performance of OOK , DPSK and homodyne BPSK based optical inter-satellite communication system," *Optics Communications*, vol. 350, pp. 276–282, 2015.

[298] P. J. Winzer and R.-J. Essiambre, "Advanced Optical Modulation Formats," *Proceedings of the IEEE*, vol. 94, no. 5, pp. 952–985, 2006.

[299] K. Elayoubi, *Study of communications channels for optical links through the atmosphere.* PhD thesis, Institut Supérieur de l'Aéronautique et de l'Espace ISAE-SUPAERO, 2019.

[300] I. Djordjevic, W. Ryan, and B. Vasic, *Coding for Optical Channels.* Springer US, 2010.

[301] Y. Chi and G. Lin, "Self Optical Pulsation Based RZ-BPSK and Reused RZ-OOK Bi-Directional OC-768 Transmission," *Journal of Lightwave Technology*, vol. 32, no. 20, pp. 3728–3734, 2014.

[302] J. P. Salvestrini, L. Guilbert, M. Fontana, M. Abarkan, and S. Gille, "Analysis and Control of the DC Drift in LiNbO3 Based Mach-Zehnder Modulators," *Journal of Lightwave Technology*, vol. 29, no. 10, pp. 1522–1534, 2011.